Queen Mary
University of London

Electronic Transport Properties of Linear Organic Semiconductors

Bunning, J. C.

The copyright of this thesis rests with the author and no quotation from it or information derived from it may be published without the prior written consent of the author

For additional information about this publication click this link.
http://qmro.qmul.ac.uk/jspui/handle/123456789/1757

Information about this research object was correct at the time of download; we occasionally make corrections to records, please therefore check the published record when citing. For more information contact scholarlycommunications@qmul.ac.uk

Electronic Transport Properties of Linear Organic Semiconductors

J. C. Bunning

Queen Mary
University of London

Department of Physics

2006

Submitted in partial fulfilment of the requirements for the degree of Doctor of Philosophy

Abstract

The electronic transport properties of certain organic semiconductors are expected to exhibit a quasi one-dimensional nature. Pulsed laser techniques have been used to study transient photoconductivity in a number of such linear molecular systems. This thesis explores carrier motion of zeolite encapsulated conjugated polymers such as polyacetylene and polypropyne, columnar discotic liquid crystals and single walled carbon nanotubes. At the time of writing, this thesis presents the first observations of transient photoconductivity for carbon nanotubes. In the systems studied: electric field, temperature and spectral dependencies are explored and the results are used to calculate a number of parameters, such as: carrier mobilities, carrier range and quantum efficiencies. Also, the effect of sample preparation has been investigated.

A variation on the Auston switch technique has enabled picosecond time resolved photocurrents to be measured on carbon nanotubes, with a rise time of the order of 100ps. A similar technique was utilised to study the encapsulated polymers, but no measurable effect was observed. The Kepler-LeBlanc Time of Flight technique has been employed to find the carrier mobility in a number of columnar discotic liquid crystals along with the quantum efficiency for carrier generation in those systems.

The results presented in this thesis have led to a greater understanding of charge transport on carbon nanotubes from which a 1D bimolecular recombination model has been proposed. We have demonstrated a novel polymeric DLC where electrons are the majority carrier and demonstrated a photogeneration mechanism controlled by Poole-Frenkel barrier lowering. We have also been able to refute the proposal that the 3D Onsager model is applicable for describing the photogeneration mechanism in most DLC's.

Contents

Title Page 1

Abstract 2

Contents Page 3

List of figures and tables 8

1 Introduction 14

1.1 Molecular Electronics 14

1.2 Conducting Polymers 15

1.3 Tertiary conjugated polymer structure 20

1.4 Encapsulation of polymers within Zeolite nanochannels 23

1.5 Carbon Nanotubes 25

1.6 Zeolites 33

1.6.1 Mordenite 34

1.6.2 Beta 35

1.6.3 Faujasite 36

1.7 Single Walled Carbon Nanotubes 37

1.8 Discotic Liquid Crystals 39

1.8.1 HAT6 43

1.8.2 HAT11 44

1.8.3 PTP9 44

1.8.4 2FHAT6 46

1.8.5 Triblock co-polymer discotic 46

1.9 DLC Phase Boundaries 47

2 Theory of Photoconduction 49

2.1 Basic Electrostatics 49

2.2 Photogeneration of charges 51

2.3 Polymer chain and nanotube orientation modelling in 3D 54

2.4 The Onsager theory of geminate recombination 56

2.5 Poole-Frenkel Behaviour (barrier lowering) 59

2.6 Polarons 60

2.7 Loss Mechanisms 61

2.7.1 Bimolecular Recombination 62

2.7.2 Charge Trapping 63

2.7.3 Transits 65

3 Experimental Techniques 67

3.1 The Lasers 67

3.2 The Co-Axial Cell 68

3.3 Testing the Co-Axial Cell 72

3.4 Quartz Rod Fibre Optic 74

3.5 High Frequency Amplification (The Phillips NE5200) 76

3.6 Impedance matching of the amplifier circuit. 77

3.7 Testing the amplifier 79

3.8 Determination of pulse arrival time to minimise jitter 81

3.9 Determination of laser pulse energy 84

3.10 Voltage step generation. 87

3.11 Discotic Liquid Crystal Cell 90

3.12 Discotic Liquid Crystal Signal Amplification 93

Chapter 4: Results 95

4.1 Polymer filled Zeolites 95

4.1.1 Absorbance of the suspending medium 95

4.1.2 Encapsulated Polymer Results 96

4.2 Discotic Liquid Crystals 97

4.2.1 - HAT6 98

4.2.2 - HAT6:PTP9 102

4.2.3 - HAT11:PTP9 105

4.2.4 - 2FHAT6 108

4.2.5 - Polymer DLC 110

4.3 Single Walled Carbon Nanotubes 114

4.3.1 DC Dark Current Evolution 115

4.3.2 Initial SWNT photoconduction studies 116

4.3.3 Test of photocurrent stability 119

4.3.4 Detailed SWNT Photosignal Studies 121

4.3.5 - A study on the effect of size separated SWNTs. 124

4.3.6 - Analysis of nanotube tail decays. 126

4.3.7 - Intensity dependence of photocurrents 128

4.3.8 – Spectral Dependence of Nanotube Photocurrents 131

Chapter 5 – Discussion of Results 134

5.1 Encapsulated Polymers 134

5.1.1 - Do the zeolites contain photoconductive material? 134

5.1.2 - Is light able to penetrate the zeolite structure? 135

5.1.3 - Are the polymer chains long enough to produce measurable carrier separation? 135

5.1.4 - Do isolated single chains retard the carrier range? 136

5.1.5 – Other Considerations 136

5.1.6 – Conclusions on Encapsulated Polymers 138

5.2 – Discotic Liquid Crystals 138

5.2.1. The applicability of the 3D Onsager Model 138

5.2.1.1 - HAT6 139

5.2.1.2 - HAT6:PTP9 140

5.2.1.3 - HAT11:PTP9 141

5.2.1.4 – 2FHAT6 142

5.2.1.5 – 3D Onsager Conclusions 143

5.2.2 – Charge Transport Mechanisms 144

5.2.2.1 – HAT6:PTP9 145

5.2.2.2 – 2FHAT6 146

5.2.3 – Tri-Block Co-Polymer DLC 147

5.2.3.1 – Isotropic Photocurrent 147

5.2.3.2 – Poole-Frenkel Behaviour 148

5.2.3.3 – Temperature dependence of dielectric constant 149

5.2.3.4 – Limits on Quantum Efficiency and Mobility 152

5.2.3.5 – Conclusions on Tri-Block Co-Polymer 154

5.3 - Carbon Nanotubes 155

5.3.1 – Nanotube Concentration Dependence 155

5.3.2 – Quantum Efficiency/Carrier Range Entanglement 159

5.3.3 –SWNT Quantum Efficiencies 162

5.3.4 – SWNT Photocurrent Decay Analysis 163

5.3.5 - Bi-Molecular Recombination in 1D 168

5.3.6 – Application of the Bi-Molecular Model 175

5.3.7 - SWNT Conclusions 187

Chapter 6 – Conclusions 188

6.1 Encapsulated Polymers 188

6.2 Discotic Liquid Crystals 189

6.3 Single Walled Carbon Nanotubes 191

6.4 Closing Remarks and Further Work 193

Publications 195

Appendix 196

Appendix 1 – Response Times and Quadrature 196

Appendix 2 – SWNT Band Gap Energies 198

Acknowledgements 199

References 200

List of figures and tables

Figures

Figure 1.1: Orbital diagram of sp^2 hybridisation. **16**

Figure 1.2: The formation of π delocalisation **17**

Figure 1.3: CIS (a) and TRANS (b) Polyacetylene structures. **18**

Figure 1.4: Logarithmic Conductivity Ladder **19**

Figure 1.5: Polymer in random coil configuration **20**

Figure 1.6: Polymer Hairpin bend. **20**

Figure 1.7: Polydiacetylene molecule with BCMU sidegroups **21**

Figure 1.8: BCMU photocurrent **22**

Figure 1.9: Cartoon of filled zeolite **23**

Figure 1.10: Graphene Sheet – An unravelled nanotube **26**

Figure 1.11: Single Walled Nanotube Diagrams [(a) Armchair Nanotube, (b) Zig-Zag Nanotube, (c) Chiral Nanotube] **27**

Figure 1.12: Graphene Unit Cells **29**

Figure 1.13: Allowed k states for nanotubes. **30**

Figure 1.14: Sketch of k states for armchair and zig-zag nanotubes. **31**

Figure 1.15: Sketch of k states for a chiral nanotube. **32**

Figure 1.16: Mordenite zeolite structure **34**

Figure 1.17: Beta zeolite structure **35**

Figure 1.18: Faujasite zeolite structure **36**

Figure 1.19: SEM image from SWNT batch used. **38**

Figure 1.20: Crystalline phase **40**

Figure 1.21: Smectic A phase **41**

Figure 1.22: Smectic C phase 41

Figure 1.23: Nematic Phase 42

Figure 1.24: Molecular Structure of HAT6 43

Figure 1.25: Molecular Structure of HAT11 43

Figure 1.26: Molecular Structure of PTP9 44

Figure 1.27: Single Molecule System (e.g., HAT6 or 2FHAT6) 45

Figure 1.28: Complementary Binary System (e.g., HAT6:PTP9) 45

Figure 1.29: Molecular Structure of 2FHAT6 Figure 1.30: Molecular Structure of Triblock Co-Polymer 46

Figure 1.31: Triblock co-polymer phases 47

Figure 2.1: A charge, q, moves in an Electric Field causing a current. 50

Figure 2.2: Basic schematic of photoconduction experiment. 51

Figure 2.3: 3D isotropic model of chain lengths 55

Figure 2.4: Charge separation in an Electric Field 56

Figure 2.5a: Total Energy of an electron/hole pair in an electric field 58

Figure 2.5b: Total Energy of an electron/hole pair in fig. 2.5a with field doubled. 58

Figure 2.6: Transit of a homogenously illuminated sample 65

Figure 2.7: Transit of an ideal Time of Flight signal 66

Figure 3.1: Co-axial geometry 69

Figure 3.2: Schematic diagram of co-axial cell 71

Figure 3.3: 3D perspective view of the 50Ω co-axial cell. 72

Figure 3.4: Testing the co-axial cell with a fast pulse. 73

Figure 3.5: Quartz Rod Coupling Efficiency 75

Figure 3.6: Fibre Optic/Electrode Interface Overlap 75

Figure 3.7: Schematic diagram of the NE52000 amplifier 77

Figure 3.8: Diagram of gain block amplifier arrangement 77

Figure 3.9: Diagram of stripline configuration 78

Figure 3.10: NE5200 Amplifier output (20 ns pulse) 80

Figure 3.11: NE5200 Output (100 ns Pulse) 81

Figure 3.12: Problems with jitter 82

Figure 3.13: Experimental arrangement 83

Figure 3.14: Light intensity calibration experiment 85

Figure 3.15: Determination of Light Intensity 86

Figure 3.16: Calibration of Photodiode 87

Figure 3.17: Valve Circuit 88

Figure 3.18: Valve Rectifier Circuit 89

Figure 3.19: Test of the voltage step generator. 90

Figure 3.20: Schematic diagram of the DLC sandwich cell 91

Figure 3.21: Circuit layout of the DLC amplifier 93

Figure 4.1: Light Transmission of Brookfield Polymer Oil 95

Figure 4.2: Transmission spectrum of unfilled TOF cell 97

Figure 4.3: Determination of sandwich cell thickness 98

Figure 4.4: Hole transits in HAT6 at different fields in the discotic mesophase 99

Figure 4.5: Determination of Transit Time for HAT6 100

Figure 4.6: Determination of HAT6 Hole Mobility 100

Figure 4.7: Photocharge created in HAT6 as calculated from the data in Figure 4.4 101

Figure 4.8: Measured Quantum Efficiency of HAT6 102

Figure 4.9: HAT6:PTP9 Example Transit when in the columnar discotic phase 103

Figure 4.10: HAT6:PTP9 Mobility 103

Figure 4.11: HAT6:PTP9 Mobility vs. Temperature 104

Figure 4.12: HAT6:PTP9 Quantum Efficiency versus Electric Field 104

Figure 4.13: HAT6:PTP9 Quantum Efficiency vs Temperature **105**

Figure 4.14: HAT11:PTP9 Hole photocurrents with Spacecharge **105**

Figure 4.15: HAT11:PTP9 Quantum Efficiency vs Electric Field **106**

Figure 4.16: HAT11:PTP9 Quantum Efficiency vs Temperature **107**

Figure 4.17: Hole Transits in 2FHAT6 at different fields **108**

Figure 4.18: Carrier Velocity for 2FHAT6 vs Electric Field **109**

Figure 4.19: Hole Mobility for 2FHAT6 versus temperature **110**

Figure 4.20: Electron and hole photocurrents in Triblock copolymer **111**

Figure 4.21: Electric field dependence of peak photocurrent for electrons **112**

Figure 4.22: Peak photocurrent with temperature **112**

Figure 4.23: The field dependence of $\{\eta\phi\}s$ **113**

Figure 4.24: Temperature dependence of $\{\eta\phi\}s$ **114**

Figure 4.25: Sample Dark Current vs Time **115**

Figure 4.26: Nanotube photocurrent (1 GHz Scope) **116**

Figure 4.27: Relative Photoconductivity of Nanotubes and Carbon Black Silicon Oil Suspensions **117**

Figure 4.28: Concentrated nanotube sample showing both transient conduction and dark currents. **119**

Figure 4.29a: Single shot nanotube signals over time. **120**

Figure 4.29b: Histogram of nanotube peak photocurrent distribution. **121**

Figure 4.30: Photocurrents for SWNT Sample 1 **122**

Figure 4.31: Peak Photocurrent vs Electric Field for SWNT Sample 1 **123**

Figure 4.32: Peak Photocurrent versus Electric Field for different SWNT concentrations as a fraction of mass **123**

Figure 4.33: Comparison between 1 mm and 0.45 mm SWNT samples **127**

Figure 4.34: Comparison of 1 mm decay tails at different fields **128**

Figure 4.35: Peak photocurrent vs. Light Intensity as wavelength is varied **129**

Figure 4.36: Peak photocurrent vs. Light Intensity as concentration by weight fraction is varied **130**

Figure 4.37: Peak photocurrent vs. Light Intensity as field is varied **130**

Figure 4.38: Peak photocurrent vs. Light Intensity as field is varied **131**

Figure 4.39: Light Intensity vs. Wavelength for OPO laser. **132**

Figure 4.40: Non-Normalised Nanotube Photoaction Spectrum with expected 1st band gap resonances superimposed. **133**

Figure 5.1: IR Transmission Spectra of sample JT6 **135**

Figure 5.2: Experimental and Theoretical Slope to Intercept ratios for HAT6:PTP9 as temperature is varied. **141**

Figure 5.3: HAT11:PTP9 Slope to Intercept Quotient **142**

Figure 5.4: 2FHAT6 Slope to Intercept Quotient **143**

Figure 5.5: Small polaron plot of HAT6:PTP9 **146**

Figure 5.6: Small polaron plot of 2FHAT6 **146**

Figure 5.7: A Poole Frenkel plot of the field dependence of $\{\eta\phi\}s$ **149**

Figure 5.8: Variation of β with temperature **150**

Figure 5.9: Variation of dielectric constant with temperature **151**

Figure 5.10: A plot of the carrier velocity and carrier range quotient against electric field using the ratio of IP to Q. **153**

Figure 5.11: A plot of the mobility/carrier range quotient against temperature from the gradient of data such as that in figure 5.10. **154**

Figure 5.12: Linear dependence of dIp/dE with concentration. **156**

Figure 5.13: Fraction of photons absorbed versus sample concentration. **157**

Figure 5.14: Measured Photocharge versus Electric Field at different concentrations **158**

Figure 5.15: Quantum Efficiency-Carrier range product over Electric field versus concentration. 159

Figure 5.16: Cutting the nanotube 161

Figure 5.17: Normalised photocurrents with decay tails 164

Figure 5.18: Analysis of averaged decay tail with a 3 GHz oscilloscope. 166

Figure 5.19: Ideal Unbound Exciton motion on a Carbon Nanotube 168

Figure 5.20: Multiple Excitons on Nanotube 169

Figure 5.21: Origin Screenshot of Fitted Data for Recombination Model 175

Figure 5.22: Application of Recombination model to figure 4.35 176

Figure 5.23: Application of Recombination Model to figure 4.36 177

Figure 5.24: Parameter I_∞ versus Sample Concentration 178

Figure 5.25: Application of Recombination model to Figure 4.37 179

Figure 5.26: Application of Recombination model to figure 4.38 179

Figure 5.27: Parameter I_∞ versus Electric Field 180

Figure 5.28: Light intensity versus polarisation angle of Nd:YAG laser 182

Figure 5.29: Parameter 'k' versus Electric Field 183

Figure 5.30: Parameter 'k' versus concentration 185

Tables

Table 1.1: Filled Zeolite Samples 33

Table 1.2: DLC Phase Boundaries 48

Table 3.1: Measured Rise Times of Co-Axial Cell 74

Table 5.1: Internal Electric Fields of Y zeolite. 134

Table A1: Semiconducting SWNT band gaps. 198

1 Introduction

1.1 Molecular Electronics

Molecular electronics is an emerging technology that promises many advantages over conventional electronics with regards to miniaturisation, performance issues and processing ability. The uses of organic materials are currently being explored and researched in abundance in this new and rapidly developing science. It is hoped that the exploitation of organic materials could lead to a new generation of cheap and disposable electronic components.

Where conventional electronics relies heavily on the use of inorganic materials (e.g. metals and silicon semiconductors), it is hoped comparable organic electronic devices such as transistors, organic field effect transistors (OFET's) and resistors will soon be strong, if not superior, competitors.

In the 1970's there was a breakthrough in the field of molecular electronics with the discovery of conducting polymers (to be discussed in the following section). Since this event, many other conducting polymers have been developed and observed. The development of Organic Light Emitting Diodes (OLEDS) using conjugated polymers is a recent success story for the field of organic electronics. Apart from OLEDS, conducting polymers have also been used and shown to function in devices such as transistors and memory cells **[1]**.

Organic materials offer considerable versatility in that their physical and electronic properties (e.g., energy levels, light absorption/emission bands etc.) can be designed on the molecular level and realised by the process of chemical synthesis. It is

this process of molecular engineering, plus their inherent processability from a materials point of view, that gives organics the potential to be far more adaptable than inorganic resources. However, one of the major disadvantages to date of organic materials is their instability and sensitivity to external influences such as water and oxygen. To ensure the durability of such components, organic devices are usually encapsulated to protect them from counter-productive reagents.

In terms of the potential benefits of processability, there is some discussion of using ink-jet technology to print conductive and semi-conductive organic materials onto substrates, which could lead to mass-production of lightweight, flexible and cheap electronic circuits **[2]**.

1.2 Conducting Polymers

Conjugated polymers have a repetitive structure of alternating single and double carbon–carbon (sometimes carbon–nitrogen) bonds. Single bonds are referred to as σ-bonds, and double bonds contain a σ-bond and a π-bond. All conjugated polymers have a σ-bond backbone. Polyacetylene can be described as having sp^2 hybridisation. Figure 1.1 is an orbital diagram of sp^2 hybridisation.

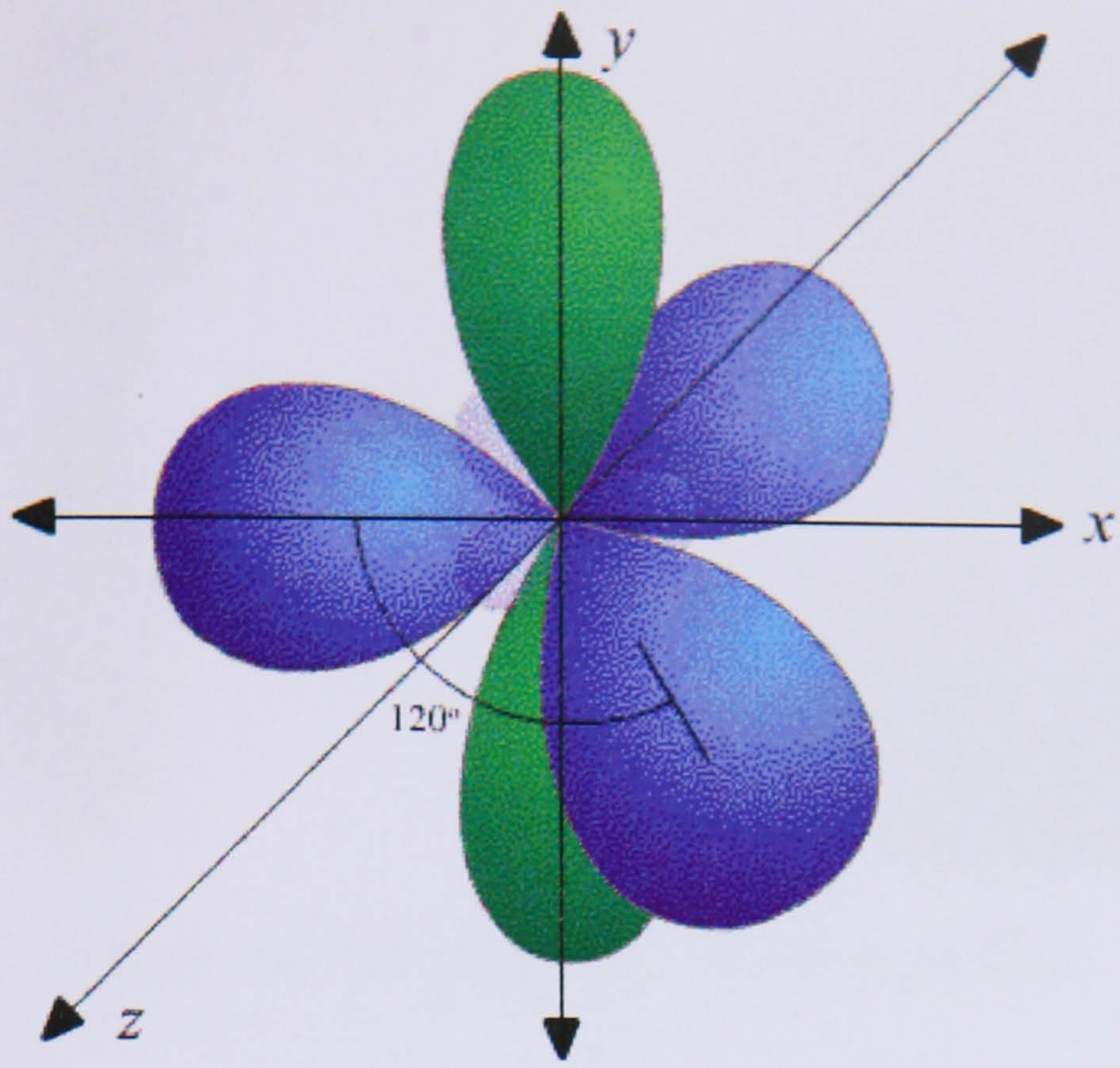

Figure 1.1: Orbital diagram of sp^2 hybridisation.

Conjugated polymers are unlike other plastics in the sense that they have the ability, under the right conditions, to conduct electricity. Much research has been performed on this particular class of polymer since Alan Heeger et al discovered this phenomenon in the 1970's **[3]**.

To understand why these polymers are conducting, consider the remaining out-of-plane p_z orbitals (shaded green in figure 1.1) on the carbon atoms. These overlap with neighbouring p_z orbitals to give π-bonds. This wavefunction overlap leads to the individual electrons belonging to the p_z orbits in each unit cell becoming indistinguishable from each other (see figure 1.2). This results in delocalisation of electrons over the full length of the linear system.

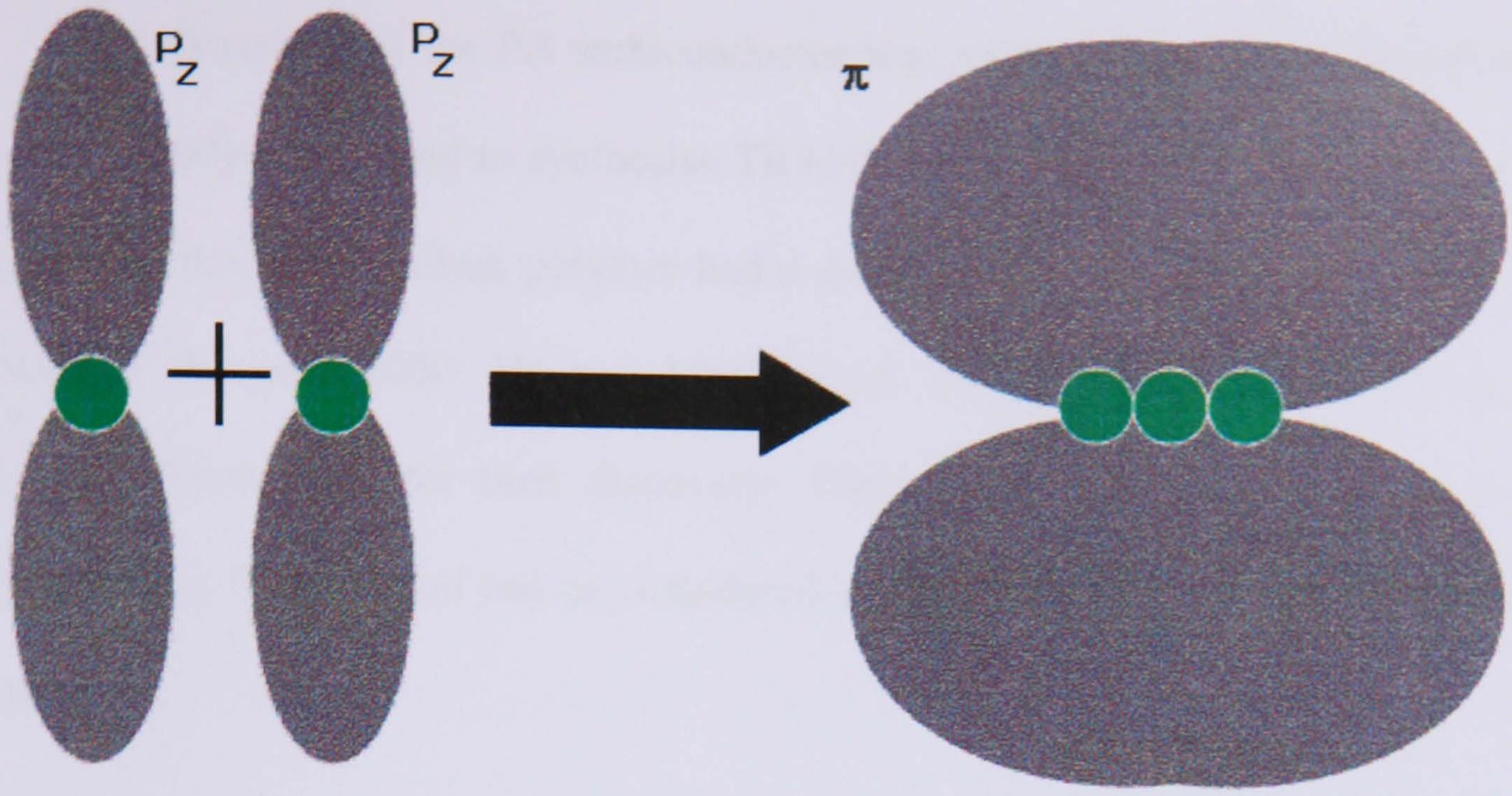

Figure 1.2: The formation of π delocalisation

Polyacetylene (PA) is the best known member within the family of conjugated polymers. It is often used as a model system for conducting polymers in theoretical studies. This is due to its simple chemical composition, an alternating single and double bond structure with only a single hydrogen atom as the side group to the carbon backbone.

The Shirakawa synthesis **[4]** process led to the production of high-quality fibrillar PA films. Polyacetylene is an attractive model compound because of the small number of CH units (two) which constitute the unit cell.

As was shown in figure 1.2, the electrons that constitute the π-bonds are delocalised over the entire molecule. In the case of PA, delocalisation results in a single (degenerate) ground state whereas in other polymers the alternating single and double bonds lead to electronic structures of varying energy levels. PA is a semiconductor with a band gap of 1.4 eV.

The discovery of the PA semiconductor was serendipitous and occurred when too much catalyst was used to synthesise TRANS-Polyacetylene (see figure 1.3) and it was noticed that the resultant polymer had a metallic appearance, that is, a reflective surface. In the year 2000: Heeger, MacDiarmid and Shirikawa were awarded the chemistry Nobel Prize for their discovery. Their Nobel lectures were published as review articles **[5, 6, 7]** and can be considered a comprehensive account of conducting polymers.

There are two isomers of polyacetylene (Fig 1.3), the CIS (top image) and the TRANS (bottom image). The CIS configuration is unstable and can be converted to the TRANS arrangement if energy is supplied to the system. The two isomers have different conduction properties so it is desirable to perform experiments using just the TRANS state due to the increased stability. To ensure a chain of pure TRANS, thermal energy is supplied with the polymer being subjected to temperatures above 150°C for a few hours.

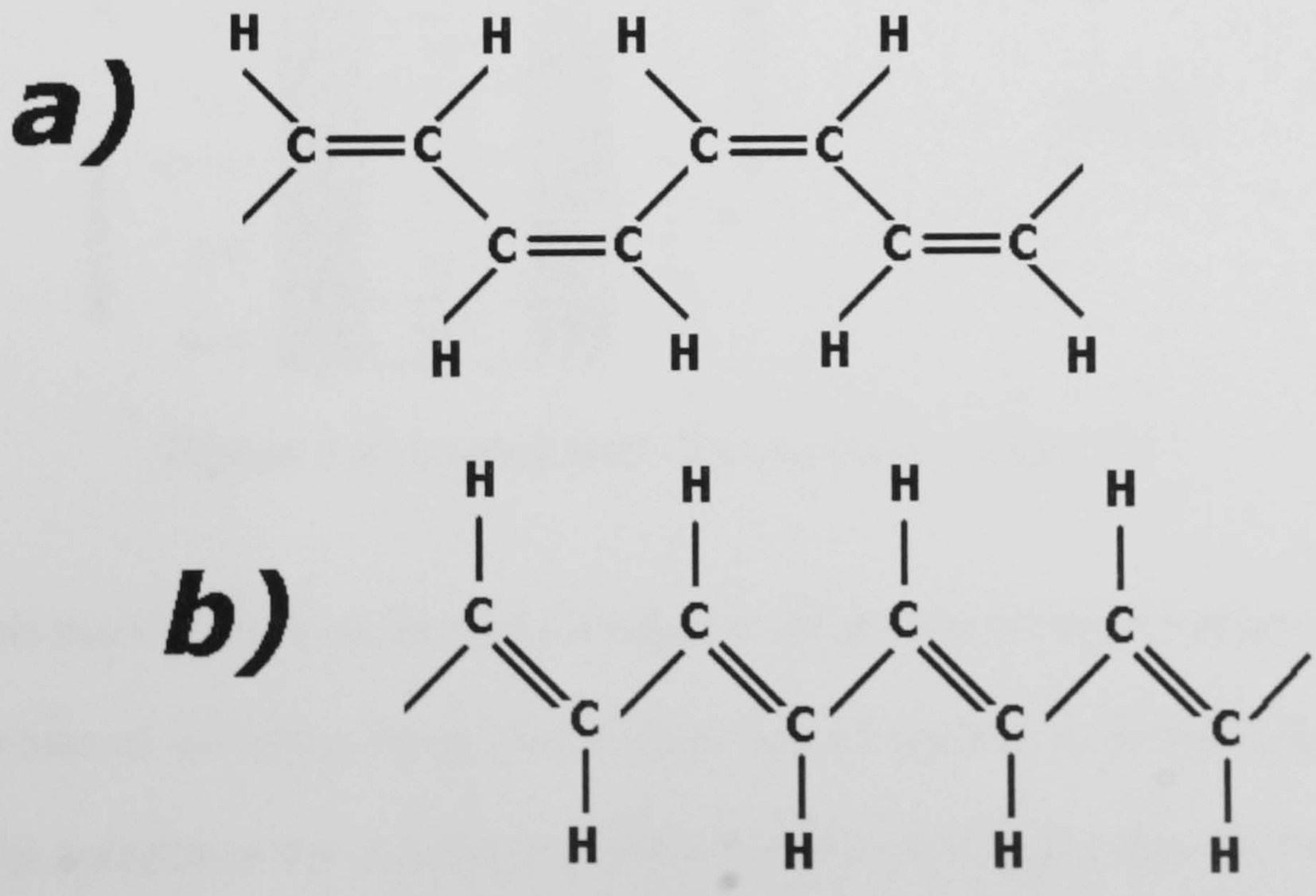

Figure 1.3: CIS (a) and TRANS (b) Polyacetylene structures.

The pure TRANS polyacetylene (Fig. 1.3b), is semiconducting with a band gap of ≈1.4 eV (TRANS). It can be made to conduct continuously (DC) in the same way as conventional silicon based semiconductors by the inclusion of dopants.

As shown in Fig. 1.4 **[5]**, the highest conductivities (measured in Siemens) of doped Polyacetylene are comparable to some metallic materials. Some observations of Polyacetylene have yielded conductivity measurements comparable to copper **[8]**. However, doping a polymer is an irreversible process and there is no experimental way to determine the charge transport properties along the carbon backbone due to the morphology and tertiary structure.

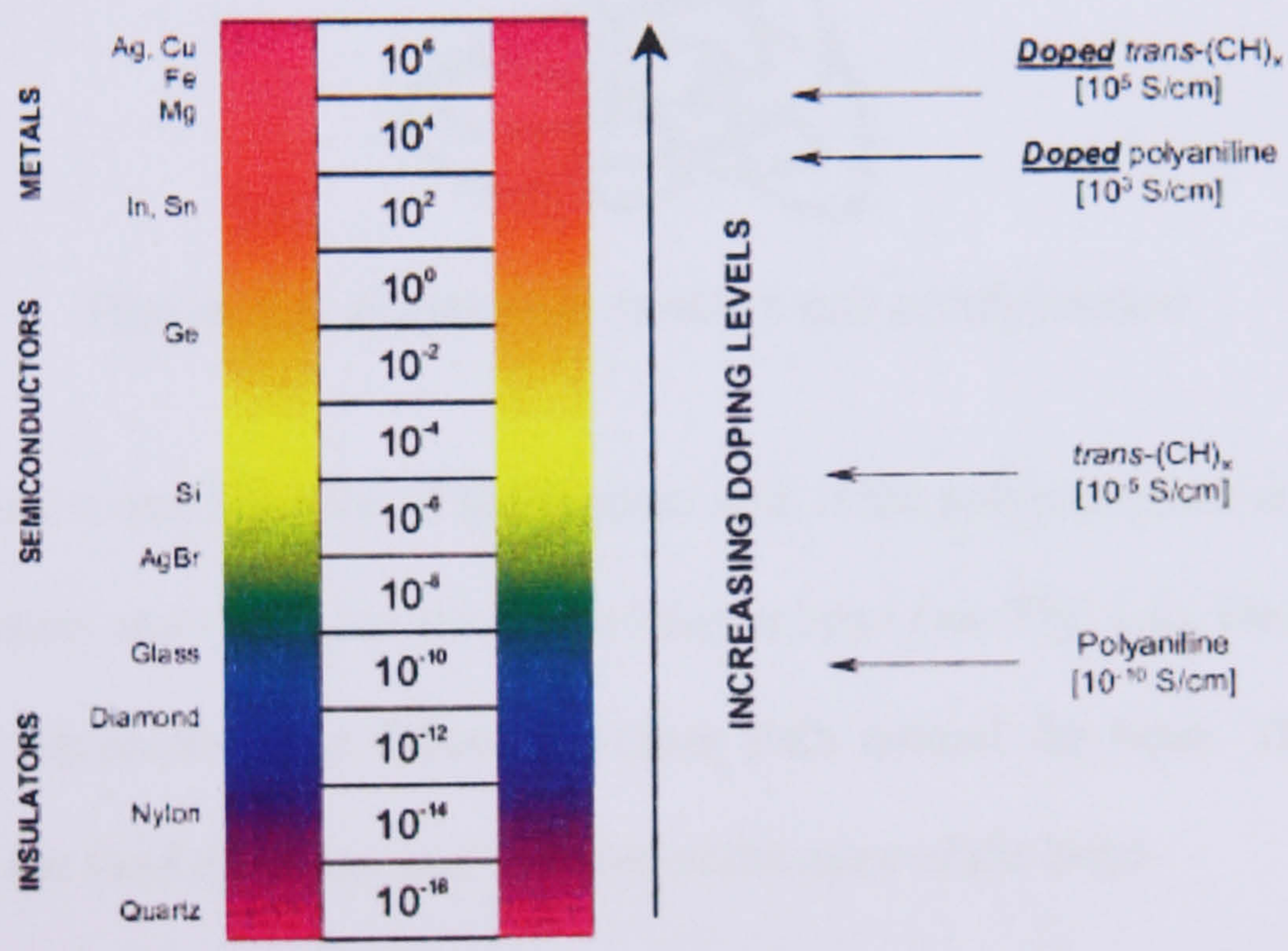

Figure 1.4: Logarithmic Conductivity Ladder [5]

This thesis centres on the photoconductive properties of organic semiconductors, where photons of sufficient energy are used in lieu of dopants to generate free mobile carriers (the energies of the incident photons are sufficiently higher than the band gap of the polymer in order to avoid the creation of bound excitons). Electrons are temporarily

excited from the valence band to the conduction band via a process that will be discussed in more detail in chapter 2.

1.3 Tertiary conjugated polymer structure

This thesis includes experiments of organic materials suspended in solution. In reality, a polyacetylene chain in solution will adopt a random coil configuration (see Fig. 1.5). In such an arrangement, the range of motion for a conduction electron is limited. An electron cannot move continuously in the direction of the electric field.

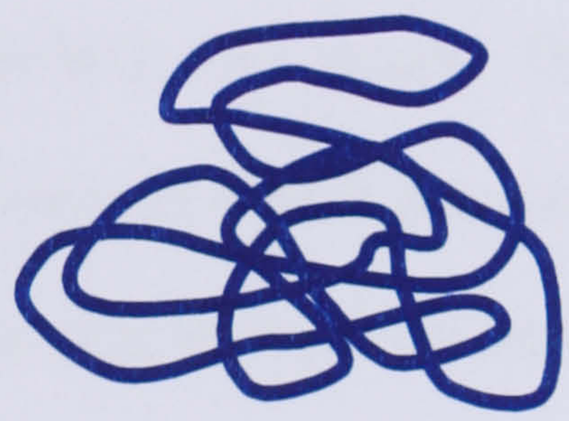

Figure 1.5: Polymer in random coil configuration

Consider a small section of the random coil. If the polymer chain is aligned with the field direction and then goes through a hairpin bend (see Fig. 1.6), electrons cannot turn back on themselves and follow the chain path around the bend. They can only move against the field direction and will stop at the apex of the bend.

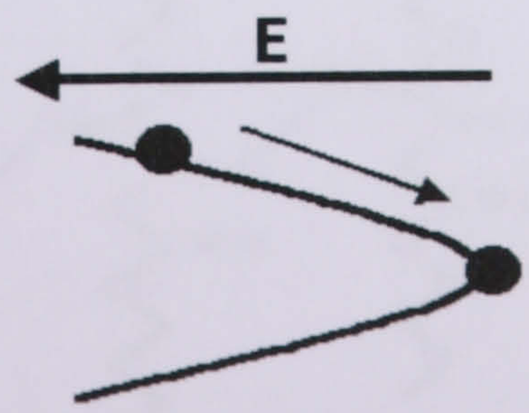

Figure 1.6: Polymer Hairpin bend.

Let us assume that the polymer chain in Fig. 1.5 has a total length of 50 μm if straightened out. Consider the section shown in Fig. 1.6. The length of this chain section may have a total horizontal distance of, say, 20 nm. Therefore, if it were possible to somehow make straight the polymer chain (and therefore the carbon backbone), the total ideal distance that an electron could potentially move would be 2,500 times further. This will result in a relatively longer-lived photocurrent event (to be discussed in following chapters).

Figure 1.7 shows a method whereby a polymer has been straightened into a long 'wire'. The material in question is a Polydiacetylene (PDA) molecule with Butylcarboxymethylurethane (BCMU) side groups. The hydrogen bonds between the adjacent side groups cause the chain to extend and straighten. This particular polymer has been investigated in a toluene solution by Donovan et al **[9]**.

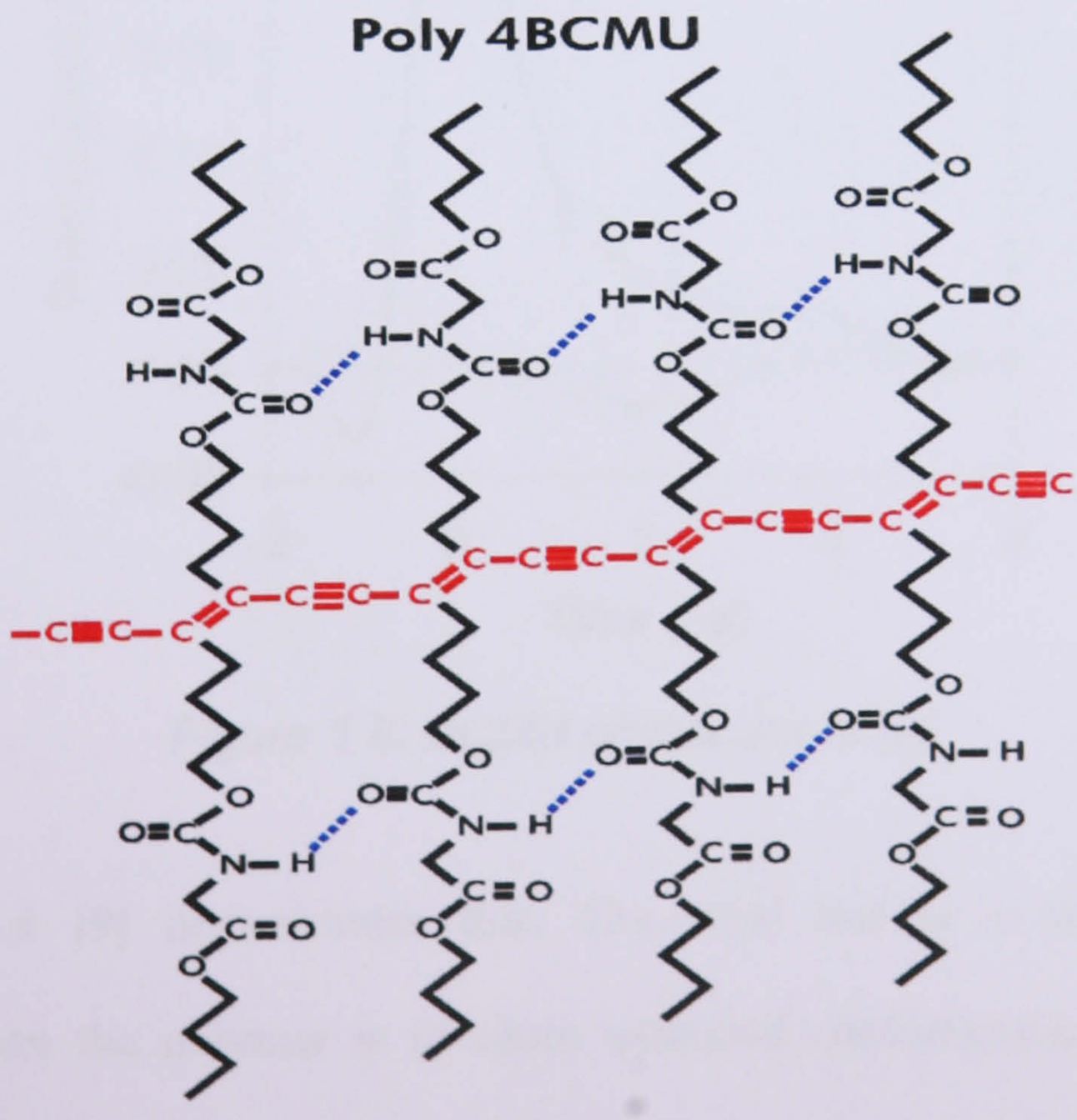

Figure 1.7: Polydiacetylene molecule with BCMU sidegroups. Hydrogen bond formation (▬▬▬▬▬▬) causes chain extension of the conjugated backbone that forms the molecular wire.

When the polymer is in the chain extended form (as shown), the material appears red in colour. At a sufficient temperature (around 80°C), there is enough thermal energy to break apart the hydrogen bonds and the sample will adopt a random coil configuration at which point the sample turns a yellow colour.

The alteration of colour is not the only change that occurs. Any photocurrents being observed will promptly vanish once the carbon backbone is no longer in the chain extended form. This is due to the fact that the electrons can no longer move far, their carrier range has been significantly reduced and therefore the measured displacement current will be negligible.

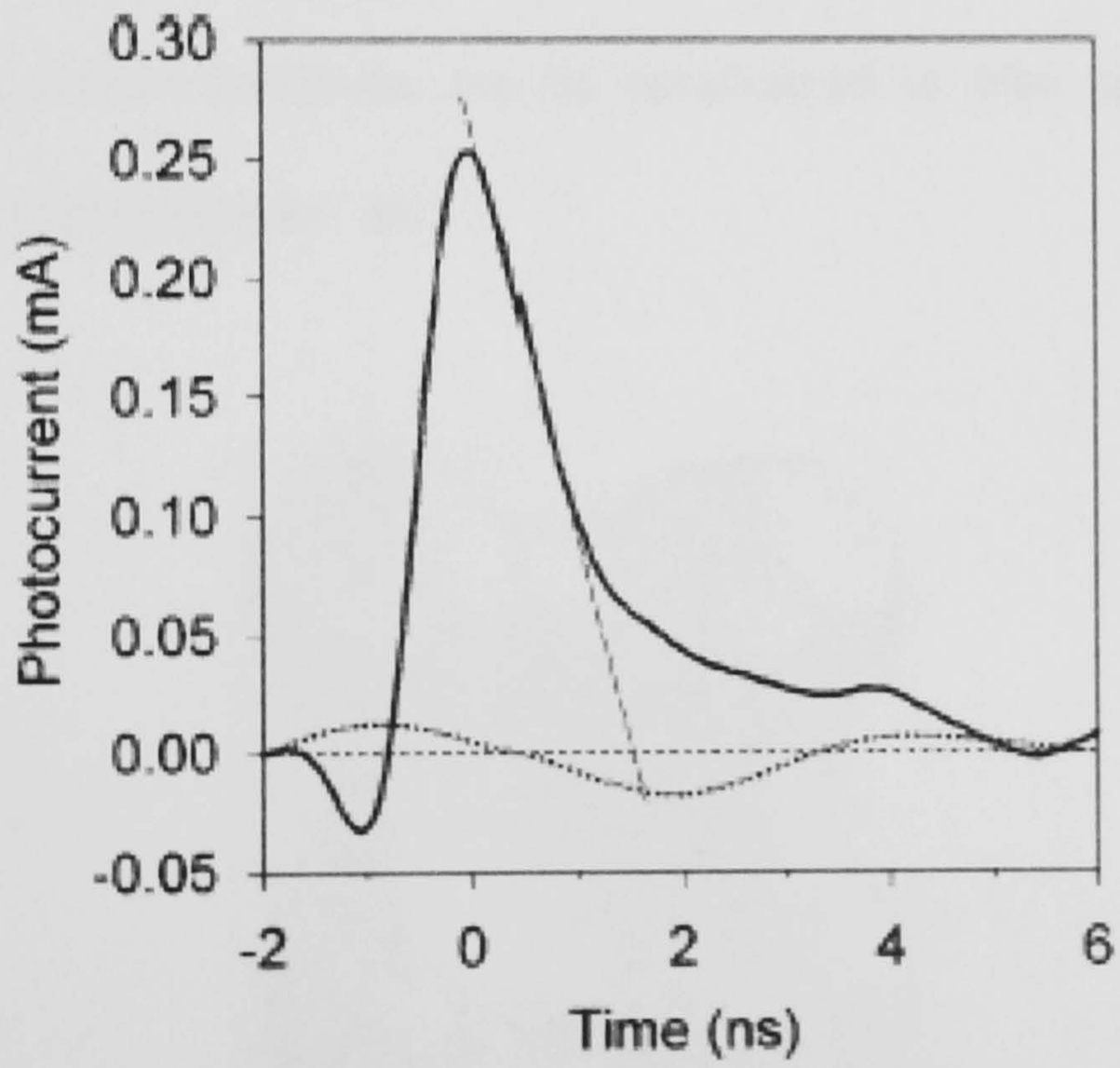

*Figure 1.8: BCMU photocurrent [**9**]*

Figure 1.8 **[9]** demonstrates this. The solid line is a measured transient photocurrent when the polymer is in chain extended conformation, the dashed line represents the photocurrent when the sample is heated above 80° C and the random coil configuration is adopted. The results show the displacement current is detected or not depending on the polymer configuration and concomitant carrier range.

1.4 Encapsulation of polymers within Zeolite nanochannels

The problem of achieving a straightened carbon backbone was touched upon in the previous section. The PDA-BCMU is an ideal polymer for resolving this problem, but recent developments have yielded another solution. It has been discovered that it is possible to polymerise acetylene gas in zeolite channels leading to straight parallel conjugated polymer chains **[10, 11, 12]**.

A zeolite is a framework silicate consisting of interlocking tetrahedrons of SiO_4 and AlO_4. Zeolites have large vacant spaces or cages in their structures that allow space for other molecules to reside. By polymerising molecules inside the zeolite nanochannels (see figure 1.9), the problem of random coil conformations can be overcome and the carbon backbone can be constrained to take up a chain extended conformation into a long straight 'wire'.

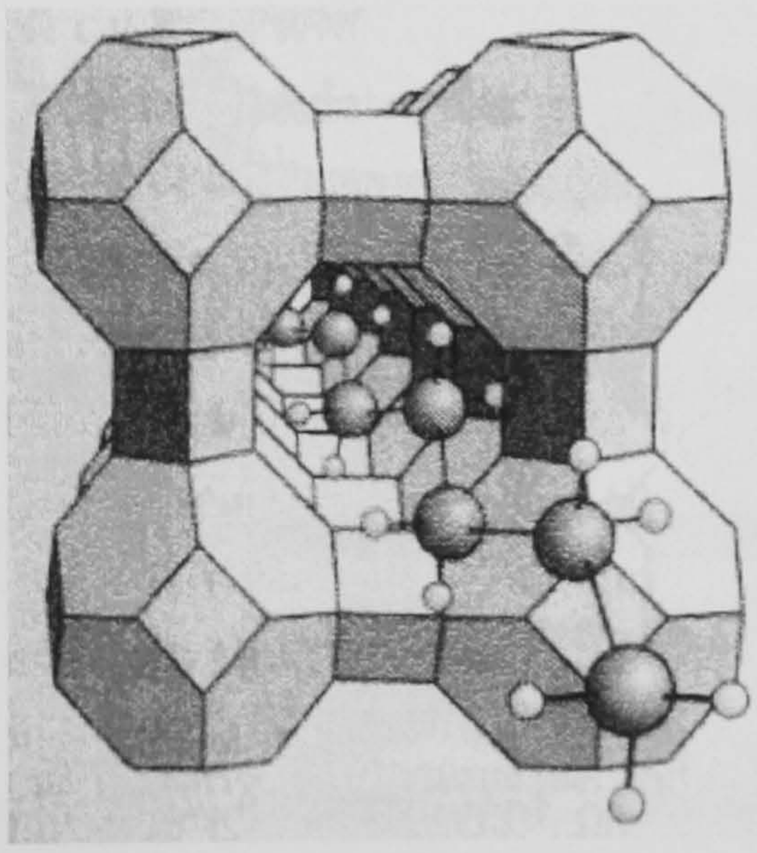

*Figure 1.9: Cartoon of filled zeolite [**13**]*

Figure 1.9 **[13]** shows a cartoon of polyethylene encapsulated within a zeolite cage. The advantages of this process are as follows:

- The pore sizes of the zeolite are large enough to allow the acetylene monomer gas to enter the cage. However, once the molecules polymerise, they are too large to pass out of the zeolite and are trapped within. Therefore, the polymer will remain permanently ***encapsulated*** within the zeolite.

- The narrow channels constrain the polymer to adopt a chain extended conformation as opposed to a random coil configuration. This adds a quasi ***one-dimensionality*** to the electron motion and excludes 2D or 3D electron-hole recombination by diffusion to neighbouring chains.

- The polymers in question will be of basic composition and so modelling the electron transport properties will be simpler. That is, there will be no complicating side group interactions.

- The fact that only one polymer chain can exist within the channels means the problems of inter-chain bimolecular recombination can be avoided.

As was said earlier, the PA polymer chains can be made to adopt the TRANS configuration by heating the filled zeolite for a reasonable period of time.

As the filled zeolites are in a powdered form, they can easily be put into a silicon oil/polymer oil suspension for easier handling during the experiment. As the filled zeolites are so strongly absorbing, the dilution of the material with silicon oil (which is transparent to UV) allows the light to pass further into the sample and so the photons are absorbed more uniformly rather than in a very shallow depth.

1.5 Carbon Nanotubes

In 1985, Kroto et al discovered the C_{60} molecule ('Buckyballs, or Buckminsterfullerine') **[14]**. In 1996, Kroto, Curl and Smalley were awarded the Nobel prize in Chemistry for their discovery. In 1991 another exotic form of carbon was discovered, appearing thread-like in nature. Although carbon filaments with diameters less than 10 nm were prepared in the 1970's and 1980's via synthesis of vapour grown carbon fibres **[15, 16, 17]**, no detailed studies were performed at the time. Since this discovery of multi-walled carbon nanotubes in 1991 by the electron microscopist Sumio Iijima **[18]**, these materials have drawn considerable interest from multiple disciplines due to their unique properties.

A significant step forward was made in 1993 by the synthesis of single walled carbon nanotubes (SWNTs) **[19, 20]** which have allowed experimentalists to test some of the theoretical predictions that have been made about nanotube properties.

A SWNT can de described as a cylinder formed from a rolled up sheet of graphene (i.e. a single atomic layer of crystalline graphite). A vector denoted by $\boldsymbol{C_h}$, which expresses the chirality of the tube, can describe the structure of such a nanotube. This vector is given by equation 1.1:

$$\bar{C}_h = n\bar{a}_1 + m\bar{a}_2 \qquad (1.1)$$

It is seen that the chiral vector, expressed by two integers ***(n,m)***, connects two equivalent sites around the circumference of the rolled-up graphene sheet (see Fig. 1.10).

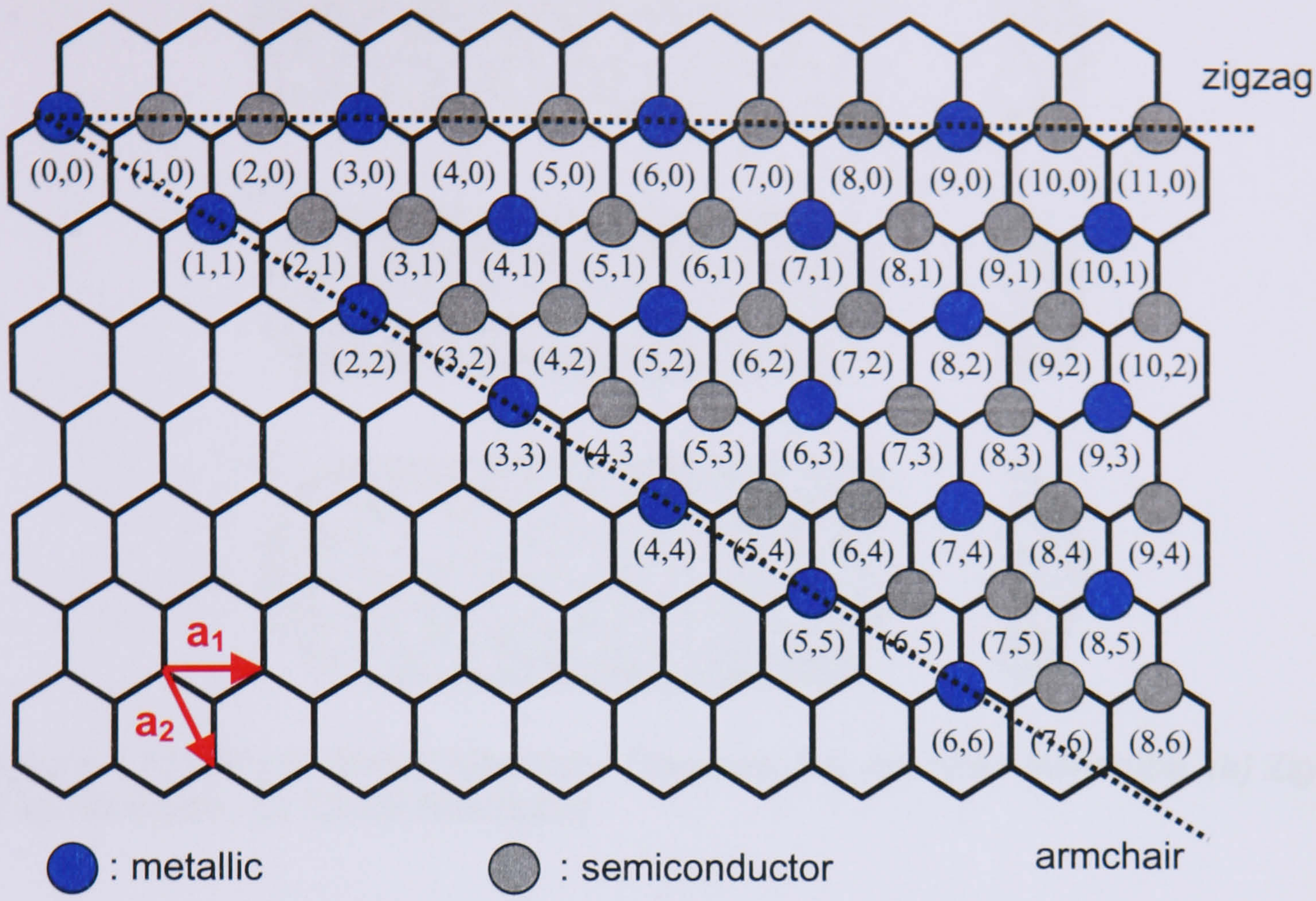

Figure 1.10: Graphene Sheet – An unravelled nanotube

The cylinder of a SWNT can be capped at either end with a hemisphere of a fullerene molecule. Nanotubes can be classified into three types depending on the appearance of their uncapped ends. In Figure 1.11 **[21]**, we see:

(a) an 'armchair' nanotube ***(n,n)***

(b) a 'zigzag' nanotube ***(n,0)***

(c) a chiral nanotube ***(n,m)***.

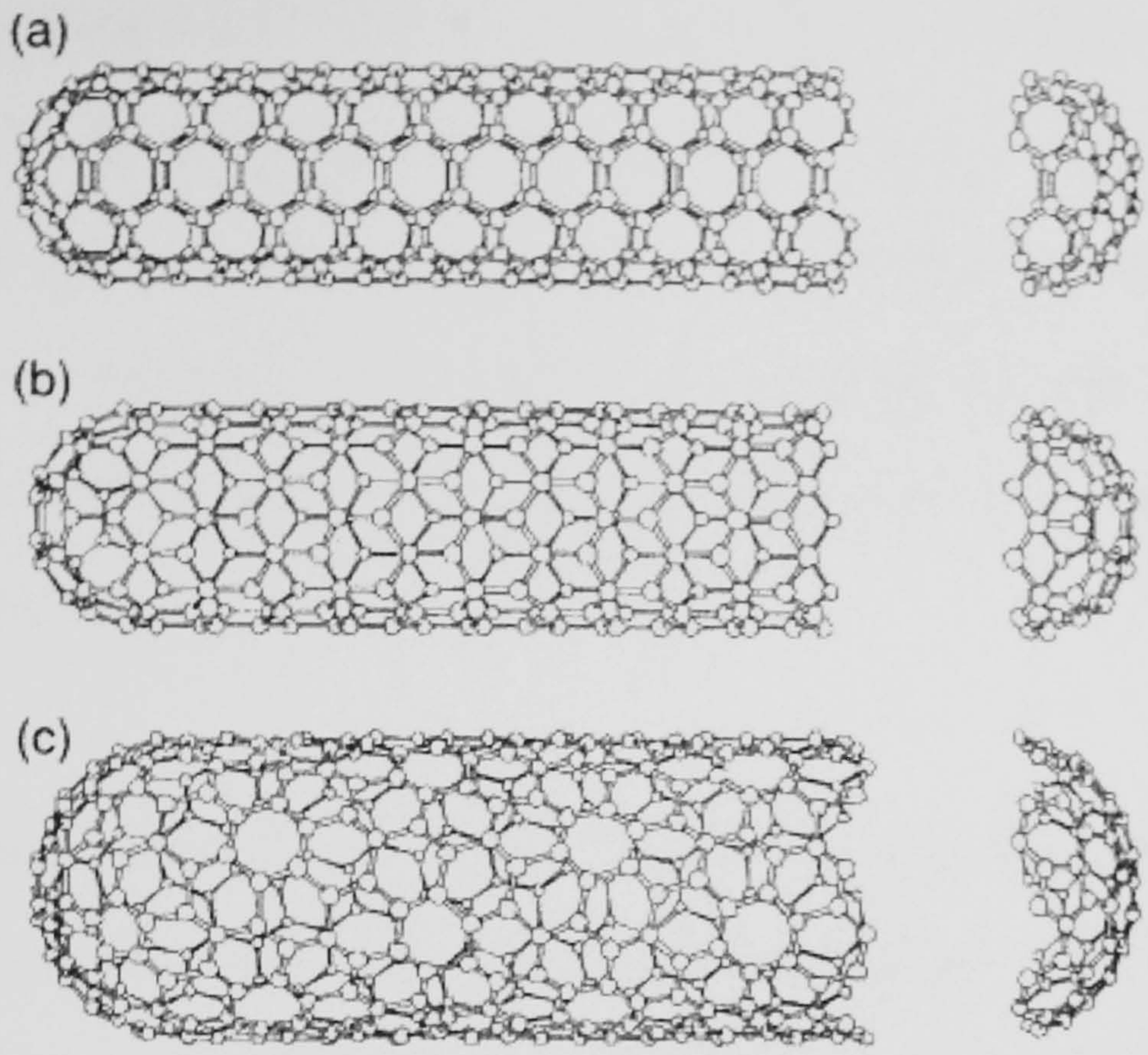

Figure 1.11: Single Walled Nanotube Diagrams [(a) Armchair Nanotube, (b) Zig-Zag Nanotube, (c) Chiral Nanotube]

SWNTs have been observed to have diameters in the range of 0.4nm – 10 nm, after which the structure becomes unstable. Most have a diameter less than 2 nm, with a length typically in the order of 1 micron, although this is usually ill-defined. Due to this large aspect ratio and small diameter, SWNTs can be considered to have a one-dimensional structure. The small circumference of the tube, less than the de Broglie wavelength of an electron, results in the electron wavefunction becoming strongly quantised in two-dimensions. Charge transport then becomes a one-dimensional process axially along the nanotube.

An interesting property that carbon nanotubes possess is that they can either be semi-conducting or metallic, depending on their chiralities. As shown in Figure 1.10, two-thirds of a nanotube distribution will be semiconducting. If $(n-m)=0$ or a multiple of 3, the nanotube will have metallic properties. All others will be semiconducting. This is the reason why all of the armchair (n,n) nanotubes are metallic by nature.

Semiconducting nanotubes are therefore relevant to this research as electrons can be excited to the conduction bands in a process similar to that occurring in photoconducting polymers. Like polymers, their one-dimensional character will be expected to affect the nature of the charge transport along the nanotube length, 1D charge transport in semiconductors differing substantially from that in 3D. This is to be explored in this thesis.

The unique electronic properties of carbon nanotubes arise due to the circumferential quantum confinement of electrons. Electrons are further confined in the radial direction due to the graphene monolayer thickness. The number of conduction and valance bands in a nanotube will therefore be dependent on the standing waves that can be established around the nanotube circumference.

Because of these two confinement issues, the electronic transport process in a nanotube becomes quasi one-dimensional along the nanotube axis and limits the electron wavevectors to this direction.

It has already been stated that the ***(n,m)*** indices which describe the rolled-up geometry of a graphene sheet, forming a nanotube, determine whether or not the tube is metallic or semiconducting. To understand how these different types of conductors arise in an all carbon sp^2 hybridized system, it is easier to consider the 2D energy dispersion of graphene.

Graphene is a semi-metal (or zero band-gap semiconductor) where the valence and conduction bands touch and are degenerate at 6 points. These 6 positions define the corners of the first Brillouin zone. The bands touch for a unique wavevector denoted as

the **K** point of the two-dimensional Brillouin zone (the corner point of the hexagonal unit cell in reciprocal space). The energy at the **K** point is equal to the Fermi energy. In reciprocal space, ***k***=0 is at the centre of the hexagon (figure 1.12).

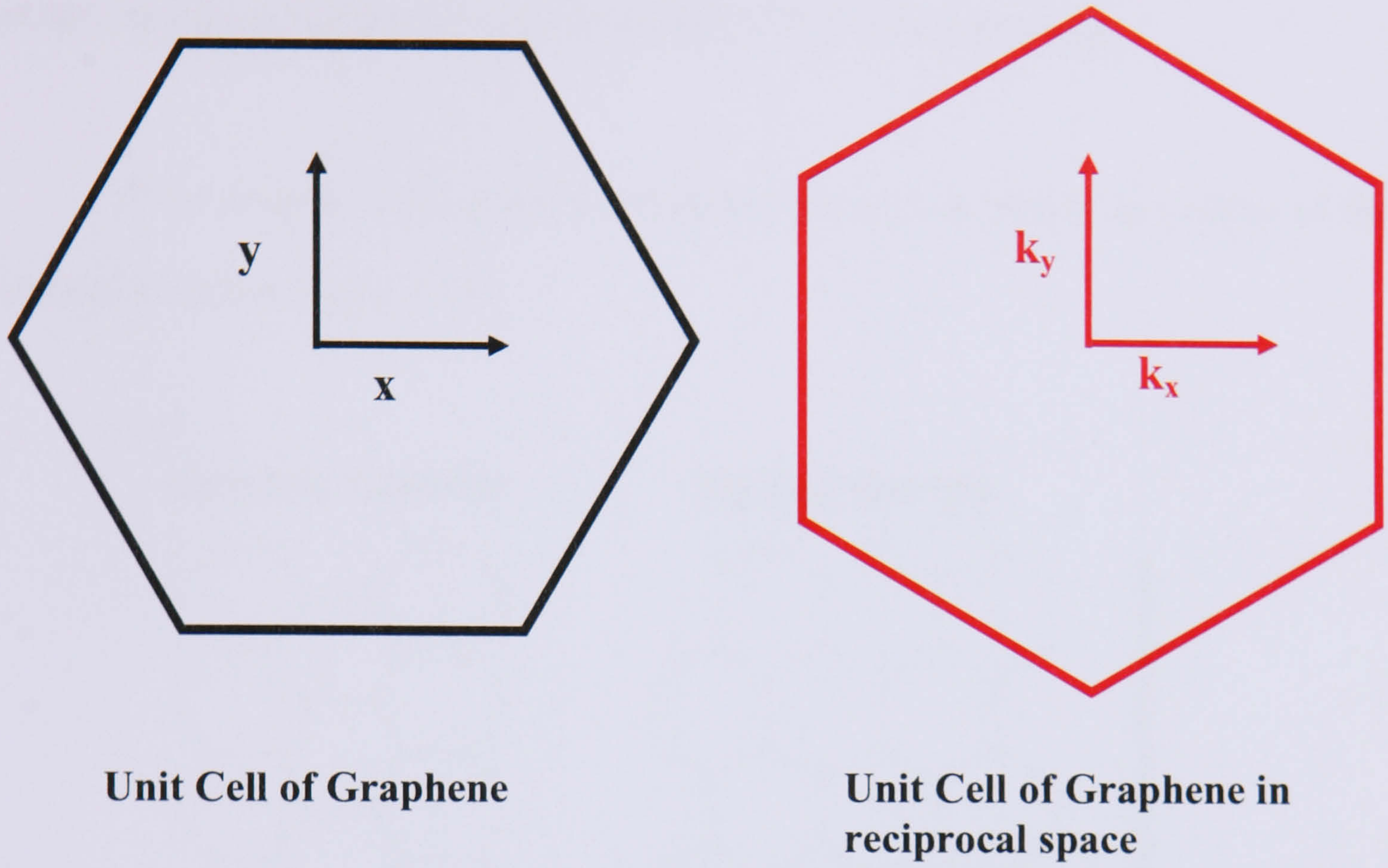

Figure 1.12: Graphene Unit Cells

Theoretical calculations **[22, 23, 24, 25]** have shown that the electronic properties of SWNT's are highly dependent on their structural geometry. However, as stated previously, theory has predicted that the tubes created from rolling up a sheet of graphene can either be metallic or semiconducting. The resulting band gaps of the latter will be dependent on the diameter of the tube and the helicity.

These factors can be used to calculate the dispersion relations of the one dimensional bands (linking wavevector to energy) using the well established dispersion relations in a graphene sheet. It was stated earlier that two-thirds of a nanotube distribution will be semiconducting. It was also said that if $(n-m)=3q$ (where q is an integer), the nanotube can effectively be considered to be metallic, where n and m are

the chiral vectors respectively. If q is zero, the nanotube will be metallic. Non-zero values of q are, in fact, very tiny band gap semiconductors but can be considered metallic, especially at room temperature. The small band gaps arise due to the curvature of the nanotube circumference. All other tubes will be semiconducting.

If we imagine looking down on a nanotube we can sketch an overlay of the allowed k-vectors (figure 1.13).

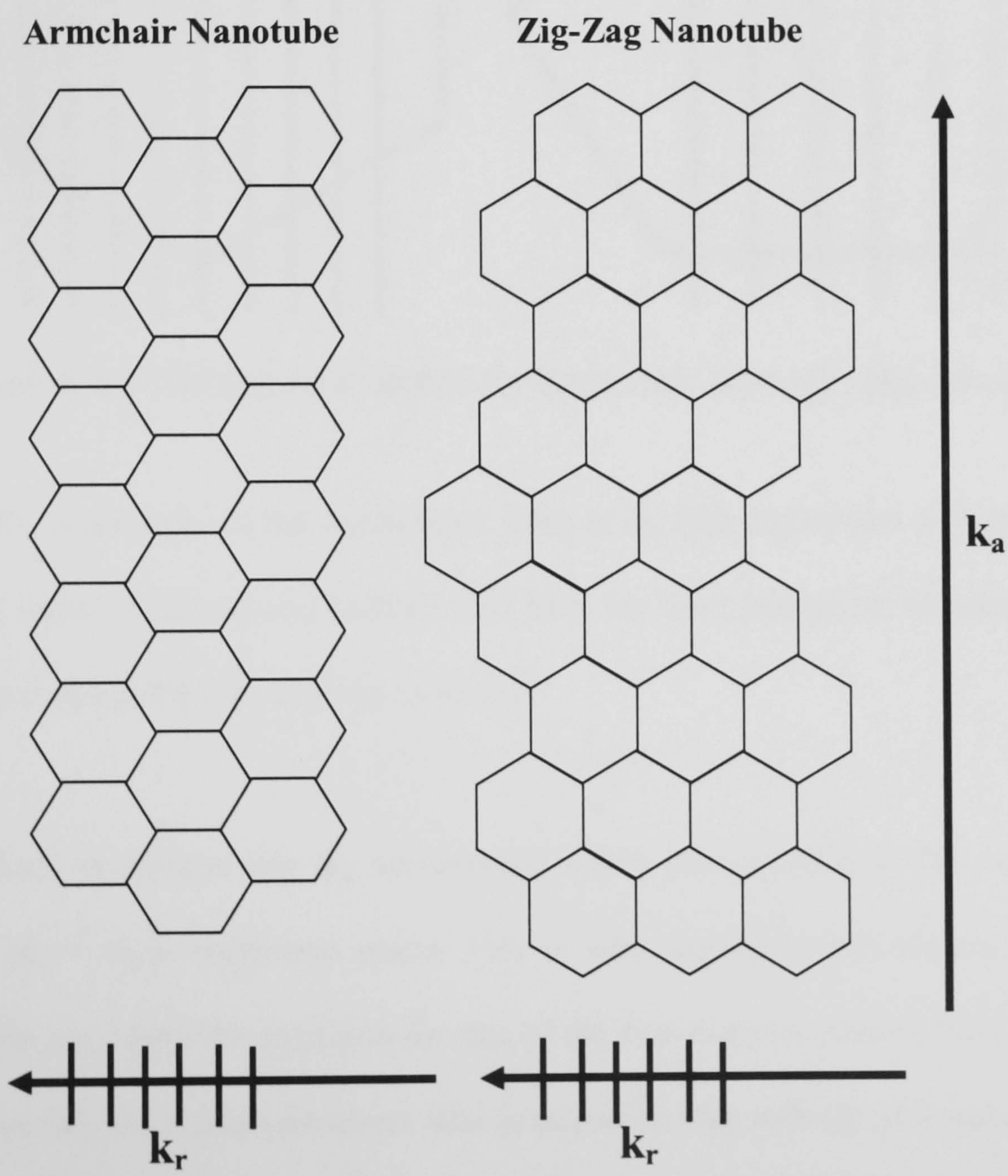

Figure 1.13: Allowed k states for nanotubes.

Figure 1.13 illustrates that the k_a wavevector can be considered continuous due to the length of the tube being relatively larger than the diameter, where the k_r

wavevectors become discreet. We can now sketch a representation of the $\boldsymbol{k_a}$ wavevectors (continuous lines) for different quantisation states of $\boldsymbol{k_r}$ (figure 1.14).

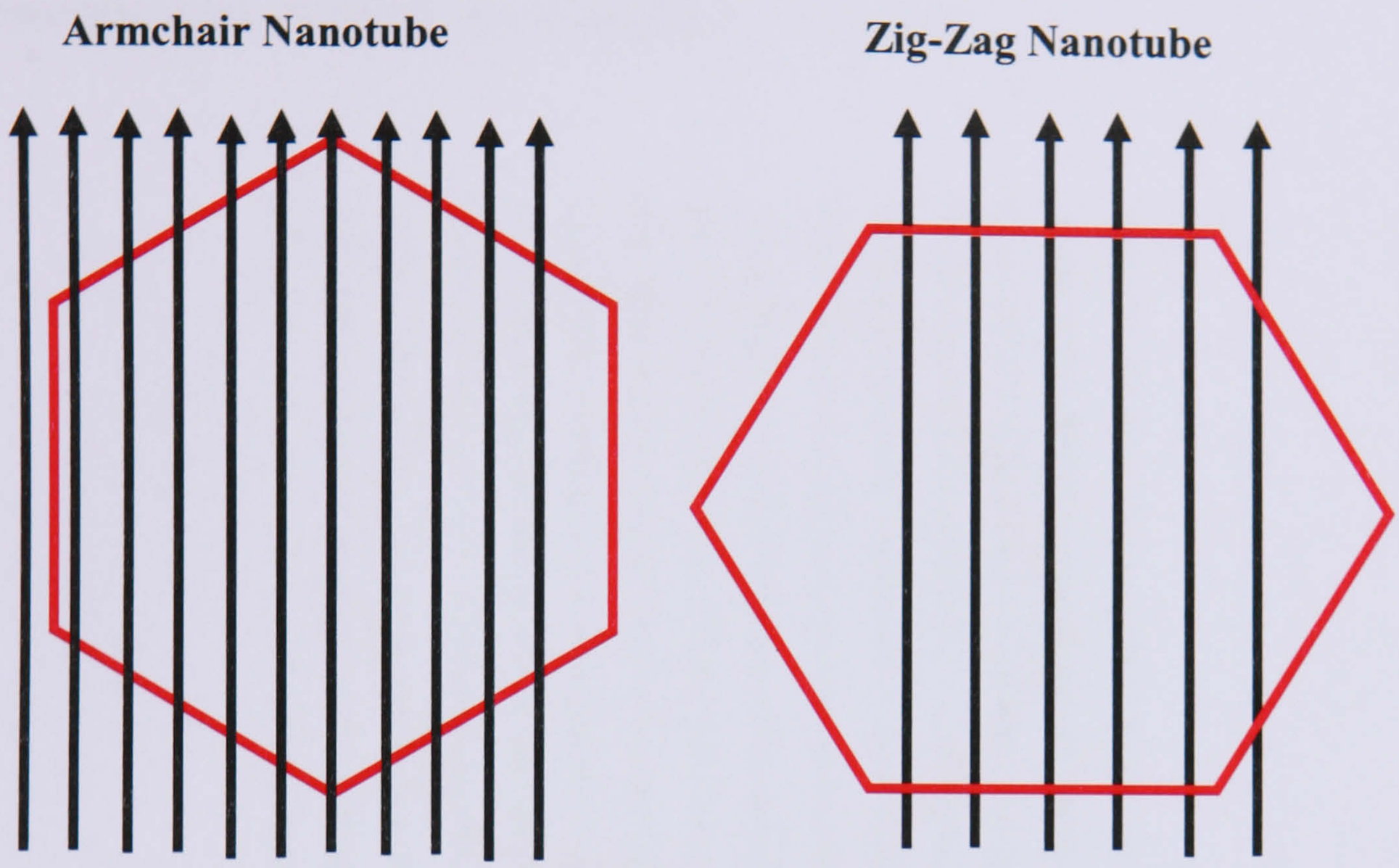

Figure 1.14: Sketch of k states for armchair and zig-zag nanotubes

The separation of the continuous lines of $\boldsymbol{k_a}$ (the separation in k space of the quantised radial wavevectors) indicate that here we have chosen an armchair tube that has a larger radius than the zig-zag nanotube.

There is always one $\boldsymbol{k_a}$ wavevector which passes through the centre of the hexagon ($\boldsymbol{k_a} = 0$) in reciprocal space. This is why armchairs will always be metallic whereas for zig-zags, the condition for one of the wavevectors passing through a vertex depends on the horizontal separation (the quantisation step radially or in other words the radius of the tube which is dependent on the specific (m,n) indicies). In the case of zig-zag tubes, a $\boldsymbol{k_a}$ wavevector will touch one or more of the vertices when the previously described condition of (n-m)=3x (where x=0, 1, 2, etc) is obtained.

For a chiral nanotube, the hexagon representing the unit cell is at an angle (the chiral angle) to the tube axis as is therefore the hexagon representing the Brillouin zone. The same special conditions required for metallic tubes (i.e. the vertical arrows representing continuous $\boldsymbol{k_a}$ to pass through the vertex) apply.

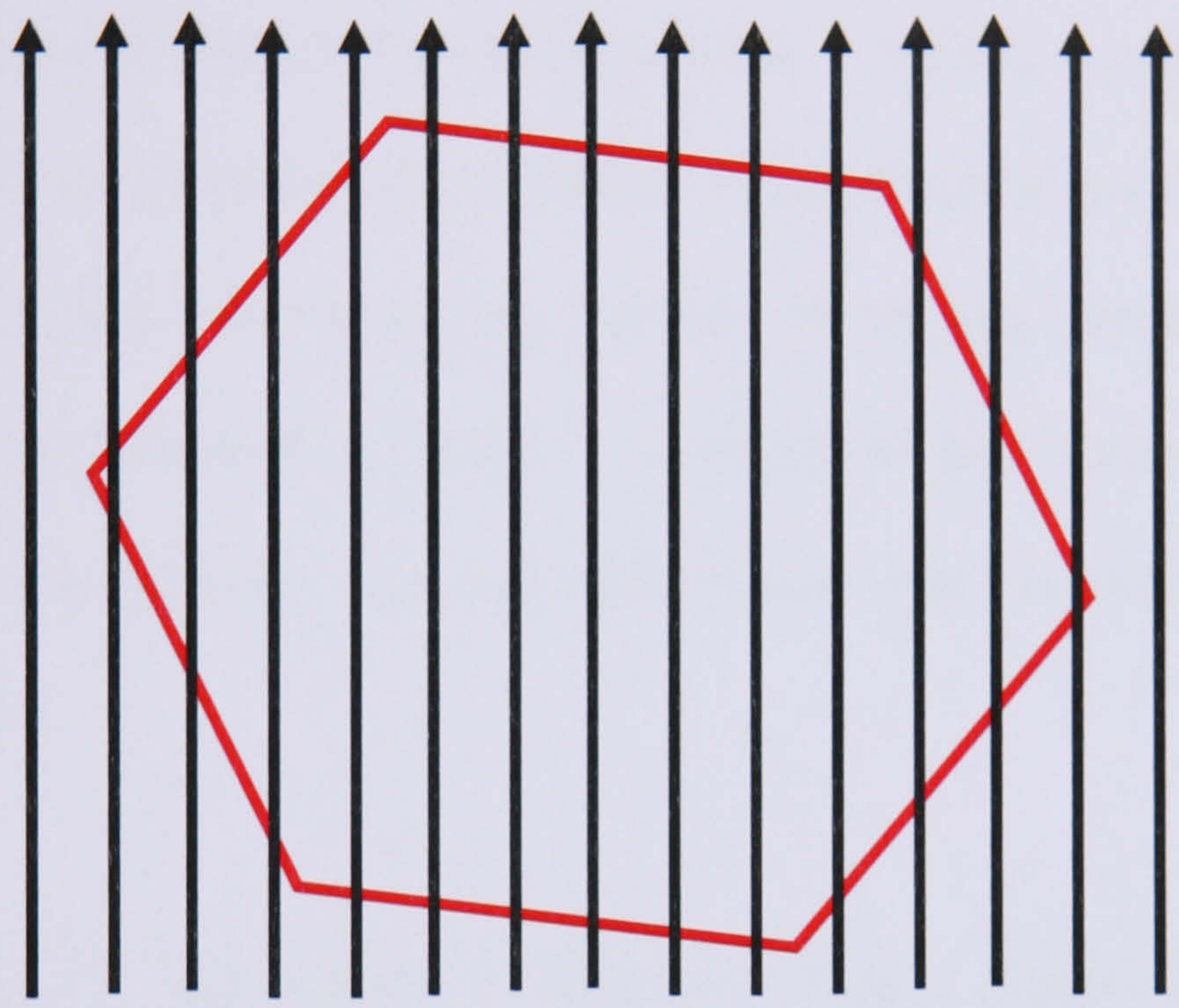

Figure 1.15: Sketch of k states for a chiral nanotube.

Independent of the chirality, the band gap energies of the SWNTs are inversely proportional to the diameter of the nanotube. Equation 1.2 **[26]** gives the relationship between diameter $\boldsymbol{d}$ and the band gap $\boldsymbol{E_g}$, where $\boldsymbol{\hbar}$ is Plank's constant divided by $\boldsymbol{2\pi}$ and $\boldsymbol{v_F}$ is the Fermi velocity for Graphene (8.1×10^5 ms^{-1}).

$$E_g = \frac{4\hbar v_F}{3d} \qquad (1.2)$$

The diameter of a $\boldsymbol{(n,m)}$ nanotube can be calculated by using equation 1.3 **[26]**, where $\boldsymbol{C_h}$ is the length of the chiral vector and $\boldsymbol{a_{C\text{-}C}}$ is the nearest neighbour C-C distance (1.42 Å in graphene, although in nanotubes the bond length is known to be slightly larger than graphene at 1.44 Å):

$$d = \frac{C_h}{\pi} = \frac{\sqrt{3}a_{C-C}\left(m^2 + nm + n^2\right)^{\frac{1}{2}}}{\pi} \tag{1.3}$$

1.6 Zeolites

The Reading chemistry group have supplied a limited number of filled zeolite samples. They have encapsulated the polymers Polyacetylene and Polypropyne within three different types of zeolite structures, namely: Mordenite, Faujasite and Beta. The samples received are tabulated in Table 1.1 and include the concentrations of carbon and hydrogen by mass. (Note: The hydrogen content may be misleading due to the absorption of water).

Sample	C (%)	H (%)	Monomer Gas	Zeolite Host
JT6	18.47	1.87	Acetylene	Faujasite
JT8	10.95	1.62	Acetylene	Beta
JT13	9.04	1.45	Acetylene	Mordenite
JT15	8.79	1.37	Acetylene	Mordenite
JT20	7.35	1.35	Acetylene	Beta
JT31	13.64	1.83	Propyne	Beta
JT35	15.59	1.96	Propyne	Beta
JT22	16.73	2.23	Propyne	Faujasite
JT28	16.96	2.15	Propyne	Faujasite

Table 1.1: Filled Zeolite Samples

The structures of the zeolite cages as shown in figures 1.16 to 1.18 have been taken from [27]. In each of the diagrams, the lines represent bonds with a silicon, aluminium or oxygen atom at the vertices.

1.6.1 Mordenite

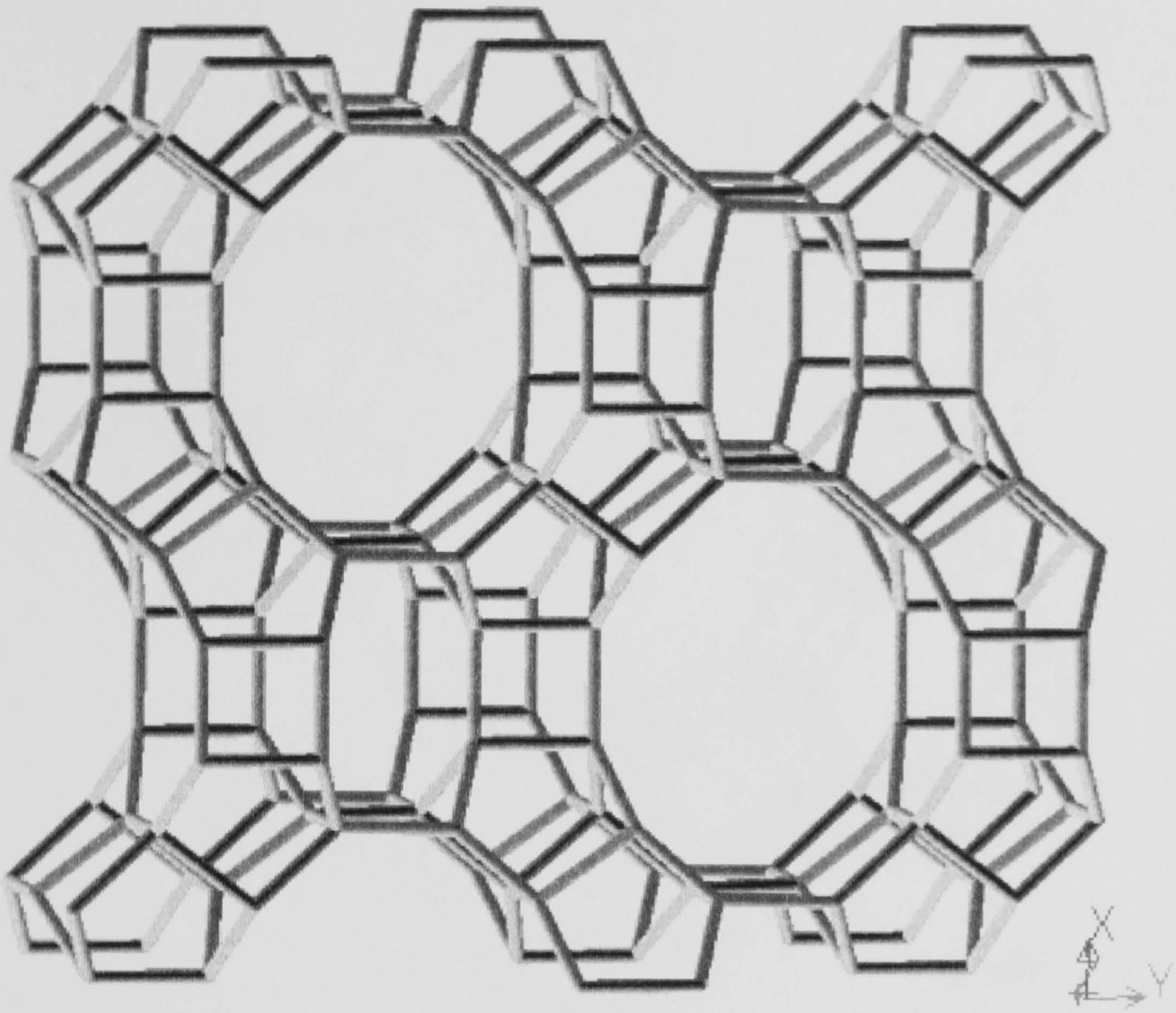

Figure 1.16: Mordenite zeolite structure

Cell parameters:

a (y-axis) = 18.256Å

b (x-axis) = 20.534Å

c (z-axis) = 7.542 Å

Volume = 2827.26Å^3

Samples: **JT13** and **JT15** and are both hosts to polyacetylene.

1.6.2 Beta

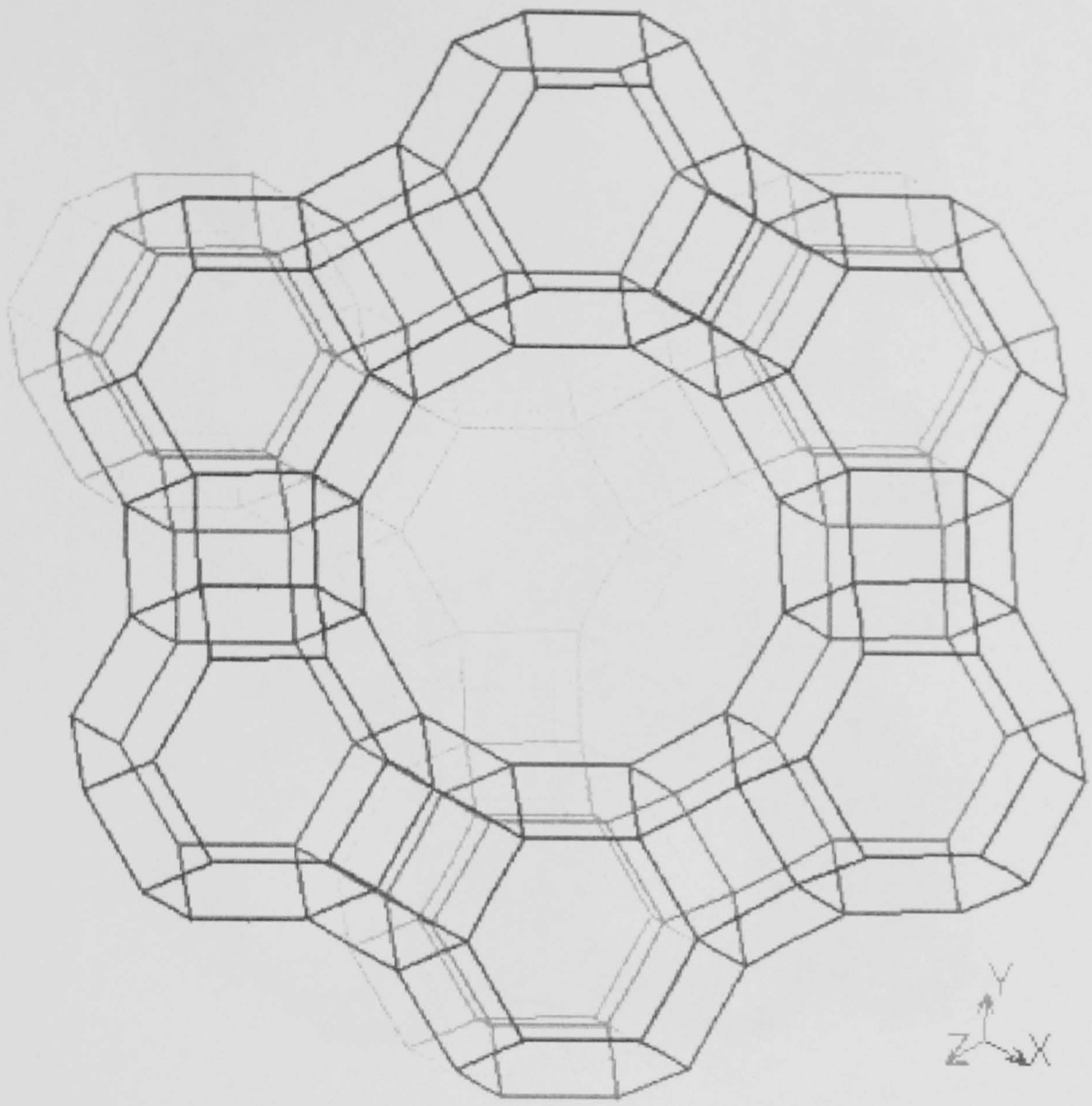

Figure 1.17: Beta zeolite structure

Cell parameters:

a = 12.632 Å

b = 12.632 Å

c = 26.186 Å

Volume = 4178.43Å^3

Samples:**JT8**, **JT20**, **JT31** and **JT35**

The first two samples play host to polyacetylene; the latter two host polypropyne.

1.6.3 Faujasite

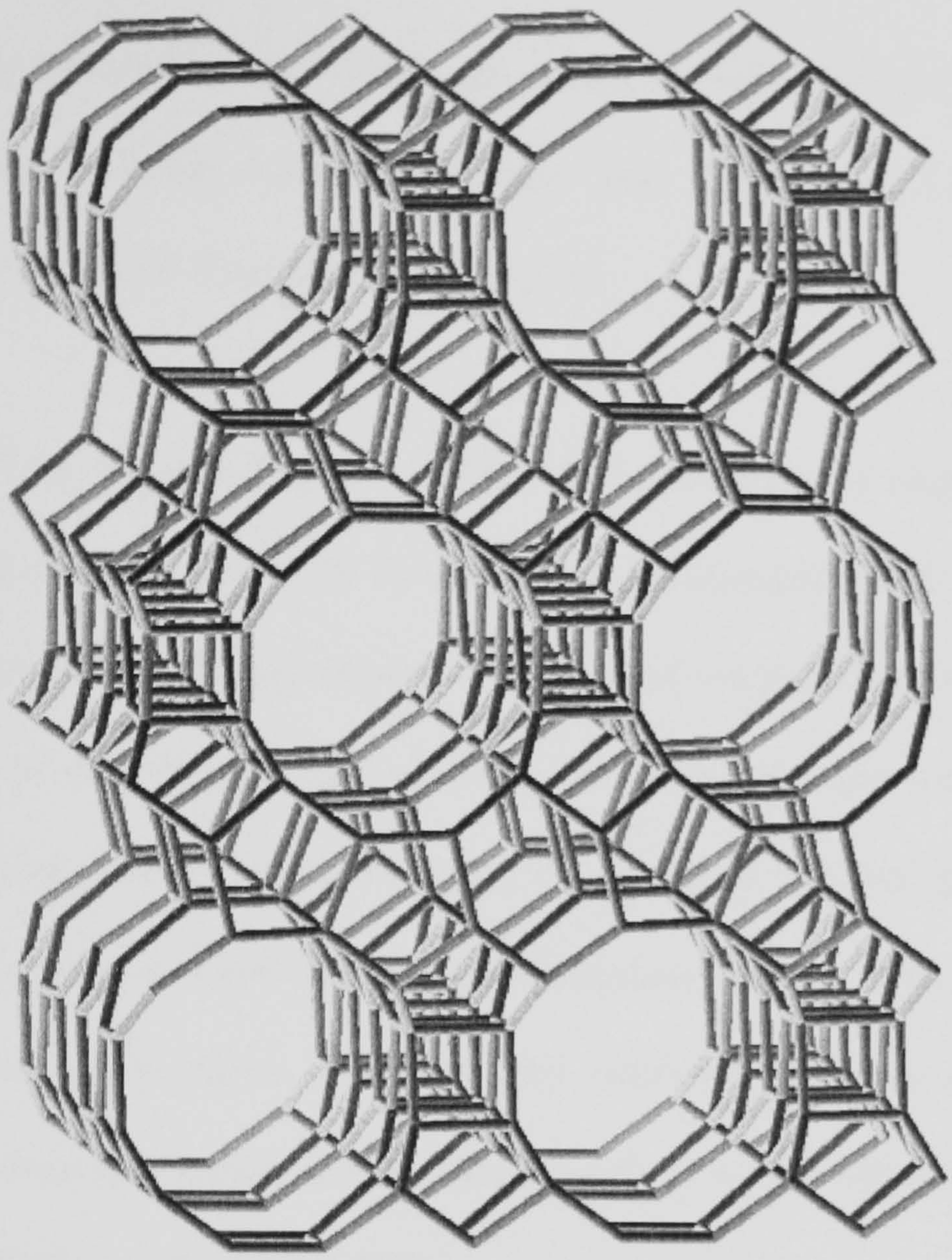

Figure 1.18: Faujasite zeolite structure

Cell parameters:

a = 24.345Å

b = 24.345Å

c = 24.345 Å

Volume = 14428.77Å^3

Samples: **JT6**, **JT22** and **JT28**. The first sample is host to polyacetylene; the latter two samples host polypropyne.

1.7 Single Walled Carbon Nanotubes

A sample of carbon nanotubes was procured from CarboLex, a commercial company conceived at the Advanced Science and Technology Commercialisation Centre at the University of Kentucky in Lexington.

"Our AP (as prepared) grade SWNT product consists of single-walled, close-ended, nanotubes which are made by the Arc method in specially made chambers. These carbon nanotubes are of average diameter 1.4nm and are found in 'ropes', which are typically 20 nm in diameter or approximately 50 tubes per rope with lengths of 2-5 microns. Impurities include approximately 35% residual catalyst (Ni, Y), which is usually encapsulated in carbon shells. Some amorphous carbon may also be found on the outer surfaces of the ropes. The only post synthesis treatment of the nanotubes comes from the homogenisation of the tubes directly from the chamber. The purity of our AP grade SWNTs is 50%-70%". **[28]**

Figure 1.19 shows a SEM image of the nanotube ropes for the batch we received from Carbolex. This image was kindly provided by Carbolex **[28]**.

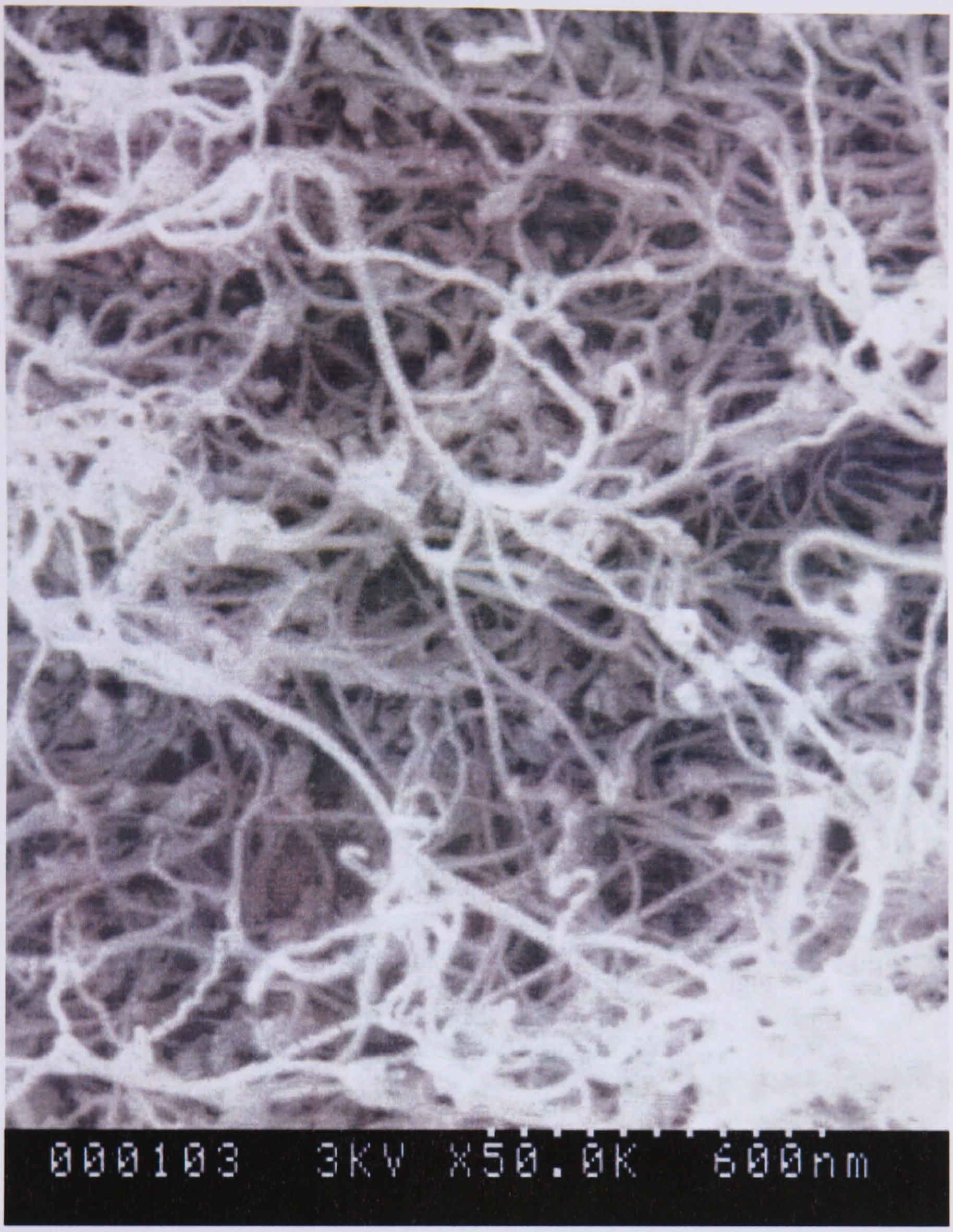

Figure 1.19: SEM image from SWNT batch used.

The SWNT material we received was treated in-house. They are solvent extracted first by hot toluene using the Soxhlet process **[29]**. This is then repeated using acetone instead of toluene. This second step removes the toluene from the nanotubes and any remaining water also. It also serves to remove soluble material from the nanotubes as well. On average, this removes about 8% to 10% by weight soluble fractions from the original supply of nanotubes we have. The exact extraction procedure is to be discussed in more detail in chapter 4.

1.8 Discotic Liquid Crystals

In 1888, Friedrich Reinitzer synthesised a new organic compound, cholesteryl benzoate, and crystallised it. He was surprised to find that the melting mechanism of this crystal was a two stage process. He observed that the crystals became a cloudy liquid at 145.5 °C which then cleared above 178.5 °C [**30**]. This material was further investigated by Otto Lehmann who discovered that the material exhibited birefringence when in the cloudy phase [**31**].

In crystals, birefringence derives from the long range ordered structure of the material which can lead to different properties in different directions. It is not expected to be seen in liquids due to the random motions of the component molecules. The fact it was seen suggested that the liquid material was showing crystalline properties and so a fourth state of matter was born.

In 1923, Daniel Vorländer [**32**] synthesised many thermotropic liquid crystals and showed that such liquid crystals are composed of long, rod-shaped molecules. The crystalline structures will then posses both orientation and positional order. When an initial melting point has been reached, the thermal energy may be sufficient to break the positional order but some degree of orientation may remain, demonstrating a preferred direction for the rod shaped molecules. At greater temperatures, the thermal energy may cause all position and orientation to be lost which will result in an isotropic phase (liquid). There can be several phases between the crystalline phase and the liquid phase (isotropic), some of which are described in the following three pages.

The crystalline phase (pre-melting temperatures) for rod-like molecules is sketched in figure 1.20 and shows very clearly that the material possesses both orientation and positional order.

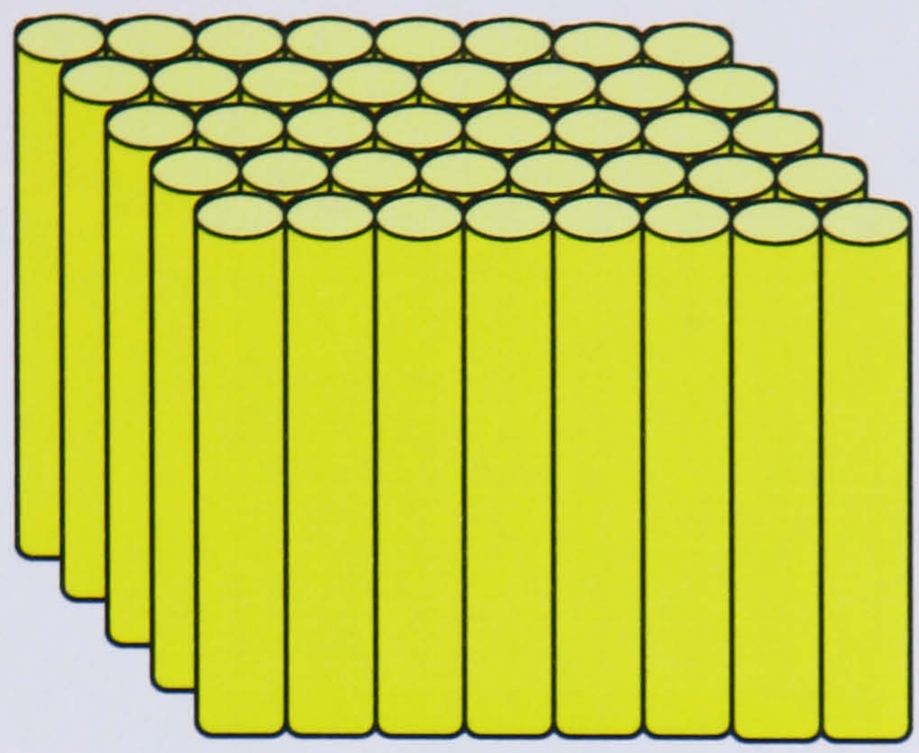

Figure 1.20: Crystalline phase

A little above the melting point, the thermal energy and resultant thermal motions of the molecules may be insufficient to disturb the layered structure of the crystal. However, the positional order of each layer may be lost as the thermal energies are enough to overcome the Van de Waals attractive force between the ends of the rods and so alignment is lost. This is called the Smectic phase.

Although several types of Smectic phases are known, the two most common phases are Smectic A (figure 1.21) and Smectic C (figure 1.22). Smectic A is when the orientation of the rods is perpendicular to the layers and Smectic C is when the orientation has a tilt angle to the layers.

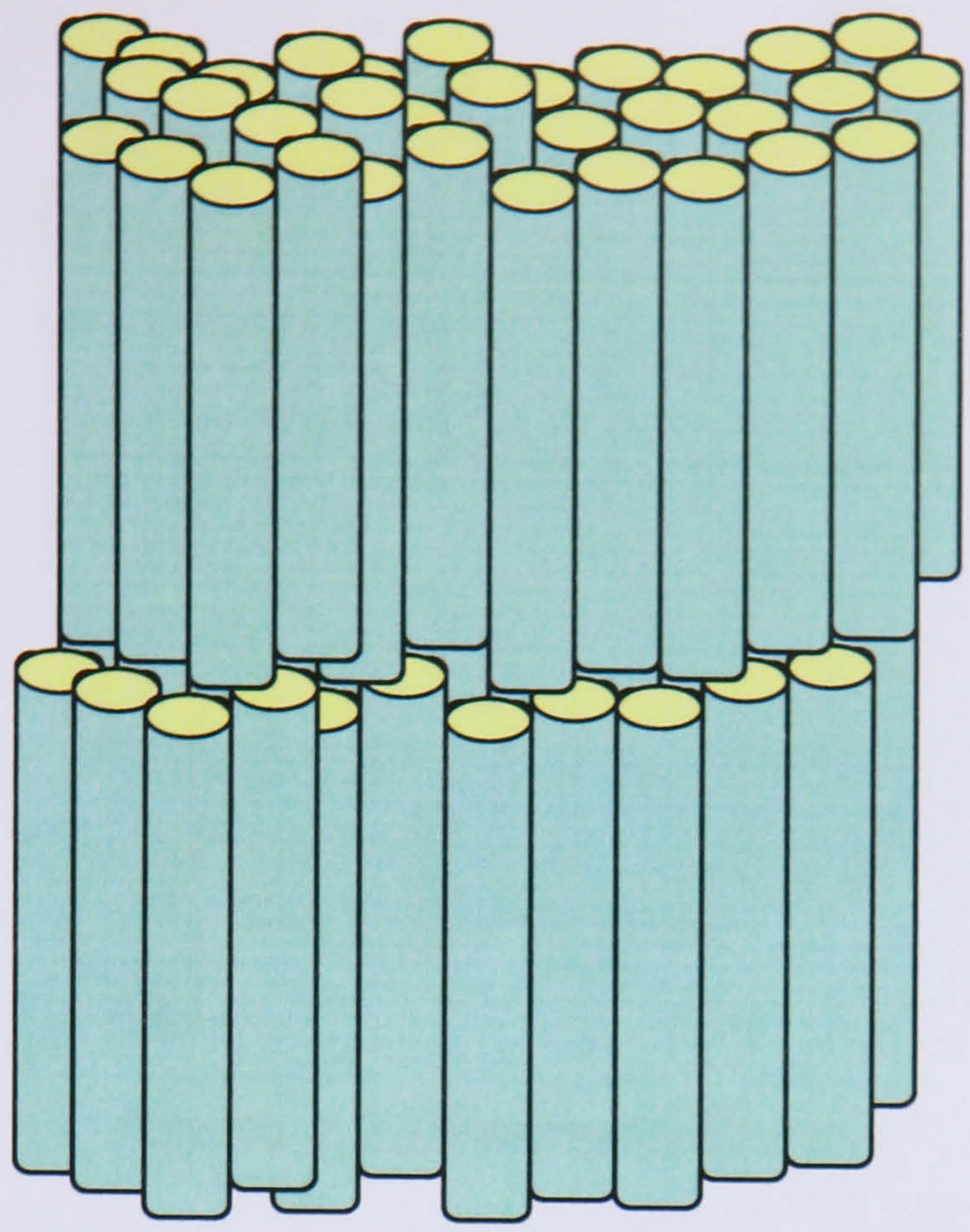

Figure 1.21: Smectic A phase

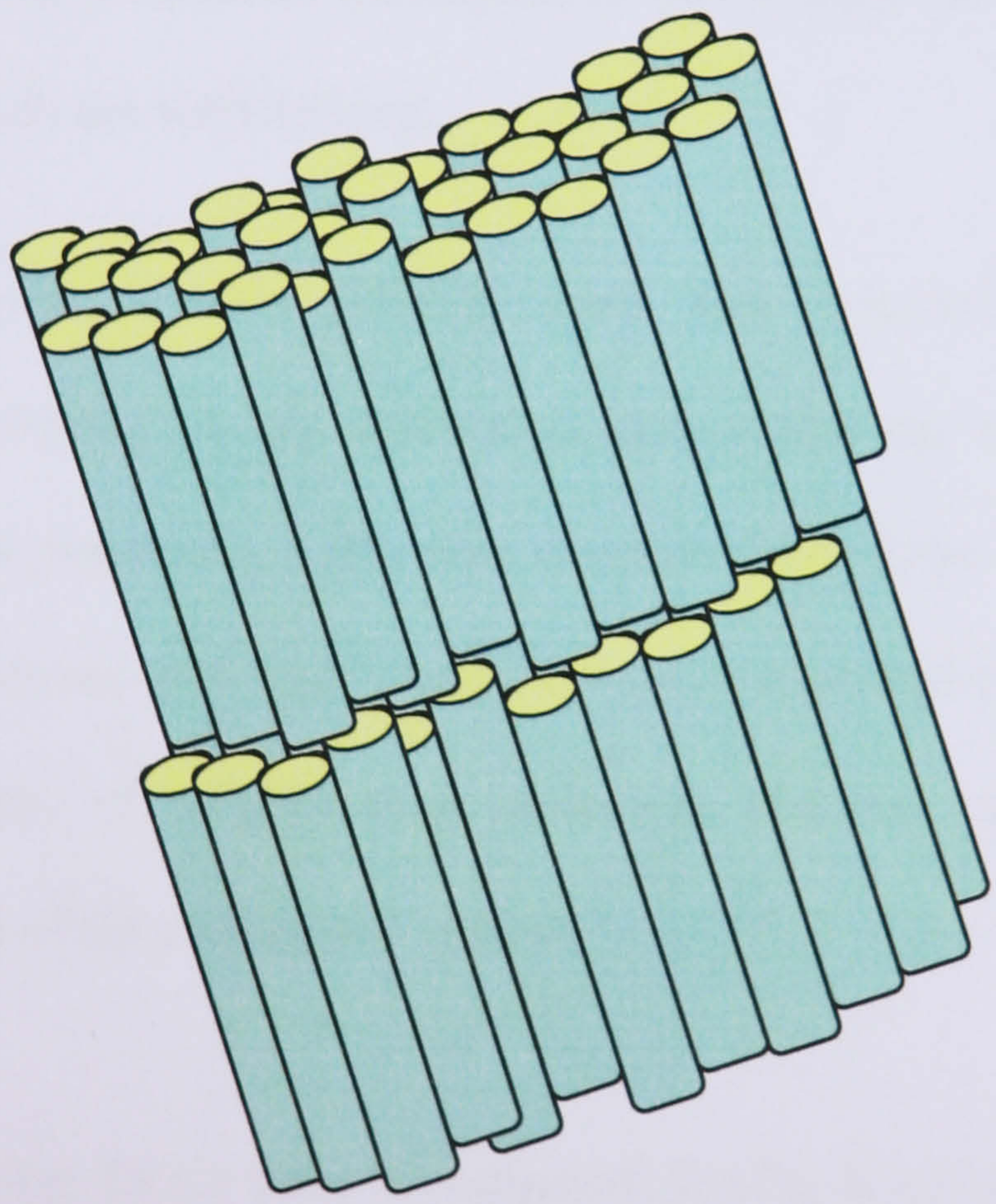

Figure 1.22: Smectic C phase

At higher temperatures, the thermal energies may be sufficient to break apart the layered structure. If this occurs but a degree of orientation still persists, we refer to this as the Nematic phase (1.23).

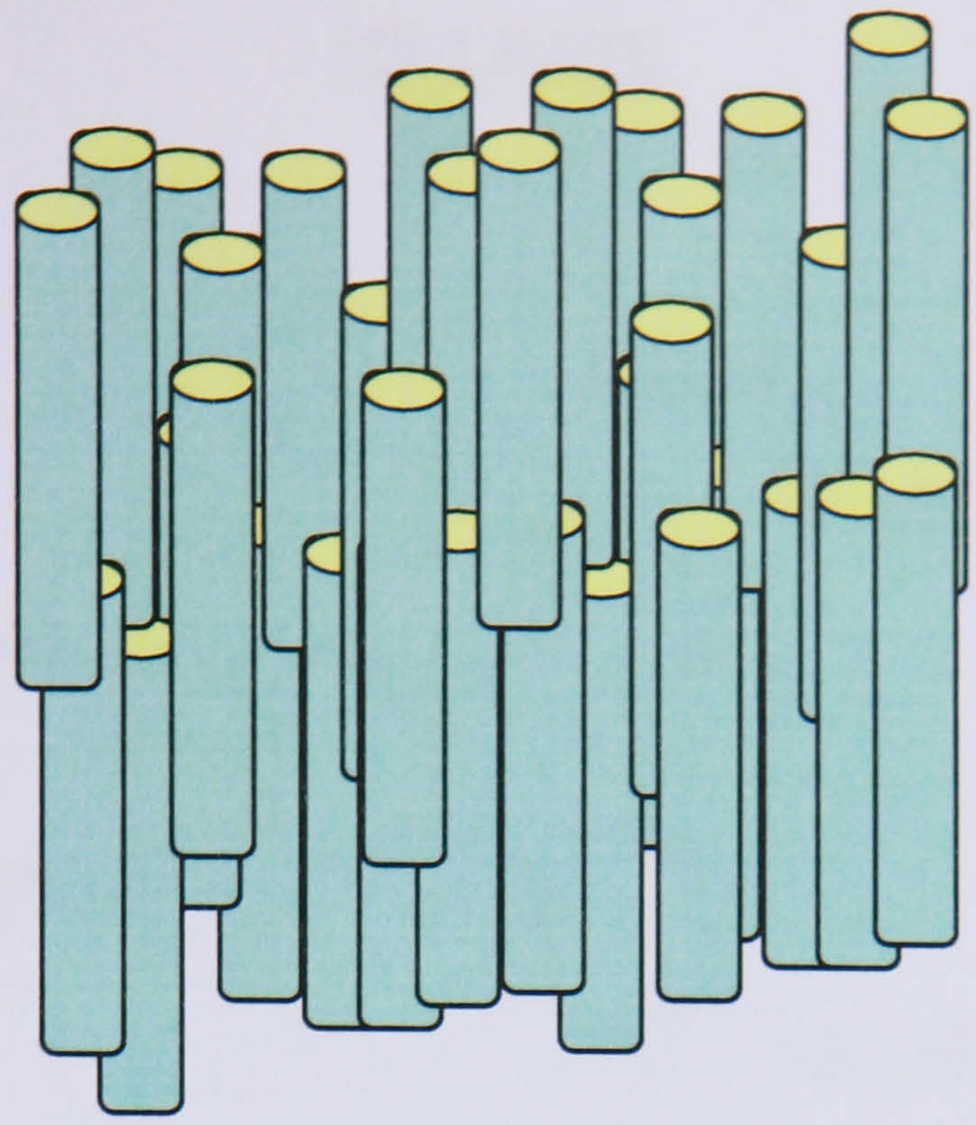

Figure 1.23: Nematic Phase

Be aware that the preceding figures show, for simplicity, that the rods in the liquid crystal phases have identical tilt angles. In reality there are variations around an average tilt angle which are well defined.

Discotic Liquid Crystals (DLCs) were first discovered in 1977 by S. Chandrasekhar **[33]** through x-ray diffraction studies and are so named due to the component molecules possessing a disc-like structure. They have the distinctive ability to self organise into stacks with high carrier mobilities expected through the stacks due to the close proximity of neighbouring molecules and the corresponding electron wavefunction overlap of the conjugated system.

In this work, five DLCs were investigated: HAT6, HAT6:PTP9, HAT11:PTP9, 2FHAT6 and a tri-block copolymer DLC [2,7-bis(2-ethoxyacetoxy)-3,6,10,11-tetrahexyloxytriphenylene]. All these materials were synthesised by the SOMS (Centre for Self Organising Molecular Systems) School of Chemistry, Leeds University. Their molecular structural diagrams follow:

1.8.1 HAT6

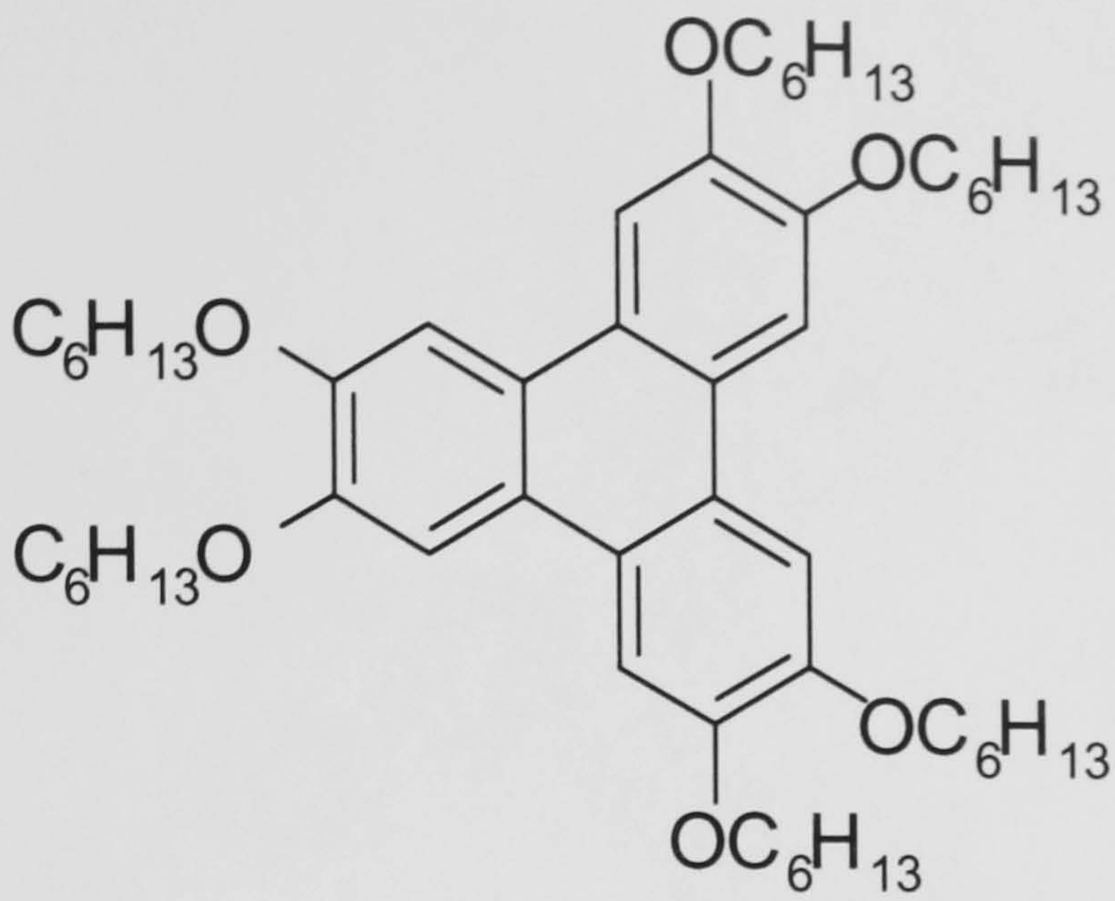

Figure 1.24: Molecular Structure of HAT6

1.8.2 HAT11

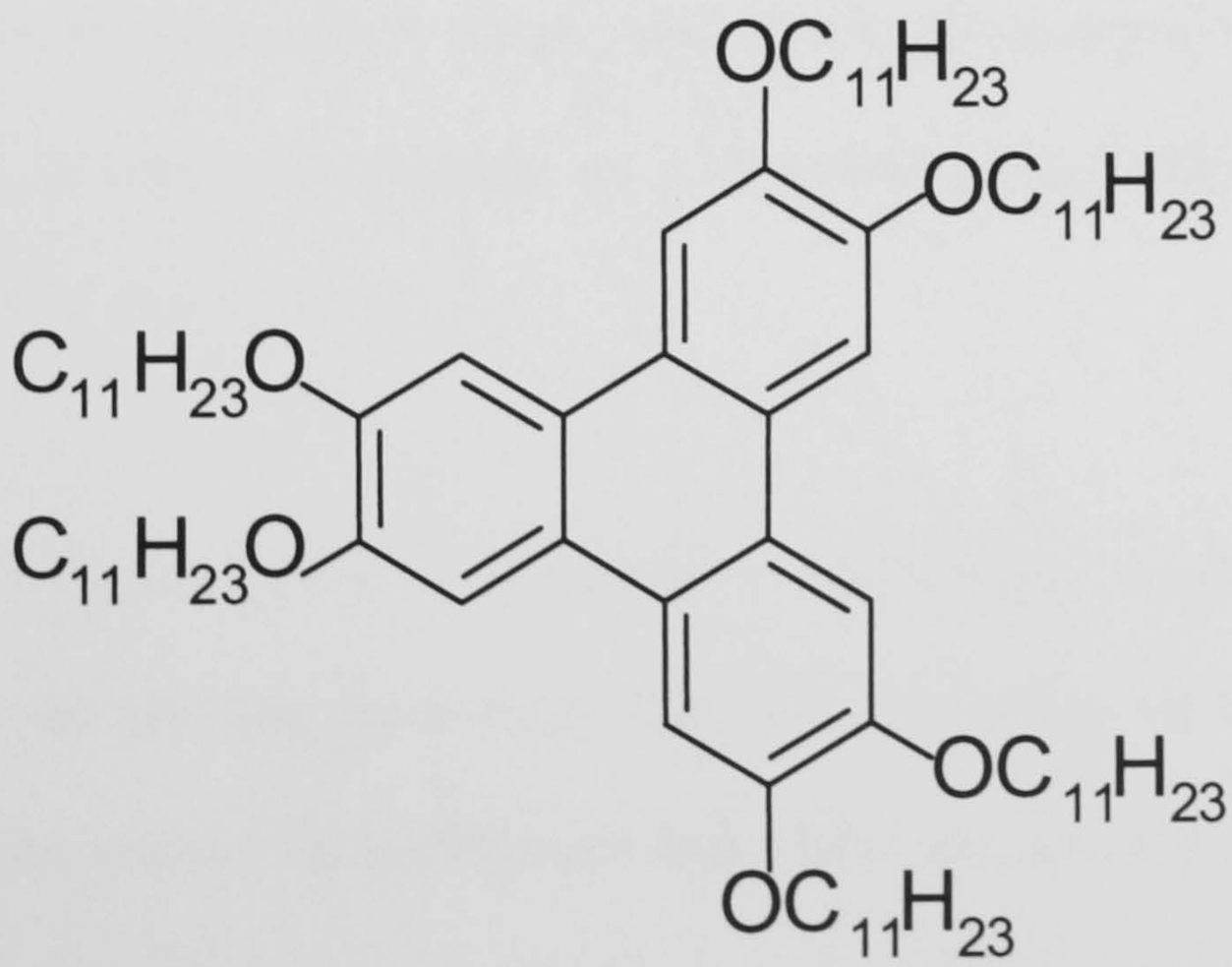

Figure 1.25: Molecular Structure of HAT11

1.8.3 PTP9

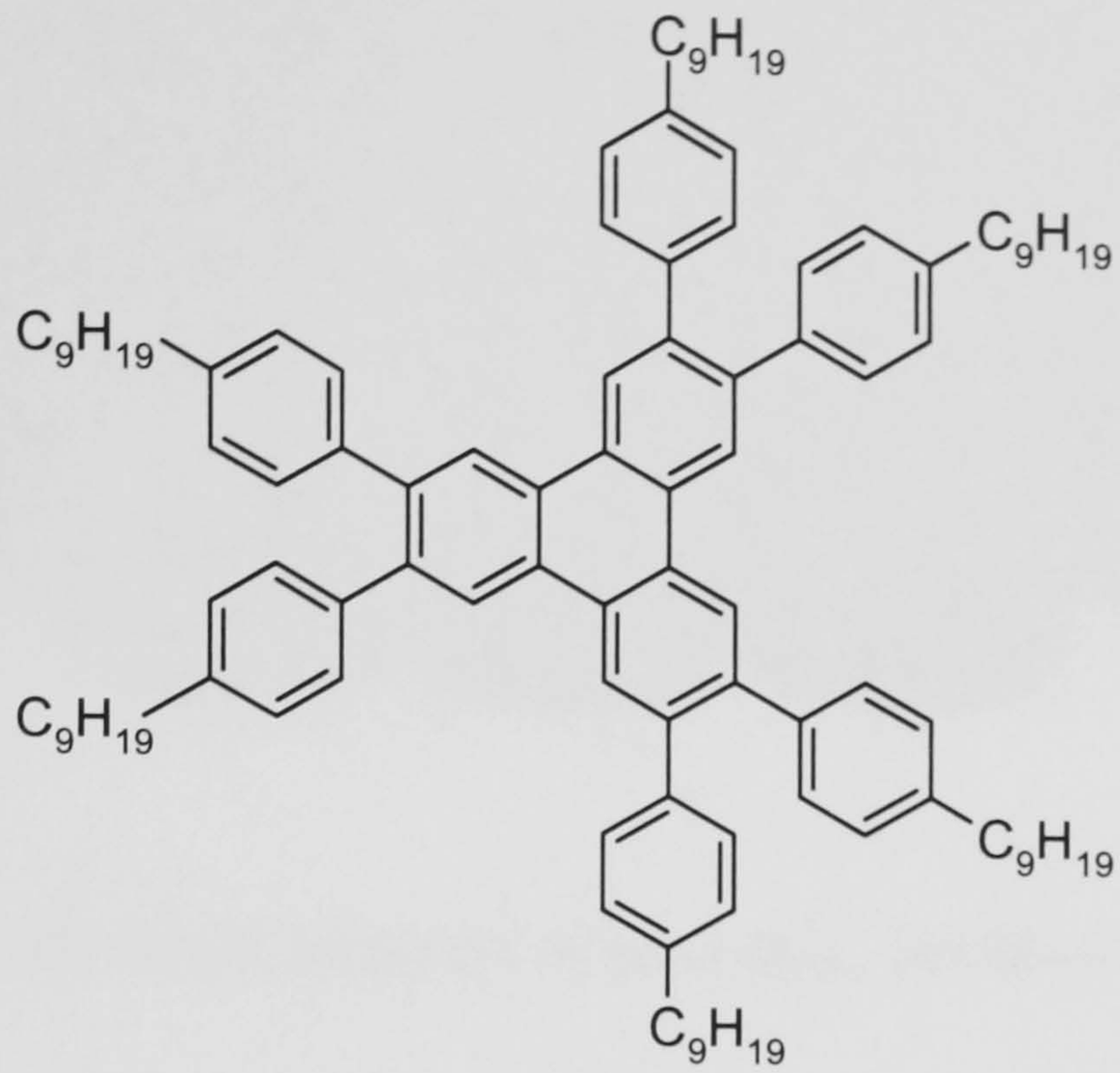

Figure 1.26: Molecular Structure of PTP9

PTP9 by itself does not possess liquid crystalline properties. It is possible, however, to form a stoichimetric mixture with PTP9 and another triphenylene based material. Figure 1.27 shows an example of a columnar stack formed with a discotic material like HAT6.

Figure 1.28 shows how a complementary 50:50 binary mixture of HAT6 and PTP9 will affect the stacking properties; note the alternation on the stack and the interleaving between stacks. This difference will affect the photoconductive properties of the material.

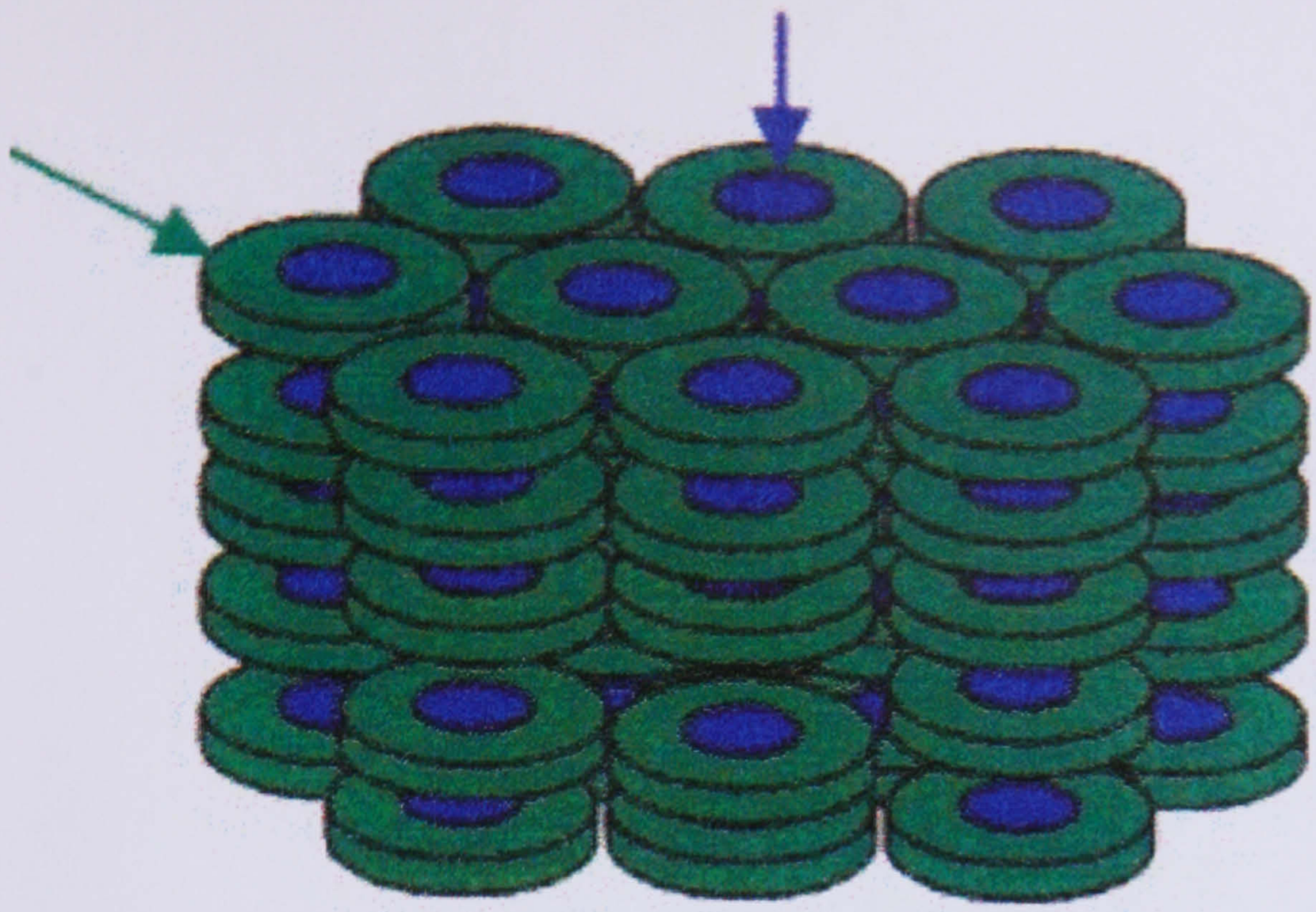

Figure 1.27: Single Molecule System (e.g., HAT6 or 2FHAT6)

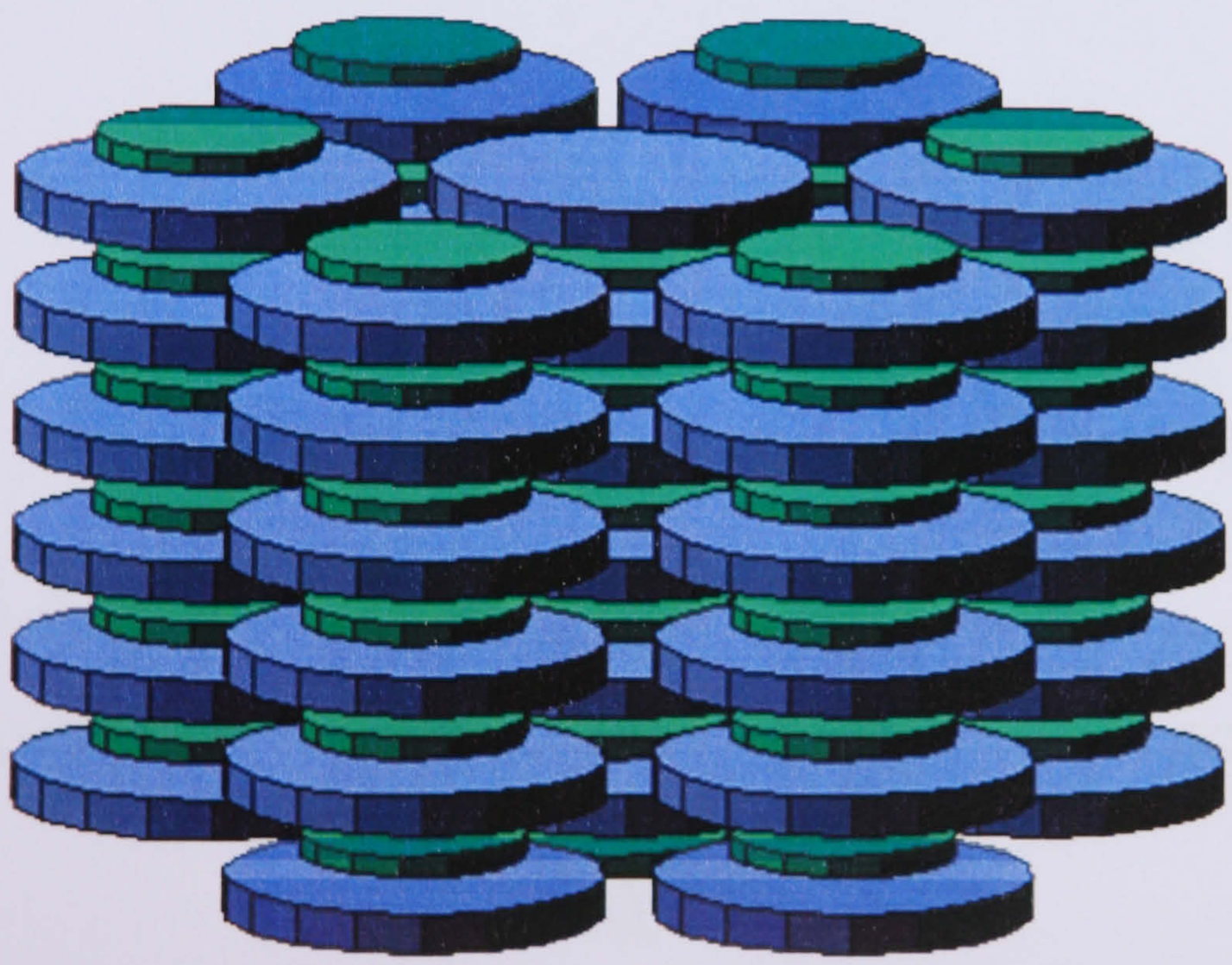

Figure 1.28: Complementary Binary System (e.g., HAT6:PTP9)

1.8.4 2FHAT6

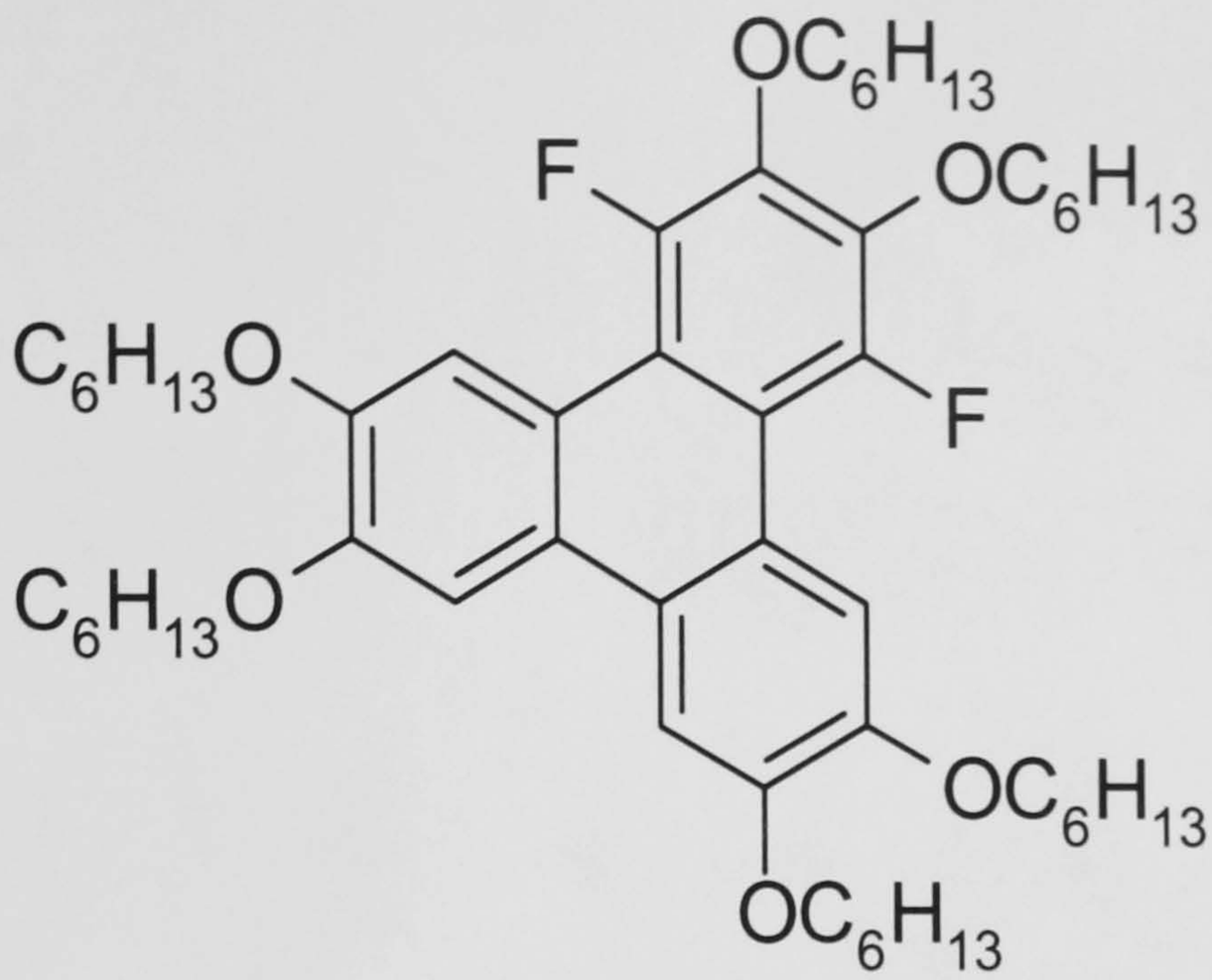

Figure 1.29: Molecular Structure of 2FHAT6

1.8.5 Triblock co-polymer discotic

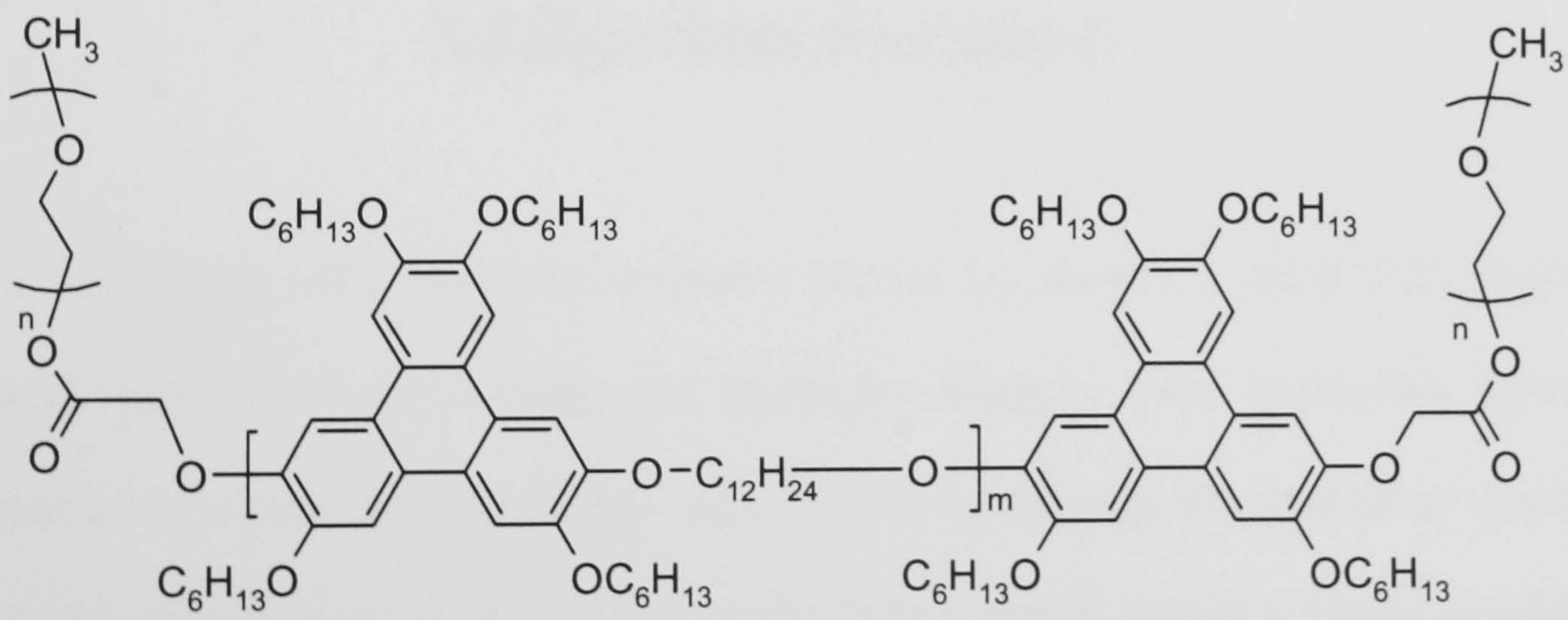

MC BP2000
m~12, n~45

Figure 1.30: Molecular Structure of Triblock Co-Polymer

The nanostructure of the tri-block copolymer is shown in figure 1.31 **[34]**.

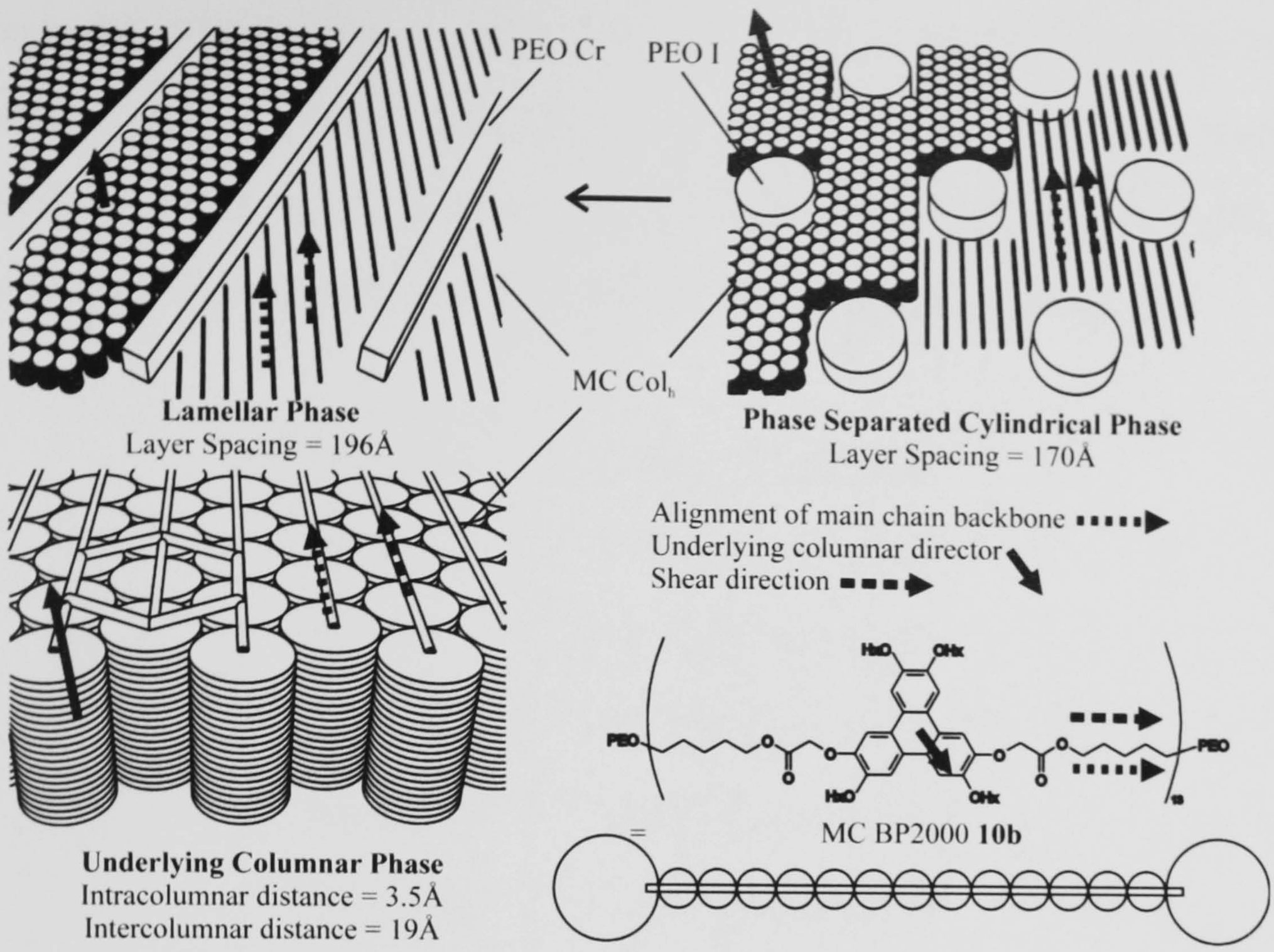

Figure 1.31: Triblock co-polymer phases

1.9 DLC Phase Boundaries

The DLCs have thermally activated phases (as shown in table 1.2). Below a threshold temperature on cooling, the molecules adopt a static crystalline structure (denoted as K) where any defects that occur will be frozen into the crystalline structure. Above this temperature at the melting point, the material enters a liquid crystalline phase referred to as the columnar phase (denoted as Col***x***, with ***x*** representing the way in which the columnar stacks are arranged).

The term 'mesophase' is generally used to describe a liquid crystal state. Whilst in the mesophase, the liquid crystalline behaviour results in the structure being constantly annealed and so any structural defects occurring would be quickly repaired, the mesophase is said to be 'self healing'. Because of this, it is expected that the

conduction properties of the liquid and non-liquid crystalline phases will be very different. At high enough temperatures, all order is lost due to the thermal energy present exceeding the van der Waals bond energies of the neighbouring discs. This is the isotropic (liquid) phase otherwise known as the clearing point (denoted as I).

Material	**Phase Boundaries**
HAT6	K 70°C Colh 100°C I
HAT6:PTP9	K 66°C Colh 155°C I
HAT11:PTP9	K 60°C Colh 170°C I
2FHAT6	K 25°C Colh 124°C I
Co-Polymer	K 47°C Colh 89°C I

Table 1.2: DLC Phase Boundaries

2 Theory of Photoconduction

2.1 Basic Electrostatics

The natures of the experiments included in this thesis rely on a property of basic electrostatics. The measurements of this thesis require an understanding of how photogenerated charge moving in an electric field between two electrodes affects current flowing in the external circuit connecting these electrodes. From such measurements, the mobilities of charge carriers in organic semiconductors, as well as the quantum efficiencies and other properties, can be deduced.

We begin by considering a basic capacitor, a device consisting of two plate electrodes separated (by a dielectric medium) a distance ***d***. If there is a potential difference, ***V***, between the electrodes, whose dimensions are relatively larger than the separation distance, a uniform electric field can be assumed which is given by equation 2.1:

$$E = \frac{V}{d} \qquad (2.1)$$

Consider now figure 2.1 which shows a charge ***q*** moving between the plates which traverses a distance ***s*** parallel to the electric field.

LIBRARY UNIV

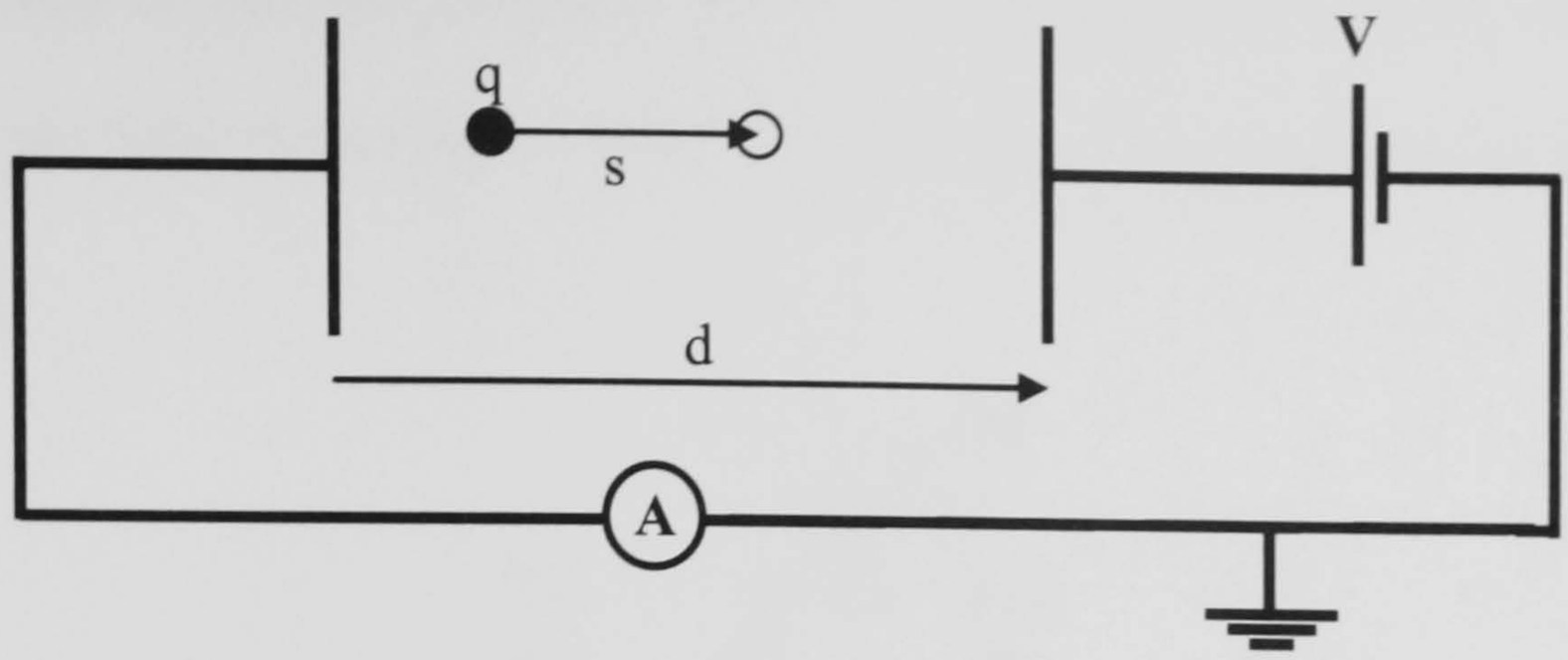

Figure 2.1: A charge, q, moves in an Electric Field causing a current.

As the electric field is uniform, the charge ***q*** moves through a potential difference, ***dV***, given by equation 2.2 which involves work, ***dW***, being done on the external circuit as demonstrated in equation 2.3.

$$dV = Es \qquad (2.2)$$

$$dW = qdV = \frac{qVs}{d} \qquad (2.3)$$

This work, ***dW***, is manifested as a charge ***Q*** moving in the external circuit from one electrode to the other through the applied potential difference ***V*** (positive charge moves from the cathode to the anode). The work done will be equal to ***QV.*** Therefore, the charge measured in the external circuit (found by integration of the current) will be equal to:

$$Q = \frac{qs}{d} \qquad (2.4)$$

Consider now a solution of polyacetylene dissolved in a solvent illuminated uniformly with UV light (fig. 2.2). The energy of the incoming photons will be sufficient to photoexcite electrons from the valence band (HOMO) to the conduction

band (LUMO) of the polyacetylene chains. In the conduction band, the electrons experience the force of the applied electric field and move along the carbon backbone.

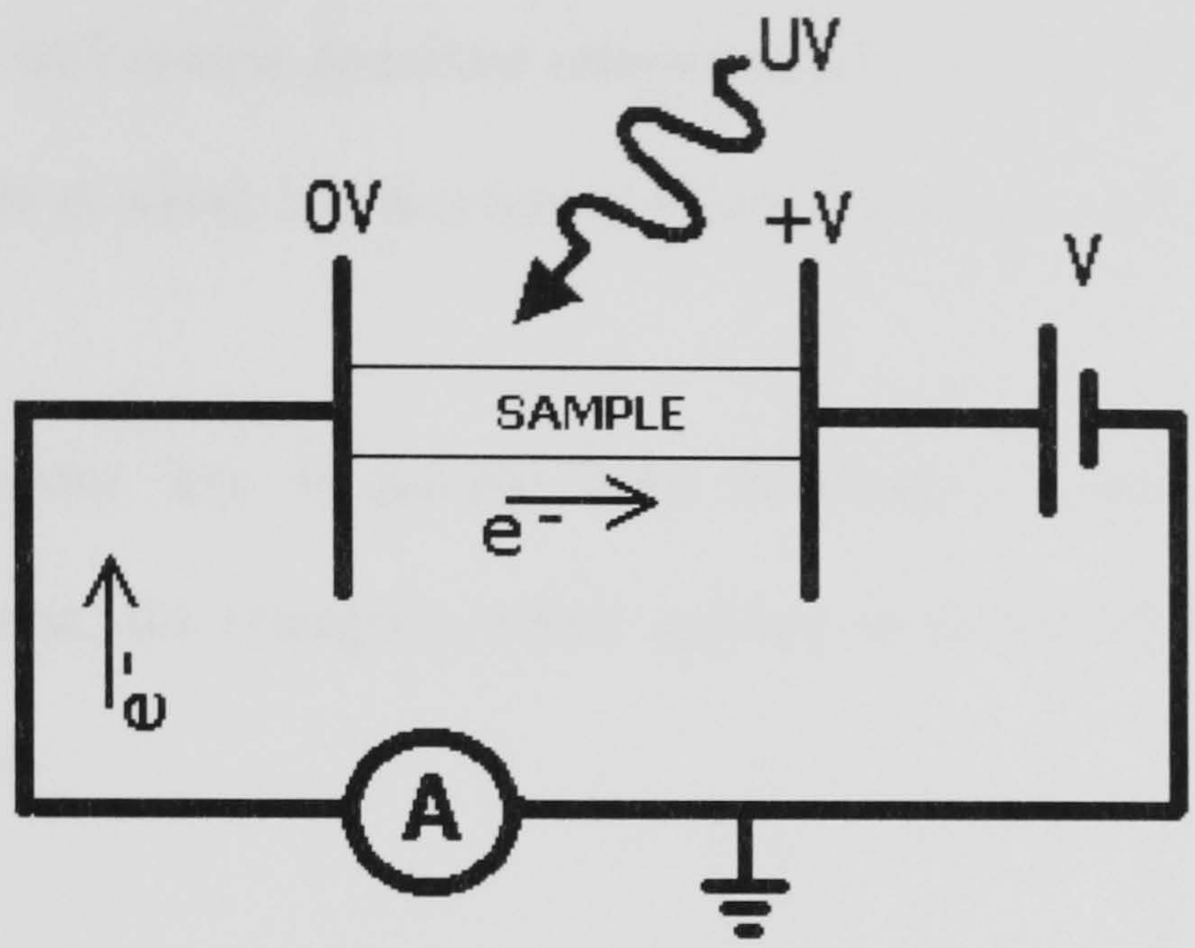

Figure 2.2: Basic schematic of photoconduction experiment.

Figure 2.2 shows a cartoon of this arrangement and demonstrates the direction of electron movement throughout the circuit. The ammeter will show a positive current by convention. In the experiments presented here, an oscilloscope will replace the ammeter in order to chart the motions of the photoexcited carriers and time evolution of the resultant photocurrent.

2.2 Photogeneration of charges

The peak value of the transient photocurrent shown in the previous chapter (Fig. 1.8) can be modelled as follows: If there are N photons per unit area in a laser pulse that are absorbed by a sample area A, then the total number of photons absorbed by the sample as the result of a laser pulse would be $N_{ph} = NA$ and therefore N_{ph} chances of excitation.

In practice however, only a fraction of these absorbed photons will cause excitations across the band gap. This fraction is the primary quantum efficiency for creating electron-hole pairs and is represented by the value η. Only a fraction of these electron-hole pairs will escape geminate recombination, as described by Onsager **[35]**, denoted by the value ϕ, which is a function of electric field and temperature.

Such behaviour has frequently been observed experimentally in organic materials (Anthracene, for example), which appears to fit the three dimensional, 3D, Onsager model **[36]**.

The quantum efficiency and the geminate recombination rates often cannot be deconvolved and are thus paired together as one entity written as $\{\eta\phi\}$, which will here on be referred to as the quantum efficiency. The total photocharge created, q, is given by equation 2.5. Combining this with equation 2.4, the measured photocharge Q via the external circuit will be given by equation 2.6.

$$q = e\{\eta\phi\}N_{ph} \tag{2.5}$$

$$Q = q\frac{s}{d} = \frac{e\{\eta\phi\}N_{ph}s}{d} \tag{2.6}$$

Let us now turn our attention to the transient photocurrent, I_p. By making the assumption that N_{ph} photons are absorbed instantaneously (we assume the light pulse is a delta function), we show the magnitude of the current is proportional on the carrier velocity v:

$$I_p = \dot{Q} = \frac{e\{\eta\phi\}N_{ph}\dot{s}}{d} = \frac{e\{\eta\phi\}N_{ph}}{d}\frac{ds}{dt} = \frac{e\{\eta\phi\}N_{ph}v}{d} \qquad (2.7)$$

We have assumed, until now, that the charge is unconstrained and free to move parallel to the field. If, however, the charge is constrained to move in a direction other than the field direction (e.g., a charge on an unaligned polymer chain), we need to replace s in the previous equations with the projected distance moved in the field direction, which we write as s_E.

Furthermore, if there are a number of charges involved, we require the average projected distance in the field direction, $\langle s_E \rangle$. Similarly, we would have an average carrier velocity in the field direction which we can denote as $\langle v_E \rangle$. Our equations for photocharge and photocurrent then become:

$$Q = \frac{e\{\eta\phi\}N_{ph}\langle s_E \rangle}{d} \qquad (2.8)$$

$$I_P = e\{\eta\phi\}N_{ph}\frac{\langle v_E \rangle}{d} \qquad (2.9)$$

If it takes a time T for an electron to travel across the whole chain of length L and the electron does not hop to a neighbouring chain then the displacement current will cease at this point. Assuming that electrons are created uniformly along the chain and that there are no trapping sites or defects, the displacement current will then fall linearly with time t, given by equation 2.10.

$$I(t) = I_P\left(1 - \frac{vt}{d}\right) = I_P\left(1 - \frac{t}{T}\right) \qquad (2.10)$$

From an ideal temporally resolved experiment the transit time, $T = d/v$, can be calculated from the duration of the photocurrent signal. If the chain lengths are known, the mobility of the electrons can be deduced from the velocity as a function of electric field.

2.3 Polymer chain and nanotube orientation modelling in 3D

To assume that encapsulated polymer chains or nanotubes in a solution will line up with the direction of the electric field is a gross over simplification. Such a sample will have no initial preferred direction and the 'molecular wires' will have an equal probability of pointing in any direction in space.

Conversely, once a DC field is applied across the sample, there are good reasons to expect that there will be some alignment due to dipole moments. However, the field for these experiments is pulsed and only applied for a few tens of microseconds at a frequency of about 1 Hz. It is therefore unlikely that such alignments will take place and so the fact that all wires are pointing in random directions in 3D space must be considered. Therefore, it is necessary to calculate the average component length (the projected length) of the wires aligned with the electric field. A chain of length L and of random orientation is depicted in figure 2.3.

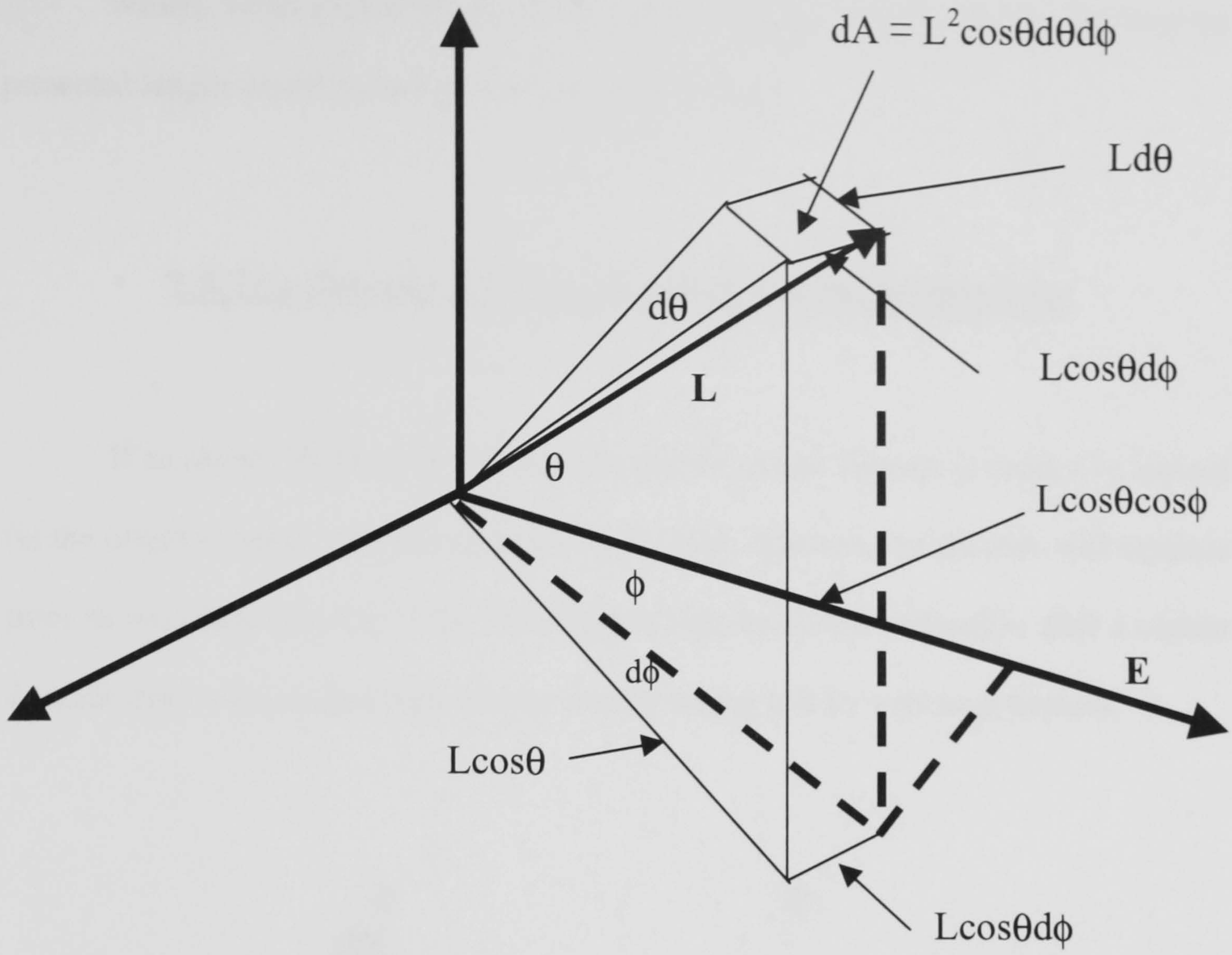

Figure 2.3: 3D isotropic model of chain lengths

Here we are assessing the component projected length $\langle L_{Proj} \rangle$ along the electric field for a molecular wire of length $\boldsymbol{L}$ at angles to the electric field of $\boldsymbol{\theta}$ and $\boldsymbol{\phi}$ respectively. We then calculate the probability of this wire being found in an infinitesimal unit area, $\boldsymbol{dA}$, and then normalise this to the total area of a sphere that can be swept out with this radius of $\boldsymbol{L}$. Double integration over all allowed angles of $\boldsymbol{\theta}$ and $\boldsymbol{\phi}$, yield the following calculation (equation 2.11):

$$\left\langle L_{\mathrm{Proj}} \right\rangle = \frac{1}{2\pi L^2} \int_{-\frac{\pi}{2}}^{+\frac{\pi}{2}} \int_{-\frac{\pi}{2}}^{+\frac{\pi}{2}} L^3 \cos^2\theta \cos\phi \, d\theta \, d\phi = \frac{L}{2\pi} \int_{-\frac{\pi}{2}}^{+\frac{\pi}{2}} \int_{-\frac{\pi}{2}}^{+\frac{\pi}{2}} \cos^2\theta \cos\phi \, d\theta \, d\phi \qquad (2.11)$$

Which, when evaluated, gives the value: $\langle L_{Proj} \rangle = 0.5\ L$ That is, the average projected length would be half of the total 'wire' length.

2.4 The Onsager theory of geminate recombination

If an electric field is applied across a sample and an electron is excited or ionised (in the original theory concerning gases) by incident radiation, the electron will separate from its twin hole (see Fig. 2.4). The electron (and hole) will thermalise after a certain distance due to their initial high kinetic energies being lost by various processes.

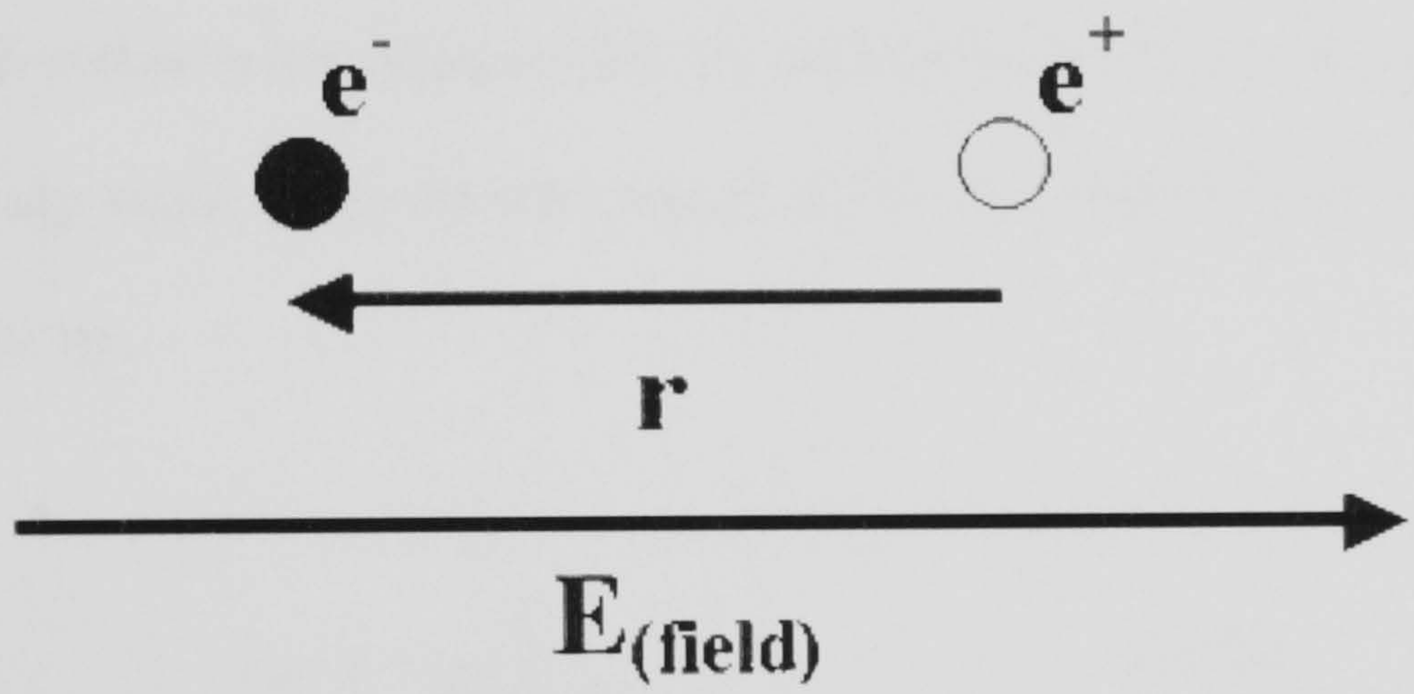

Figure 2.4: Charge separation in an Electric Field

Now the relative distance between the electron/hole pair can be considered. The potential energy between the electron and hole is given by the standard electrostatic potential equation (denoted as U_1).

$$U_1 = -\frac{e^2}{4\pi\varepsilon\varepsilon_0 r} \qquad (2.12)$$

As the electron has moved a distance r from its original position in the applied electric field, it has lost a potential energy given by U_2.

$$U_2 = -eEr \qquad (2.13)$$

Therefore, the total potential energy of the excited electron is equal to:

$$U_r = -\frac{e^2}{4\pi\varepsilon\varepsilon_0 r} - eEr \qquad (2.14)$$

As shown in Fig. 2.4, an electron may thermalise a distance b from its twin hole. The Coulomb radius is the distance that an electron/hole pair would separate to have a potential energy equal to the thermal energy in the Coulomb field alone. The Coulomb radius is given by:

$$r_{KT} = -\frac{e^2}{4\pi\varepsilon\varepsilon_0 kT} \qquad (2.15)$$

In order to escape geminate recombination, the electron has an energy barrier $\Delta\varepsilon$ to overcome. The probability P will therefore be thermally activated and have the form of equation 2.16. The precise nature of $f(E)$ will depend on the dimensionality of the problem.

$$P = f(E)\exp\left(-\frac{\Delta\in}{kT}\right) \qquad (2.16)$$

Figures 2.5a and 2.5b are plots of U_1 (**blue line**), U_2 (**red line**) and U_r (**black line**) versus r. In Figure 2.5b, the electric field has been increased by a factor of two. It is shown that the distance p and the energy barrier $\Delta\epsilon$ will decrease if the applied electric field strength E is increased.

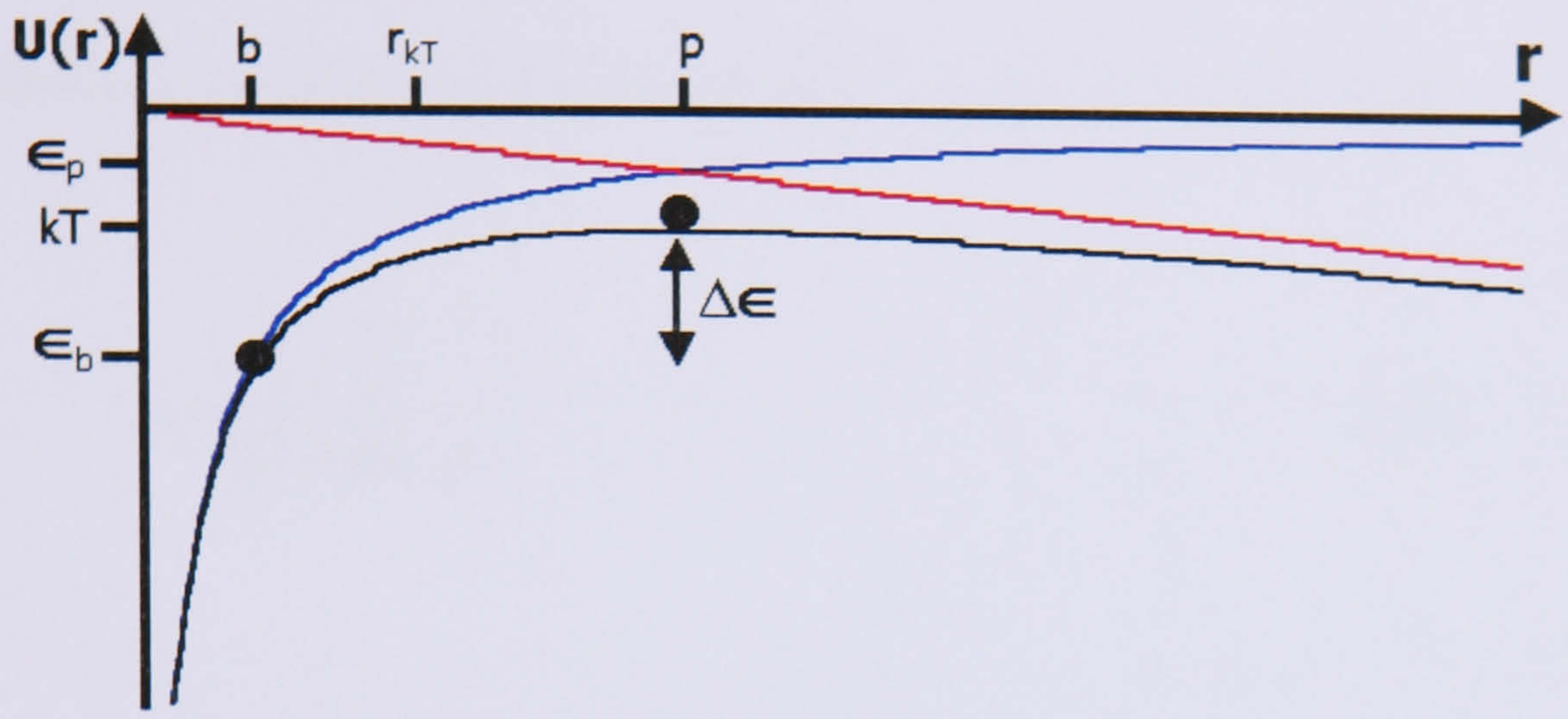

Figure 2.5a: Total Energy of an electron/hole pair in an electric field

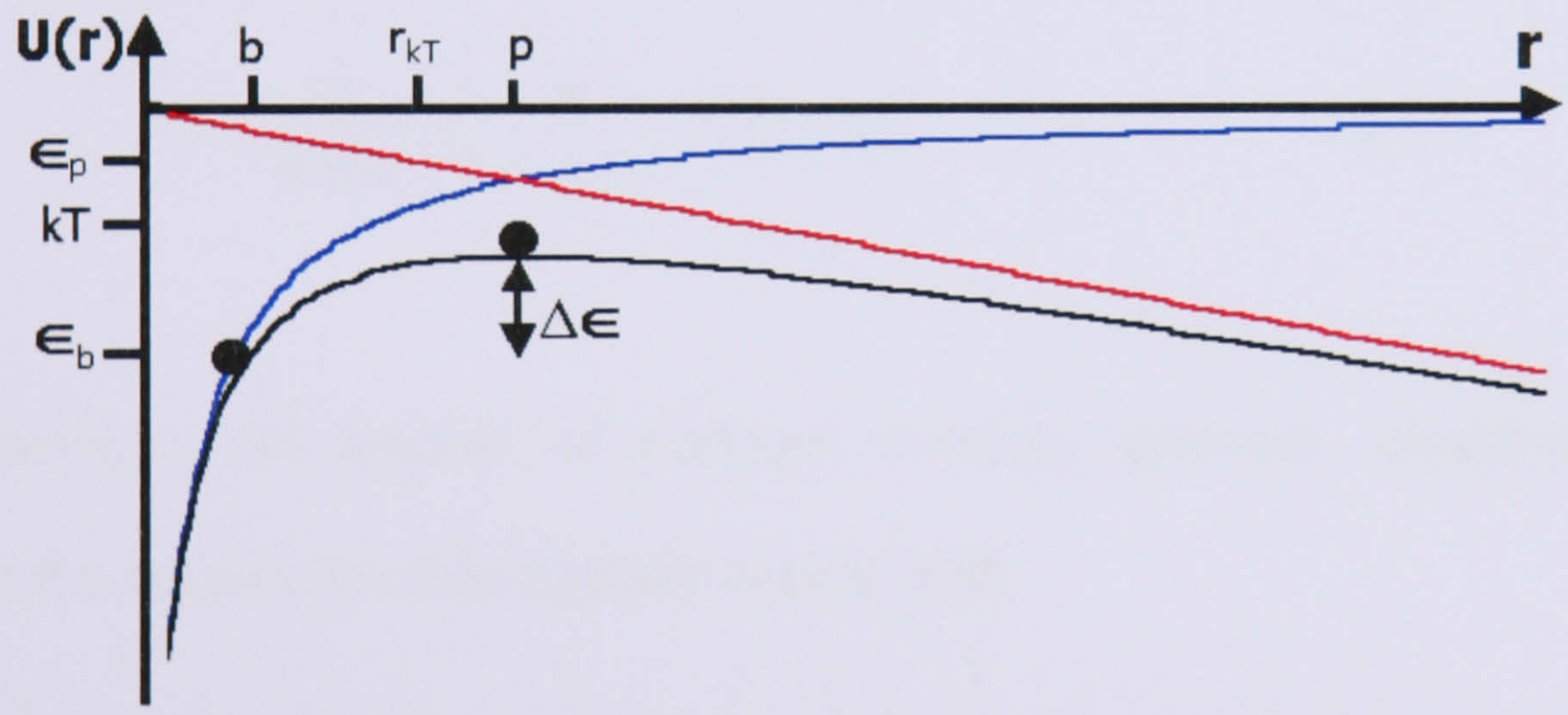

Figure 2.5b: Total Energy of an electron/hole pair in fig. 2.5a with field doubled.

The relationship between p and E and the relationship between $\Delta\epsilon$ and E are derived as follows. If we define r to be the distance of charge separation, we are looking at the point where $U(r)$ is a maximum. The precise value of r where this occurs can be found by differentiation of Equation 2.14, as shown in Equations 2.17 and 2.18.

$$\frac{dU}{dr} = \frac{e^2}{4\pi\varepsilon\varepsilon_0 r^2} - eE = 0 \tag{2.17}$$

$$r^2 = \frac{e^2}{4\pi\varepsilon\varepsilon_0 eE} = r_{kT}\frac{kT}{eE} \tag{2.18}$$

As this value of ***r*** is equivalent to our distance of escape, ***p***, we can write:

$$p = \sqrt{\left(\frac{e}{4\pi\varepsilon\varepsilon_0 E}\right)} \tag{2.19}$$

$$\Delta\in = \left(-\frac{e}{4\pi\varepsilon\varepsilon_0 p} - eEp\right) - \left(-\frac{e}{4\pi\varepsilon\varepsilon_0 b} - eEb\right) \tag{2.20}$$

$$\Delta\in = \frac{e}{4\pi\varepsilon\varepsilon_0}\left(\frac{1}{b} - \frac{1}{p}\right) + eE(b-p) \tag{2.21}$$

Therefore, the number of electrons escaping geminate recombination will depend on the magnitude of the applied electric field.

2.5 Poole-Frenkel Behaviour (barrier lowering)

Equation 2.19 gives the distance, in an applied electric field, that an electron would have to separate from its twin hole in order to escape the electrostatic attraction. The overall potential energy of the charge carrier at this distance will be dependent on the electric field. The presence of an electric field changes this energy, in respect to a zero field case, by the following amount:

$$U(p,E=0)-U(p,E)=\Delta U(E)=-\sqrt{\frac{e^3E}{4\pi\varepsilon\varepsilon_0}}=-\frac{\beta}{2}E^{1/2} \tag{2.22}$$

Where we have defined β to be...

$$\beta=\sqrt{\frac{e^3}{\pi\varepsilon\varepsilon_0}} \tag{2.23}$$

...where equation 2.23 is the commonly encountered Poole-Frenkel coefficient.

If this energy difference, ΔU, is less than the thermal energy, kT, then there is a negligible effect on photocarrier generation. The effect on photocarrier generation becomes more pronounced when this energy difference is greater than the thermal energy (i.e., at higher fields). Therefore, this effect (known as the Poole-Frenkel) effect occurs in the case where:

$$E>\left(\frac{kT}{\beta}\right)^2\equiv\frac{kT}{er_{kT}} \tag{2.24}$$

2.6 Polarons

In molecular crystals where there is strong electron-phonon coupling, this coupling may cause an electron in a LUMO (or hole in a HOMO) to distort the surrounding lattice such that the charge carrier potential energy is reduced. This is referred to as a polaron. The reduction in potential energy is the binding energy, E_b, of the polaron.

The charge carrier is now effectively sitting in a potential well it has created for itself. To move to an adjacent molecule, it requires a similar distortion to appear at that lattice site through thermal effects or it requires the configuration of the two sites to be momentarily equalised allowing tunnelling from one to the other.

Holstein showed a chain of diatomic molecules and the effect of adding an electron to one of the molecules causing a distortion (change in interatomic separation). This is known as the Holstein small polaron and is when the local electron-phonon coupling extends no further than one molecular unit. Holstein derived a relationship between the 1D carrier mobility and temperature of a small polaron [37]. The relationship is given by equation 2.25, where J is the bandwidth and a is the inter-atomic spacing.

$$\mu = \frac{ea^2}{kT}\frac{1}{\hbar}\left(\frac{\pi}{2E_b kT}\right)^{\frac{1}{2}} J^2 \exp\left(-\frac{E_b}{2kT}\right) \qquad (2.25)$$

2.7 Loss Mechanisms

The preceding sections have described the process of photogeneration of charges and their motions. The following sub-sections describe the some of the loss mechanisms of charge in organic materials.

2.7.1 Bimolecular Recombination

As discussed previously, a photoexcitation event leading to the creation of an electron/hole pair may give rise to a photocurrent under the right conditions. When the applied electric field is removed, the unbound and separated electron/hole pair may recombine due to electrostatic attraction.

However, if there are high numbers of charge carriers present in a system, initially unrelated electrons and holes may interact with each other and recombine during the photocurrent event. This process is known as bimolecular recombination.

In a 3D semiconductor system, e.g. silicon, when in steady state, if the light intensity is sufficiently high, bi-molecular recombination will occur with a characteristic rate constant β and the rate equation for carrier generation is given by:

$$\frac{dn}{dt} = -\beta np = -\beta n^2 \qquad (2.26)$$

In this equation, p and n are the numbers of positive and negative charge carriers respectively (their product can be written as n^2 as the carriers are created in equal numbers). This equation is solved to find the number of carriers, $n(t)$, at time t after an initial population of n_0 begins to recombine.

$$\int_{n_0}^{n(t)} \frac{dn}{n^2} = -\int_0^t \beta dt \qquad (2.27)$$

$$\frac{1}{n(t)} - \frac{1}{n_0} = -\beta t \qquad (2.28)$$

$$\frac{1}{n(t)} = \frac{1}{n_0} - \beta t = \frac{1 - \beta n_0 t}{n_0} \tag{2.29}$$

Current density, j, then decays with time

$$j = nev \tag{2.30}$$

$$j(t) = \frac{n_0 ev}{1 - \beta n_0 t} \tag{2.31}$$

2.7.2 Charge Trapping

Semiconducting systems may have features or defects in their molecular structure which lead to the formation of traps. An unbound charge carrier may encounter such a trap and become immobilised. The depth of the trap, the local temperature and the magnitude of any applied electric field will determine the trap release rate.

In the presence of traps with a trap time, τ, the time evolution of the carrier density, n, in response to a generation rate, G, is given by:

$$\frac{dn}{dt} = G - \frac{n}{\tau} \tag{2.32}$$

After a delta function light pulse which creates n_0 carriers at t=0:

$$\frac{dn}{dt} = -\frac{n}{\tau} \tag{2.33}$$

$$n = n_0 \exp\left[-\frac{t}{\tau}\right] \tag{2.34}$$

The photocurrent would show a similar decay.

In 1D, the presence of traps would have a much more noticeable effect than in a higher dimensional system. In fact, in contrast to a 3D system where the trap time is invariant with electric field, in 1D the distance to trap, s, is invariant with field (equation 2.35) and the time to trap is predicted to vary with field (equation 2.36).

$$s = v_d \tau = \mu E \tau \tag{2.35}$$

$$\tau = \frac{s}{\mu E} \tag{2.36}$$

This is because a carrier moving along an isolated chain/tube would have no possibility to negotiate its way around a defect. Furthermore, it will find the defect as a result of its drift motion in contrast to 3D where carriers find defects as a result of thermal, diffusive motion.

2.7.3 Transits

Another mechanism for charge loss in the system is if the sample is in direct contact with electrodes and charge recombines at one of the electrodes. If the entire sample mass was illuminated homogenously, one would expect (in the absence if any other loss mechanisms) to see an ideal photocurrent with a triangular decay of the characteristic of figure 2.6 (assuming the electrodes to be non-ohmic). Here, Time=0 is at the point of applied delta function light pulse where ***T*** is the time at which the photocurrent ceases.

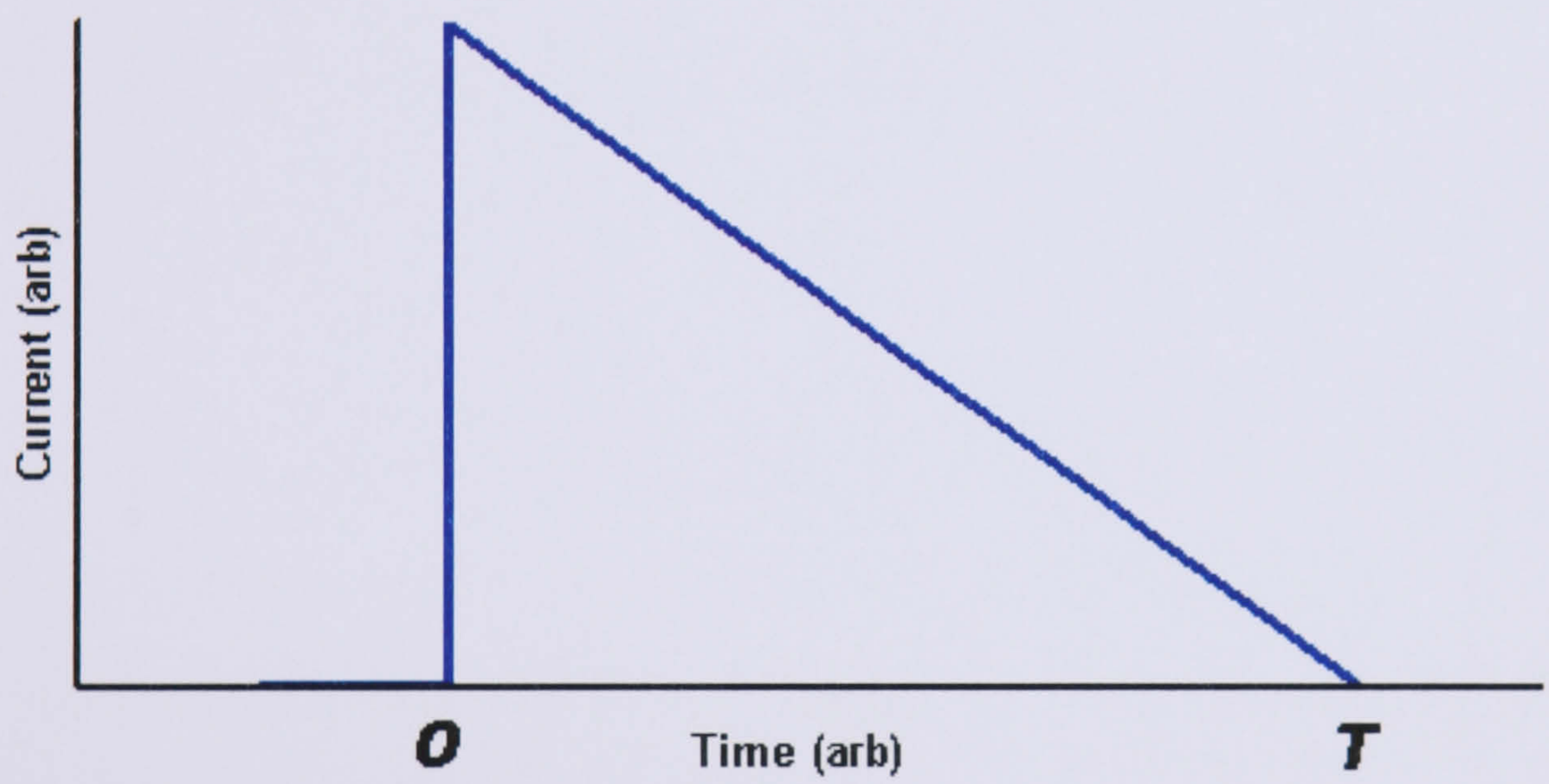

Figure 2.6: Transit of a homogenously illuminated sample

However, if the charge carriers were excited at one electrode and then traversed the sample mass before recombination at the counter electrode (Time of Flight), an ideal photocurrent would appear as in figure 2.7:

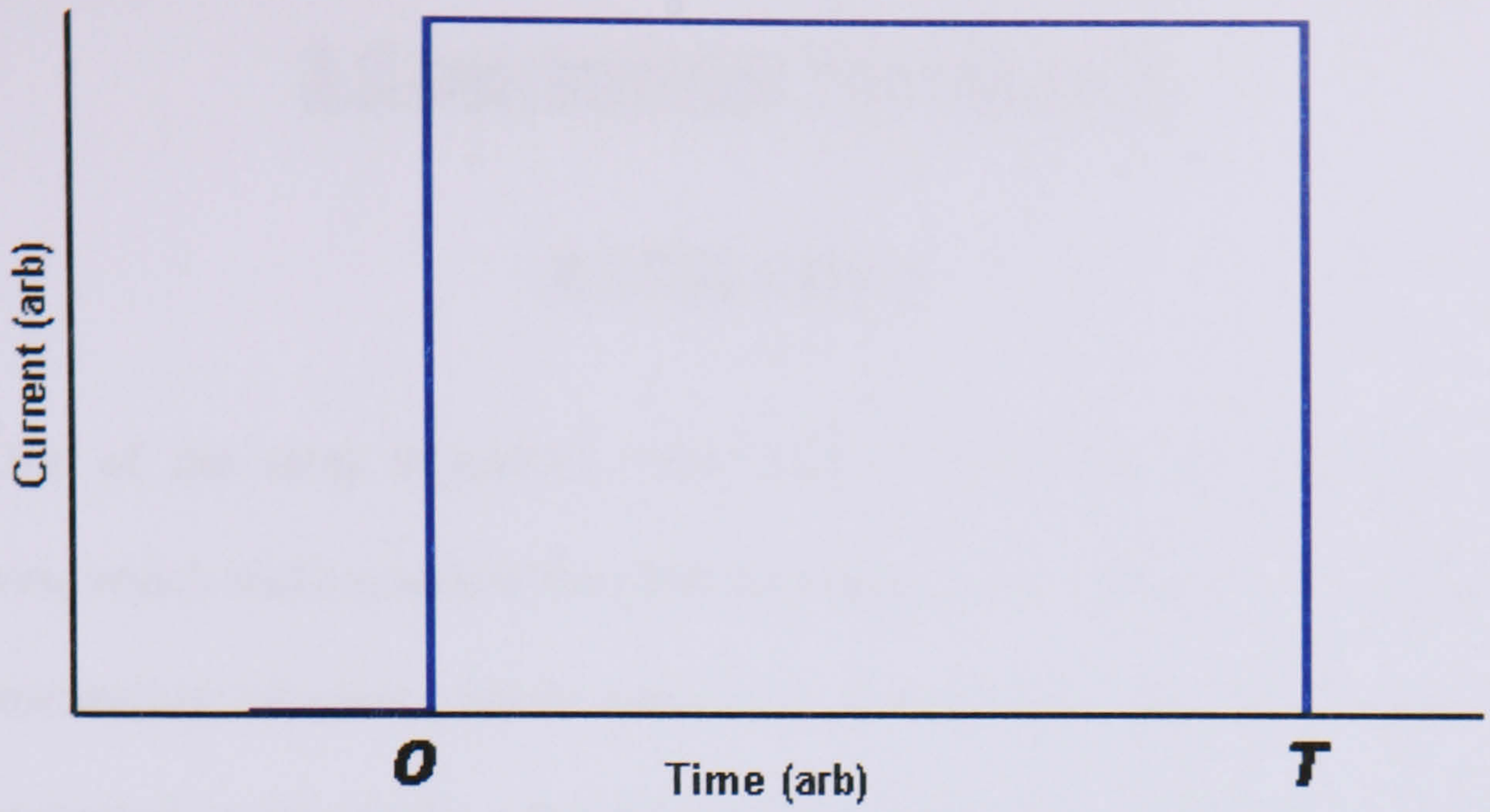

Figure 2.7: Transit of an ideal Time of Flight signal

3 Experimental Techniques

3.1 The Lasers

One of the most important tools used in these experiments are the lasers themselves, which make possible the photoexcitation of the organic semiconductors. As we are measuring transient photoconductivity, pulsed light lasers are employed. The results presented in this thesis were obtained by using three different types of laser, a pulsed Nd:YAG, a Nitrogen laser and an Optical Parametric Oscillator (OPO).

The fundamental wavelength of a Nd:YAG laser is 1064nm which, by the use of peripheral n^{th} harmonic generation crystals, can be used to produce in addition: 532, 355 and 266nm wavelengths.

When the flash lamp fires, a population inversion is established in the Nd:YAG rod but because of the presence of a saturable absorber dye at the 100% reflecting mirror, there are high losses in the cavity and stimulated emission cannot initially build up. However, if there is an intense enough noise spike in the radiation, this may saturate the dye by promoting the molecules to their excited state and making the dye transparent (self-induced transparency).

Once this has happened, the stimulated emission may build up as a brief high intensity pulse, part of which is emitted at the output coupler, the rest travelling back down the cavity to repeat the process. This results in a train of fast pulses separated by the round trip time of the laser cavity. A fast photodiode detects the presence of a large pulse which then triggers a Pockel cell to allow just one large pulse to pass through. This pulse is of the order of 25ps FWHM.

The second laser used for the 'slower' experiments is a Nitrogen laser at 337nm which gives a 6ns pulse and a nominal energy of 5 mJ per pulse. This laser is especially useful in the Discotic Liquid Crystal experiments where the photocurrent lasts a time much longer than the laser pulse. This laser is preferable in these experiments as it is easier to use and requires less maintenance.

The OPO laser is tuneable and able to produce coherent pulses of light between 410nm and 2550nm. It is pumped by a 355nm ND:YAG laser. An optical parametric process is a three photon interaction, in which one photon (the pump photon) splits into a pair of less energetic ones which will not, in general, have the same energies. This energy conversion process can be considered the reverse of sum frequency generation, where two photons combine to form a third, more energetic photon.

3.2 The Co-Axial Cell

In previous studies with polymers, the transient photocurrents take place on a very fast time scale and can hence be considered as high frequency events. Circuit theory becomes more complex at higher frequencies and the experiment becomes more difficult as the problems of impedance must be addressed. Earlier experiments [38] utilized a primitive measurement system that gave rise to large sample capacitance.

The ***RC*** time constants of such experiments led to integration of the photocurrents and meaningful data such as the real time evolution of the photocurrent was not obtained. The co-axial cell served two purposes: to allow the measurements to

be taken with a high frequency response and to allow the study of suspended samples such as SWNTs and encapsulated polymers.

Photocurrents with sub nanosecond temporal resolution are achieved here by impedance matching the sample to the external equipment in a global 50Ω architecture, a technique adapted from Auston [**39**]. For this to work, the sample must appear as a 50Ω transmission line, connected to a 50Ω terminating resistor at the measurement system via 50Ω co-axial cables. The 50Ω transmission line means that any voltage change on the electrodes caused by a displacement current will propagate out to the measurement system with little distortion or reflection.

The simplest and most elegant theory of impedance engineering is that of the co-axial arrangement. The layout of a co-axial system is cylindrically symmetric and utilises an inner conductor separated from an outer conductor by a dielectric medium.

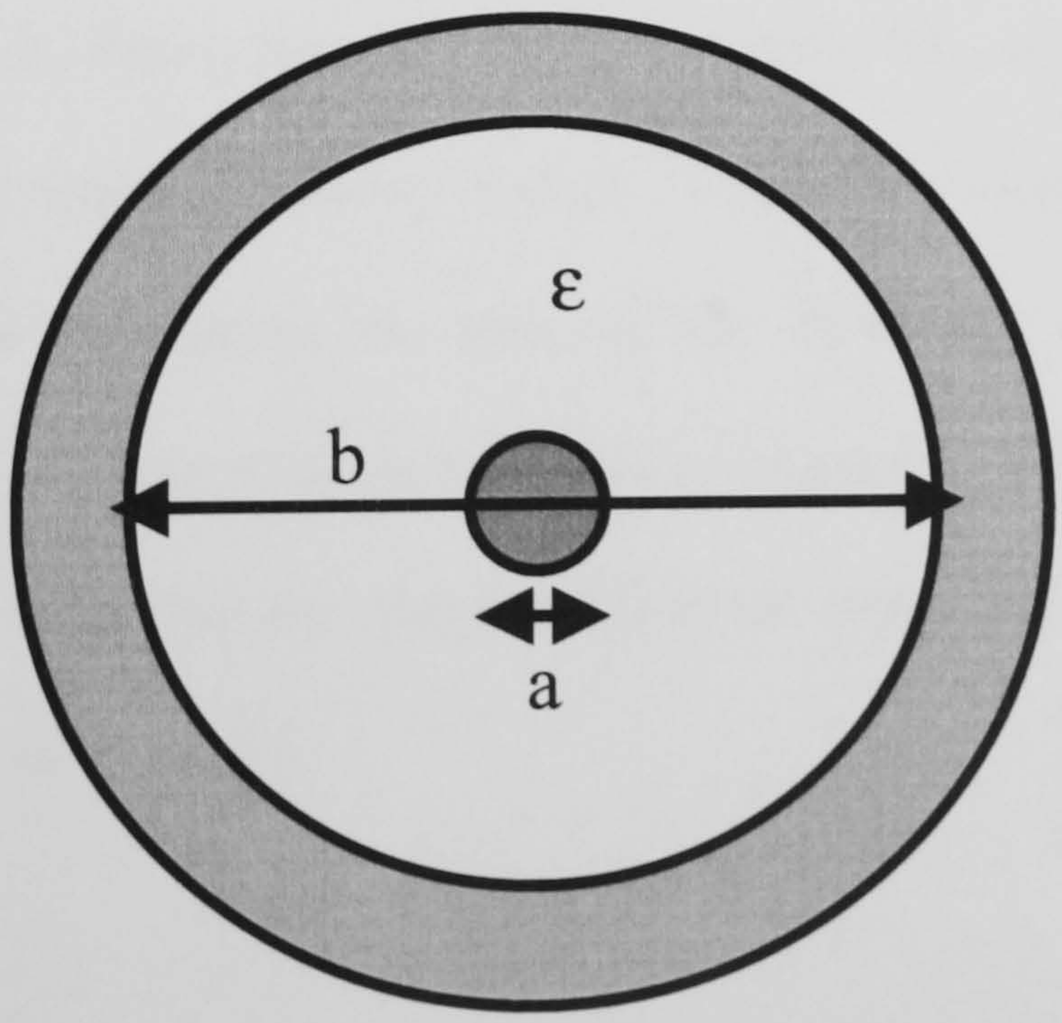

Figure 3.1: Co-axial geometry

Figure 3.1 shows a cross section of co-axial geometry. The central conductor has a diameter a and is surrounded by a dielectric material with a dielectric constant ε and a diameter b. The dielectric material is sandwiched between the two conductors. The impedance of this arrangement $\mathbf{Z_0}$ is given by equation 3.1. η is equal to 377Ω: the impedance of free space.

$$Z_0 = \frac{1}{2\pi}\frac{\eta}{\sqrt{\varepsilon}}\ln\left(\frac{b}{a}\right) \qquad (3.1)$$

Macor was chosen to be the dielectric medium of the sample cell. Macor is a machinable glass ceramic manufactured by Corning which possesses several useful properties. It is easily machined, has zero porosity, is non-wetting, resilient to most solvents and does not deform. It is an excellent insulator at high voltages and at high temperatures.

A Macor rod of 40mm diameter was purchased. The material has a dielectric constant of 6.03 at the required frequency range. Substituting these values into equation 3.1 to obtain a 50Ω impedance, the ratio of the diameters yields: **b =7.75031a**. Therefore, the central conductor has to be 5.2mm in diameter. The outer conductor will be a grounded metal jacket that fits snugly around the cylindrical cell. The plan for the co-axial cell is shown in figure 3.2.

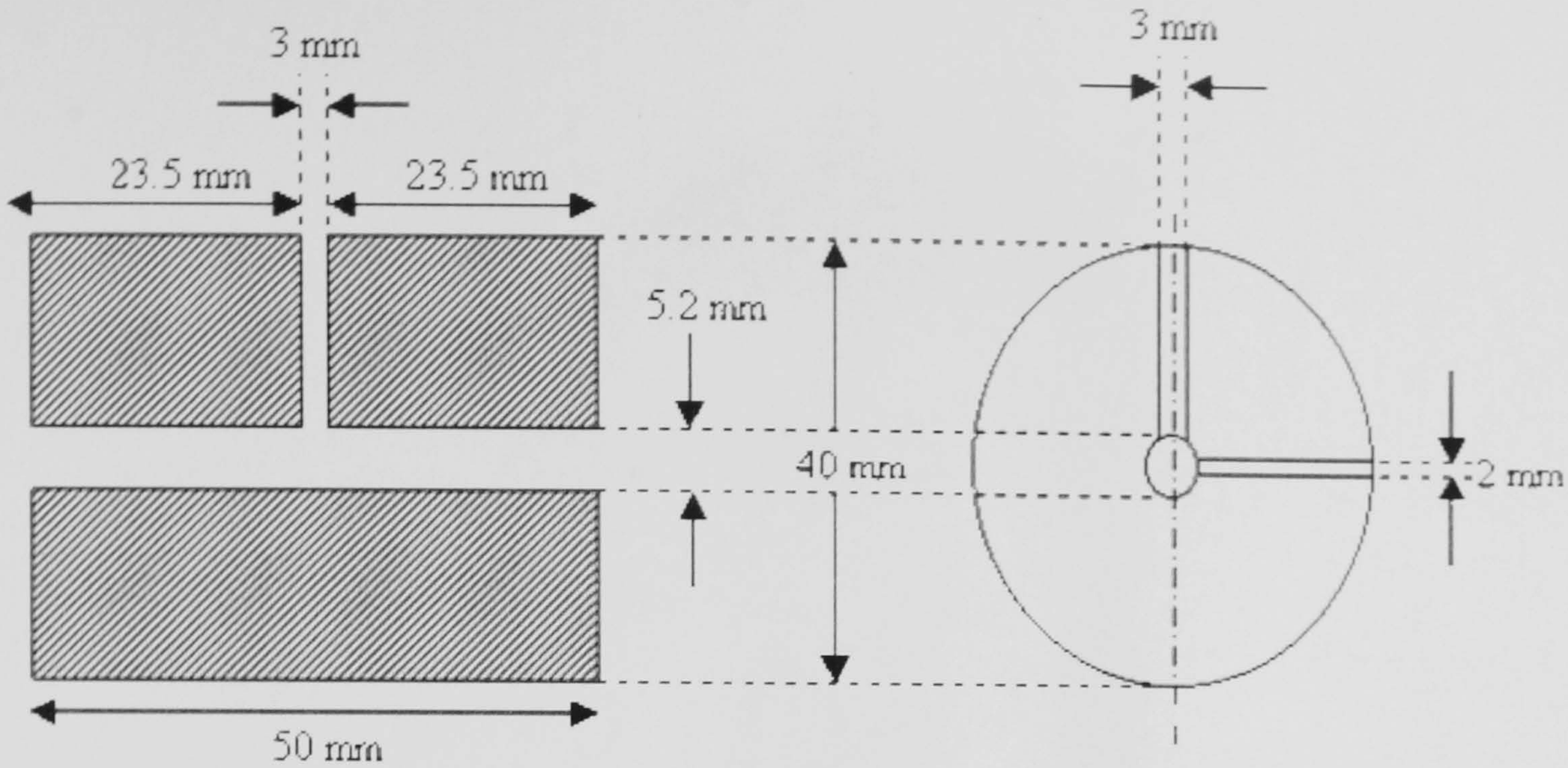

Figure 3.2: Schematic diagram of co-axial cell

Cylindrical brass electrodes were fashioned matching the 5.2mm diameter of the internal channel (as required for the 50Ω impedance geometry). Their lengths can be varied in order to change the electrode gap in the middle of the cell. The brass electrodes are soldered onto 50Ω semi-rigid co-axial cables.

The 2mm channel through the Macor wall acts as a conduit for a quartz rod, which allows light to enter the cell externally from a laser source and excite the solution in the electrode gap. The 3mm vertical channel acts as a sample well allowing the cell to be filled with material after it has been assembled and sealed.

Figure 3.3 shows a 3D diagram of how the cell appears when fully assembled. The Macor ceramic cell, **CC**, is in the form of a cylinder of diameter 40mm. Semi rigid coaxial cables, **SRC**, enter the 5.2mm bore down the centre of the cylinder forming electrodes at either end leaving a gap between electrodes in the centre to form a sample well, **SW**. This sample well is accessed via a 2mm quartz optical fibre, **OF**. The whole ensemble is contained in a grounded metal jacket, **GMJ**, which forms the outer conductor of the co-axial arrangement.

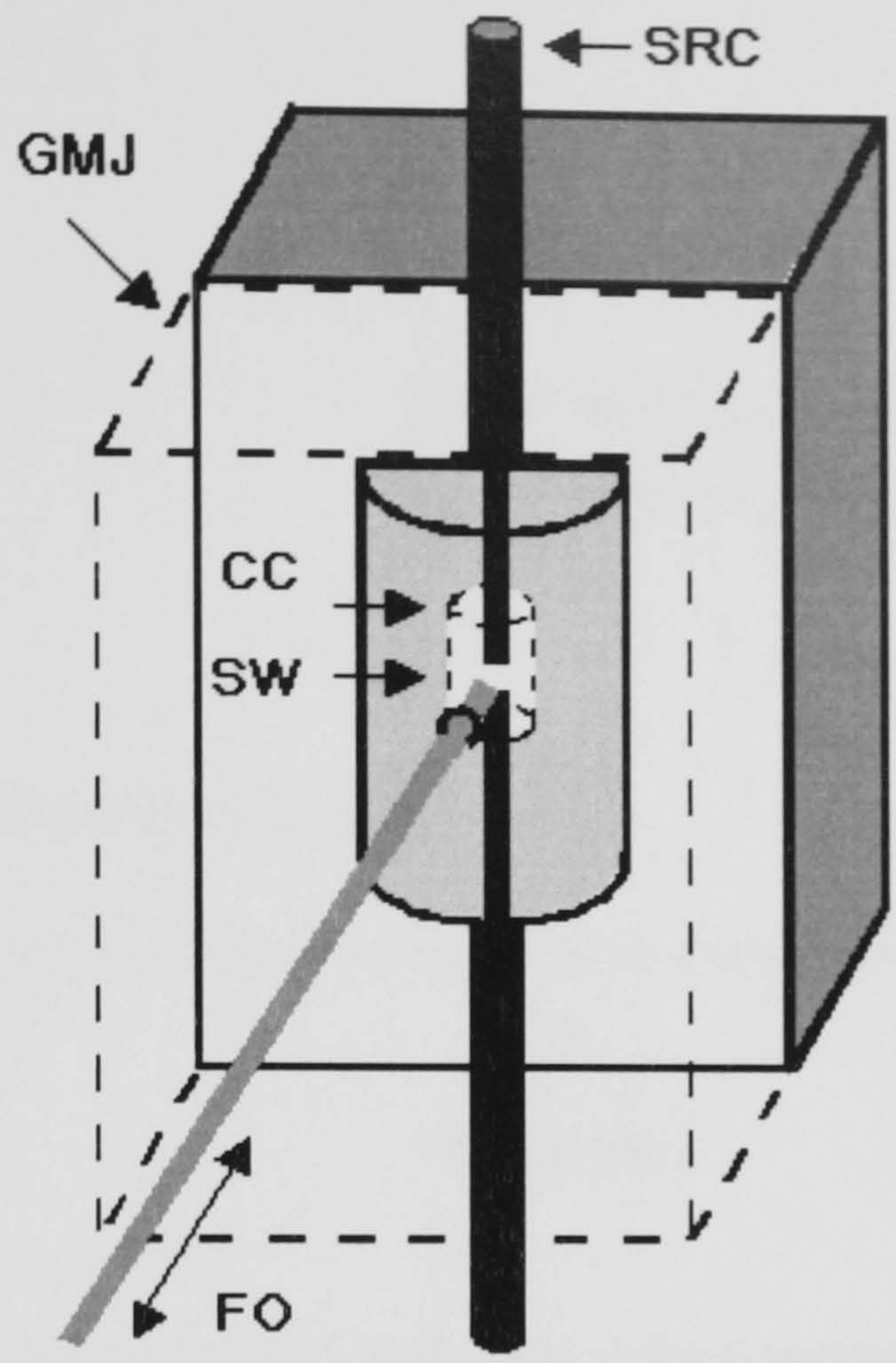

Figure 3.3 – 3D perspective view of the 50Ω co-axial cell.

3.3 Testing the Co-Axial Cell

To determine the step response of our coaxial sample cell plus oscilloscope we have used the leading edge of a voltage pulse delivered by a TD-1110C Tunnel Diode Pulse Driver from "Picosecond Pulse Labs" with a calibrated risetime of 38ps. The output from the TD-1110C was used as input into a 6 GHz LeCroy Wavemaster Oscilloscope (nominal rise-time of 75ps) in order to obtain the true oscilloscope response.

The voltage step was also used as input into one end of the co-axial cell and the output from the cell displayed on the scope. To make the cell a continuous co-axial conductor, the electrode gap was packed with carbon black which led to an overall cell resistance of 21Ω. Figure 3.4 shows the outputs obtained with the red line representing

the direct output from the pulse generator with the blue line being the output from the co-axial cell.

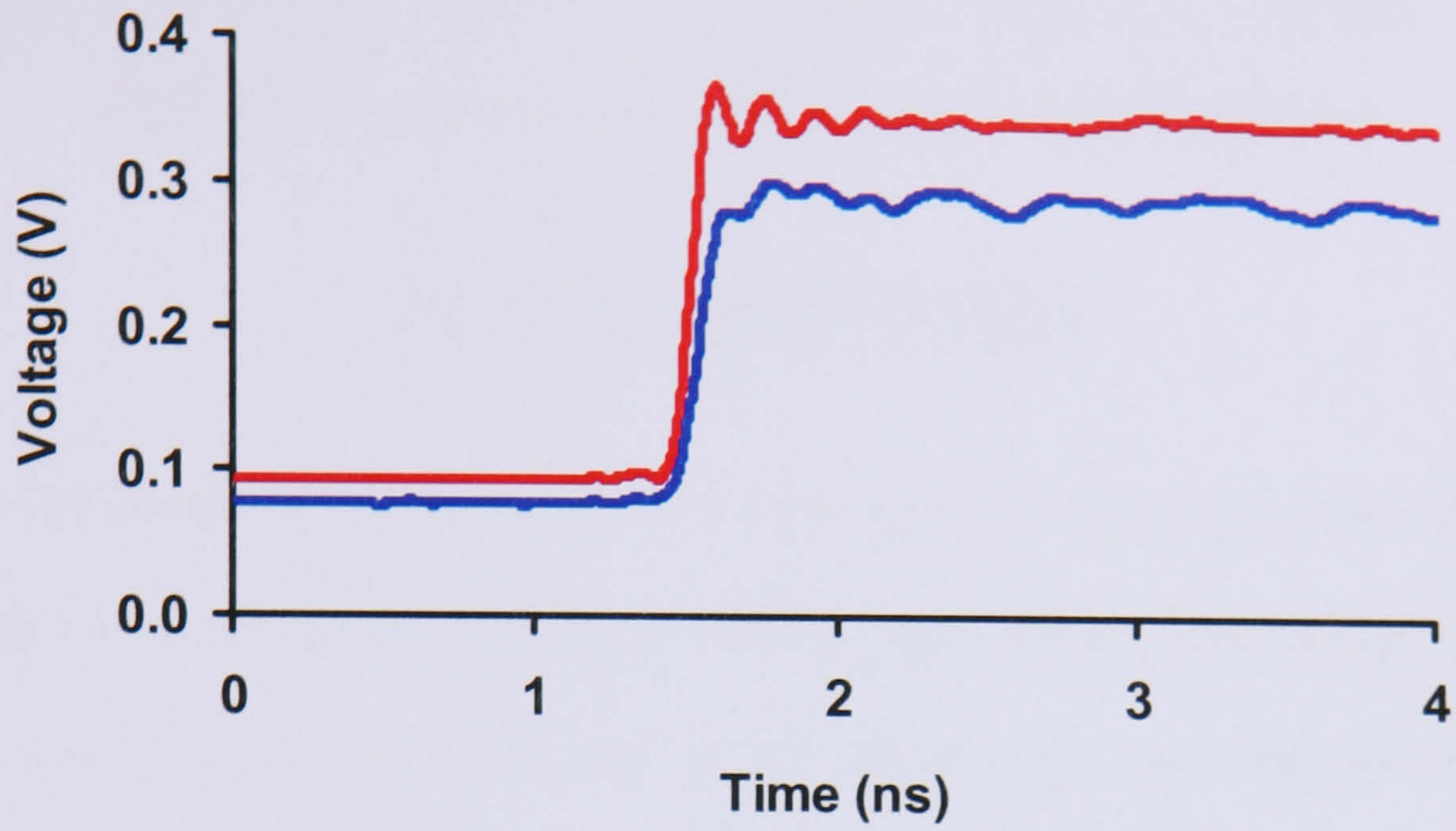

Figure 3.4: Testing the co-axial cell with a fast pulse (Red Line = Output from Pulse Generator, Blue Line = Output from Co-Axial Cell)

From the data in Figure 3.4, we determine that the rise-time of the original signal (generator plus scope) was 92ps whereas the rise-time when the signal passed through the cell was 133ps. If two systems with different risetimes are connected in series, the overall rise time can be found by adding the individual risetimes in quadrature as per equation A.1 [**Appendix 1**]. From this we can determine that the rise time of the 6 GHz scope is 84ps, which increases to 128ps when the co-axial cell is used and for the 5 GHz scope, the overall rise time of the signal is found to be 150 ps.

We also used the pulse generator to measure the risetimes of other oscilloscopes with different bandwidths which were also used in these experiments. The results from this test are tabulated in Table 3.1.

Oscilloscope Bandwidth (GHz)	Total Rise Time (ps)	Rise Time of Scope (ps)
6.0	92	84
4.0	99	91
3.0	114	107
1.0	244	241
0.2	1240	1239

Table 3.1 – Measured Rise Times of Co-Axial Cell

3.4 Quartz Rod Fibre Optic

As previously stated, light will be delivered to the sample via a short length (≈ 5 cm) of 2mm diameter quartz rod. It is possible to know the intensity of light emitted by the laser and focussed onto the end of the quartz rod, but, like all fibre optic arrangements, losses are present in the system. In this arrangement, fibre loss is negligible due to the short length of the rod but coupling losses can factor in. It is necessary to determine the attenuation of laser light caused by the quartz rod.

A bolometric light detector manufactured by Laser Instruments Ltd. was used to measure the light intensity of IR (1064 nm) laser light. Initially, the laser shutter was closed so a background reading could be taken (averaging at 9.08 AU). The shutter was then opened and the beam was focussed onto the end of the quartz rod.

The light intensity measured here averaged at 39.36 AU. When the rod was removed from the path of the beam, the average intensity was 49.96 AU. The second background mean reading was 9.11 AU. With this information, the transmission efficiency of the quartz rod in this example was found to be, on average, 64% (see fig. 3.5).

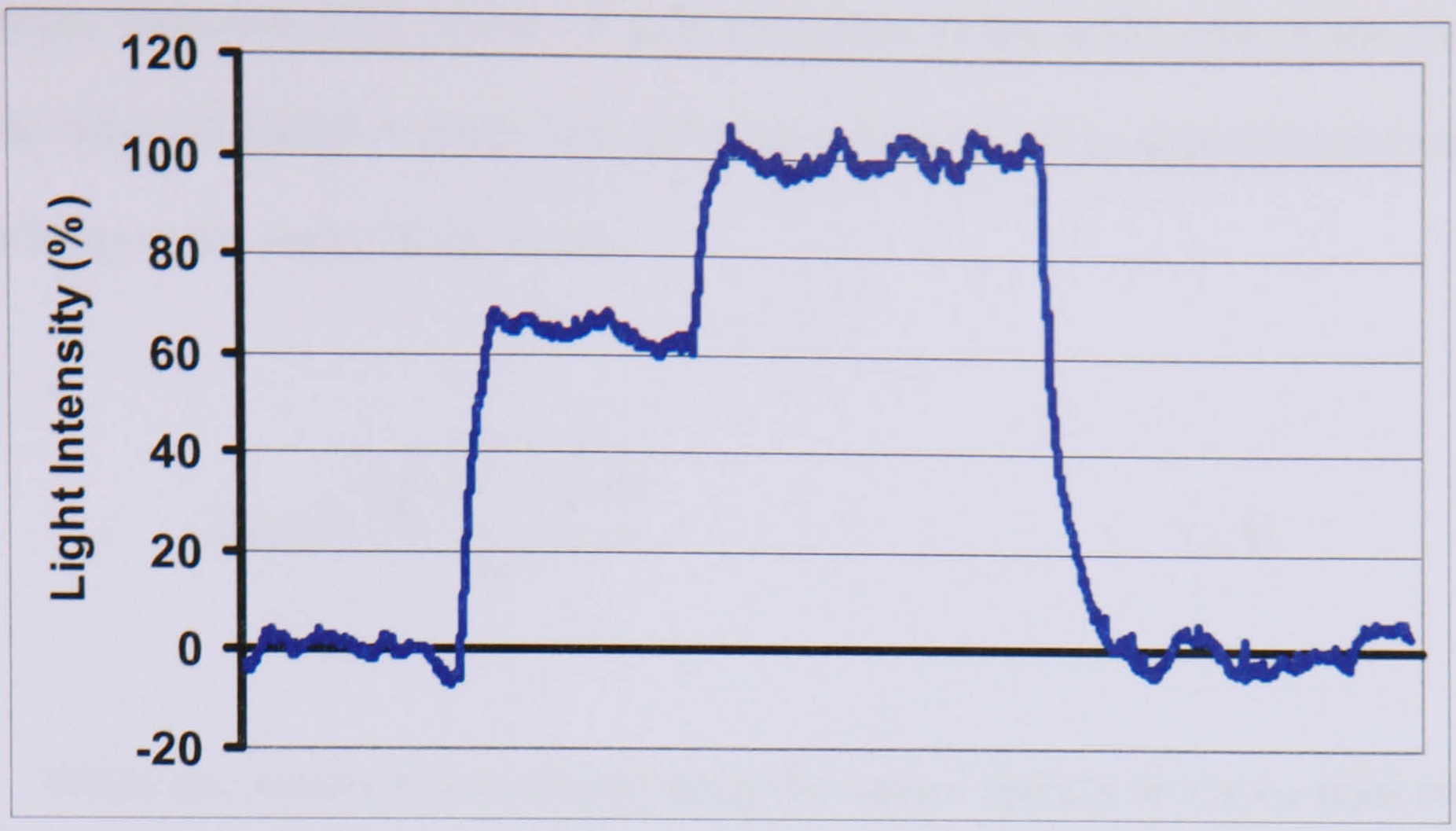

Figure 3.5: Quartz Rod Coupling Efficiency

As the electrode gap is 1mm and is centred between a 2mm diameter fibre optic, overlap will occur resulting in only a fraction of the light reaching the sample. It is necessary to calculate what fraction of the sample the incoming light will interact with (note, we make the assumption that the light flux is distributed uniformly over the area of the fibre optic cross section). Figure 3.6 demonstrates this.

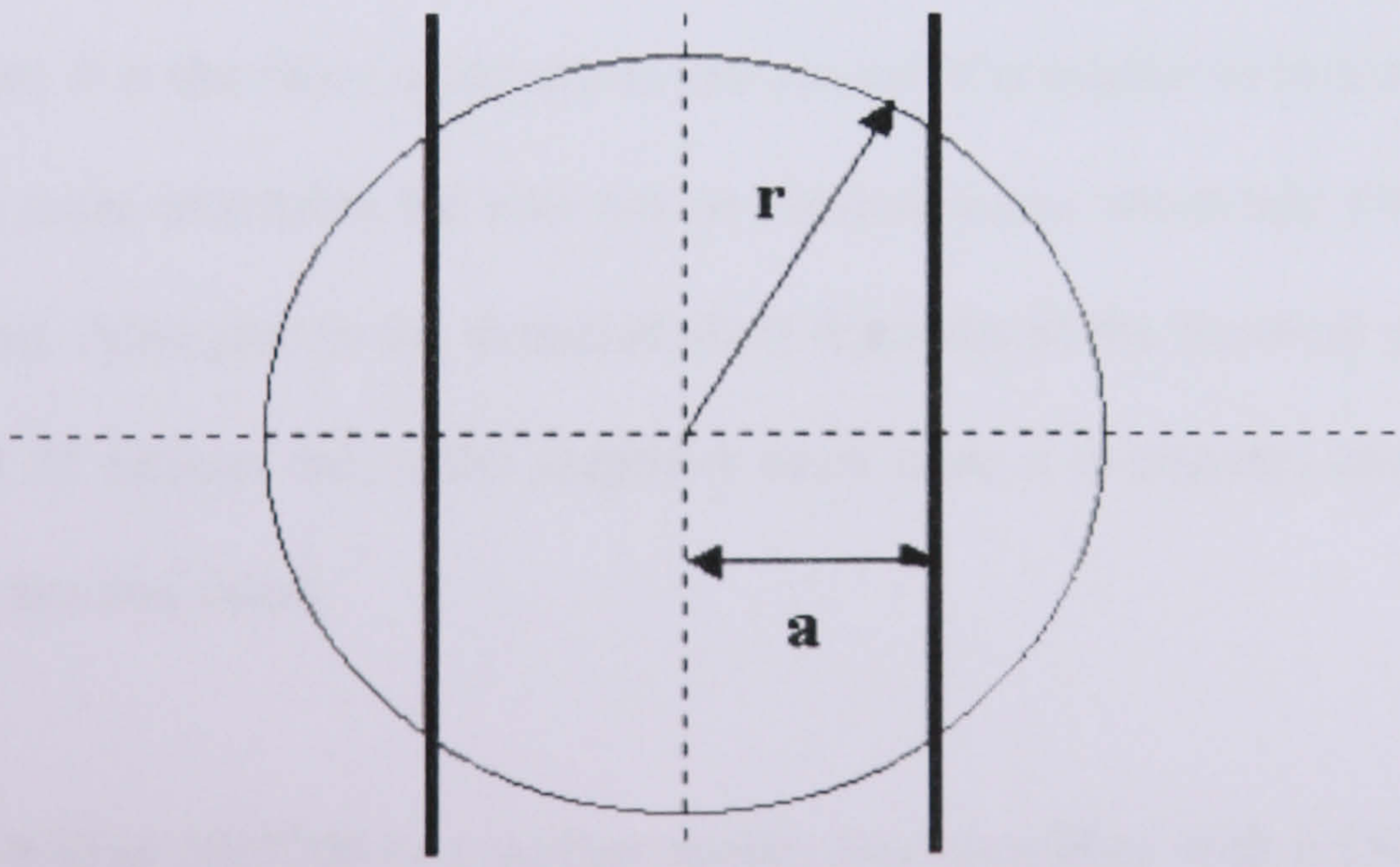

Figure 3.6: Fibre Optic/Electrode Interface Overlap

The values of ***r*** and ***a*** in this particular case are 1mm and 0.5mm respectively. The area contained between the electrodes (the thick black lines) can be calculated by

an integral (equation 3.2), which we then normalise to the entire area of the circle to find the ratio. We define x in this case to be the horizontal left to right direction with the origin being at the centre of the circle.

$$Ratio = \frac{4\int_0^a \sqrt{r^2 - x^2}\,dx}{\pi r^2} \qquad (3.2)$$

When this equation is evaluated using the values specific to the co-axial cell, the ratio of the illuminated area to the entire area is 61%. Therefore, the transmission of light from the laser source to the sample can be said to be (0.61*0.64) ≡ 39%.

3.5 High Frequency Amplification (The Phillips NE5200)

From experience, the signals from the polymers are likely to be extremely small (in the order of a few hundred microvolts). This poses a problem when using a digitising oscilloscope, which may have a comparable maximum vertical resolution of the same order. It is therefore necessary to use a suitable amplifier so that the signals not only become more detectable but also can be resolved more accurately when following their evolution. Also, due to the expected short lifetimes of the transient photocurrents (in the order of nanoseconds), the amplifier must have a reasonably high bandwidth (and hence a fast rise time).

The Phillips NE5200 is a surface mount dual amplifier with a DC to 1.2 GHz frequency response (see Fig 3.7 for a schematic of the chip). It has a low noise figure (NF = 3.6 dB @ 900 MHz), which makes it ideal for most RF applications. Most importantly, it has the required 50Ω impedance matched inputs and outputs. The amplifiers typically have an 8 dB gain at 1 GHz (when Vcc = 5V).

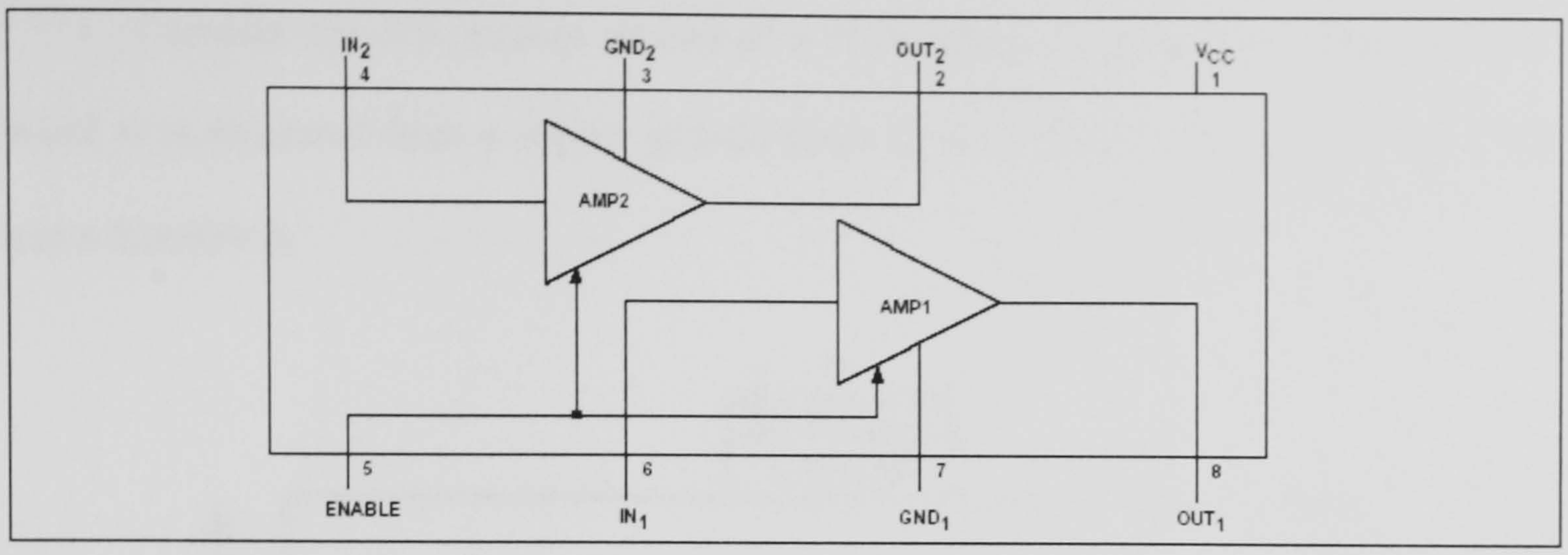

Figure 3.7: Schematic diagram of the NE52000 amplifier

With any amplifier, there is invariably a trade off between speed (bandwidth) and gain represented by the gain-bandwidth product. As a consequence, the 8 dB gain (an amplification of ≈ 2.5 is not sufficient by itself and so a gain block must be used. For the amplifier used in this project, two NE5200 chips were wired in series with both amplifiers on each chip being utilised. Blocking capacitors were used to avoid DC saturation and offsets. The capacitor values are chosen so that they act as shorts above a required frequency.

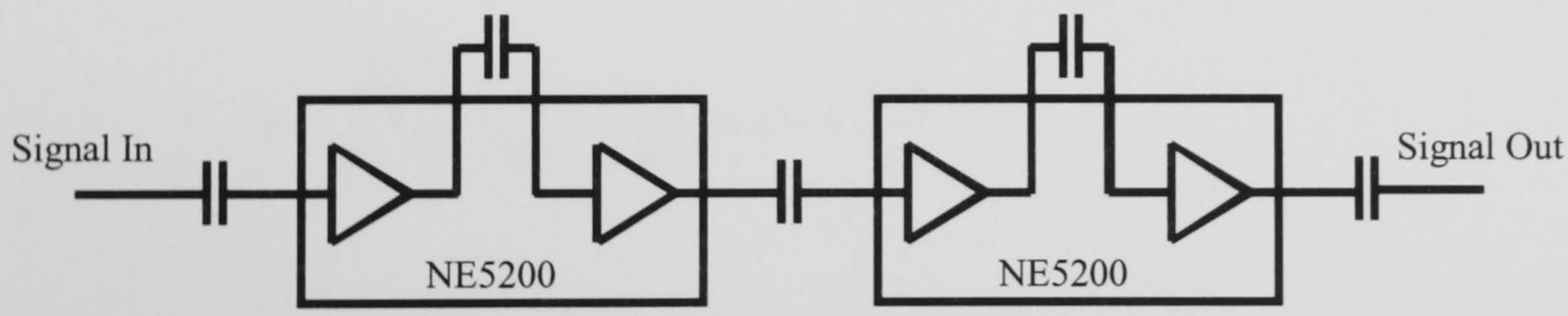

Figure 3.8: Diagram of gain block amplifier arrangement

3.6 Impedance matching of the amplifier circuit.

Impedance matching requires every point along the transmission line to be 50Ω, even the tracks on the circuit board. Engineering the impedance of a circuit board is a little more involved than the co-axial method and requires the use of striplines.

Consider fig. 3.9, a cross section of a PCB, where a conducting copper strip of width **w** is separated from a copper ground plane by a dielectric material of permitivity **ε** at a distance **h**.

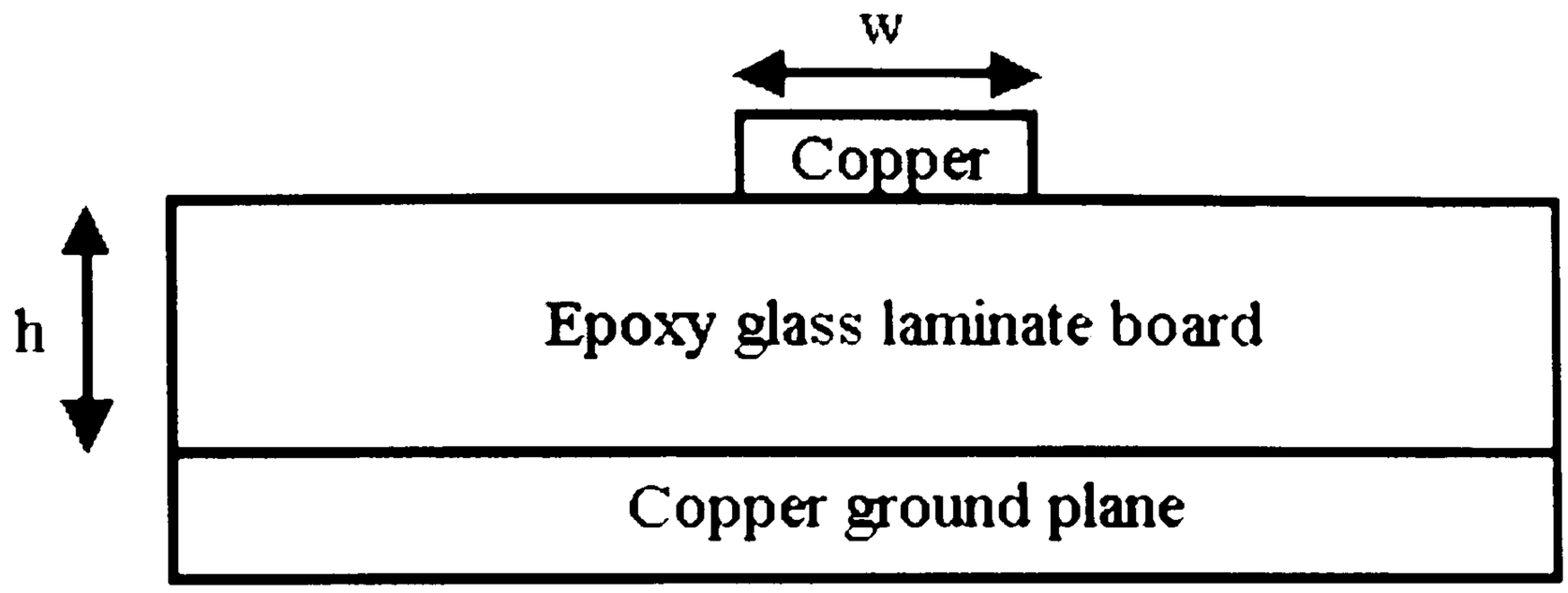

Figure 3.9: Diagram of stripline configuration

To engineer the impedance $\mathbf{Z_0}$ of this stripline configuration, we use the following equations [**40**]:

$$\frac{2h}{w} = \frac{e^{h'}}{4} - \frac{e^{-h'}}{2} \tag{3.3a}$$

$$h' = \sqrt{\left(\frac{\varepsilon+1}{2}\right)}\frac{Z_0}{60} + \frac{\varepsilon-1}{\varepsilon+1}\left(0.226 + \frac{0.12}{\varepsilon}\right) \tag{3.3b}$$

The board used has a dielectric constant of 3.5 at the relevant frequency and a thickness of 1.6mm. Substitution into the above equation yields a ratio of **w=1.8825h** for a target impedance of 50Ω. Therefore, the tracks must have a width of 3mm.

The circuit was constructed onto a piece of FOTOBOARD manufactured by Microponents, which is an epoxy glass laminate coated with a thin layer of copper on

both sides. The circuit layout was designed on a PCB design program called PIA. The track layout can be printed onto a transparency and placed over the surface of the board, which is coated with photoresist. This can be exposed under a UV light source and the exposed surfaces can then be stripped in a sodium hydroxide solution.

The unexposed photoresist remains hard after developing to form the circuit pattern and remains unaffected by the etching process. The exposed copper areas are then etched away in a Ferric Chloride solution leaving the circuit layout behind. The remaining photoresist can then be washed off using acetone. The components are carefully soldered onto the board with the voltage supply, inputs and outputs being connected to 50Ω BNC sockets via short, miniature RG 174 50Ω co-axial cables.

3.7 Testing the amplifier

The constructed amplifier was tested using a Lyons Instruments PG73N Bipolar pulse generator, which is capable of providing a 20 ns pulse. The output from this was passed through an attenuator in order to avoid saturation of the block amplifier configuration.

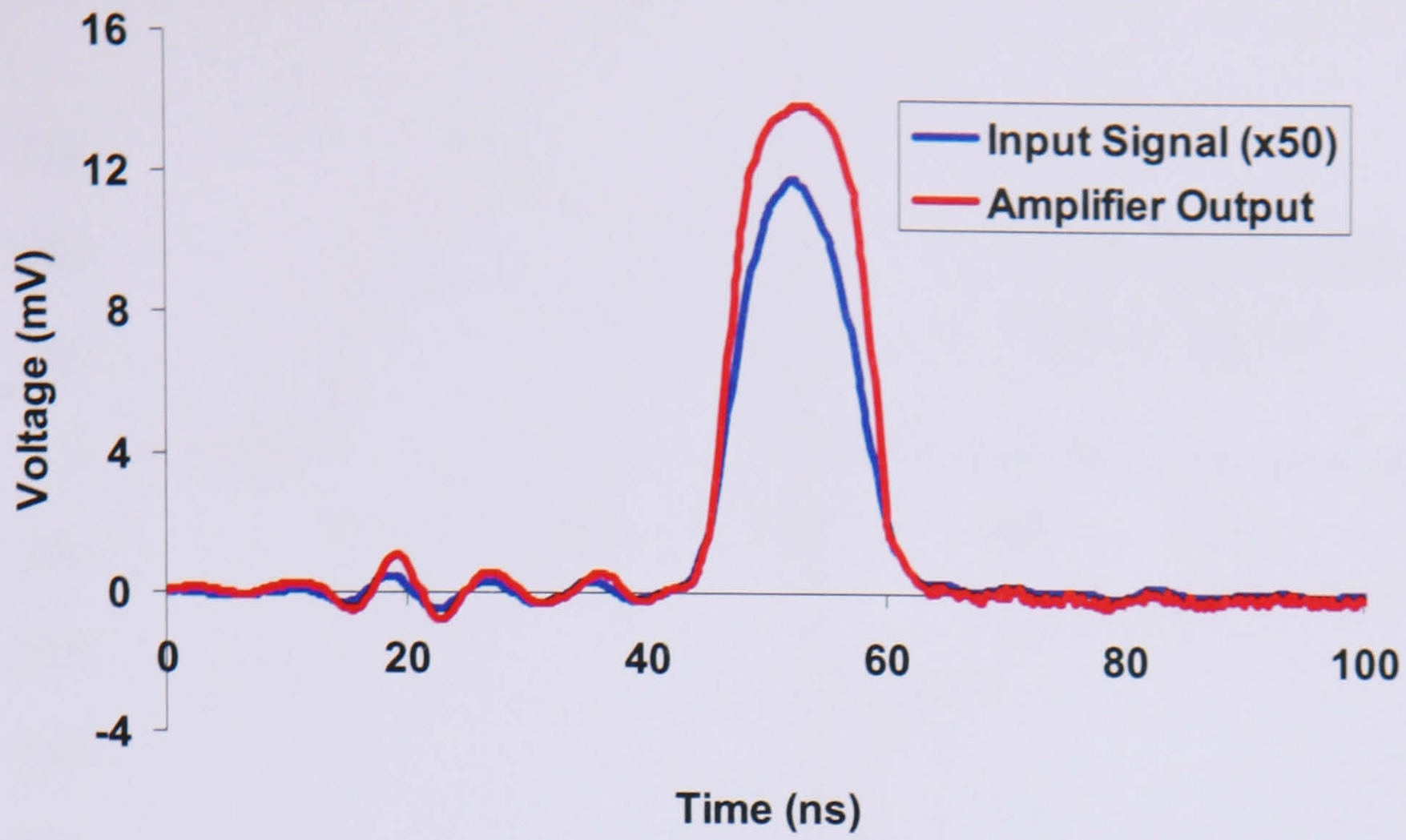

Figure 3.10: NE5200 Amplifier output (20 ns pulse)

Figure 3.10, displays both the input pulse and output pulse to and from the amplifier (the input signal is magnified by a factor of 50 in order for a meaningful comparison). The digitised plot from the oscilloscope has a temporal resolution of 0.25 ns (i.e. 1 point per 0.25 ns). The calculated gain at this frequency is 42.6 (33 dB). As shown, the amplifier is adequate for the reproduction of the signal at this fast timescale.

Figure 3.11 shows comparatively the input and output signals from the amplifier when a pulse of 100 ns is applied. At this lower frequency, the gain is higher (as expected) with a value of 70.7 (37 dB). However, capacitance effects have caused ringing in the circuit as demonstrated by the negative undershoot.

This occurs only after the input pulse has ceased, before that the signal appears to be satisfactorily reproduced. It is reasonable therefore to ignore this undershoot, as it does not appear to distort the signal of interest. Also, it is unlikely that any transient photocurrents from the encapsulated polymers will be of this duration and therefore will not be subject to this deformation.

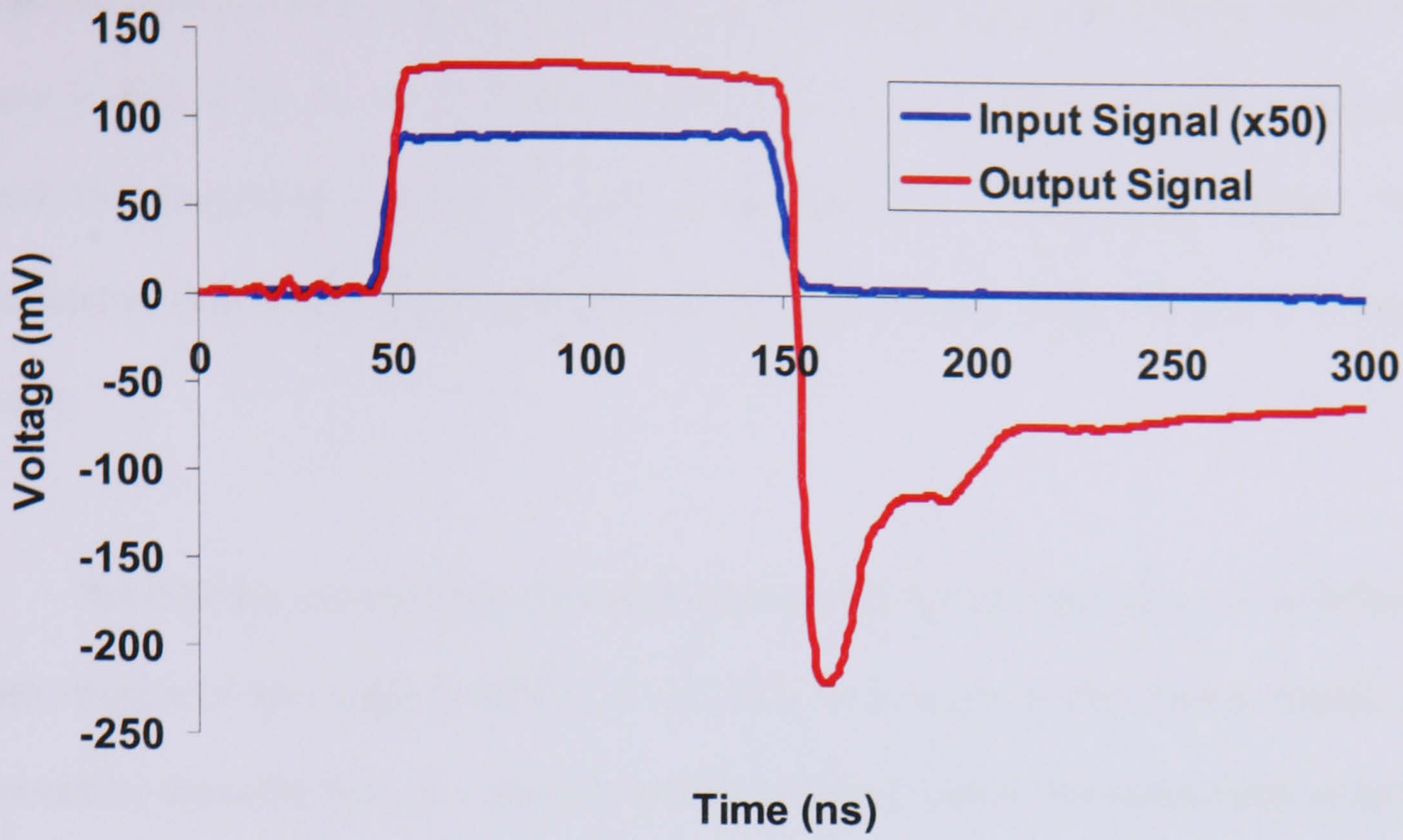

Figure 3.11: NE5200 Output (100 ns Pulse)

3.8 Determination of pulse arrival time to minimise jitter

Like most experiments, statistical fluctuations and random errors exist in each and every reading which impair the accuracy of a single result but can be overcome by averaging over a large data set. In the case of photoconduction measurements, signal averaging can be used to extract the true nature of the photocurrent from a number of noisy signals.

Owing to the speed of transient photocurrent experiments, it is necessary to synchronise the arrival of the light pulse (and hence, the position of the photocurrent) to a relative temporal event. That is, to trigger the oscilloscope at a specific time before the photocurrent signal so that each photocurrent event overlaps and a useful average can be taken.

It is therefore necessary to reduce the amount of '***jitter***', a fluctuation in the triggering position. The problems associated with signal jitter are shown graphically below in Fig. 3.12. as an extreme example. Assume we have a repetitive, identical signal that originally reaches its peak 3 ns after the oscilloscope triggers. This hypothetical experiment is now repeated two more times but a trigger jitter of ± 1.5 ns is present.

We now have three identical signals (dashed lines), but they all occur at different times relative to the trigger position. If we took an average of these three signals (as depicted by the solid line), it is shown that the average is not a true representation of the signal in question. The shape has broadened and the magnitude has decreased. No meaningful data can be extracted.

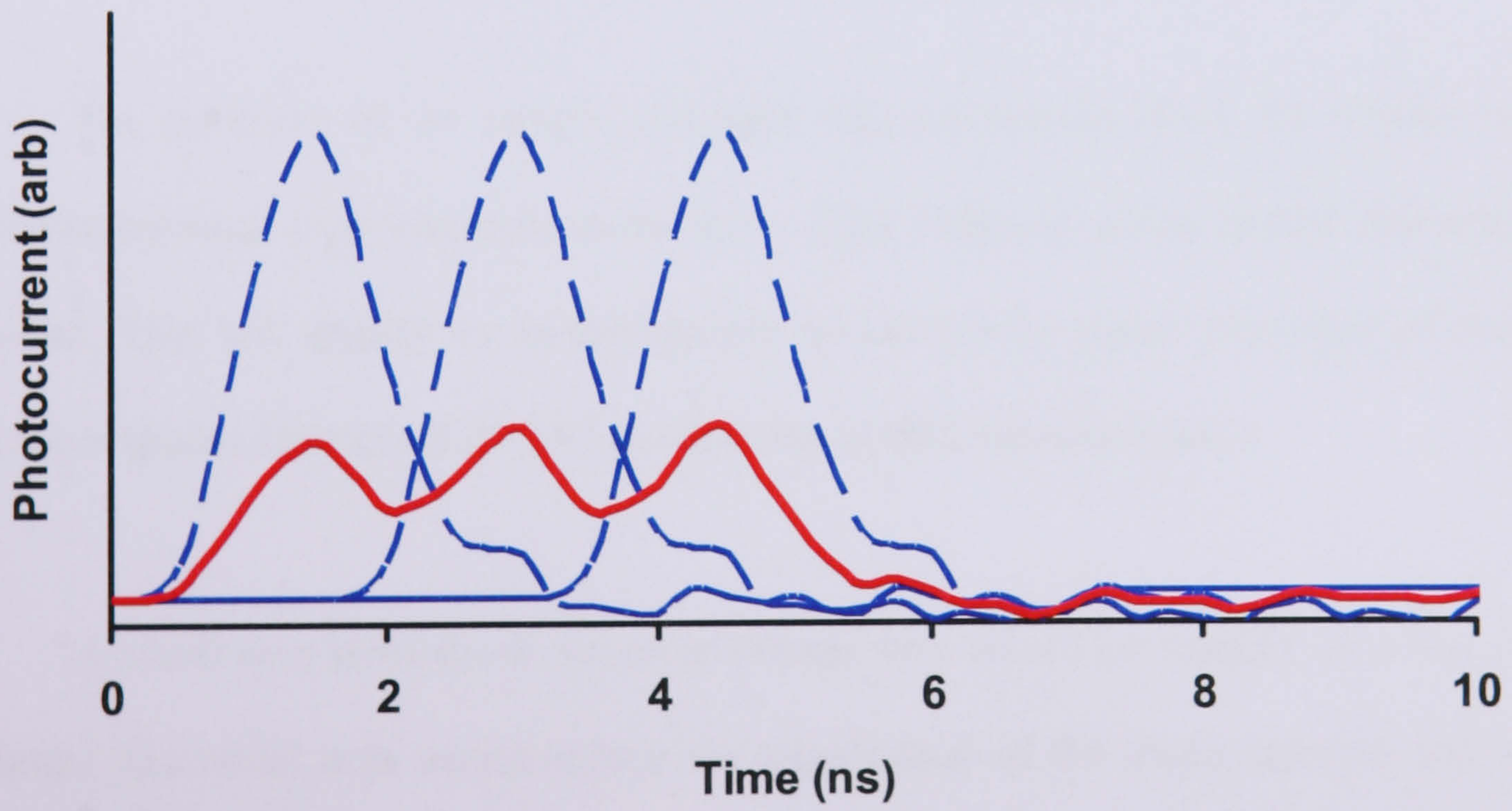

Figure 3.12: Problems with jitter

A suitable synchronised event has to be chosen. The flash lamps of the laser are triggered by an external signal at a frequency of the users choice, but this would be unsuitable for a trigger signal due to the random nature of the delay between the

flashlamp firing and the light pulse generation in a passively mode locked laser. It is more practical to trigger off of the light pulse emitted by the laser using a beam splitter and a fast light detector (see Fig. 3.13).

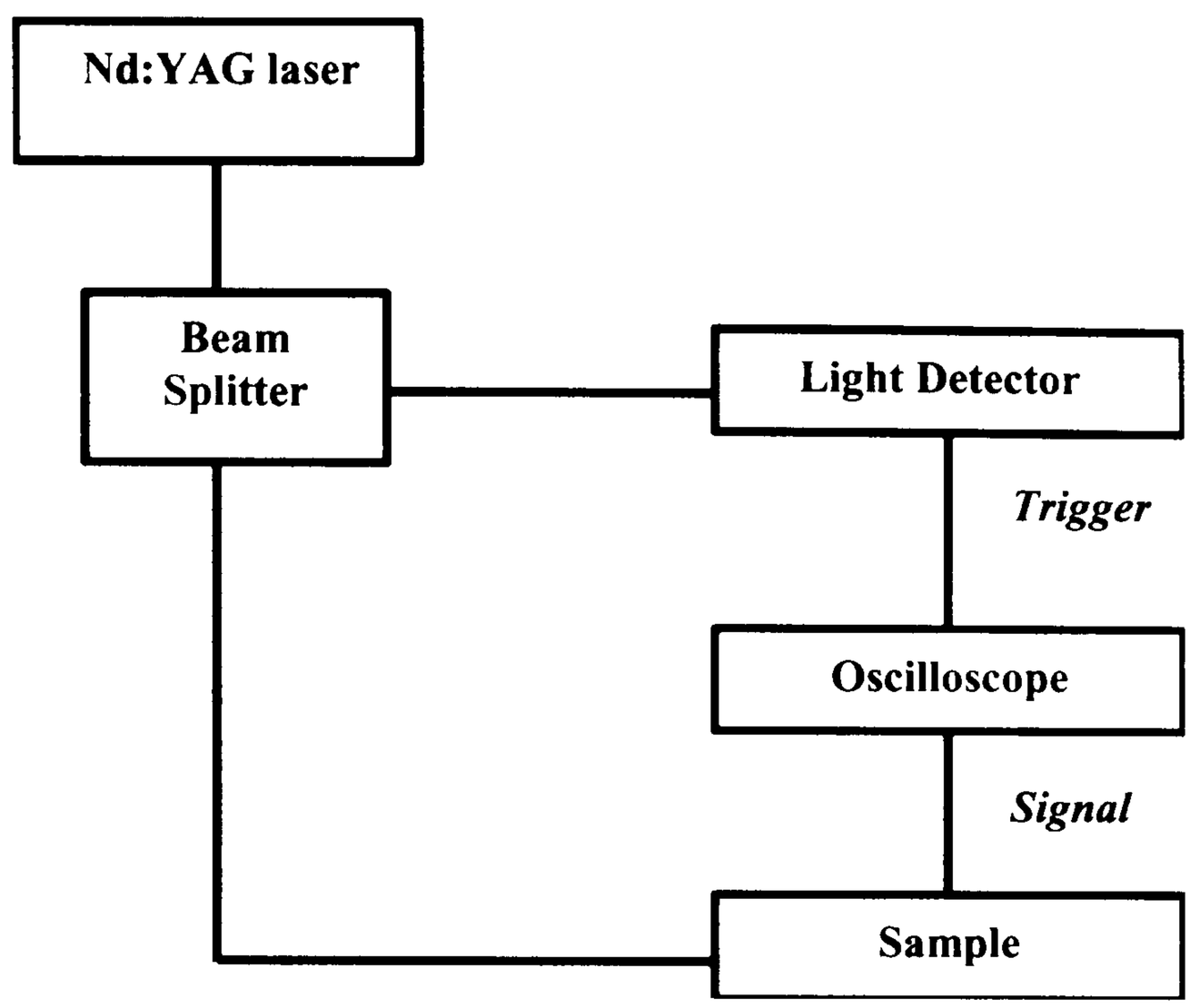

Figure 3.13: Experimental arrangement

The positions of the sample and light detector remain fixed, the relative time therefore between a photocurrent event and a light detection event should also remain constant. This will qualify as an appropriate synchronising signal providing of course that the response (rise-time) of the light detector is both rapid and static.

A small area photodiode wired in reverse-bias would be suitable as a fast light detector. The small area would reduce the capacitance of the diode junction and thus decrease the rise time.

3.9 Determination of laser pulse energy

The bolometric detector was mentioned in section 3.4, as a device capable of measuring the power of incident radiation and hence the light intensity. pulse energy and number of photons per pulse. It is important to know this quantity as the number of photons incident on the sample is usually directly proportional to the size of signal.

A measurement can be taken with the device before and after an experiment to roughly ascertain the energy per pulse. However, this does not take into account the individual energy fluctuations due to pulse irreproducibility during the experiment. It would be useful to obtain the energy of the individual pulses and the photocurrent events simultaneously. This would allow an averaged photocurrent signal to be obtained together with an average number of incident photons.

The solution to this problem was to use the trigger photodiode for a dual purpose. The oscilloscope can display both the photocurrent signal and the trigger signal at the same time. After a reasonable number of averages, there will be an averaged photocurrent signal along with an average peak trigger voltage. The magnitude of this voltage will be dependent on the intensity of the incident radiation pulse.

An experiment was performed to relate this peak voltage to the light intensity. The particular photodiode used for this experiment was chosen because its output exhibits linear behaviour as a function of the light intensity. Very high intensities will saturate the photodiode however, and non-linear behaviour will occur so a fixed ND (neutral density) filter was used to keep the intensity from reaching this saturation point.

The schematic of the experimental set-up is shown in fig 3.14. A beam splitter is used to direct light towards the photodiode, with the majority of the beam entering the bolometric detector (positioned where the sample will normally be). The detector output is sent to a computer so that the intensity can be measured continuously and an average can be taken. Initially the laser aperture was closed to allow a background reading to be taken. It was then opened and the relative difference between the detector readings yielded the intensity of the beam.

The detector measures the power of the radiation (Js^{-1}) and the repetition rate of the laser is known (in this case it was 6 Hz). This information is sufficient to determine the total energy per individual pulse, from which the total number of photons can be deduced.

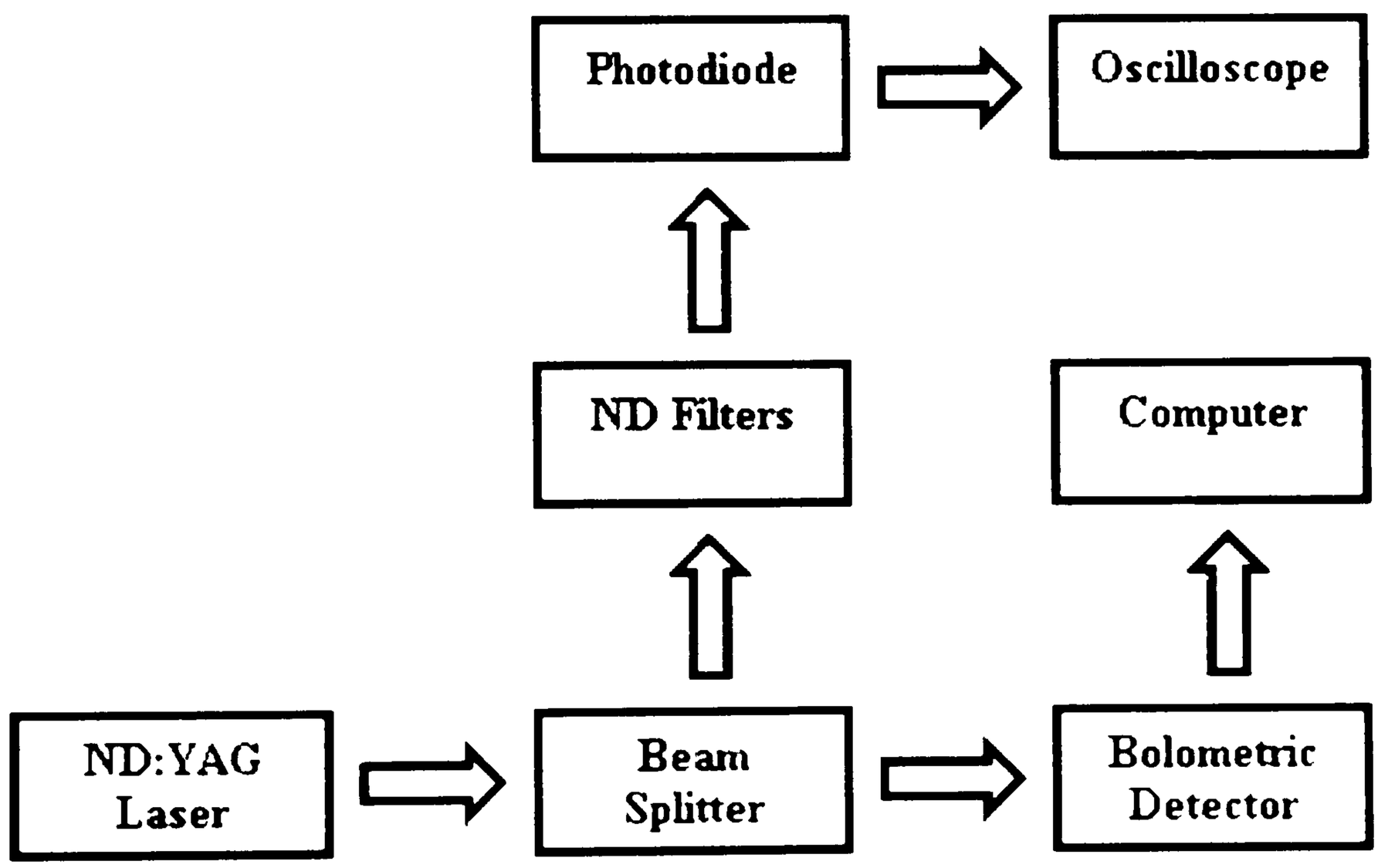

Figure 3.14: Light intensity calibration experiment

When the laser shutter is open, the photodiode triggers with each laser pulse and an average of this trigger signal can be taken. This can later be compared with the averaged light intensity. The experiment is then repeated with various ND filters of

known transmission in between the beam and the photodiode. The linearity of the detector was in this way verified).

Figure 3.15 shows the relative intensity of the laser light compared to the background. The low plateaus occur when the shutter is closed, the higher ones being the caused by the laser illumination. By taking an average of these plateaus and then subtracting the background averages, the pulse energy can be determined.

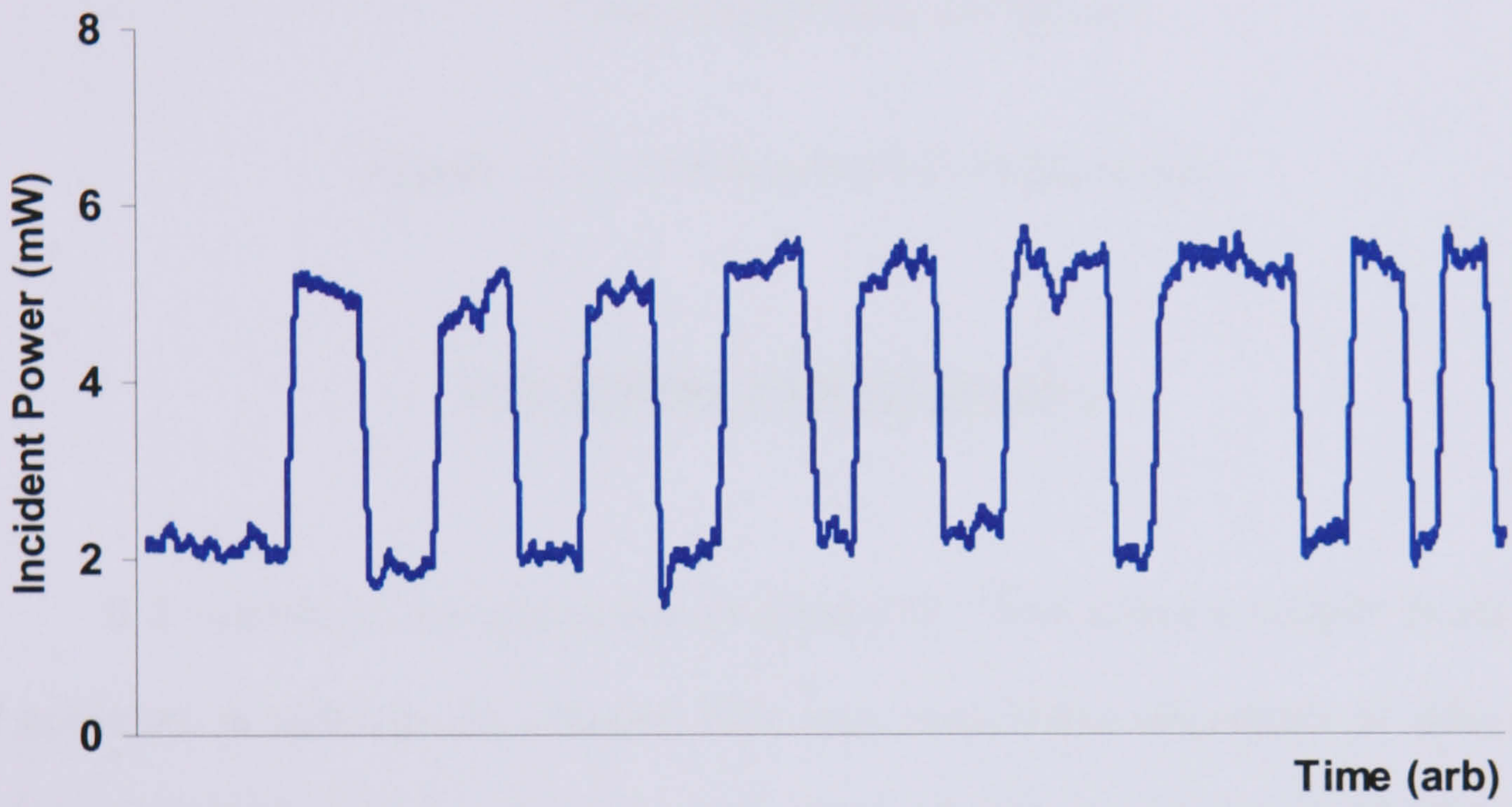

Figure 3.15: Determination of Light Intensity

Figure 3.15 shows the calibration of the detector. The pulse power has been converted to the number of photons per pulse and the relationship between this and the trigger voltage is plotted.

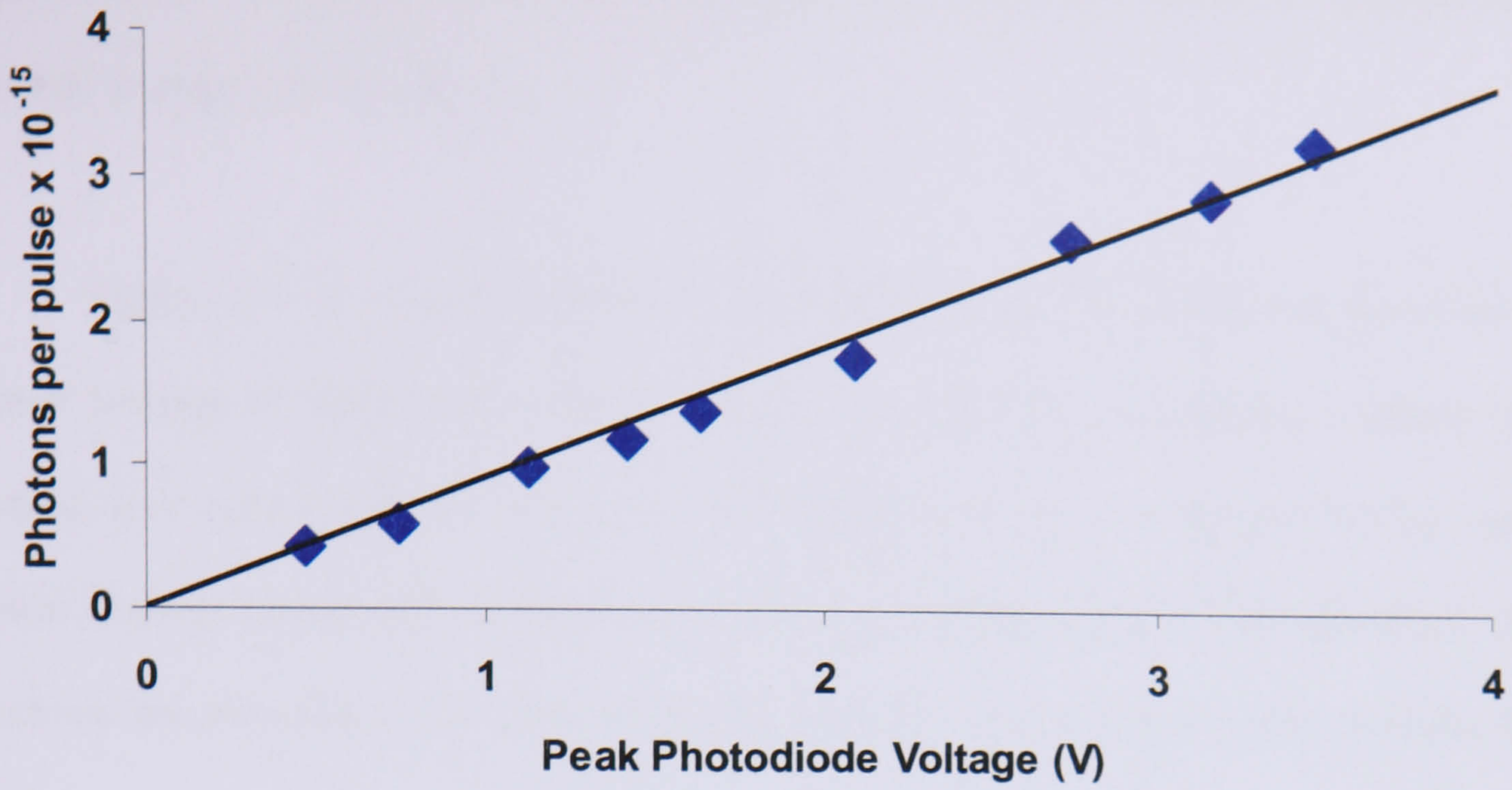

Figure 3.16: Calibration of Photodiode

3.10 Voltage step generation.

It is sometimes not appropriate to apply a DC field across a sample. In the case of polymers in solution, the constant field may cause some alignments to take place within the sample and as such, the random 3D orientation model of the chains is not applicable. Also, there is a chance that the polymers will undergo electroplating to the electrodes. With a carbon nanotube sample (where a significant number of them are metallic by nature), electrical breakdown becomes much more likely and the risk to the measuring equipment becomes significantly higher. Consequently, it is necessary to apply a pulsed electric field for a reasonably small time (in the order of microseconds).

Modern electronics (e.g. transistors, integrated circuits etc.) are not designed to work at high voltages. To create short pulses at high voltages (up to 3 kV), 'old' technology has to be utilised, specifically the use of a valve. The A2426 valve, which was manufactured by English Electric Valves (company no longer in existence), is

capable of switching high voltages at high speeds and this was used in the construction of a fast voltage step generator.

Figure 3.17 is a circuit diagram of the valve circuit. The cathode of the valve is heated leading to thermionic emission. When a voltage V_{CG} is applied between the cathode and control grid (in this case, -40V), the electrons are repelled and an open circuit between anode and cathode results. When this control grid is then grounded, the electrons are attracted by the grid voltage $\mathbf{V_G}$ (+125V) and a closed circuit grounds the anode.

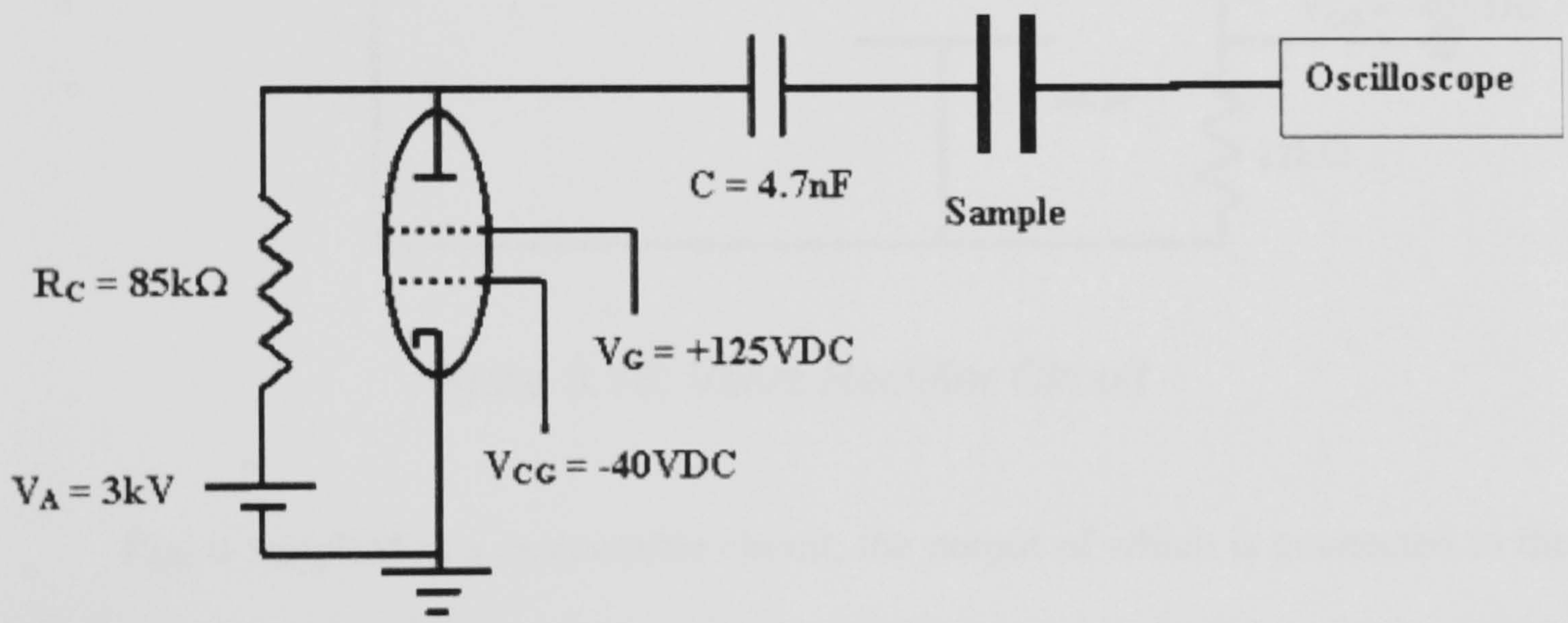

Figure 3.17: Valve Circuit

The 85 kΩ resistance acts as a current limiter. As the resistance of the valve when open can be considered infinite, the applied voltage of 3 kV in this instance is what the capacitor charges up to. When the control grid is then grounded and the valve becomes conducting, the capacitor discharges and results in a voltage pulse of opposite sign to the applied voltage. Providing the pulse is short and very little current is drawn by the sample, a square negative voltage pulse of –3 kV will result.

Figure 3.18 is a circuit diagram of the rectifier circuit used to supply the appropriate grid voltages to the valve.

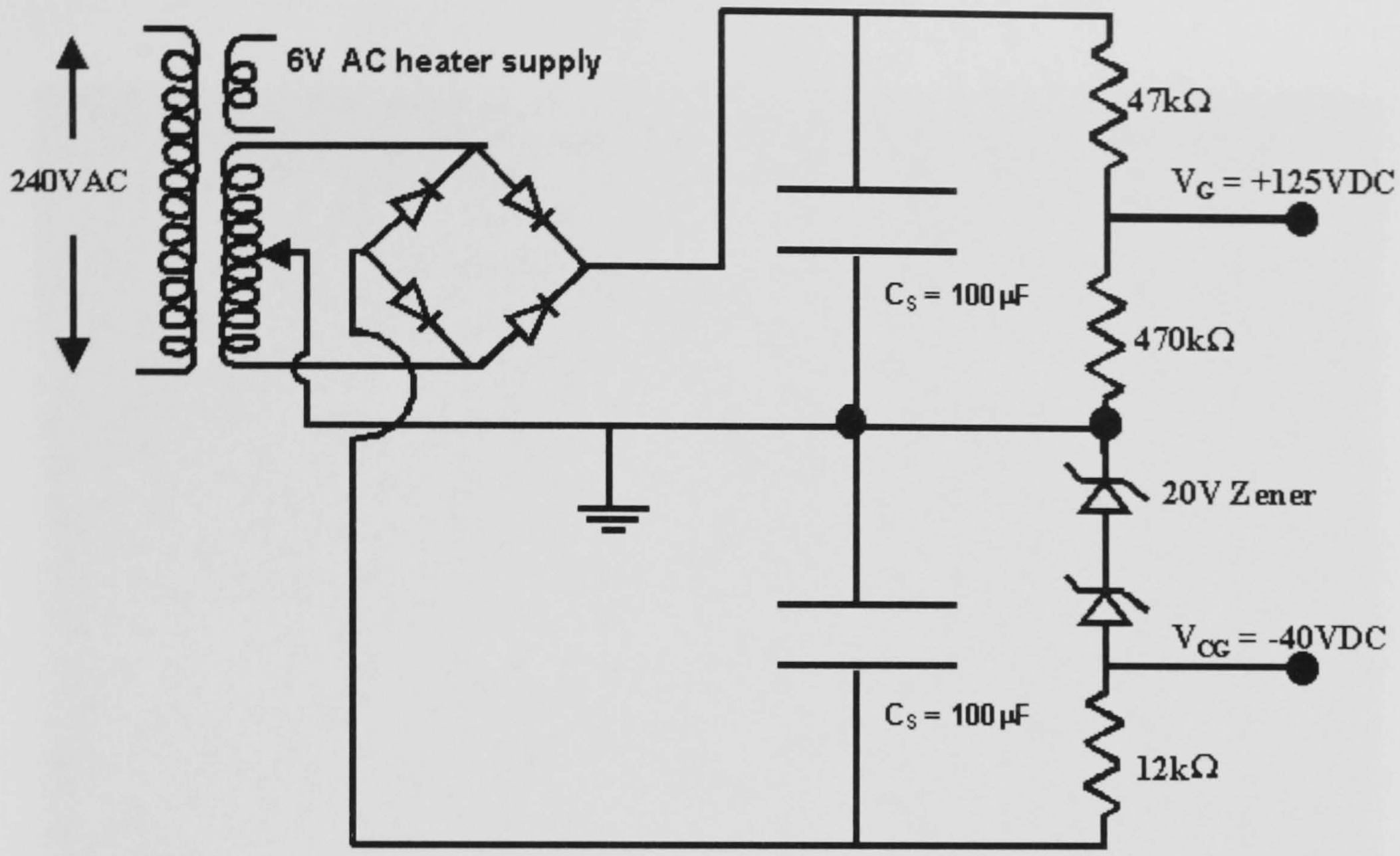

Figure 3.18: Valve Rectifier Circuit

V_{CG} is supplied to a monostable circuit, the output of which is connected to the control grid of the valve. The monostable itself is triggered by the laser with a variable delay. The purpose of this is to synchronise the trigger of the voltage step with the arrival of the laser pulse.

Figure 3.19 shows an oscilloscope display of the voltage step (500V, attenuated by a high voltage probe, factor of 1000), which is represented on channel 1 (the yellow trace). Channel 2 (the green line) is the external trigger from the laser and lastly channel 3 is the output of the photodiode used to measure the arrival of the laser pulse. As the timebase of the oscilloscope is set to 50 microseconds per division, the latter signal is represented as a sharp vertical drop at the centre of the display due to the rapidity of this

event which lasts in the order of nanoseconds. The oscilloscope was triggered from the falling edge of the light pulse and the trace demonstrates that the light arrives at the sample approximately 10 μs after the application of the voltage step.

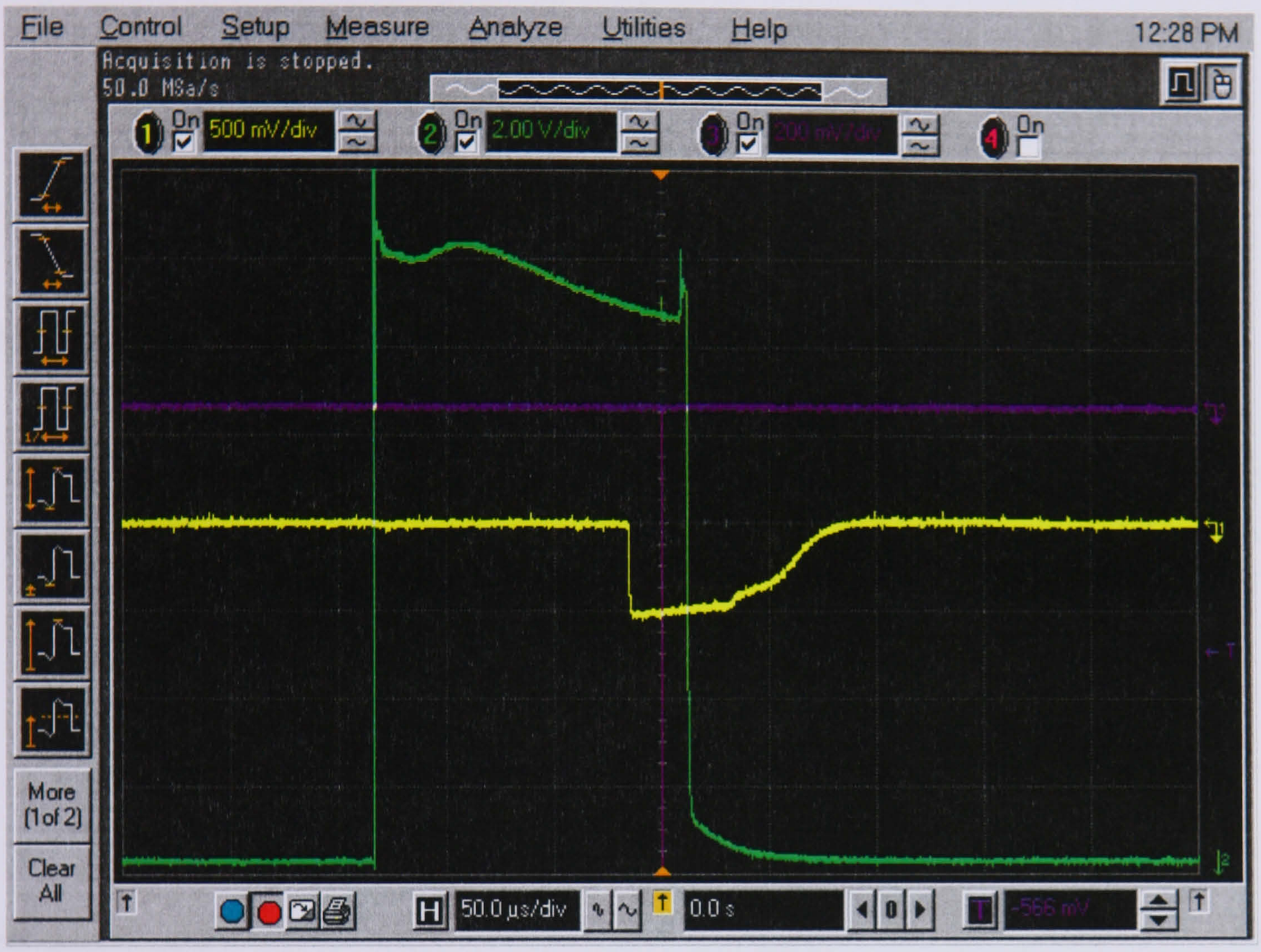

Figure 3.19: Test of the voltage step generator.

3.11 Discotic Liquid Crystal Cell

The basis of all experiments contained in this thesis relies on the application of an electric field established across a sample. Due to a unique property of Discotic Liquid Crystals (hereafter referred to as DLCs), particularly their ability to self assemble, it is possible to form columns of these molecules with a common orientation and apply electrical contacts at either end of the stack. More accurately, it is possible to form a DLC stack between two previously made electrode surfaces. This arrangement offers the advantage of being able to create charge carriers at an electrode/sample

interface and observe the carrier motion through the sample until recombination occurs at the counter electrode. This is known as the Time of Flight technique (TOF) as described by Kepler and LeBlanc [**41**].

The cell used to perform this type of experiment can be appropriately referred to as a sandwich cell, the basics of which are depicted in figure 3.20.

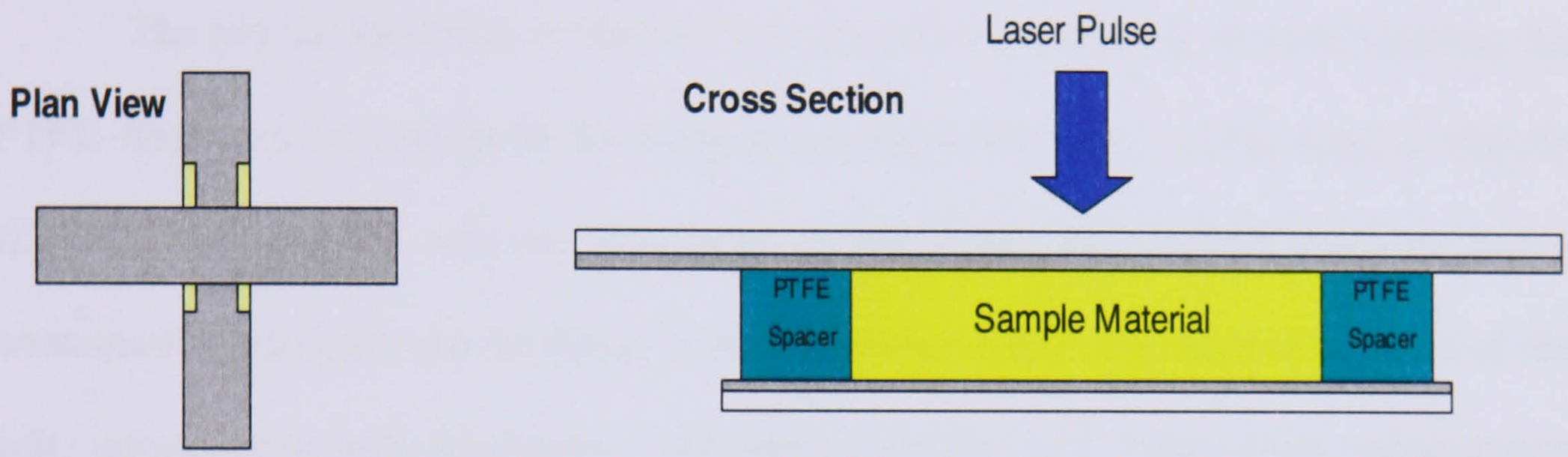

Figure 3.20: Schematic diagram of the DLC sandwich cell

The electrodes were fabricated by evaporating Aluminium onto two optically flat quartz slides, one of which is made semi-transparent with the transmission being measured at the appropriate wavelength. They were then placed in a spectrophotometer to measure the transmission of light at 337nm (the wavelength of the Nitrogen laser and the wavelength used in all DLC experiments).

The cell is assembled by the following procedure: Firstly, the bottom slide is placed into a specially constructed sample holder (electrode side up) and two thin strips of PTFE are cut and washed in solvent and then placed onto the slide. The second slide is then positioned in the centre and at right angles to the first (electrode side down). The arrangement is held in place by a covering plate that can be tightened and results in the slides being clamped together and held rigid. Screw clamps with attached wires are then

tightened onto the evaporated electrodes, which allow the cell to be connected to the measuring circuit.

The sample holder is on a temperature-controlled base and utilises a 100W cartridge heater and a K-Type thermocouple. It is possible to maintain a constant temperature in the range from room temperature to approximately 250°C.

The precise thickness of the cell (i.e., the electrode spacing as determined by the PTFE film) can be measured by using a spectrophotometer (in this case, a Hitachi U3000). The unfilled cell can be placed in the beam path of the machine and a transmission spectrum can be taken. Due to reflections from the internal surfaces of the cell, constructive and destructive interference results and Fabry-Perot transmission peaks are observed.

The relationship between wavelength, λ, through a cell of thickness d is given by equation 3.4:

$$2dn=m\lambda \qquad (3.4)$$

Where m is the order and n is the refractive index of the material (in this case air, with $n=1$). Therefore, by looking at the transmission spectra and the resulting interference peaks, the exact value of the thickness can be deduced.

By using these methods, the transmission of the laser light onto the sample is known as well as the sample thickness. The next step is to fill the cell with DLC material. A small amount of material is placed onto the bottom electrode next to the

electrode gap. The entire cell is then heated to a temperature that corresponds to the isotropic phase of the DLC. The material melts and by capillary action, flows into the electrode gap and fills the space between. The sample is then cooled below the isotropic phase and into the discotic or crystalline phase where TOF experiments can be performed.

3.12 Discotic Liquid Crystal Signal Amplification

Time of Flight signals obtained from DLC's generally have a lifetime in the order of microseconds, it is not necessary therefore to utilise a high-speed amplifier. The amplifier of choice was a Phillips NE592 video amplifier with a bandwidth of 120 MHz and a gain of 40. The schematic diagram of the amplification circuit is shown in figure 3.21.

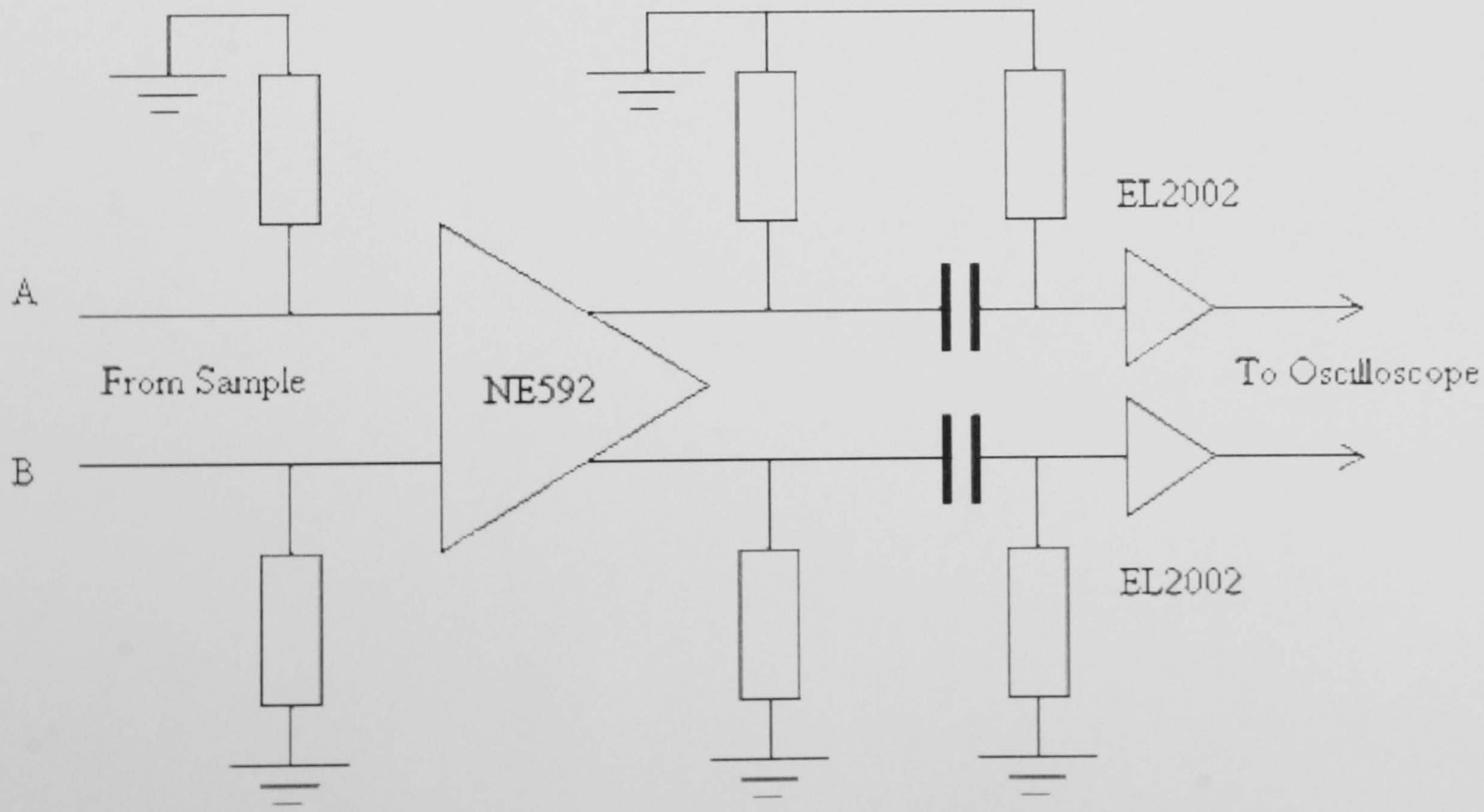

Figure 3.21: Circuit Layout of the DLC Amplifier

The device itself is a differential amplifier with one input connected to the sample and the other left floating. The latter will sample just the background noise which is then subtracted from the input channel. The output of the amplifier is AC coupled to remove the small DC offset present in the device and fed into two Elantec EL2002CN line drivers which act as unity gain amplifiers that are able to supply the necessary current which the NE592 may not be capable of.

Chapter 4: Results

4.1 Polymer filled Zeolites

The encapsulated polymers prepared at Reading University by Prof. David Cardin and Ms. Tabitha Roberts were gratefully received at the start of this project. Various suspensions of these zeolites filled with different materials were suspended in both silicon oil and the Brookfield Polymer Oil at different concentrations and tested for photoconduction using the co-axial cell and stripline cell.

4.1.1 Absorbance of the suspending medium

It was prudent to ensure that the oil was transparent to light of the wavelengths used in these experiments. The frequency quadrupled Nd:YAG laser is capable of producing light at: 1064 nm, 532 nm, 355 nm and 266nm. The transmission of light at these wavelengths through the Brookfield oil of path length 10mm was (74%, 63% 49% and 0.1% respectively) as shown in figure 4.1. This was measured using a Perkin-Elmer FT-IR machine.

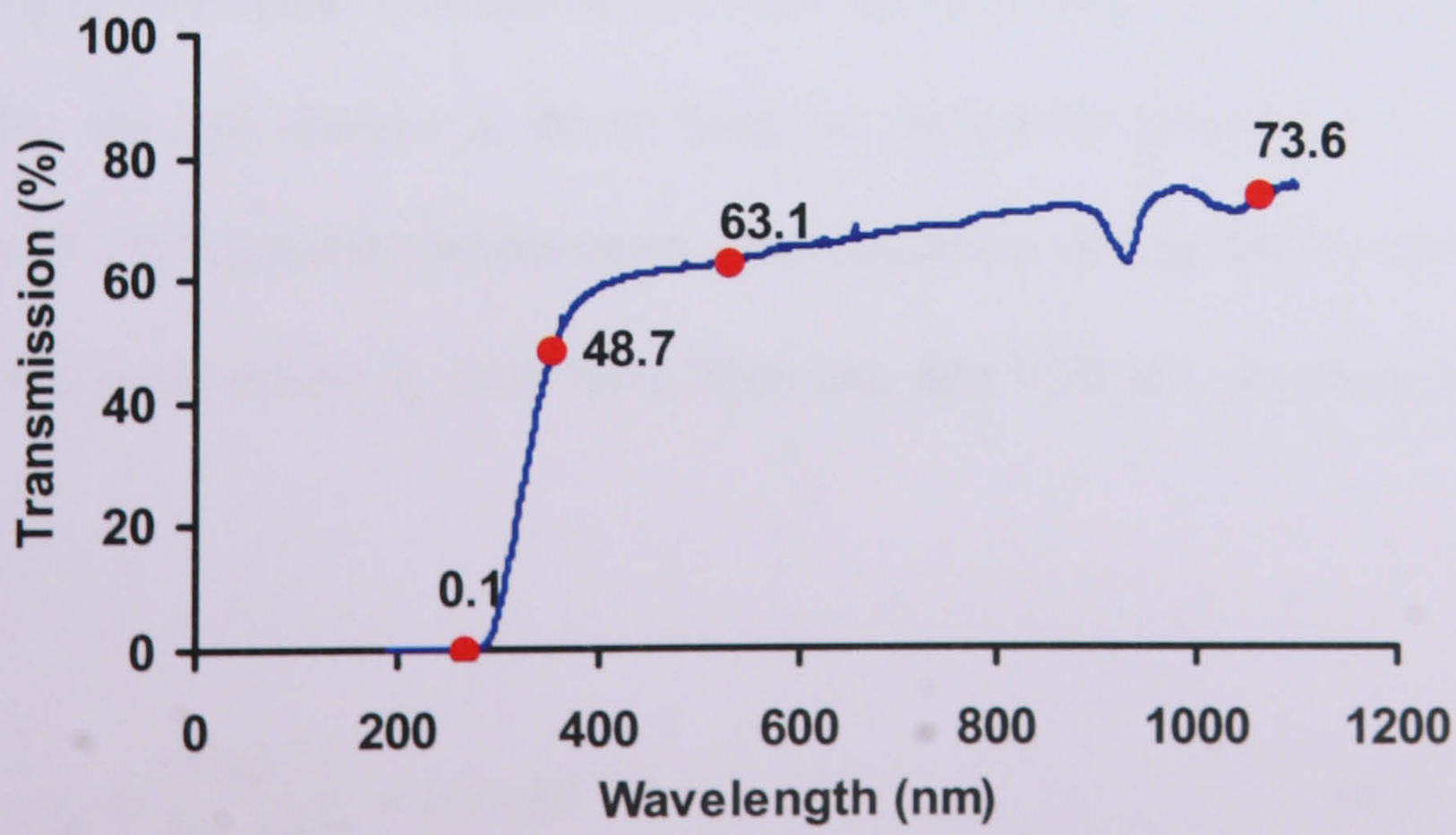

Figure 4.1: Light Transmission of Brookfield Polymer Oil

Figure 4.1 suggests that the oil becomes strongly absorbing below 300nm. Therefore, the 266nm wavelength could never be used in these experiments.

4.1.2 Encapsulated Polymer Results

The three wavelengths available from the Nd:YAG laser were used to probe the encapsulated polymers and excite the material within. The typical number of photons incident on the sample per pulse for each of these wavelengths was in the order of: (1064nm: 10^{16}, 532nm: 10^{15}, 355nm: 10^{15}). Electric fields up to 3 MVm^{-1} were applied. Sample concentrations by mass fraction varied between 1 x 10^{-4} and 1 x 10^{-3}. When an amplifier was used, signal gain was expected to be in the order of 40.

No signals were observed with zeolite-encapsulated polymers.

This was either because there were no signals present at all or that the size of the signals were too small to be measured. The digital oscilloscope has a minimum vertical resolution of 5 mV per division with 10 points per division which corresponds to its maximum sensitivity. By assuming 0.5 mV to be the lower limit of signal detection after averaging and noise subtraction and with the knowledge that the amplifier has a gain of 40, we can deduce a lower limit on detectable photocurrents using this equipment. If any transient photocurrents were occurring during these experiments, we can state that their values, i_p, must have been less that 0.25 μA, as given by equation (4.1).

$$i_p < \frac{5\times10^{-4}V}{40\times50\Omega} = 2.5\times10^{-7}A \qquad (4.1)$$

If we assume that the lifetime of this hypothetical signal was in the order of a nanosecond and we were using the infra-red output of the laser and a typical field of 2.68 MVm^{-1}, we can infer possible values of the photocharge created and the resultant quantum efficiency: $\boldsymbol{Q} < (2.5 \times 10^{-7}\ A) \times (1 \times 10^{-9}\ s) = 2.5 \times 10^{-16}\ C$. Using equation 2.6, this works out to a convolved value of $\{\eta\phi\}s < 1.63 \times 10^{-16}$ m, a very small value indeed.

It was necessary to narrow down the possible reasons why these signals were either non-existent or so small that they could not be detected. This is to be discussed in the following chapter.

4.2 Discotic Liquid Crystals

A TOF sandwich cell was constructed using the method described in chapter 3. Before material was introduced to the cell, the 'unfilled sandwich' was placed in the beam path of a Hitachi U-3000 spectrophotometer and a transmission spectrum was taken. This is shown in figure 4.2 and shows a Fabry-Perot transmission spectrum.

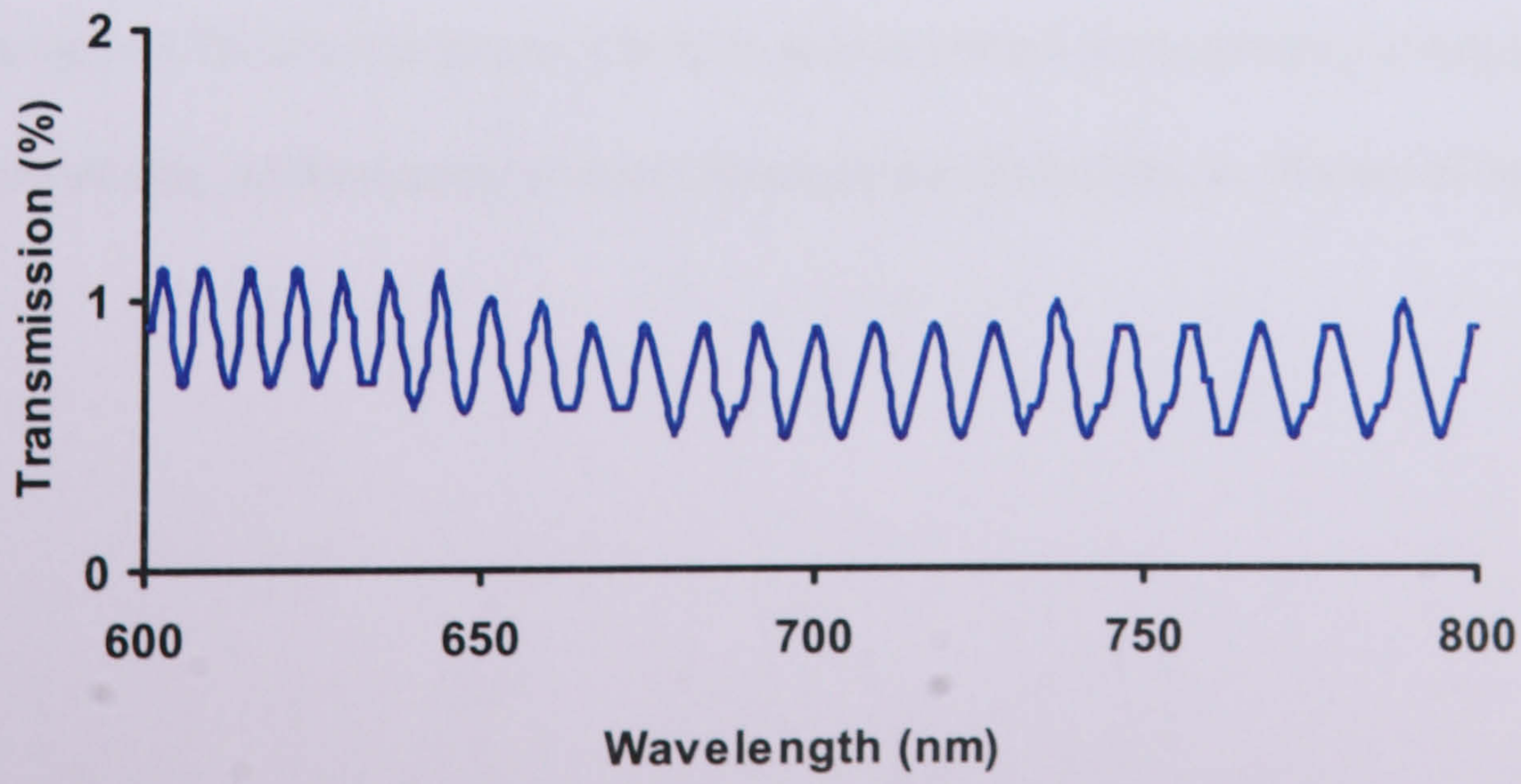

Figure 4.2: Transmission spectrum of unfilled TOF cell

Recalling equation 3.4, a plot of the inverse of the peaks ($1/\lambda_{peak}$) versus the order (***m***) will result in a linear fit. The absolute value of the gradient will be equal to ***1/2d,*** where ***d*** is equal to the path length between the inner reflecting surfaces of the quartz slides (i.e., the electrode gap). This is plotted in figure 4.3.

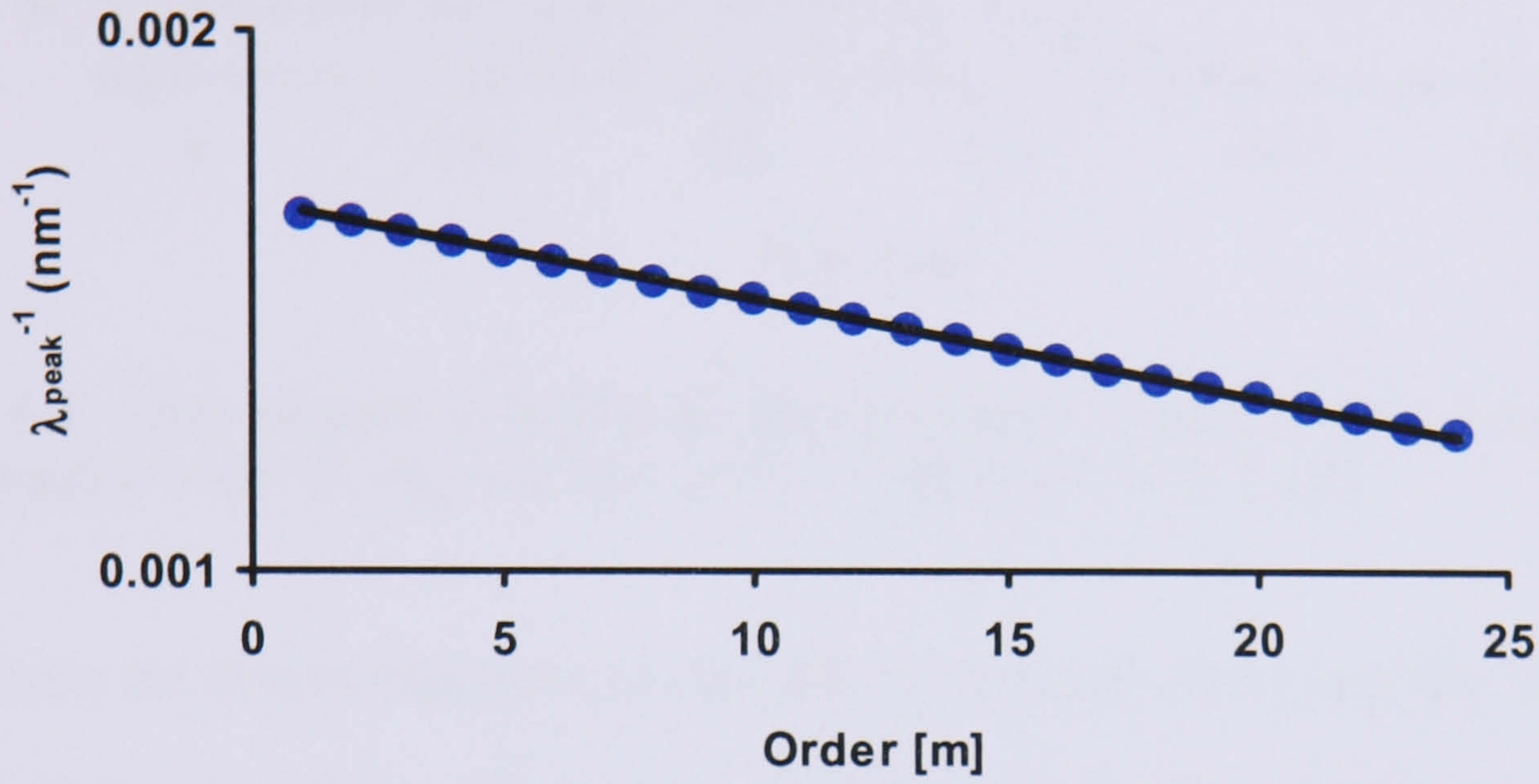

Figure 4.3: Determination of sandwich cell thickness

By evaluation of the slope in figure 4.3 (equal to 1.79 x 10^{-5} nm^{-1}), the spacing of the cell is determined to be 28 μm. This cell was later filled with 2FHAT6 and the results from this experiment are to be discussed shortly.

4.2.1 - HAT6

In the HAT6 discotic phase, the hole photocurrents demonstrate, through time of flight experiments, uninterrupted transits between the electrodes, as shown in figure 4.4.

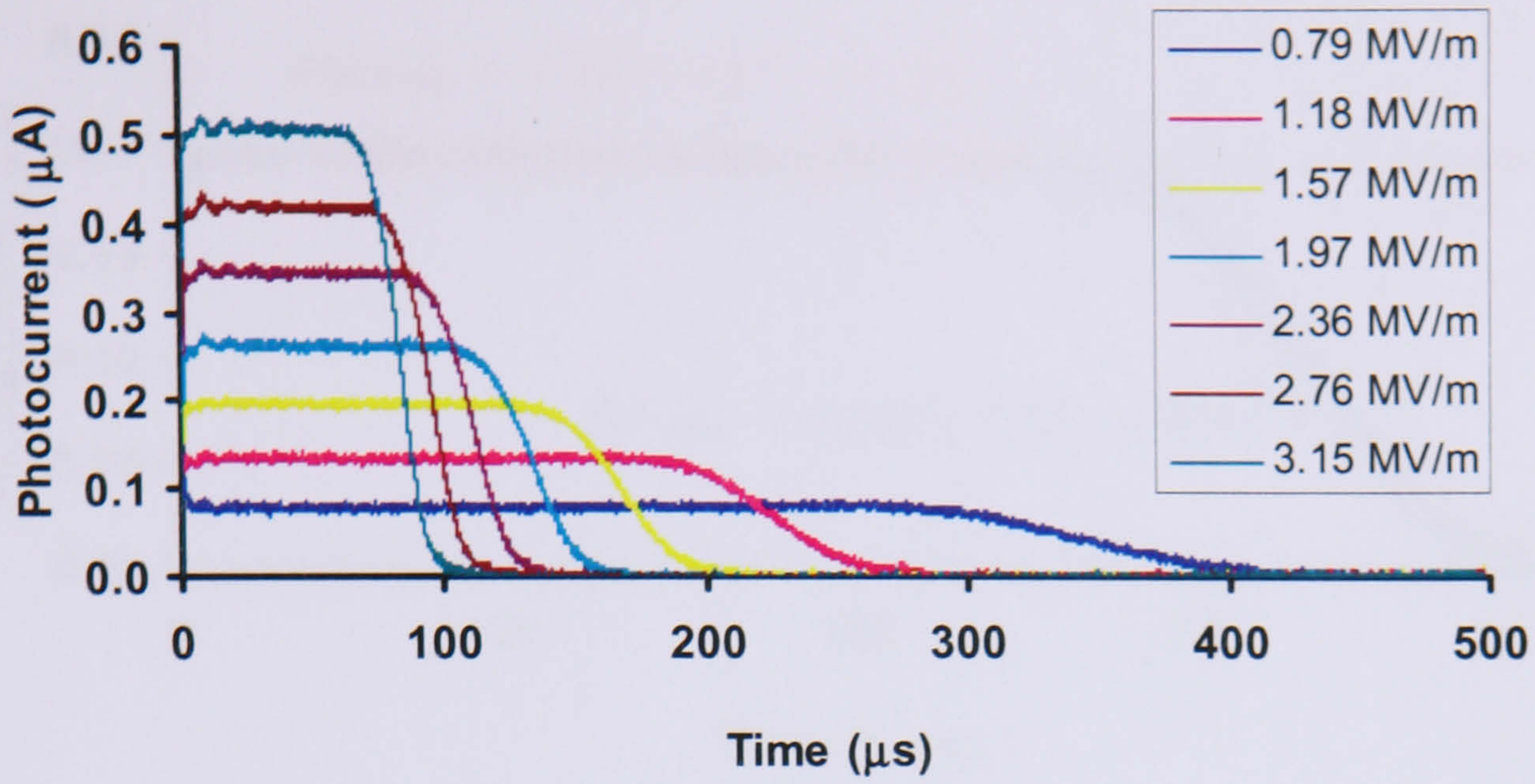

Figure 4.4: Hole transits in HAT6 at different fields in the discotic mesophase (Temperature = 85° C, N_{ph} = 4.17 x 10^{10}, λ = 337nm, d=12.7 μm)

From the data in Figure 4.4, we are able to calculate carrier mobility. When the majority of the carriers have traversed the sample length, ***d***, a rapid decay in current is observed as the carriers recombine at the counter electrode. By dividing the sample length by the time at which this drop off occurs (the transit time), we can calculate the velocity of the carriers. By plotting the carrier velocity versus electric field, we can determine the hole mobility, μ_h, from the slope of the plot: $\mu_h = (dv/dE)$.

To ensure that the transit time is assessed in a consistent way, the following method was employed. Figure 4.5 shows the HAT6 transit at 1.57 MVm^{-1}. By forcing two linear fits through both the plateau and the decay, we obtain two equations which can be solved simultaneously. The point where the fits intersect (i.e., the value of ***t*** where the two equations balance) is the point chosen as the transit time.

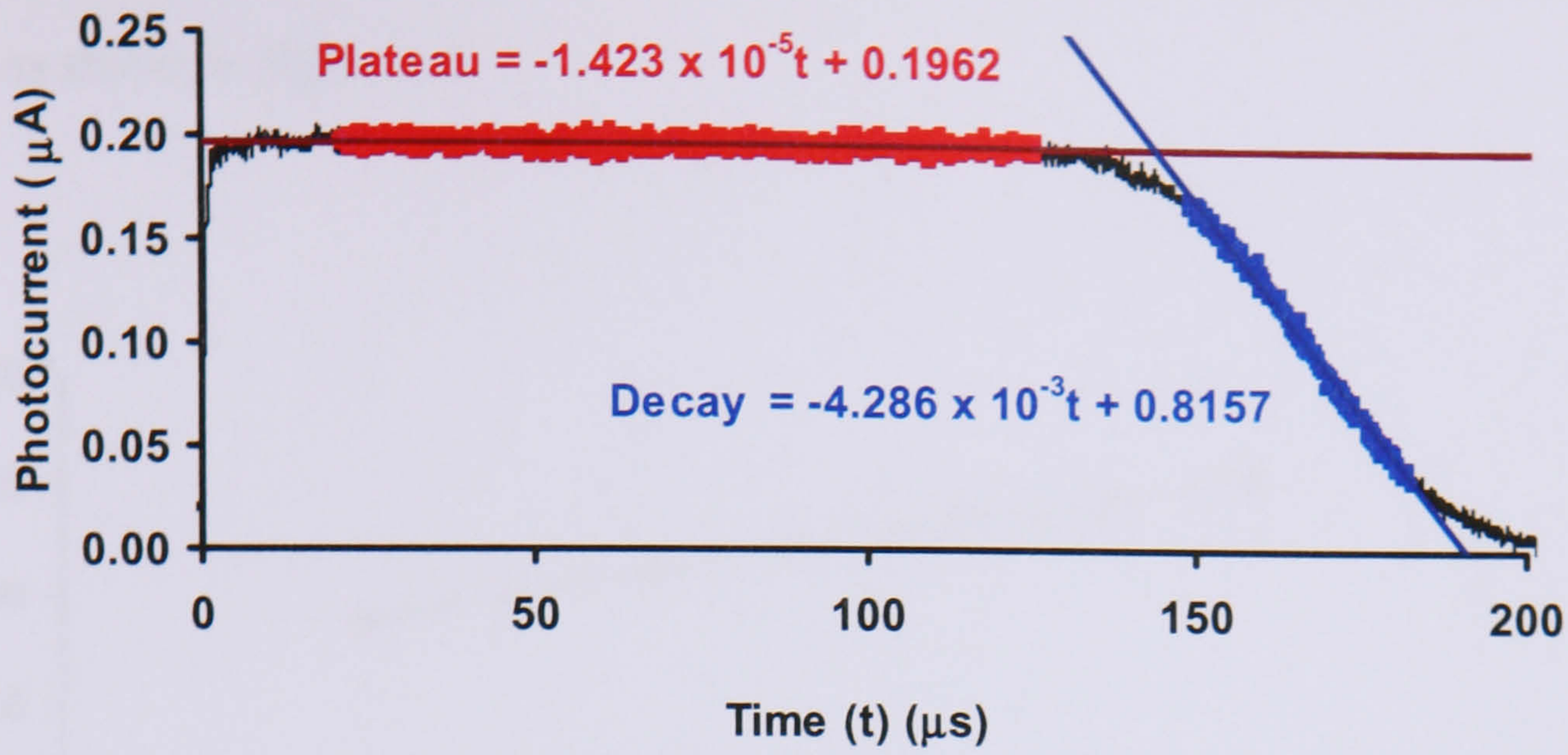

Figure 4.5: Determination of Transit Time for HAT6 ($E=1.57\ MVm^{-1}$, Temperature = 85° C, $N_{ph} = 4.17 \times 10^{10}$, $\lambda = 337nm$, $d=12.7\ \mu m$)

When the two equations given in Figure 4.5 are solved simultaneously, we deduce a transit time equal to 145 µs and as we know the sample thickness, we are able to infer a carrier velocity of $8.82 \times 10^{-2}\ ms^{-1}$. This procedure is applied to the transits at all fields and a plot of carrier velocity versus electric field is shown in figure 4.6. From figure 4.6, a mobility of $\mu_h = 5.74 \times 10^{-4}\ cm^2\ V^{-1}\ s^{-1}$ can de deduced from the slope.

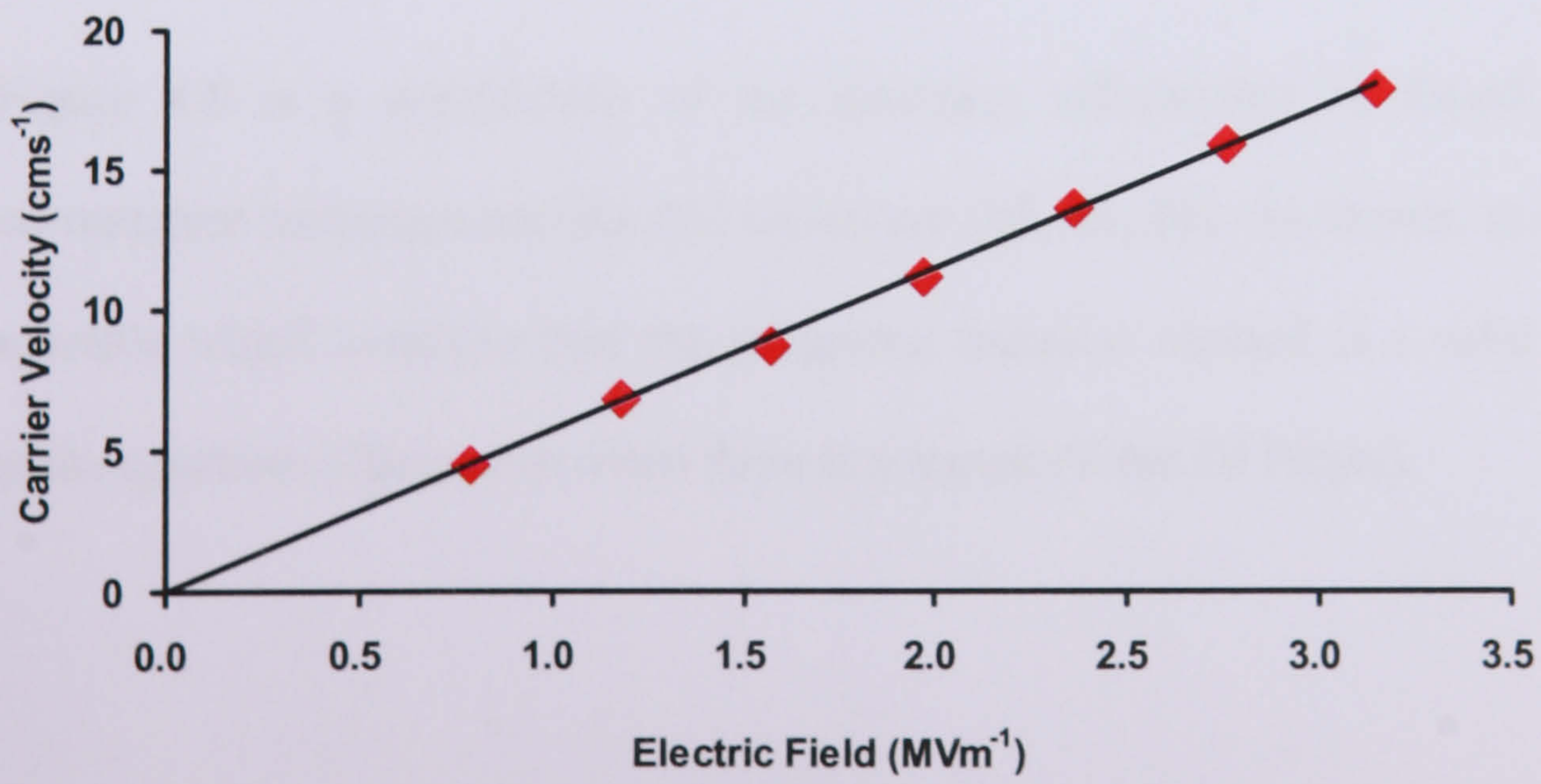

Figure 4.6: Determination of HAT6 Hole Mobility (Temperature = 85° C, $N_{ph} = 4.17 \times 10^{10}$, $\lambda = 337nm$, $d=12.7\ \mu m$)

Integration of the currents from figure 4.4 will give us the total photocharge created as shown in figure 4.7.

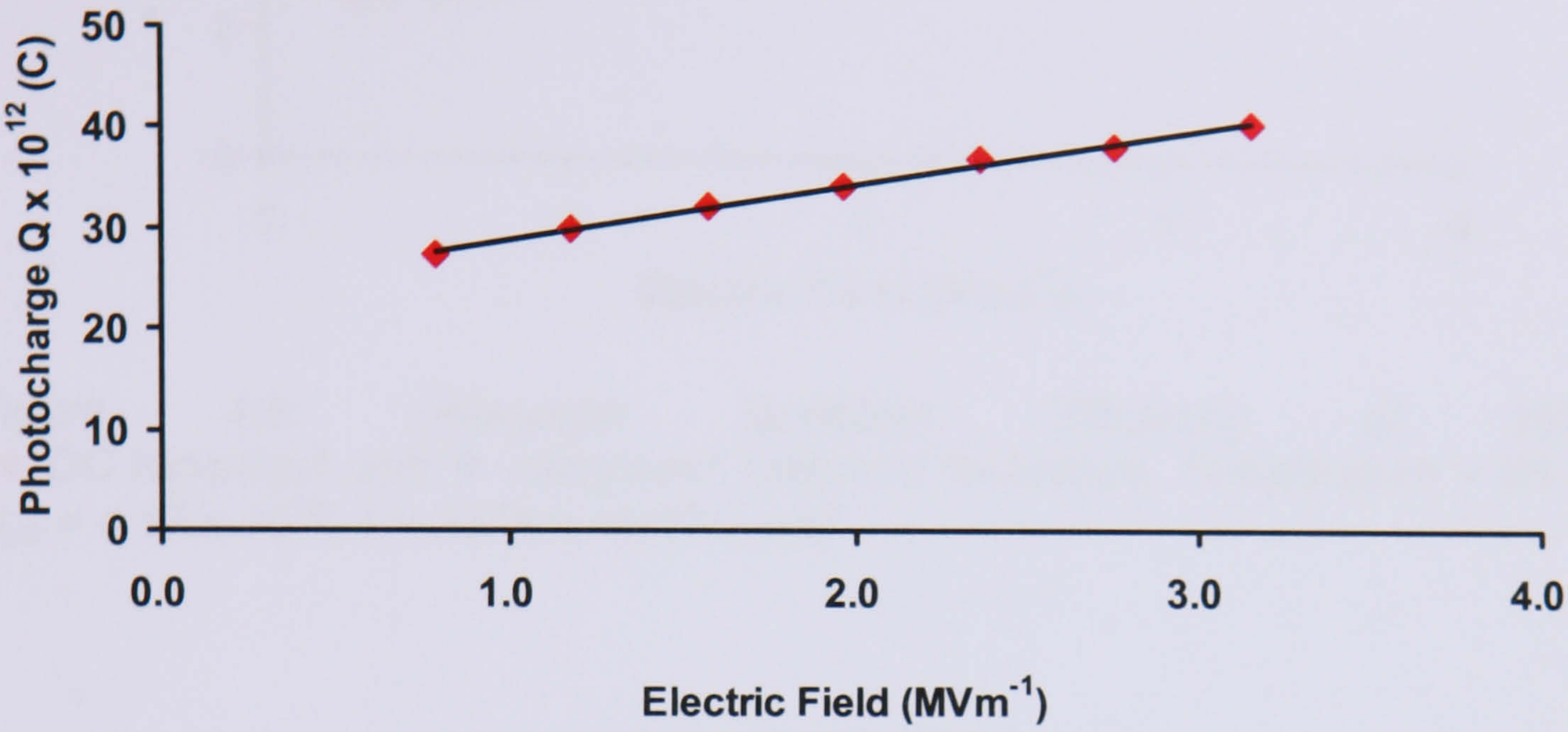

Figure 4.7: Photocharge created in HAT6 as calculated from the data in Figure 4.4 (Temperature = 85° C, N_{ph} = 4.17 x 10^{10}, λ = 337nm, d=12.7 μm)

Recalling equation (2.8) with the knowledge that the carrier range is equal to the electrode separation, we can use the measured photocharge to calculate the quantum efficiencies of the material at different fields.

Figure 4.8 is a comparison of the quantum efficiencies as found by the integrated transient technique and the DC technique [**42, 43, 44**]. As shown, the results are comparable which confirms that the integrated transient method is a valid way of deducing the quantum efficiencies when there is a transit (Time Of Flight).

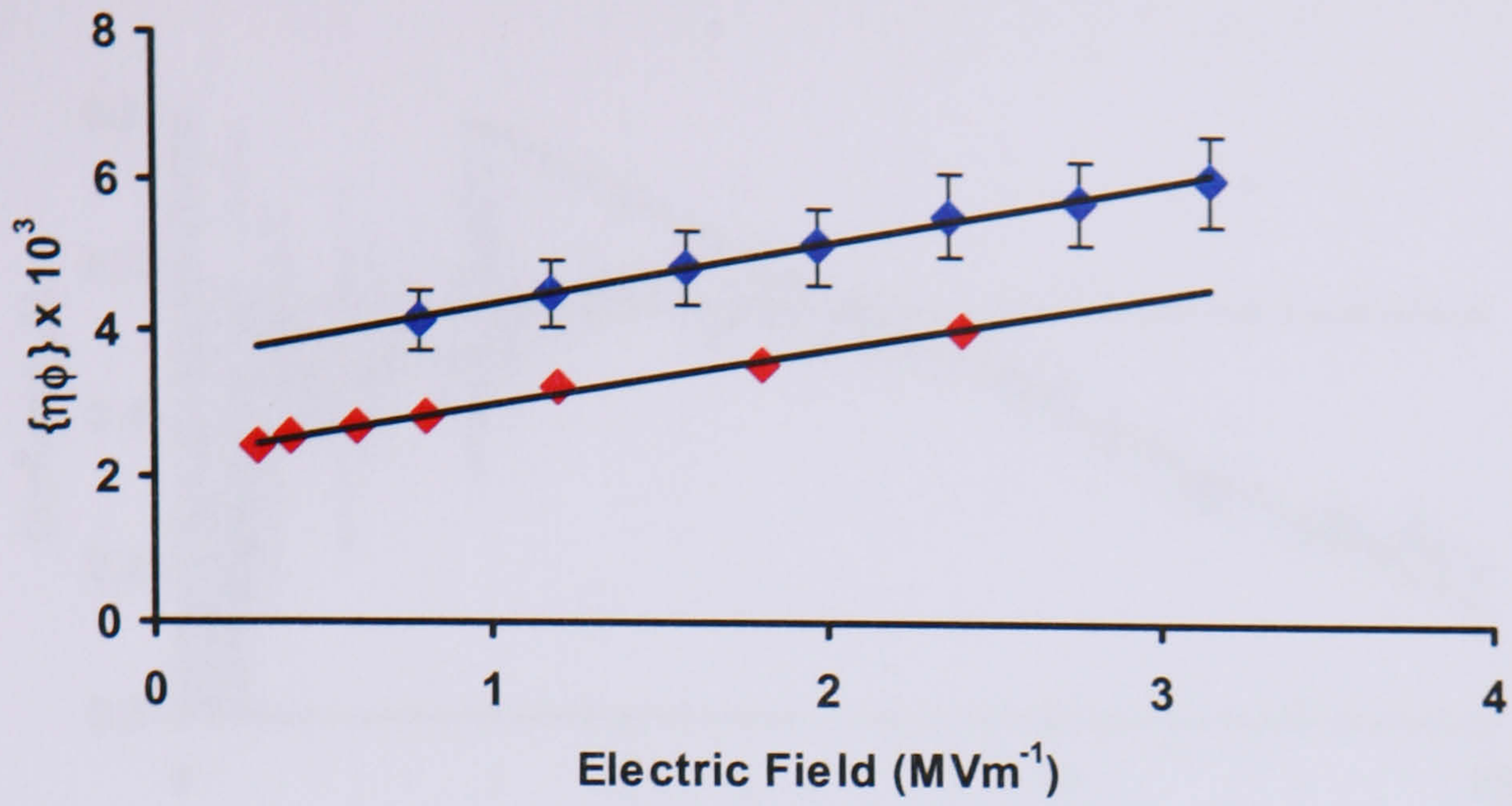

Figure 4.8: Measured Quantum Efficiency of HAT6 (◆ DC technique and ◆ Integrated Transient technique, Temperature = 85° C, N_{ph} = 4.17 x 10^{10}, λ = 337nm, d=12.7 μm)

4.2.2 - HAT6:PTP9

Other molecules based on the triphenylene motif can complement the material HAT6. One such material is PTP9 and a resulting binary mixture of HAT6:PTP9 can be produced in a 50:50 stoichimetric combination. HAT6:PTP9 has observable hole transits. Figure 4.9 is an example of a transit.

Figure 4.10 is a plot of the carrier velocity versus Electric Field at 90°C, the slope of which allows us to deduce a value for the hole mobility equal to: μ_h = 1.45 x 10^{-2} $cm^2 V^{-1} s^{-1}$.

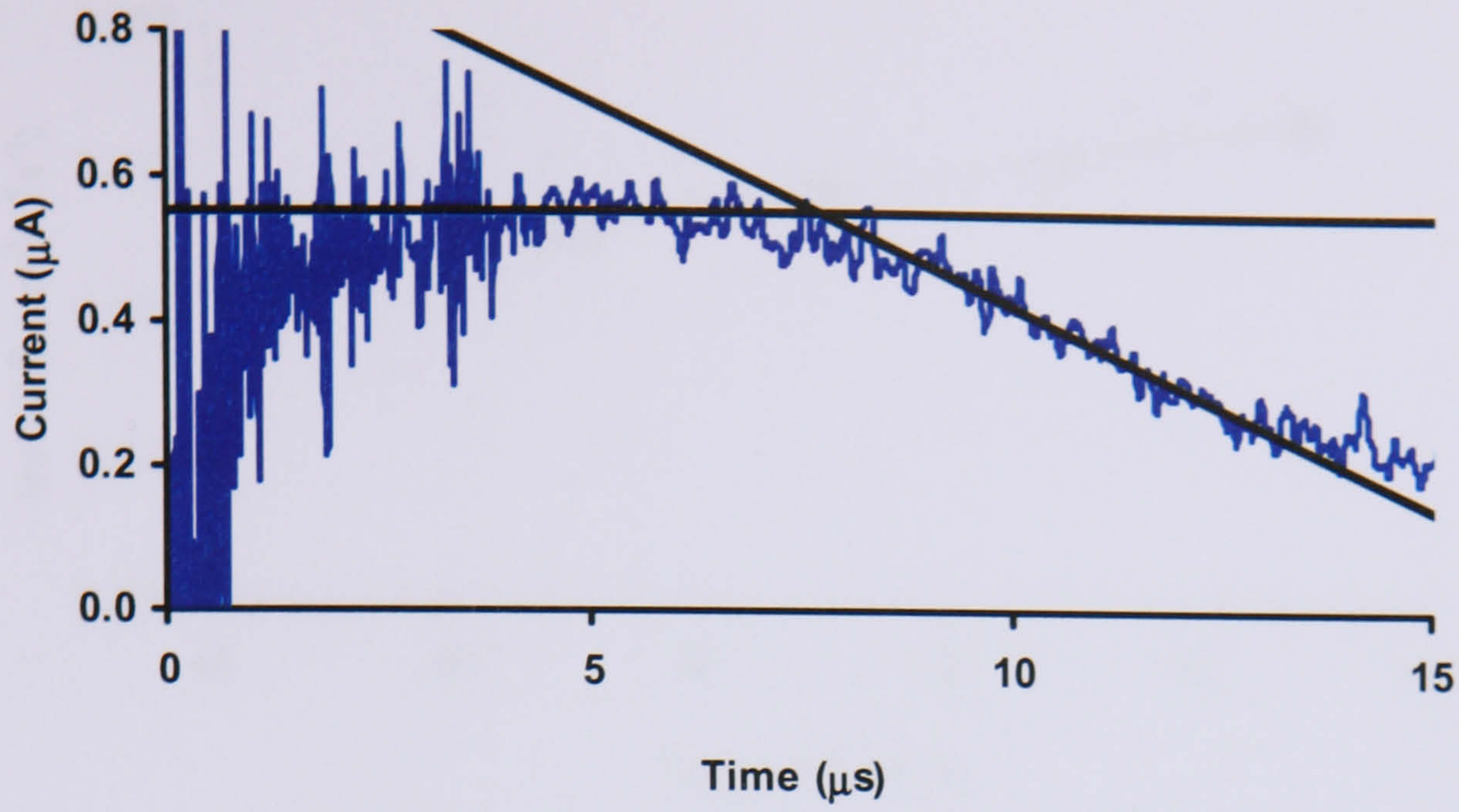

Figure 4.9: HAT6:PTP9 Example Transit when in the columnar discotic phase (λ=337nm, N_{ph}=4.42 x 10^{11}, d=11 μm, E = 1.36 MVm^{-1}, T=90°C)

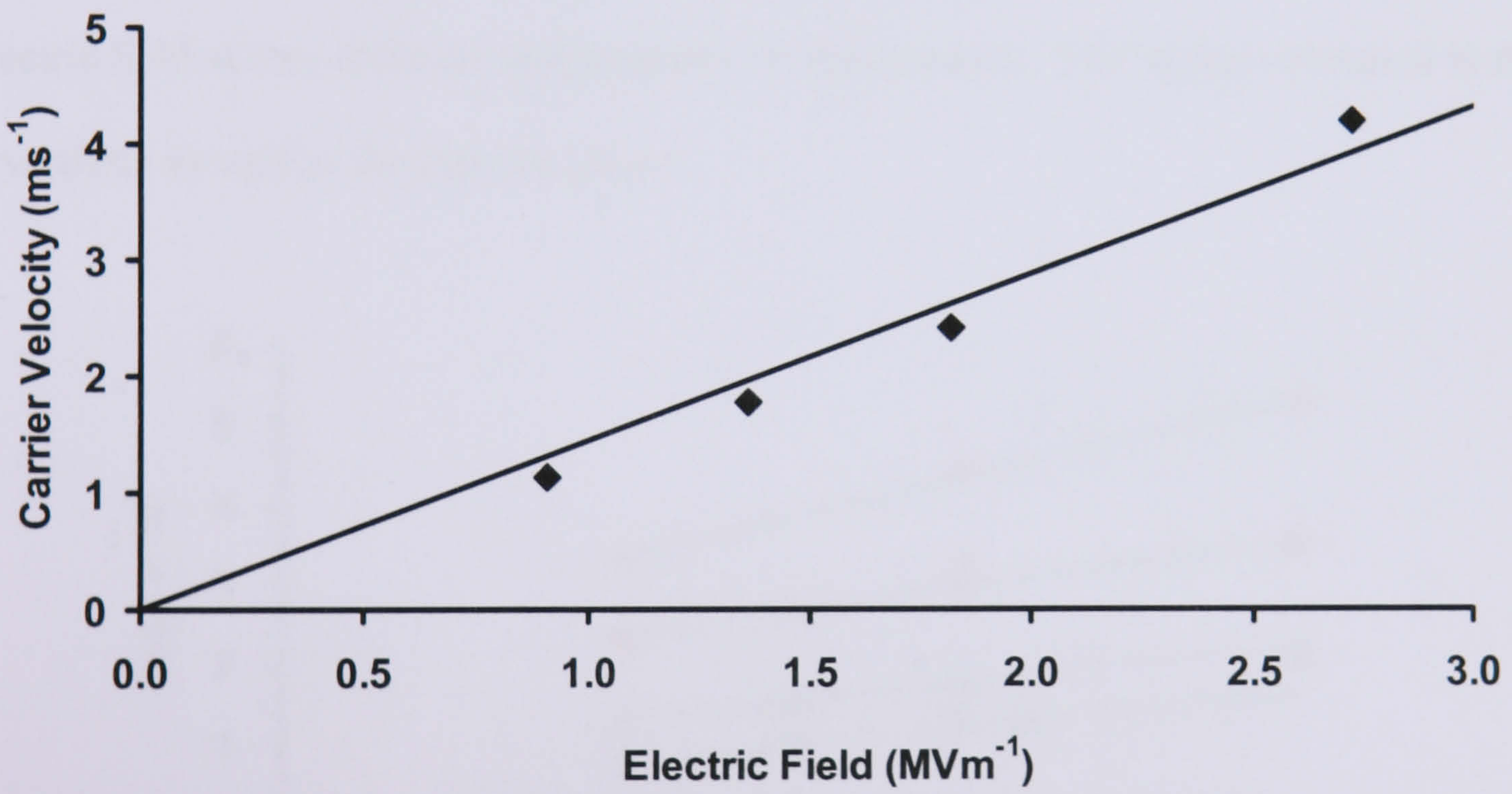

Figure 4.10: HAT6:PTP9 Mobility (λ=337nm, N_{ph}=4.42 x 10^{11}, d=11 μm^{1}, T=90°C)

The experiment from which figure 4.10 was derived was repeated at different temperatures. Figure 4.11 shows a plot of mobility versus temperature.

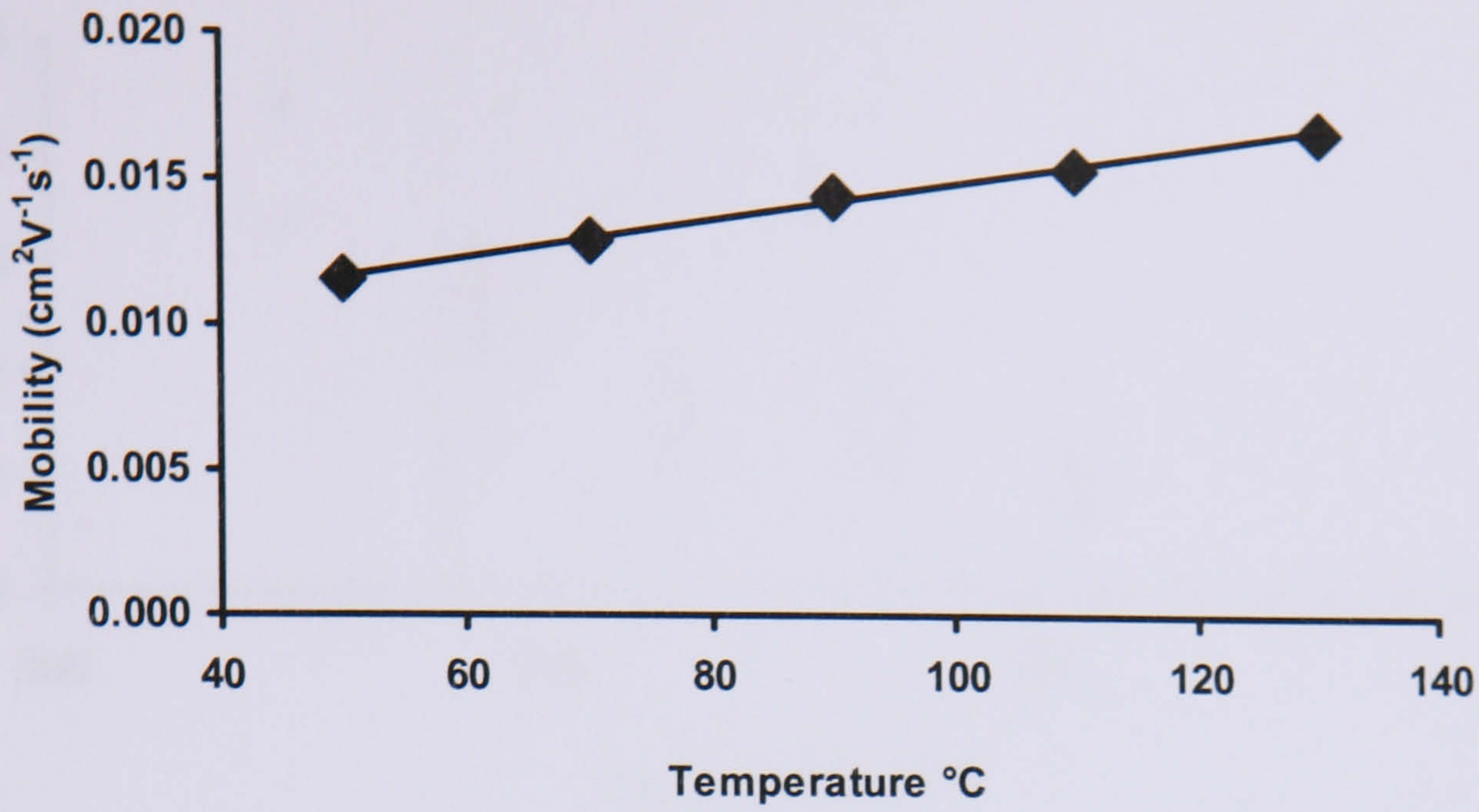

Figure 4.11: HAT6:PTP9 Mobility vs. Temperature (λ=337nm, N_{ph}=4.42 x 10^{11}, d=11 μm)

Figure 4.12 shows a linear relationship between the quantum efficiency and electric field at four different temperatures. In this material, TOF signals occurred in the crystalline as well as the discotic phase.

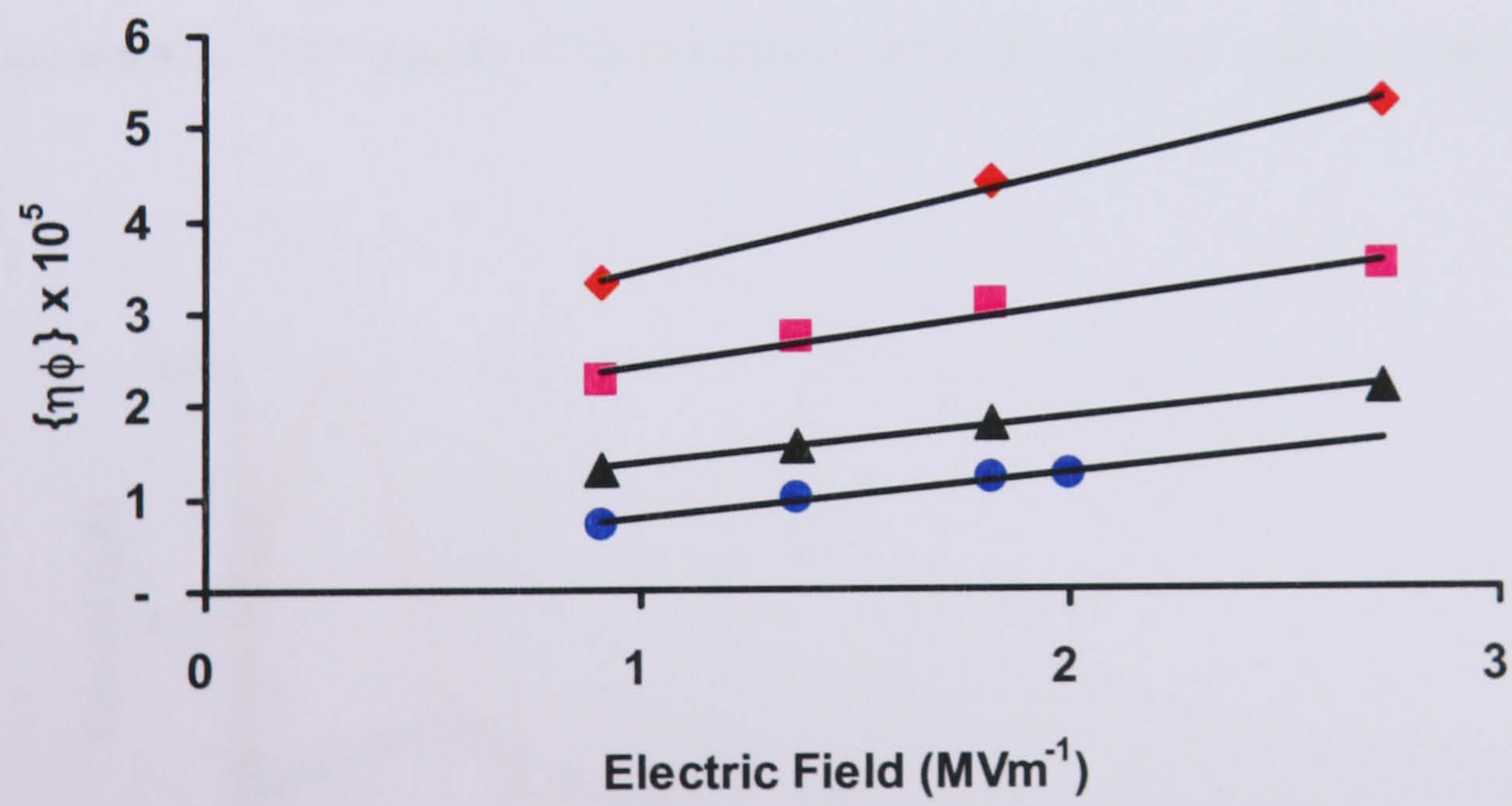

Figure 4.12: HAT6:PTP9 Quantum Efficiency versus Electric Field (◆=50°C, ■=70°C, ▲=90°C, ●=130°C, λ=337nm, N_{ph}=4.42 x 10^{11}, d=11 μm)

Figure 4.13 shows the measured quantum efficiencies at three fields over a range of temperatures. The dashed line represents the crystalline/discotic phase boundary (339 °K), otherwise known as the melting point.

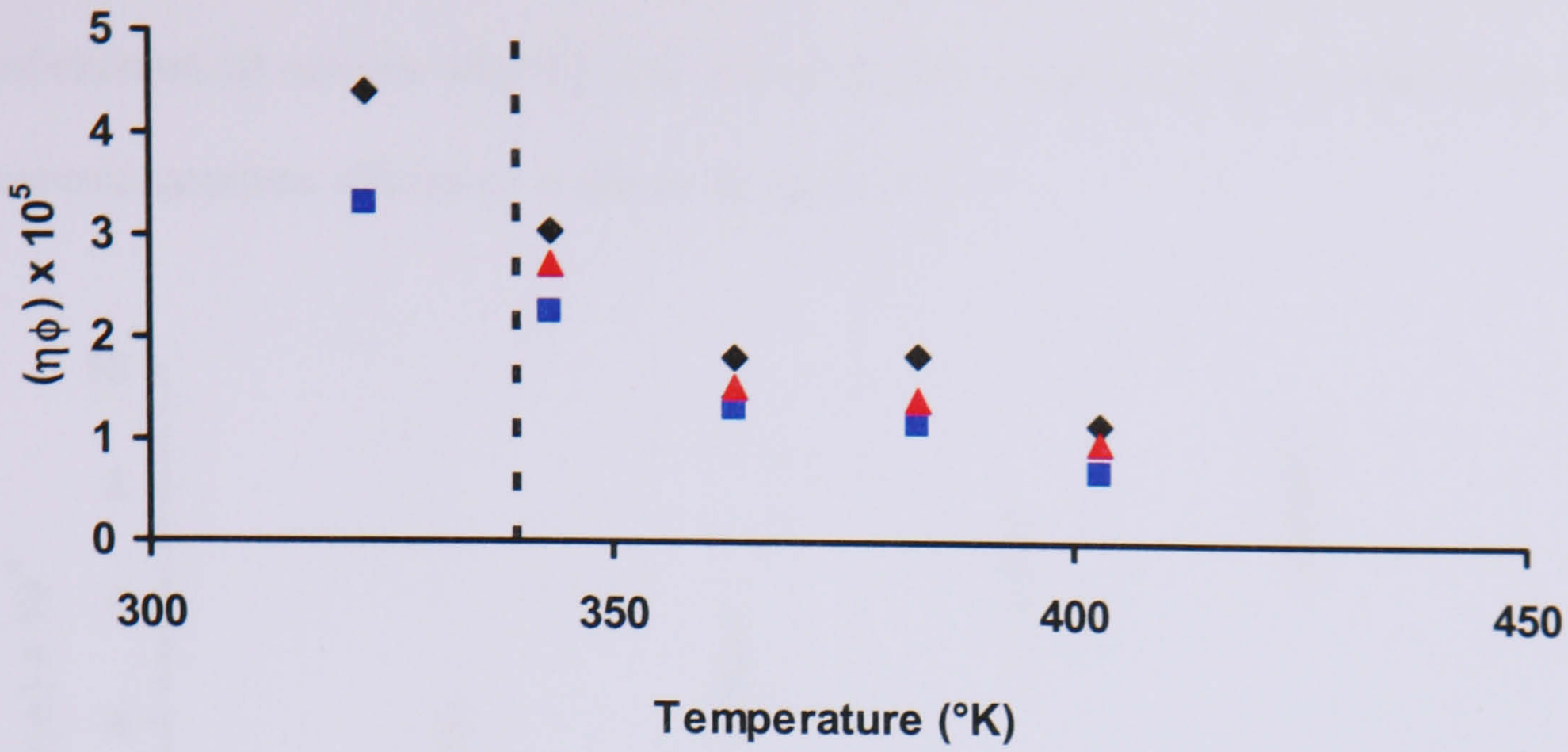

Figure 4.13: HAT6:PTP9 Quantum Efficiency vs Temperature (◆=0.9 MVm^{-1}, ▲=1.8 MVm^{-1}, ■=2.7 MVm^{-1}, ---- line = 339.15°, λ=337nm, N_{ph}=4.42 x 10^{11}, d=11 μm)

4.2.3 - HAT11:PTP9

Early work on the HAT11:PTP9 mixture shows evidence of spacecharge. Figure 4.14 demonstrates TOF signals of hole carriers with the obvious effect of spacecharge present.

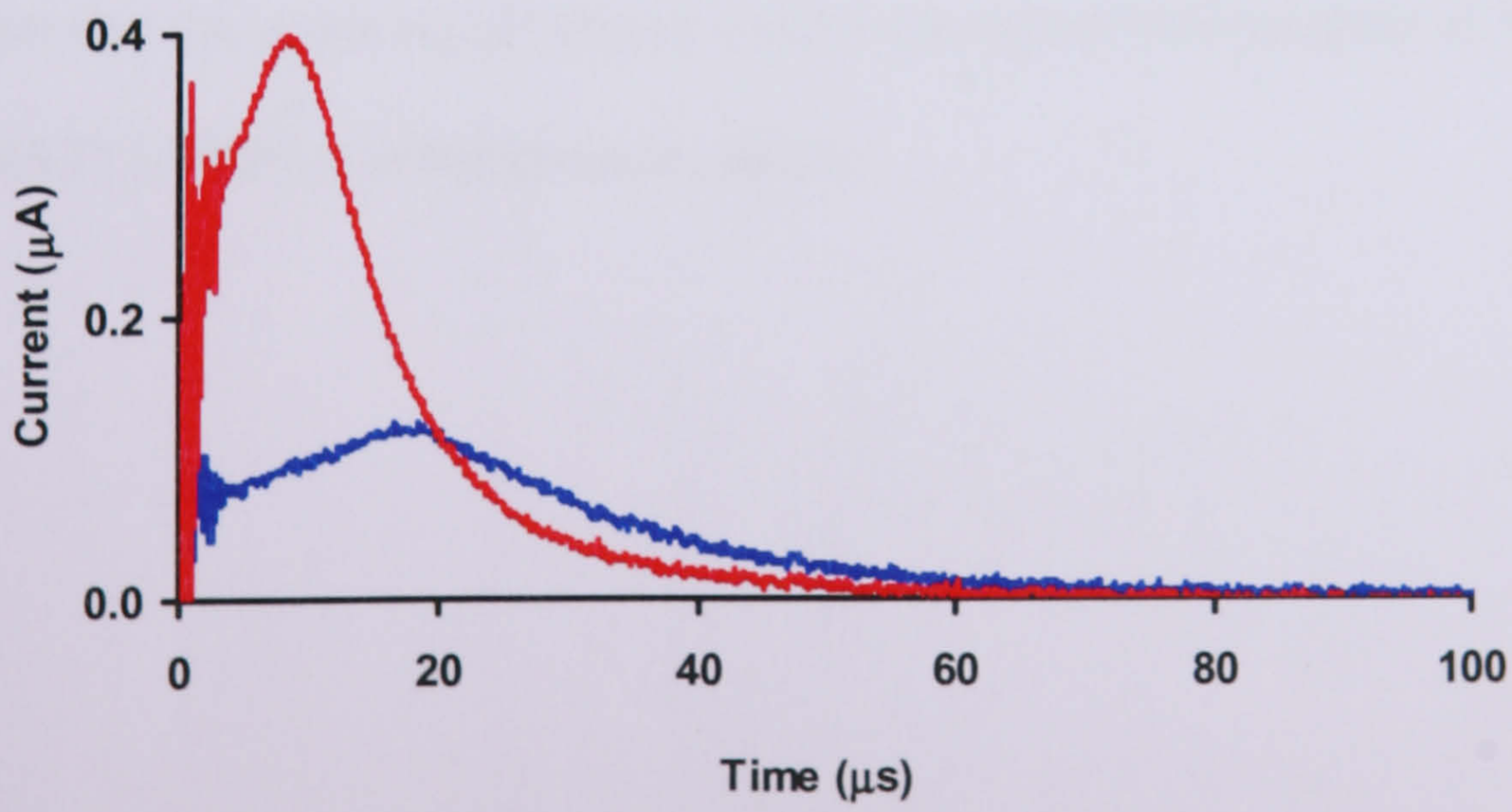

Figure 4.14: HAT11:PTP9 Hole photocurrents with Spacecharge (Red Line = 0.89 MVm^{-1}, Blue Line = 0.45 MVm^{-1}, d=11.2 μm, λ=337nm, N_{ph}=8.27 x 10^{10}, T=130° C).

While spacecharge makes the determination of mobility a difficult one, there are good theoretical reasons why this will not affect the measured quantum efficiency. The measured quantum efficiency is shown in figure 4.15.

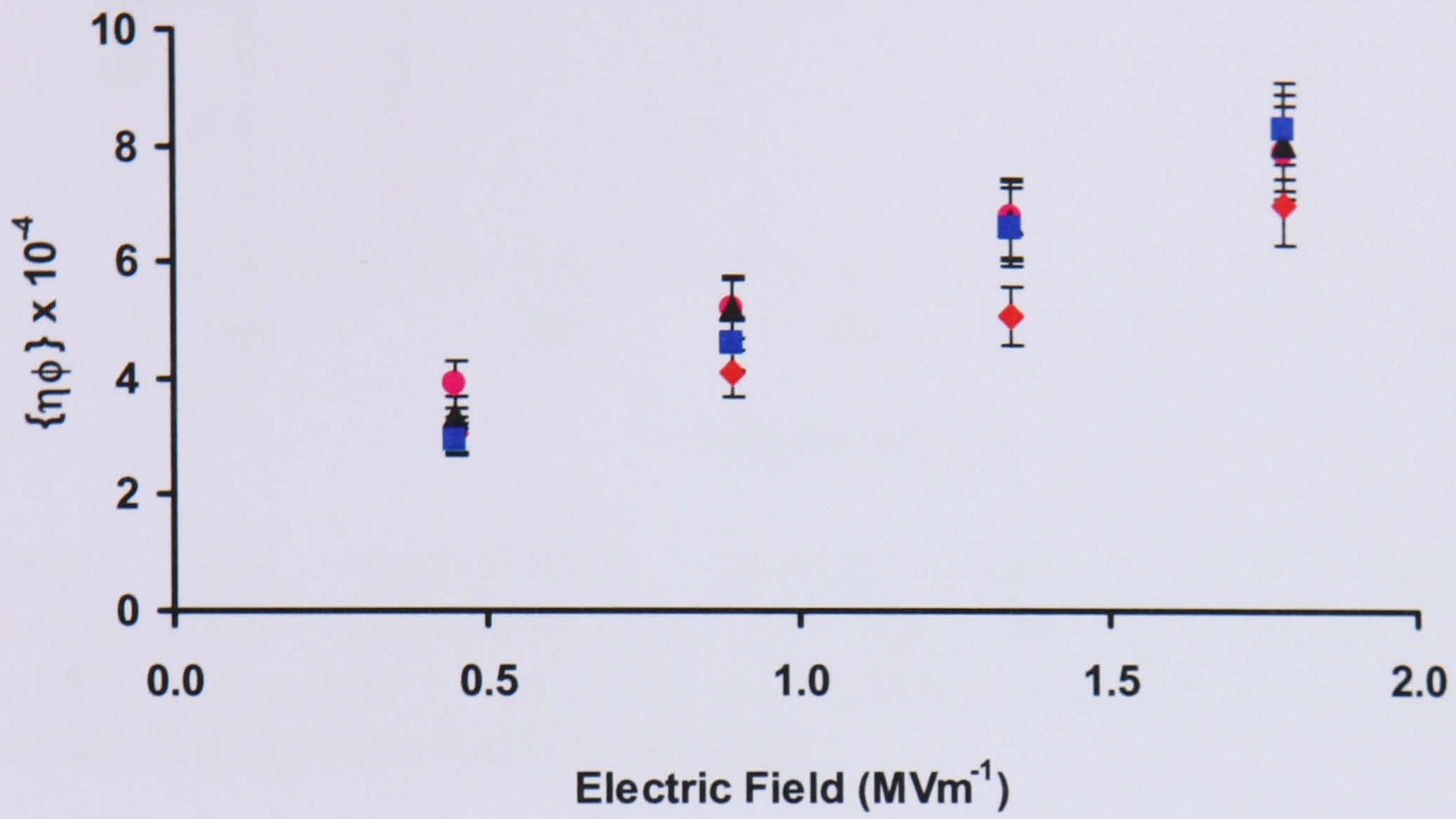

Figure 4.15: HAT11:PTP9 Quantum Efficiency vs Electric Field (◆=70°C, ●=90°C ▲=110°C, ■=130°C, d=11.2 μm, λ=337nm, N_{ph}=8.27 x 10^{10})

Figure 4.15 shows that the quantum efficiency of HAT11:PTP9 does not vary significantly with temperature. This result is illustrated more clearly in Figure 4.16, which shows that the quantum efficiency can be considered independent of temperature when the HAT11:PTP9 is in the discotic regime.

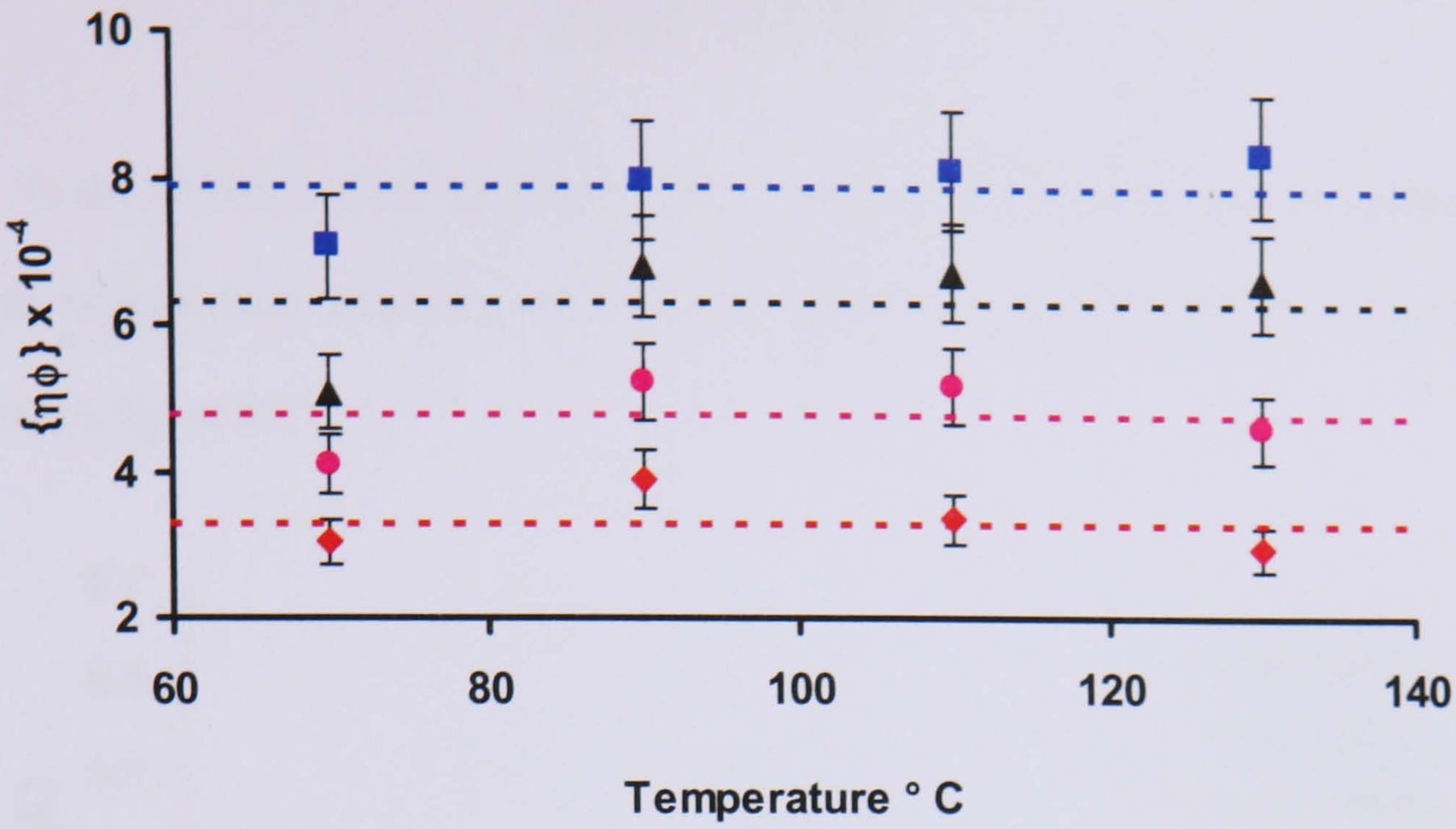

Figure 4.16: HAT11:PTP9 Quantum Efficiency vs Temperature (◆=0.46 MVm^{-1}, ●=0.89 MVm^{-1} ▲=1.34 MVm^{-1}, ■=1.79 MVm^{-1}. d=11.2 μm, λ=337nm, $N_{ph}=8.27 \times 10^{10}$. The dashed lines represent the average values for each field over the temperature range)

4.2.4 - 2FHAT6

In the 2FHAT6 discotic phase, the hole photocurrents demonstrate, through time of flight experiments, uninterrupted transits between the top electrode to the bottom as depicted in figure 4.17.

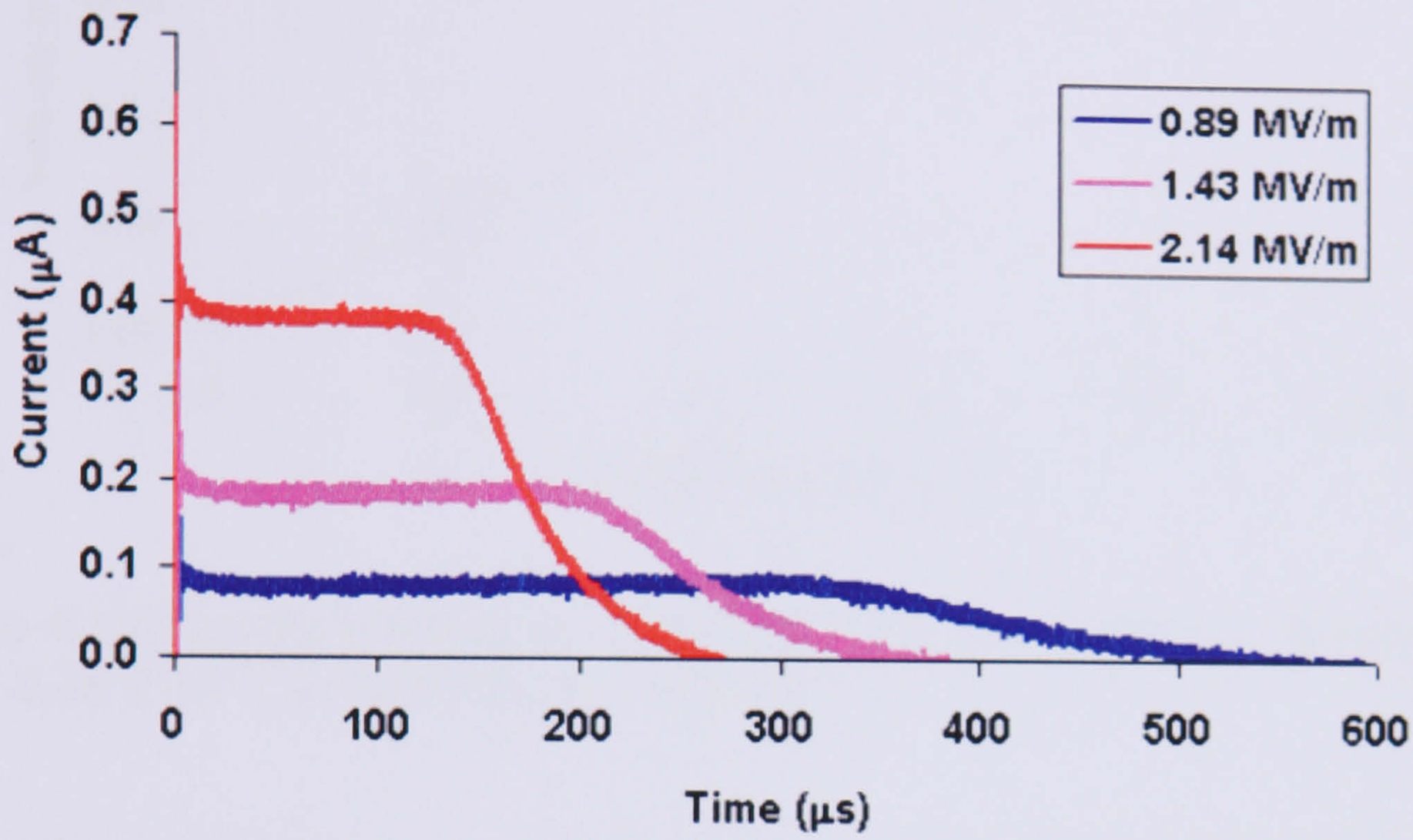

Figure 4.17: Hole Transits in 2FHAT6 at different fields (d = 28 microns, $N_{ph} = 4.28 \times 10^{12}$, $\lambda = 337nm$, T = 100°C)

The results shown in figure 4.17 show characteristic transits: flat plateaus that persist until the fastest carriers recombine at the counter electrode followed by a decaying tail caused by a distribution in carrier velocities. They also have an initial spike, which is almost certainly caused by motion of electrons before recombination at the top electrode.

As the field is increased, the velocities of the carriers increase and the transit time decreases. A plot of velocity versus electric field results in a linear relationship whose gradient gives the mobility of the material as usual. In the case of the data in

Figure 4.17, this is shown in Figure 4.18 and results in a measured mobility of 9.53 x 10^{-4} $cm^2 V^{-1}s^{-1}$.

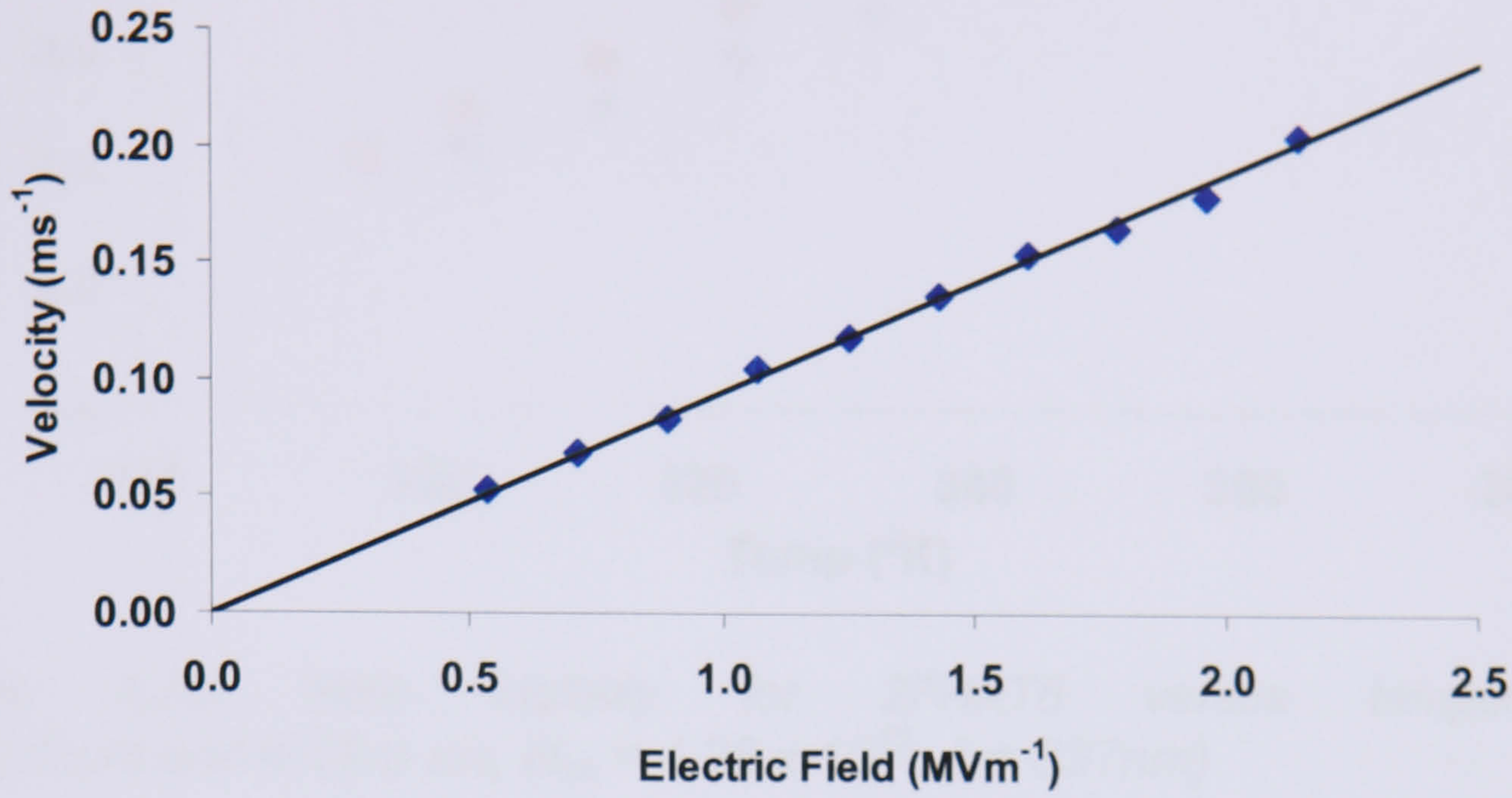

Figure 4.18: Carrier Velocity for 2FHAT6 vs Electric Field (d = 28 microns, N_{ph} = 4.28 x 10^{12}, λ = 337nm, T = 100°C)

The same experiments were performed at different temperatures and then once again with a different sample thickness (12.5 μm). Figure 4.19 is a plot of how the mobilities of both samples of 2FHAT6 change over a temperature range.

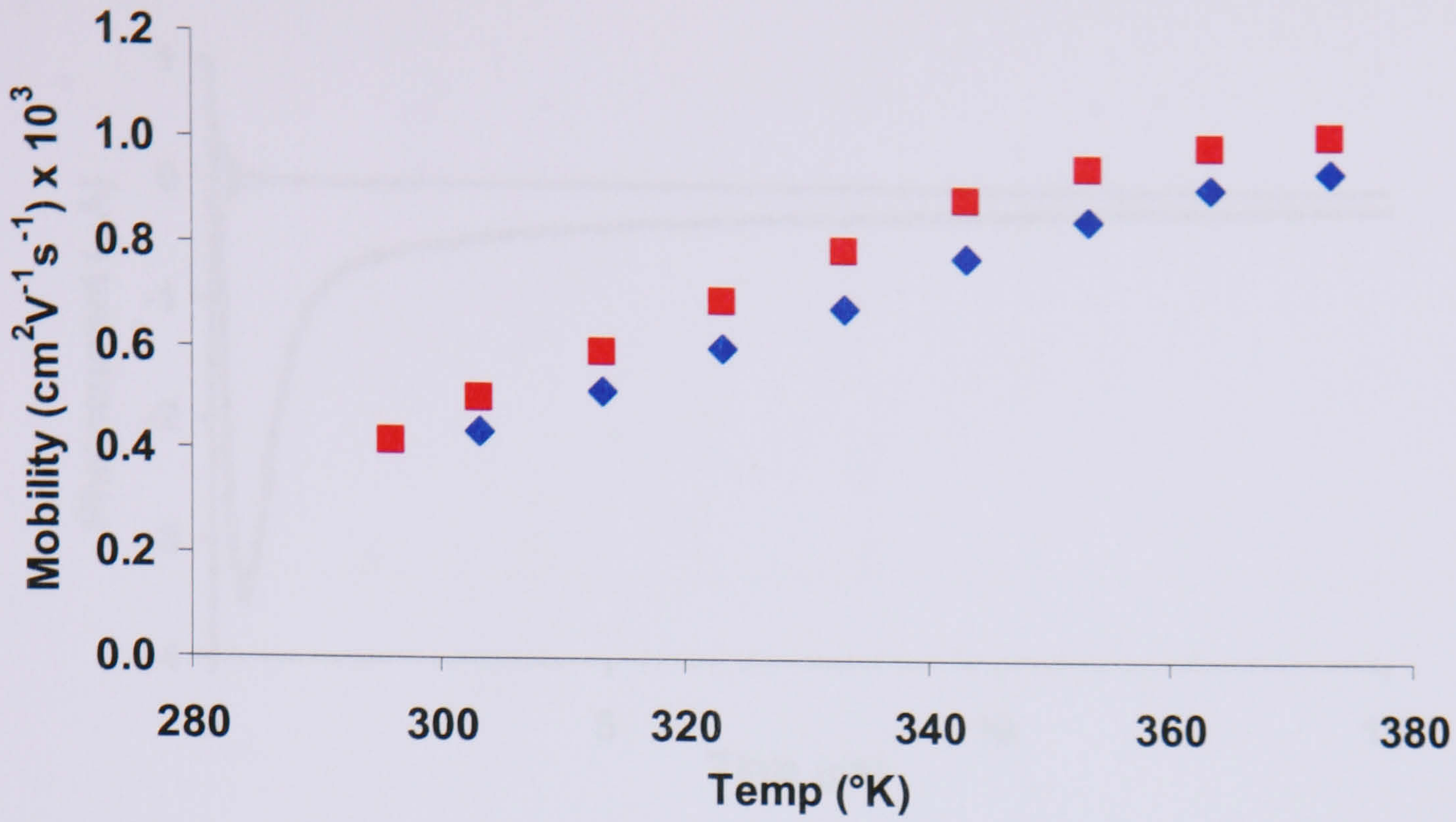

Figure 4.19: Hole Mobility for 2FHAT6 versus temperature (■ 12.5 μm and ◆ 28.0 μm, N_{ph} = 4.28 x 10^{12}, λ = 337nm)

4.2.5 - Polymer DLC

Time of Flight experiments performed with discotic liquid crystals usually show hole mobilities and quantum efficiencies to be larger than that for electrons. It is of interest then to find a material where electrons dominate. Figure 4.20 shows comparatively the electron photocurrents and the hole photocurrents.

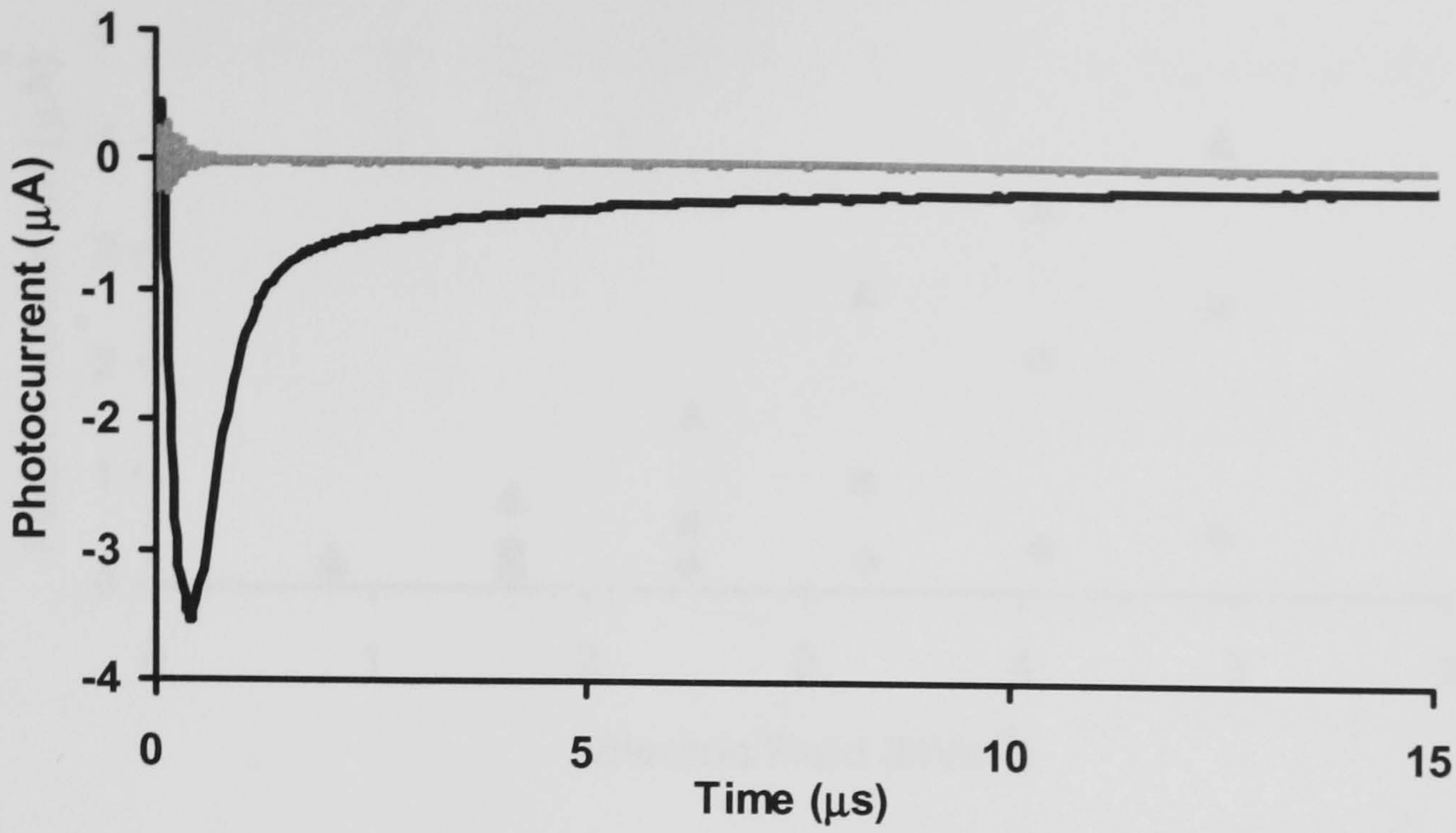

Figure 4.20: Electron and hole photocurrents in Triblock copolymer (Black Lines and Grey Lines respectively, E = 4.1 MV/m, d = 12 μm, T = 70 °C and N_{ph}=6.92 x 10^{14})

The data shown in Figure 4.20 shows conclusively that this material is not a hole transporter (the initial burst of activity displayed is nothing more than RF interference from the Nitrogen laser). This is a situation unlike that found in other discotics based around a triphenylene system.

It also demonstrates that a definite mobility cannot be deduced, as the electron photocurrent is not a transit. The decay of the photocurrent is also of interest, exhibiting an initial fast decay followed by a second decay component which lasts much longer.

Figure 4.21 shows the peak photocurrent plotted as a function of electric field for various temperatures.

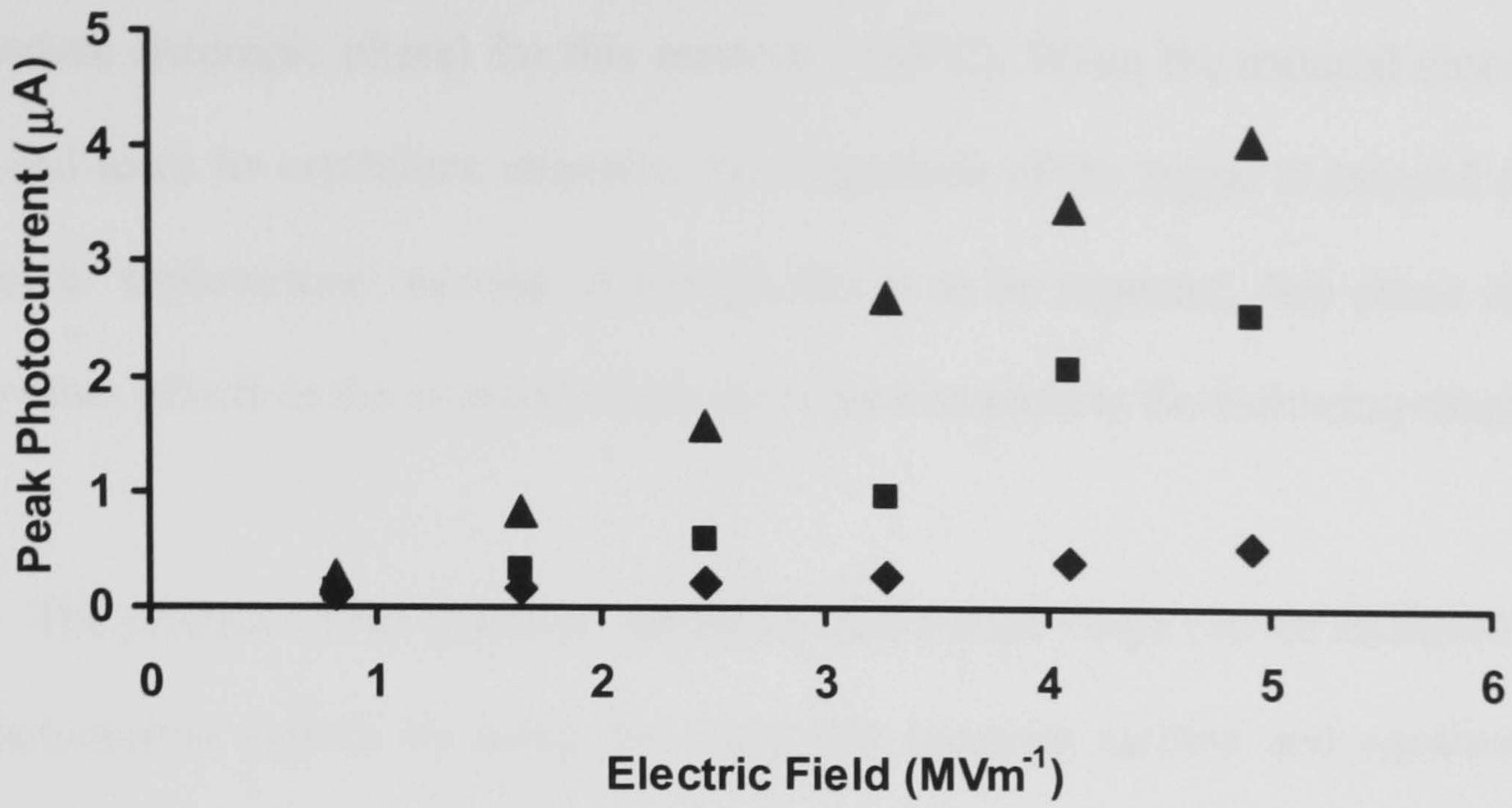

Figure 4.21: Electric field dependence of peak photocurrent for electrons at ◆ = 30 °C, ■ = 50 °C and at ▲ = 70 °C (d = 12 μm and N_{ph}=6.92 x 10^{14})

The peak photocurrent scales linearly with field. However, this is not the case with temperature. Figure 4.22 demonstrates that the peak photocurrent does initially increase with temperature but drops off above a temperature that is identifiable with the phase boundary between the discotic and the isotropic.

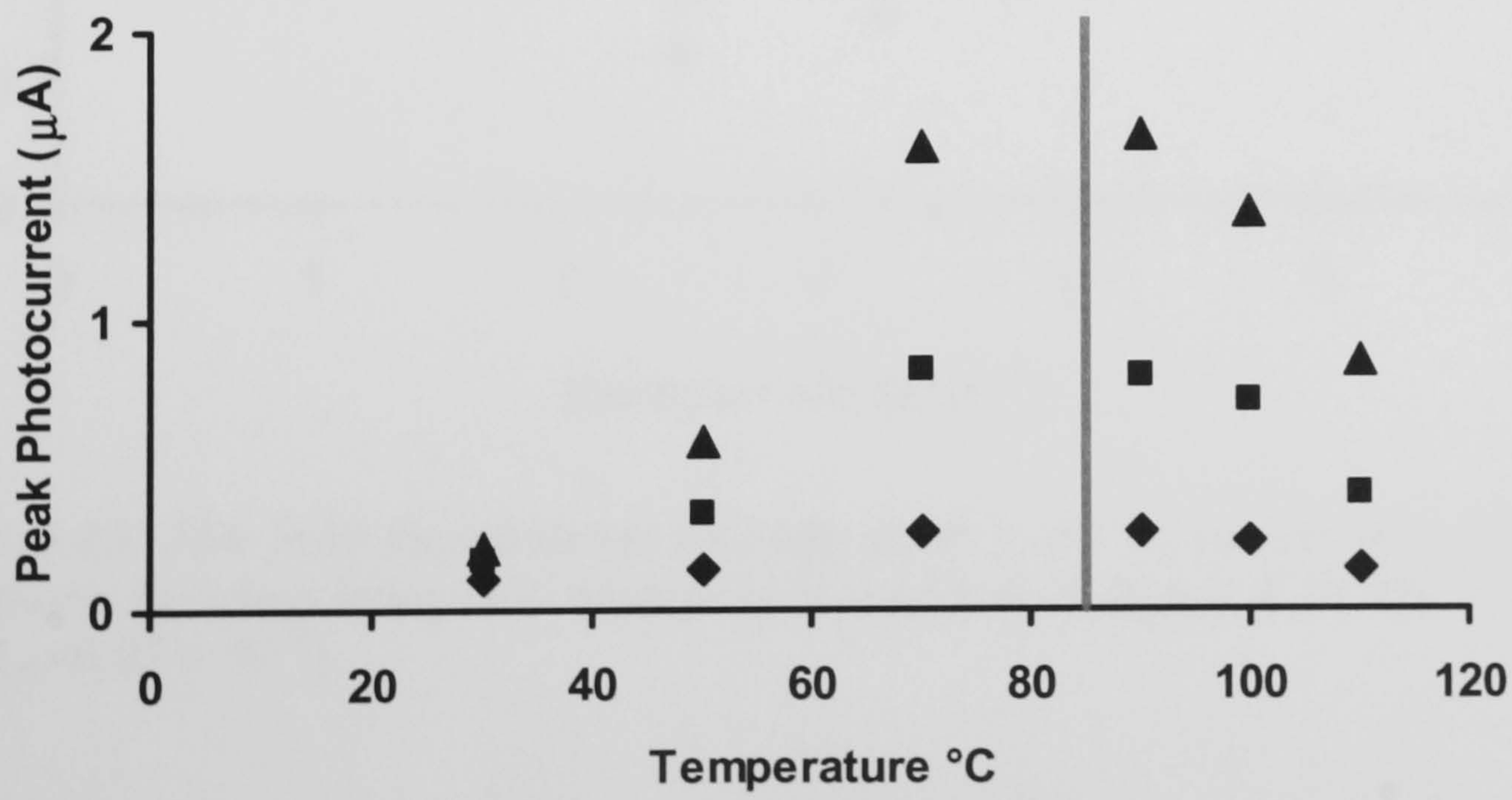

Figure 4.22: Peak photocurrent with temperature at: ◆ = 0.82 MVm^{-1}, ■ = 1.64 MVm^{-1} and at ▲ = 2.50 MVm^{-1}

The grey line in figure 4.22 represents the minimum observed clearing temperature (isotropic phase) for this material (>85°C). When the material enters this phase and loses its crystalline structure, the magnitude of the signal is reduced due to the loss of triphenylene stacking. Although this is to be expected, this phase change causes other effects in the material which are to be discussed in the following chapter.

The product of the quantum efficiency and carrier range can be extracted from the photocurrent signals by using the integrated transient method and equation 2.6. Figure 4.23 demonstrates that this product is super-linear in field and increases with temperature.

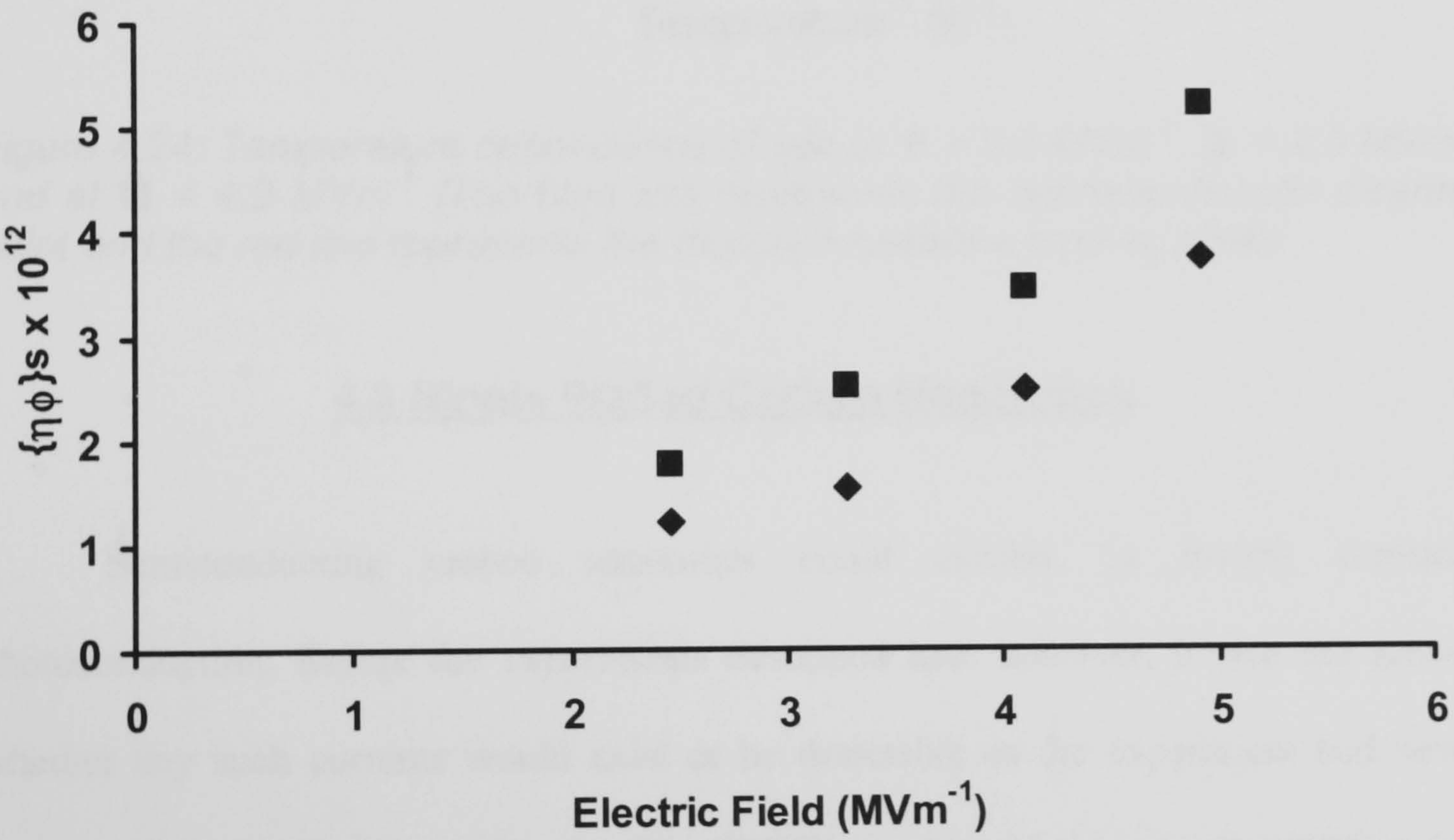

Figure 4.23: The field dependence of {ηφ}s at ◆ = 90 °C and at ■ = 100 °C. Data found by taken integral of signals such as those in figure 4.20. (d = 12 μm and N_{ph}=6.92 x 10^{14})

Figure 4.24 shows how the product *{ηφ}s* varies with temperature. As there are no transits present in this sample, equation 2.6 has been used to find the quantum efficiency-carrier range product. Like the electric field dependence, the photogeneration

product is also superlinear with temperature. Figure 4.24 shows examples at low, intermediate and high fields.

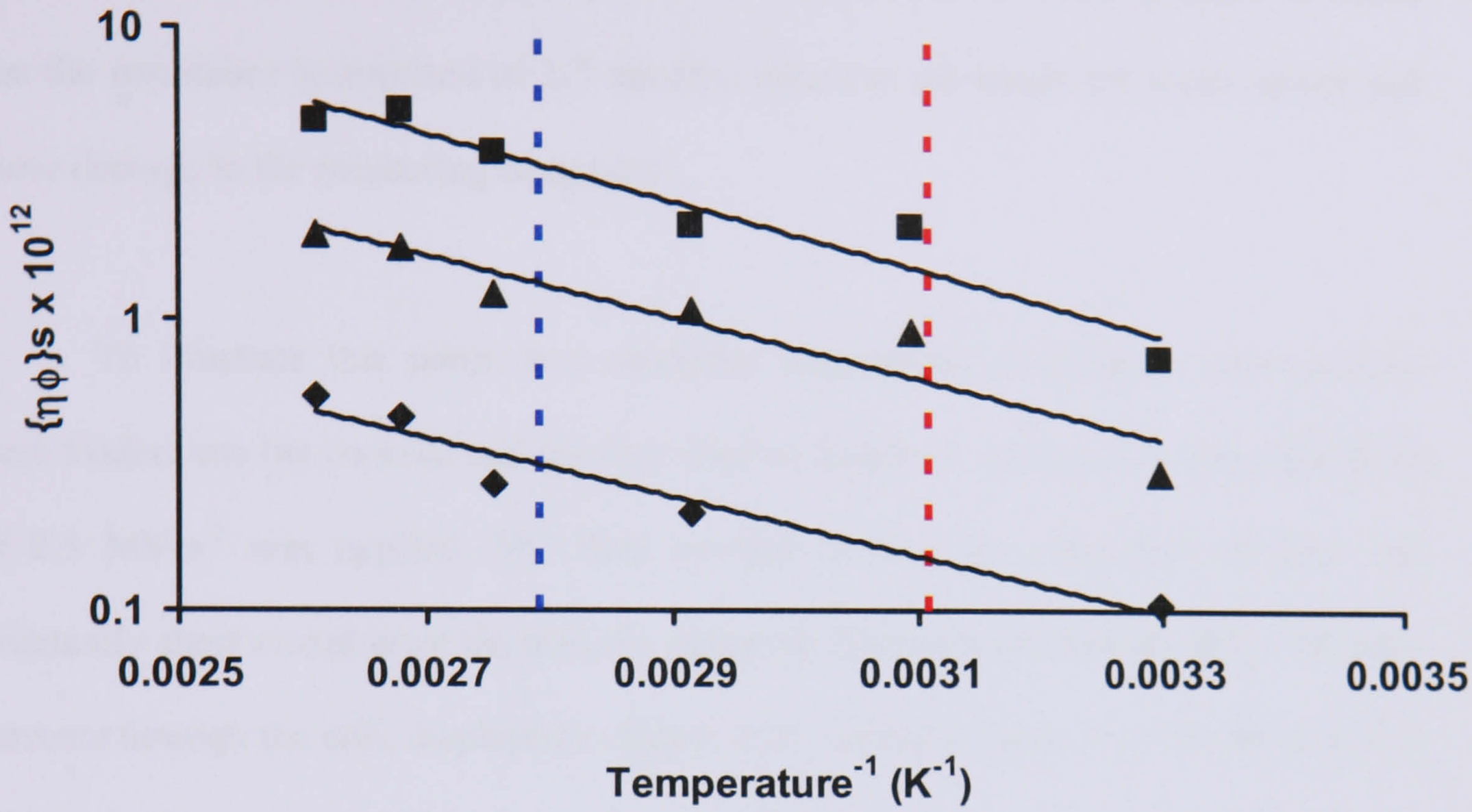

Figure 4.24: Temperature dependence of ηφs at ◆ = 0.8 MVm^{-1}, ▲ = 2.5 MVm^{-1} and at ■ = 4.9 MVm^{-1} (The blue line represents the isotropic/discotic clearing point and the red line represents the discotic/crystalline melting point).

4.3 Single Walled Carbon Nanotubes

Semiconducting carbon nanotubes could exhibit, in theory, transient photoconduction. Before the experiments described here however, it was not known whether any such currents would exist or be detectable as the experiment had never been carried out. Consequently, the first SWNT experiment was not quantitative and was merely verification that the samples showed photoactive behaviour. Further detailed studies were carried out thereafter.

4.3.1 DC Dark Current Evolution

Before a photoconduction experiment was performed, it was prudent to check that the nanotubes (comprised of 1/3 metallic tubes) in oil would not short circuit and cause damage to the measuring equipment.

To illustrate this point, two nanotube suspensions of different concentration were loaded into the co-axial cell (as described in chapter 3, section 3.2) and a DC field of 0.5 MVm^{-1} was applied. The dark currents evolve as a function of time and eventually short circuit once the metallic nanotube filaments are formed [**45**]. The dark currents through the cell, displayed in figure 4.25, were measured by, observing with a digitising voltmeter, the voltage across a 1kΩ resistor in series with the co-axial cell.

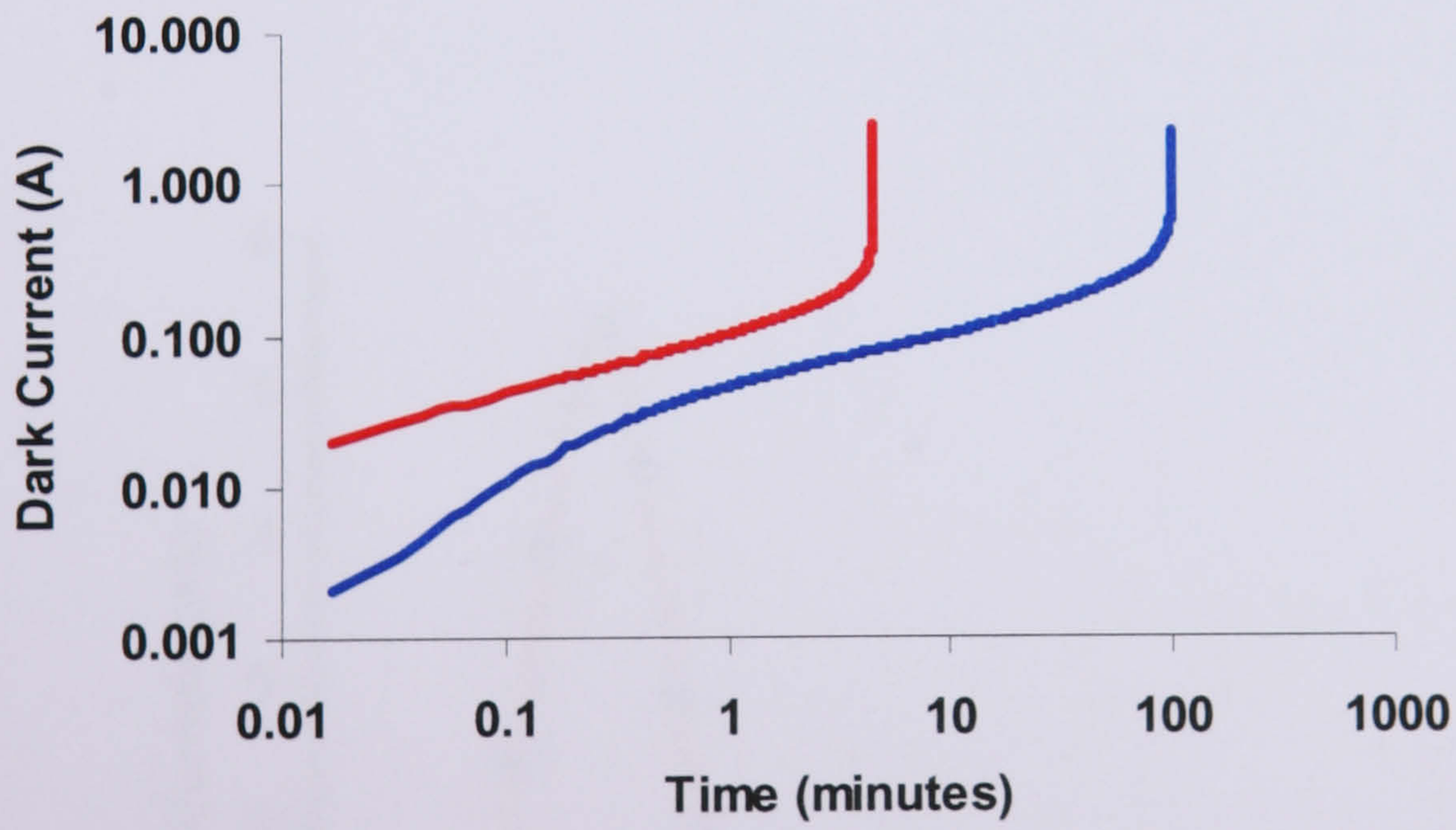

Figure 4.25: Sample Dark Current vs Time (Sample Concentration by mass fraction: Red Line = 10 x 10^{-3}. Blue Line = 2 x 10^{-3})

As shown in figure 4.25, the dark current increased with time until breakdown occurred at which point the power supply cut out. It should be noted that double log plot was necessary to deal with the variation. It is seen that the DC field causes short-

circuiting and breakdown after 290 seconds and 6000 seconds for the higher and lower concentration solutions respectively. At even higher fields, breakdown occurred much more quickly (in the order of seconds). To reduce the risk of this occurring in an experiment with the cell connected to the oscilloscope, the voltage step generator (described in chapter 3) was employed.

4.3.2 Initial SWNT photoconduction studies

The first photoconduction experiment performed was crude, in which an unrecorded concentration of SWNTs of unknown purity were suspended in silicon oil and placed into the co-axial cell. Firstly, pulsed UV light (355 nm) from the Nd:YAG laser was used to illuminate the sample and then the green light (532 nm), with no obvious effects detected. When the infrared light (1064 nm) was used, the following signal was observed (fig 4.26) with the arrival of the light occurring at 1 ns after the trigger event.

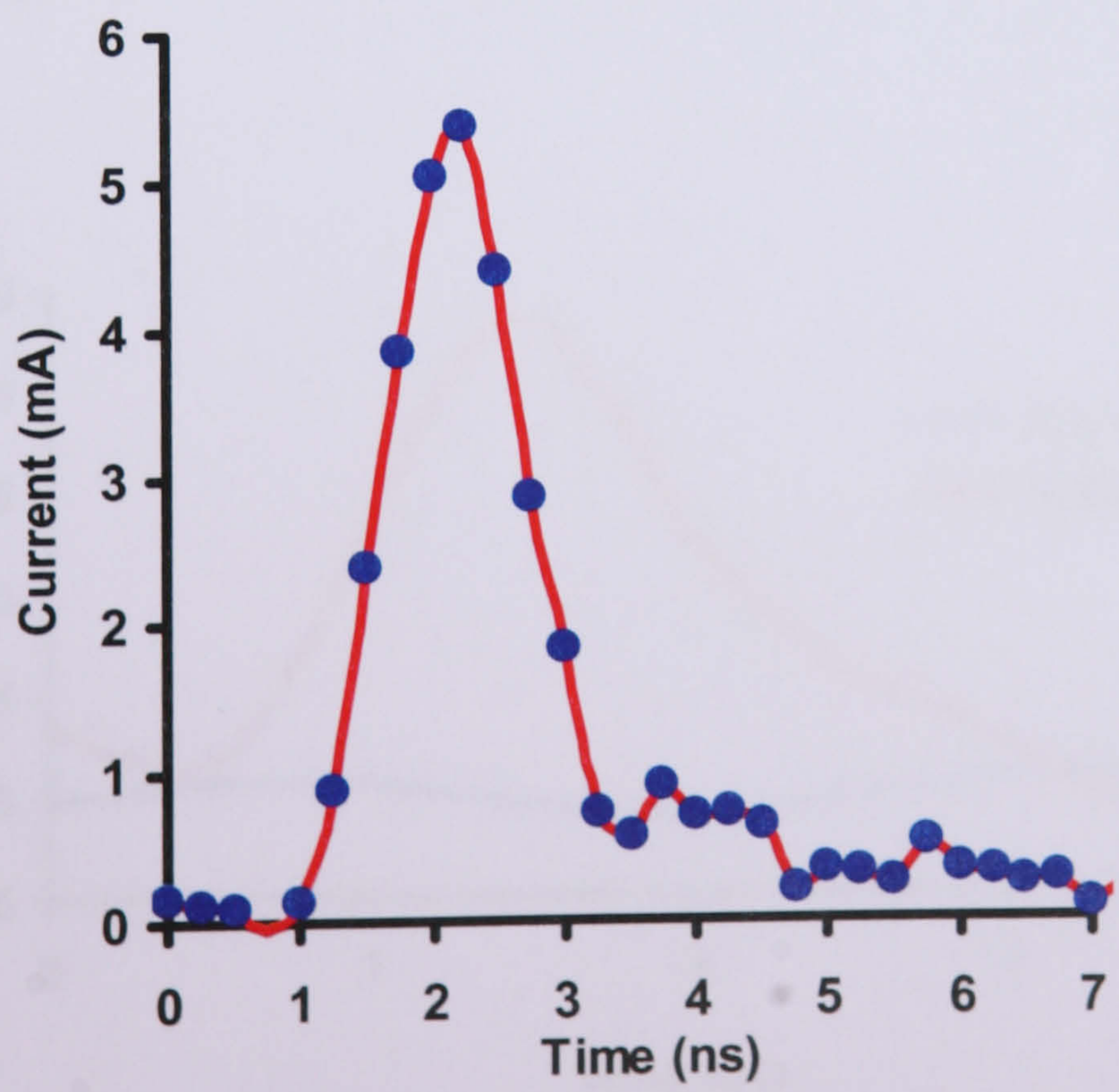

Figure 4.26: Nanotube photocurrent (1 GHz Scope)

Due to the unknown quantities involved, the experimental results were meaningless as no quantitative information could be extracted. However, the experiment proved that the sample in question was indeed showing evidence of photo-induced conductivity. The following research was then to make detailed measurements of this effect.

The next logical step was to ensure that the signal observed was, in fact, a true photocurrent and not an artefact. Replacing the SWNT suspension with a suspension of carbon black in silicon oil tested this and the results are shown in Figure 4.27. The light intensity for the carbon was 4.0 x 10^{14} photons per pulse with the SWNT intensity being 4.6 x 10^{14} photons per pulse.

The SWNT suspension was 0.02% nanotubes by mass. The carbon black sample was 5 times more concentrated at 0.1% carbon by mass. The results imply that the signal seen with the nanotube suspension is a real effect produced by light interacting with the nanotubes.

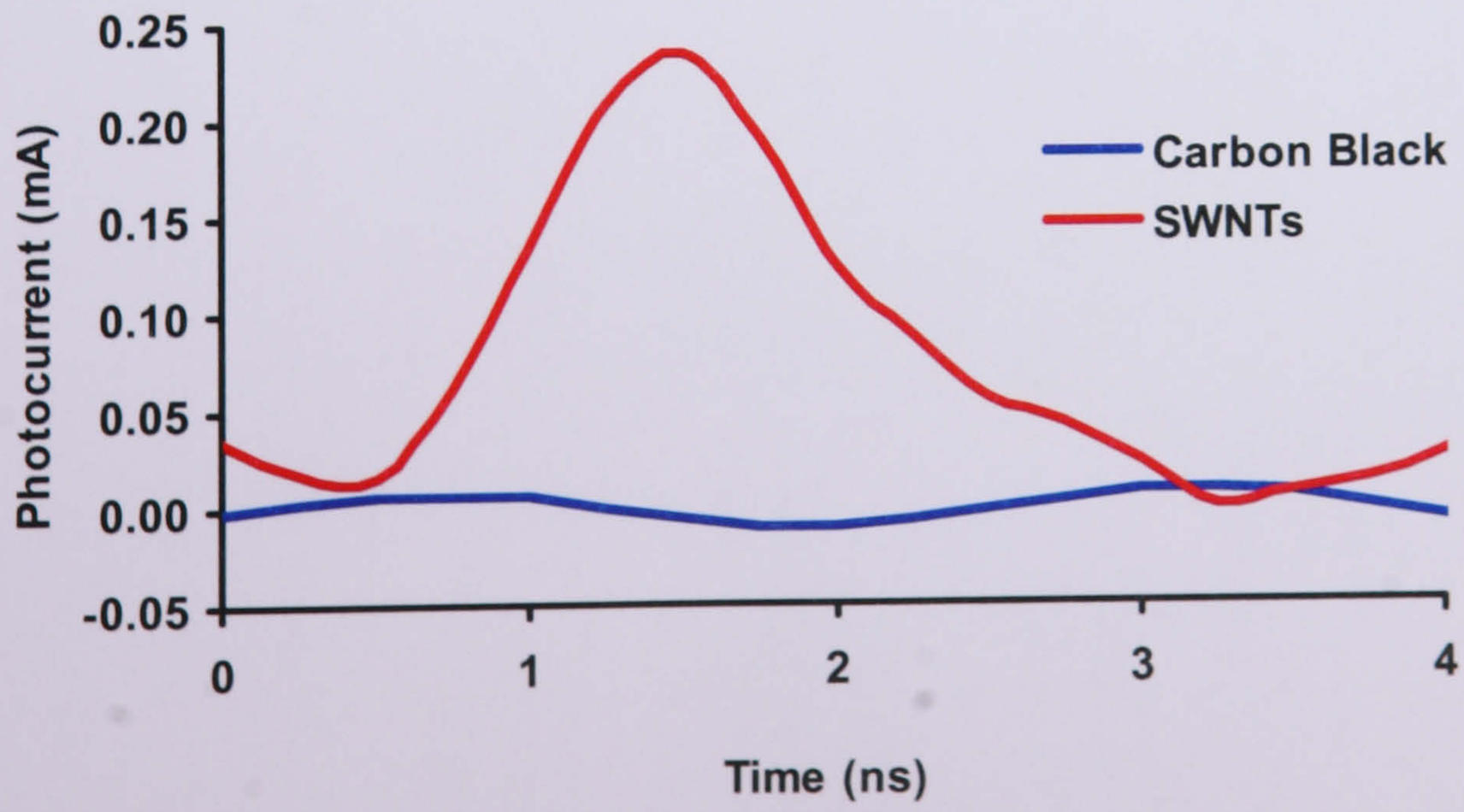

Figure 4.27: Relative Photoconductivity of Nanotubes and Carbon Black Silicon Oil Suspensions @ 1 MV/m Electric Field

The results shown in Figures 4.26 and 4.27 were obtained using an Agilent Infinium 1 GHz digital oscilloscope which has a slower rise time compared to other oscilloscopes used in this project. It is obvious from the signals that the transient nanotube photocurrent is a fast event and it was prudent to utilise oscilloscopes with higher bandwidths (and hence, faster rise times).

A LeCroy Wavemaster oscilloscope with a bandwidth of 3 GHz was subsequently used. During the research project however, 'malfunctions' of the oscilloscope led to temporary replacements of higher specifications from the manufacturer. Some of the data presented here was captured using 5 GHz or 6 GHz oscilloscopes.

It was noticed that at higher sample concentrations, the nanotube suspension presented a considerably reduced resistance. If the results were collected over a longer time range without performing a background subtraction, then a dark current mimicking the shape of the applied voltage pulse can be seen, as demonstrated in figure 4.28.

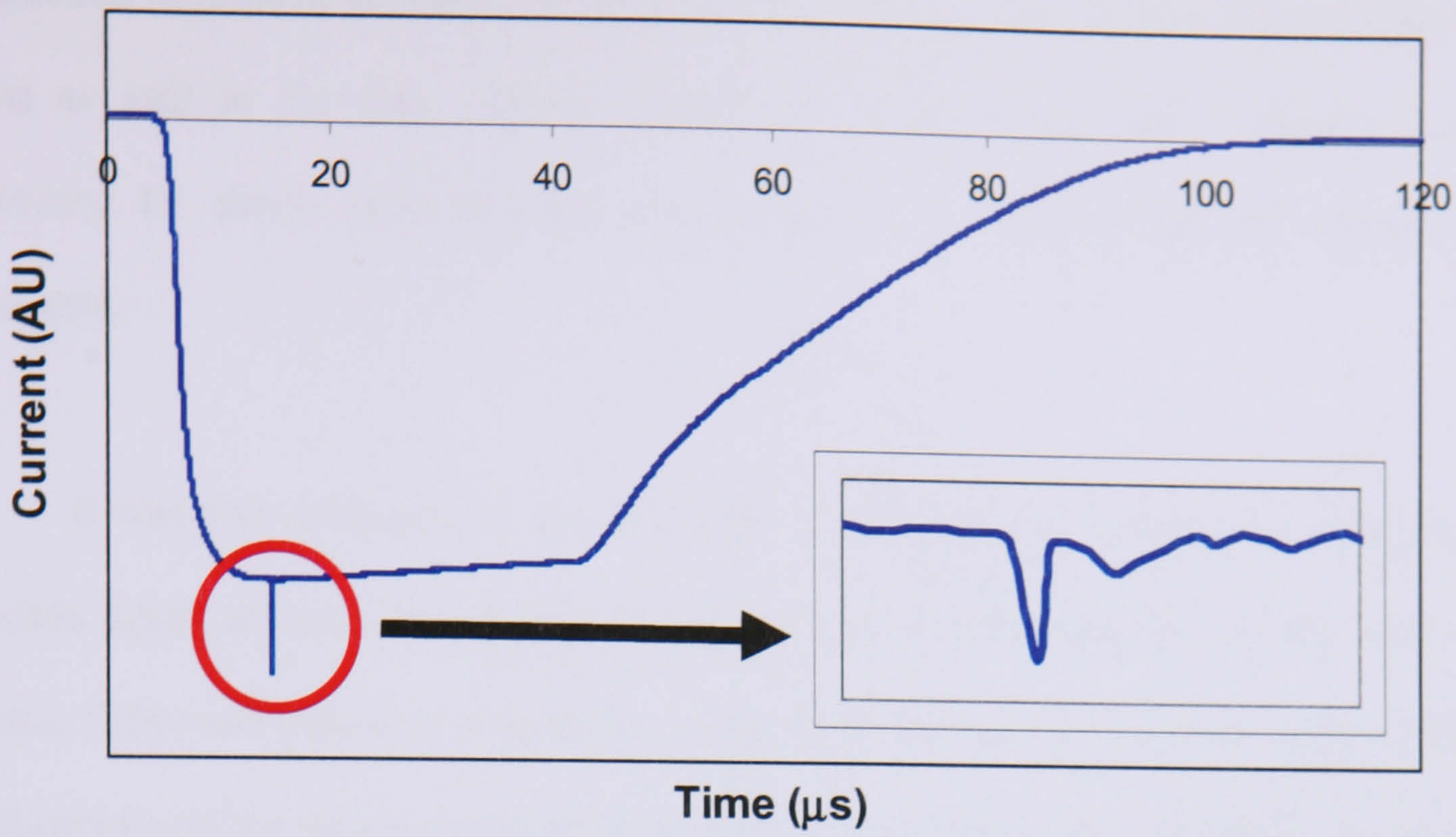

Figure 4.28: Concentrated nanotube sample (~ 1.0 x 10^{-2} fraction by weight) showing both transient conduction and dark currents.

It is interesting to see the transient photocurrent superimposed upon the dark current (see Figure 4.28). The DC conductivity arises due to, presumably, a network of metallic tubes which creates a conduction path from one electrode to the other. The pathway is of high resistance which is most likely due to the presence of poor tube junction contacts and the possibility that some of the pathway is comprised of semiconducting tubes. This is a similar mechanism to that which gives rises to conductivity in figure 4.25.

Great care was taken during the nanotube experiments as it was possible that the network could develop leading to an increase in dark current or possible breakdown. This would cause the oscilloscope to malfunction.

4.3.3 Test of photocurrent stability

All nanotube samples were suspended in the Brookfield polymer oil. All results are averaged (at least 64 times) in order to reduce white noise with a background

subtraction to remove systematic noise (e.g. coherent electromagnetic radiation from the laser) as well as the dark current component. As the signals are averaged, it was necessary to check pulse-to-pulse reproducibility to ensure that the results are consistent.

It was also necessary to check that the signals did not change over time due to possible dipole effects causing alignments, or sample photo-degradation. The laser and electric field were pulsed at a repetition rate of 4 Hz and left to run for an hour with the oscilloscope taking single shot measurements once every minute. The results are shown in Figure 4.29a.

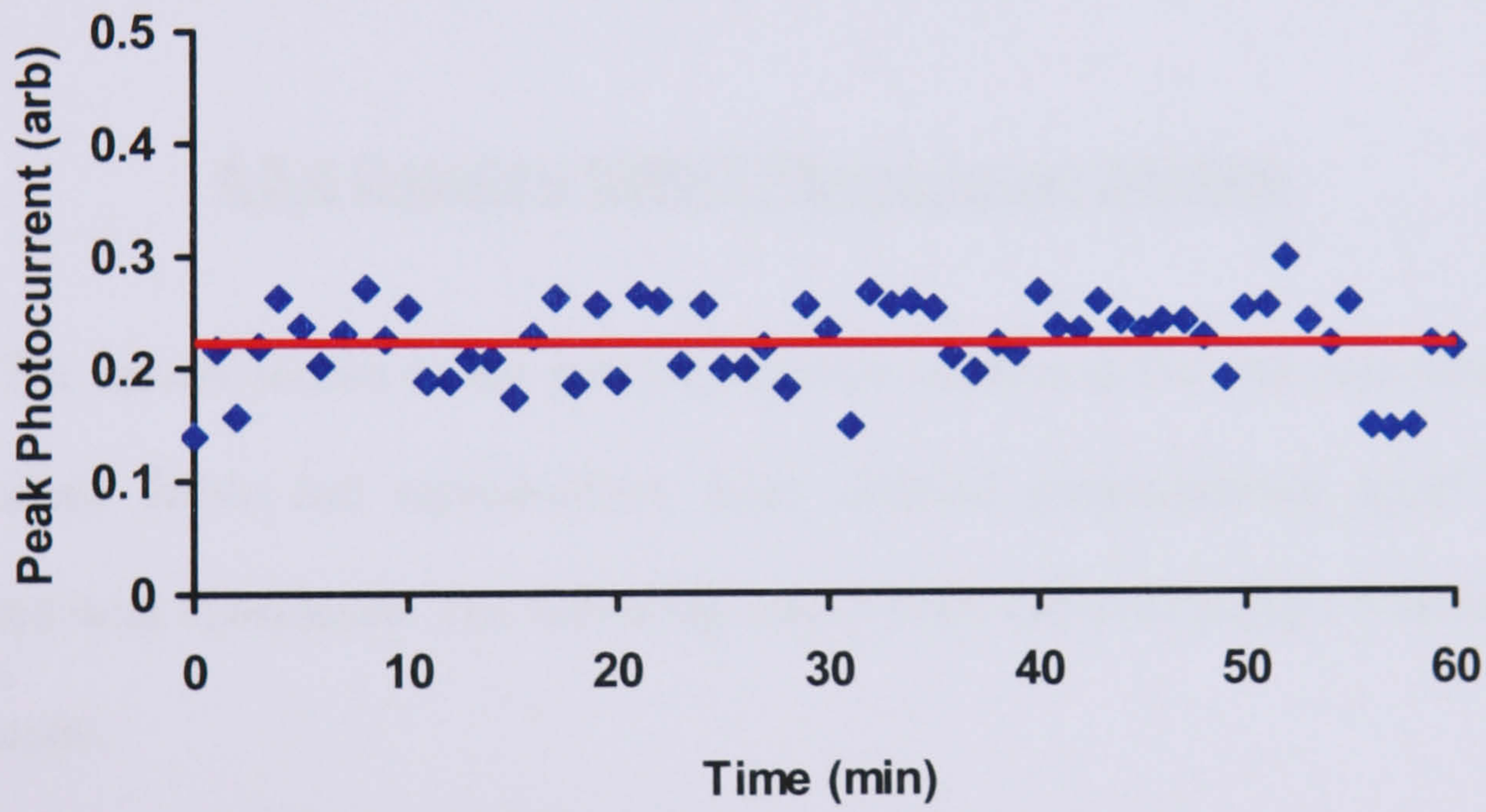

Figure 4.29a: Single shot nanotube signals over time.

As shown, the photocurrents from nanotubes are reproducible and stable over time. The red line represents an average of all 60 points; the variation in signal size per pulse can be explained by fluctuations in light intensity. A histogram of the distribution of single-shot peak photocurrents is shown in Figure 4.29b. The limited number of data points available suggests a skewed Gaussian distribution.

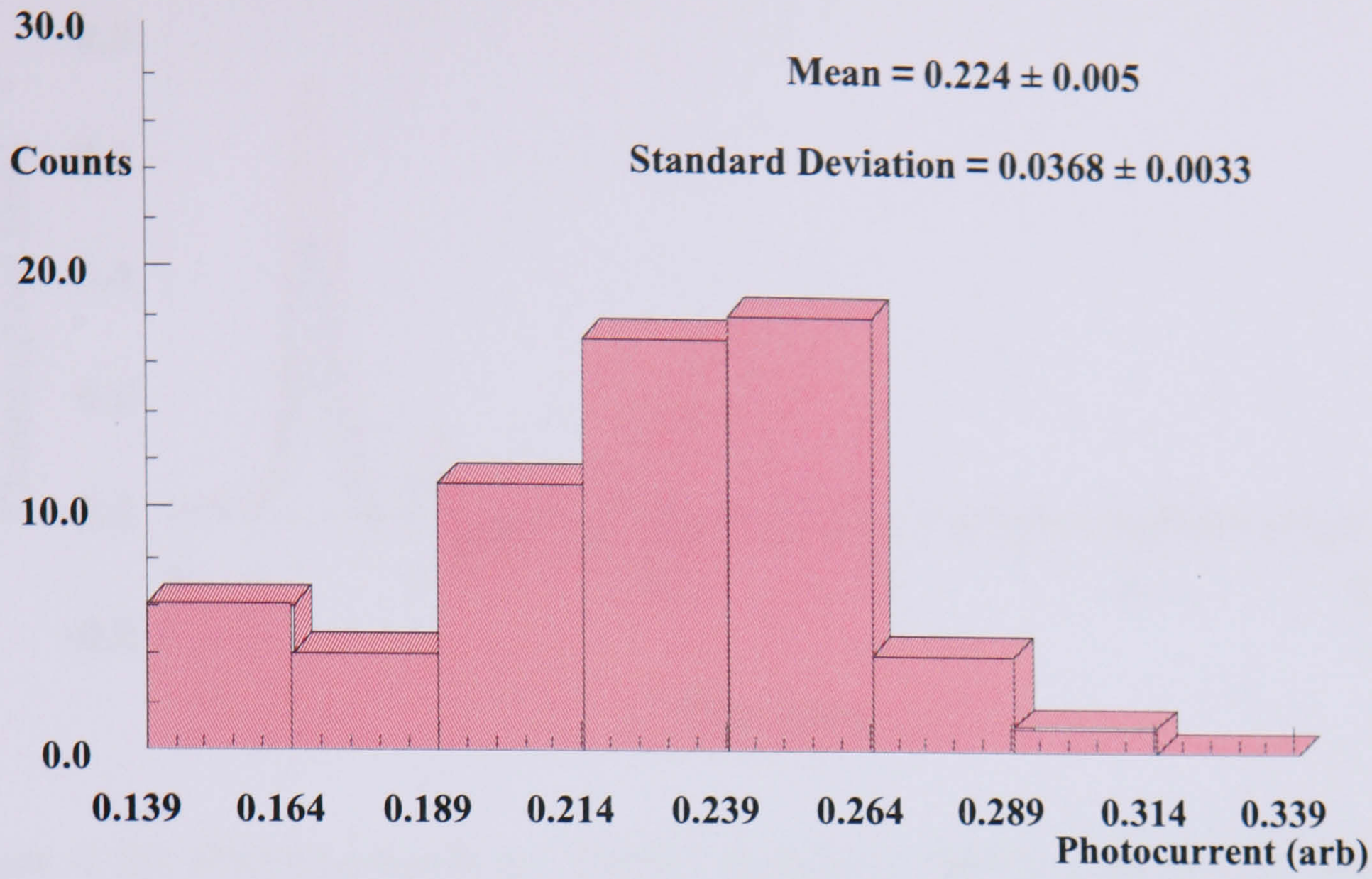

Figure 4.29b: Histogram of nanotube peak photocurrent distribution.

4.3.4 Detailed SWNT Photosignal Studies

The results shown in the previous section confirmed that the nanotube signals were indeed stable and reproducible, more detailed measurements could then be performed with confidence. The following results were captured using a 5 GHz LeCroy oscilloscope.

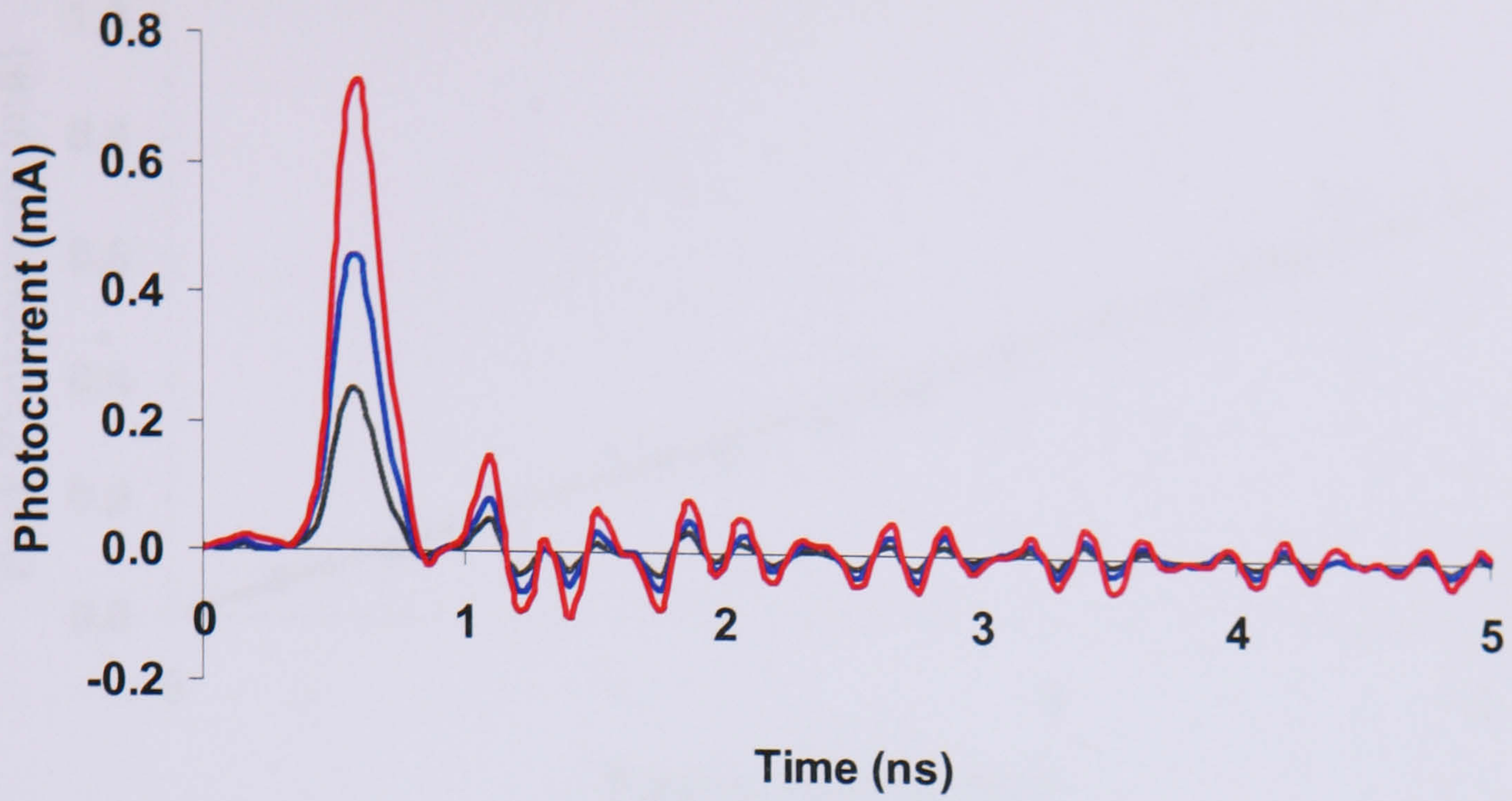

Figure 4.30: Photocurrents for SWNT Sample 1 (Black Line = 1.00 MVm^{-1}, Blue Line = 1.92 MVm^{-1}, Red Line = 2.68 MVm^{-1}, Sample Concentration by mass fraction = 1.9 x 10^{-4}, Average Number of Incident Photons = 3.87 x 10^{15})

Figure 4.30 shows the arrival of the light pulse at the sample after 0.35 ns relative to the trigger origin. The photocurrent has ceased by 0.85 ns for all three fields, implying that the event lasts for a maximum of 500 ps. The shape of the photocurrent around the peak is symmetrical, which implies that even with a fast 5GHz oscilloscope with a rise-time of around 90 ps, the photocurrent is still too rapid to be resolved and is thus limited by the rise-time of the device. However, the integral of the photocurrent will still give the photocharge created so this does not affect any measurements of the quantum efficiency. Figure 4.31 shows that the peak photocurrent scales linearly with applied electric field.

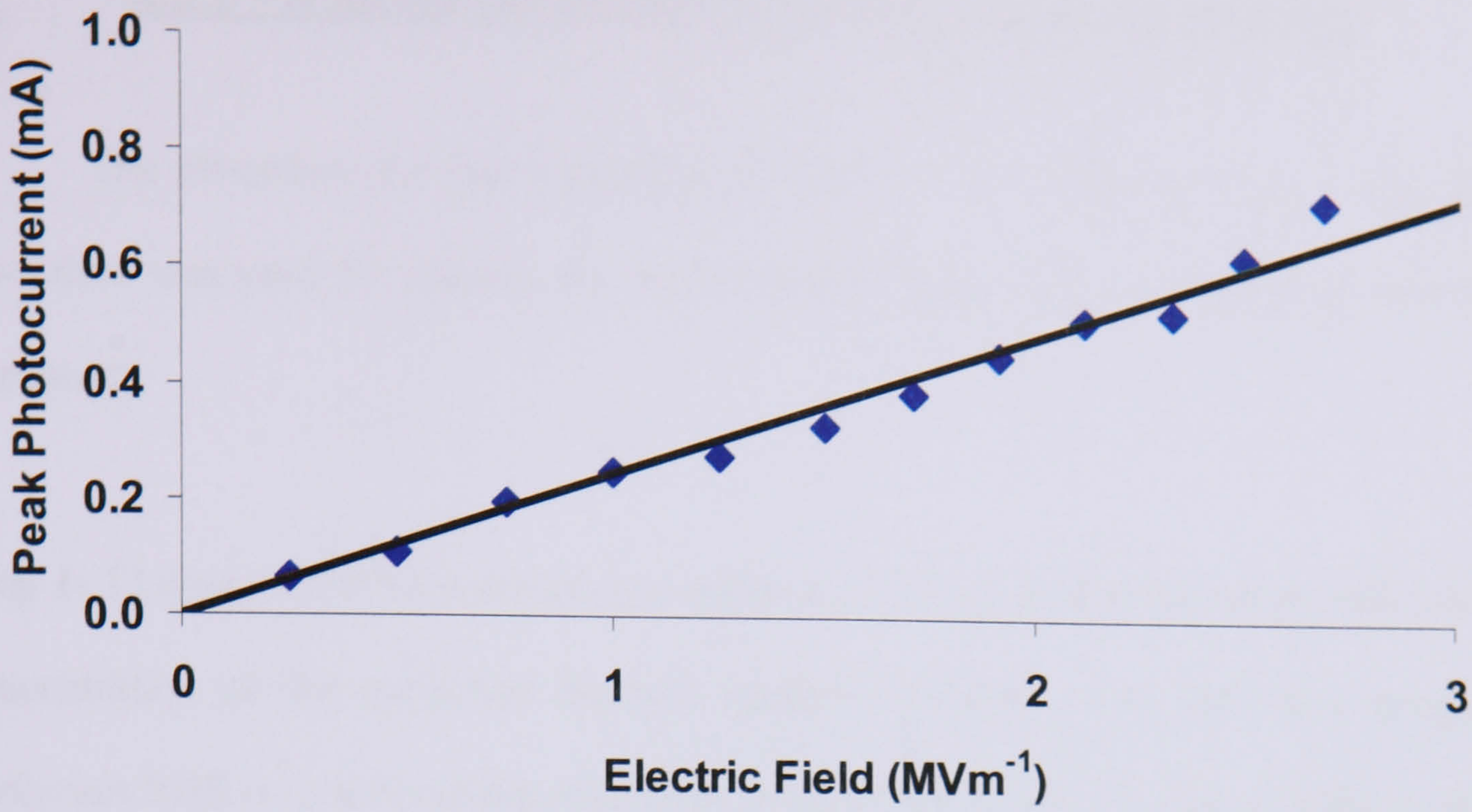

Figure 4.31: Peak Photocurrent vs Electric Field for SWNT Sample 1 (Sample Concentration by mass fraction = 1.9 x 10^{-4}, Average Number of Incident Photons = 3.87 x 10^{15})

The experiment described above was repeated for different sample concentrations, specifically, concentrations of: 1.12 x 10^{-3}, 5.60 x 10^{-4} and 1.90 x 10^{-4} as a fraction of mass giving a respective nanotube sample mass in each experiment of 19.3 μg, 9.65 μg and 3.27 μg. The averaged results of these experiments are given in figure 4.32.

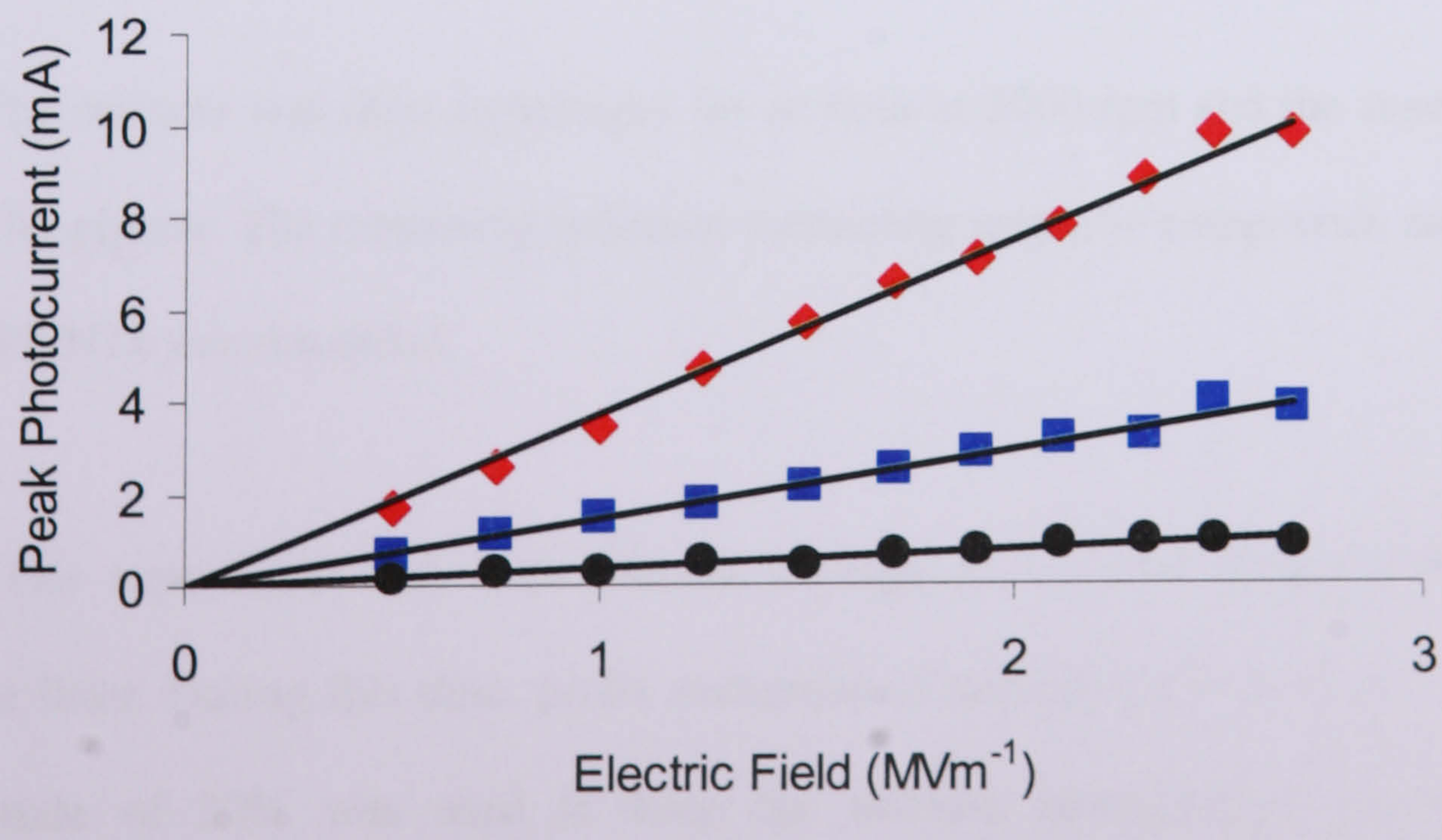

Figure 4.32: Peak Photocurrent versus Electric Field for different SWNT concentrations as a fraction of mass (◆ 1.12 x 10^{-3}, ■ 5.60 x 10^{-4} and ● 8.20 x 10^{-5}).

4.3.5 - A study on the effect of size separated SWNTs.

The procedure for size separation of SWNTs is as follows (Note – The same procedure was used for making the normal SWNT suspensions except steps 4-6 were bypassed):

Step 1: 12.6mg of SWNT material was added to 100 cm^3 of distilled water with a 0.5% concentration of the surfactant Sodium Dodecyl Sulphate. This first step using the surfactant SDS is to achieve the dispersion of nanotube ropes. The use of SDS is one of the better established techniques for achieving such dispersion [**46**].

Step 2: A 500W sonic probe operating at 25 kHz then sonicated this mixture in an attempt to break up the ropes. For half an hour the mixture is exposed to a 5 second on, 5 second off sonic pulse at 30% of the maximum probe power. It is then exposed to a pulse sequence of 5 seconds on, 1 second off at 60% of the maximum power for a total of 15 minutes. During this period the solution will absorb a lot of energy and so an ice bath is used to keep the mixture cool.

Step 3: The mixture was then centrifuged for an hour at 5000 rpm and the supernatant collected by pipette. The remaining sediment containing graphitic compounds and large ropes of SWNTs was discarded.

Step 4: The supernatant was then filtered through a 2 micron Isopore Millipore membrane filter. During this time, probe sonication (2 seconds on 9 seconds off) with an amplitude of 20% was used to keep the mixture homogenised and prevent sedimentation. The material that had passed through the filter paper was retained for further filtrations.

Step 5: The filter was removed and the filtered solid (the material which had accumulated on the paper) was then washed with water and methanol to remove the SDS surfactant. The SWNTs were removed imperfectly from the membrane by sonication of the membrane in either methanol or dichloromethane and then evaporating off the solvent.

Step 6: Steps 4 and 5 were repeated with the collected filtrate on a 1 micron Fluoropore millipore membrane filter and then on a .45 micron Millipore membrane filter.

Step 7: The remaining size separated SWNTs were then dispersed into oil by sonication with the probe for approximately 10 minutes at an amplitude of 70% and a pulsation of 5 seconds on, 5 seconds off.

Note: Filtration steps individually could take 12-18 hours continuously to complete.

An average nanotube of length, L = 1 μm and 1.4 nm diameter has a molecular weight of 1.95×10^{6} and a mass of 3.23×10^{-21} kg. The density of the polymer oil is 0.87 g/cm^{3}. Our cell sample volume is 21.2×10^{-3} cm^{3} which would contain 18 mg of oil. If the cell hosted a nanotube suspension of weight fraction 1×10^{-3}, there would be 5.7×10^{12} nanotubes suspended in the sample.

A nanotube of length 1 μm can sweep out a volume of 5.2×10^{-19} m^{3}. A simple criterion for determining a connecting nanotube network would be if the volume per nanotube is less than the nanotube sphere of radius. A sample with a weight fraction of 1×10^{-3} would have a volume per nanotube figure of: 3.7×10^{-21} m^{3}. This exceeds the

minimum limit by a factor of 140. All the sample concentrations used here are above the minimum limit threshold and so we could be approaching the regime where weak tube/tube interactions could play a role in the experiments.

4.3.6 - Analysis of nanotube tail decays.

From the filtration procedure described previously, we obtained samples from the 1 μm filter paper and the 0.45 μm filter paper. These two samples are crudely size selected with the former having a length distribution containing a relatively higher number of tubes of length between 1 μm and 2 μm in comparison to the 0.45 μm sample which has a higher distribution of shorter tubes in the range 0.45 μm to 1 μm. It was hoped that these differences in length would manifest themselves physically in a photoconduction experiment.

The samples collected from the two filter papers were placed in suspension and the standard photoconduction experiments were performed. Figure 4.33 shows a comparison between the photocurrents measured at 2.68 MVm^{-1}. It was not necessary to normalise the photocurrents as the peaks of both separate experiments were fortuitously similar.

There is a distinct observable difference between the two samples that demonstrates the effect of differing length distributions.

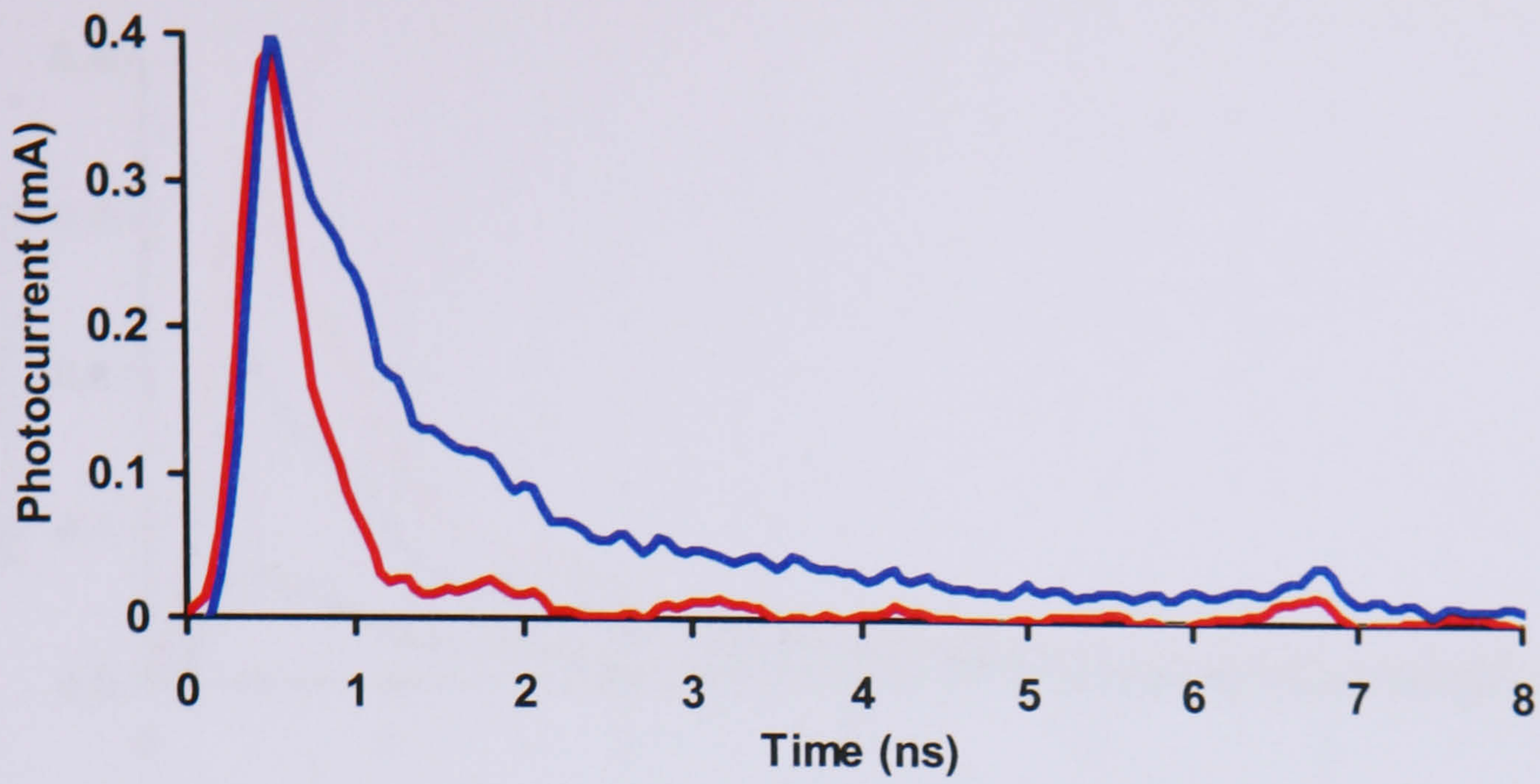

Figure 4.33: Comparison between 1 μm and 0.45 μm SWNT samples (1 μm sample – Blue Line / 0.45 μm sample – Red Line) [0.45 μm sample parameters: Nph = 2.3 x 10^{15}, Sample Conc. = 4.07 x 10^{-5}. 1.00 μm sample parameters: Nph = 2.5 x 10^{15}, Sample Conc. = 1.11 x 10^{-4}.]

Figure 4.33 illustrates that when the average length of isolated nanotubes is increased in a SWNT sample, there is an emergence of an unambiguous photocurrent decay.

It is noted in figure 4.33 that there is a very small second peak at around 6.7 ns. This is due to the mode locked nature of the Nd:YAG laser, where a second pulse is selected by the Pockel cell and appears at a time after the initial peak equal to the round trip time of the laser. Figure 4.34 shows how the magnitude of the photocurrent varies with applied electric field.

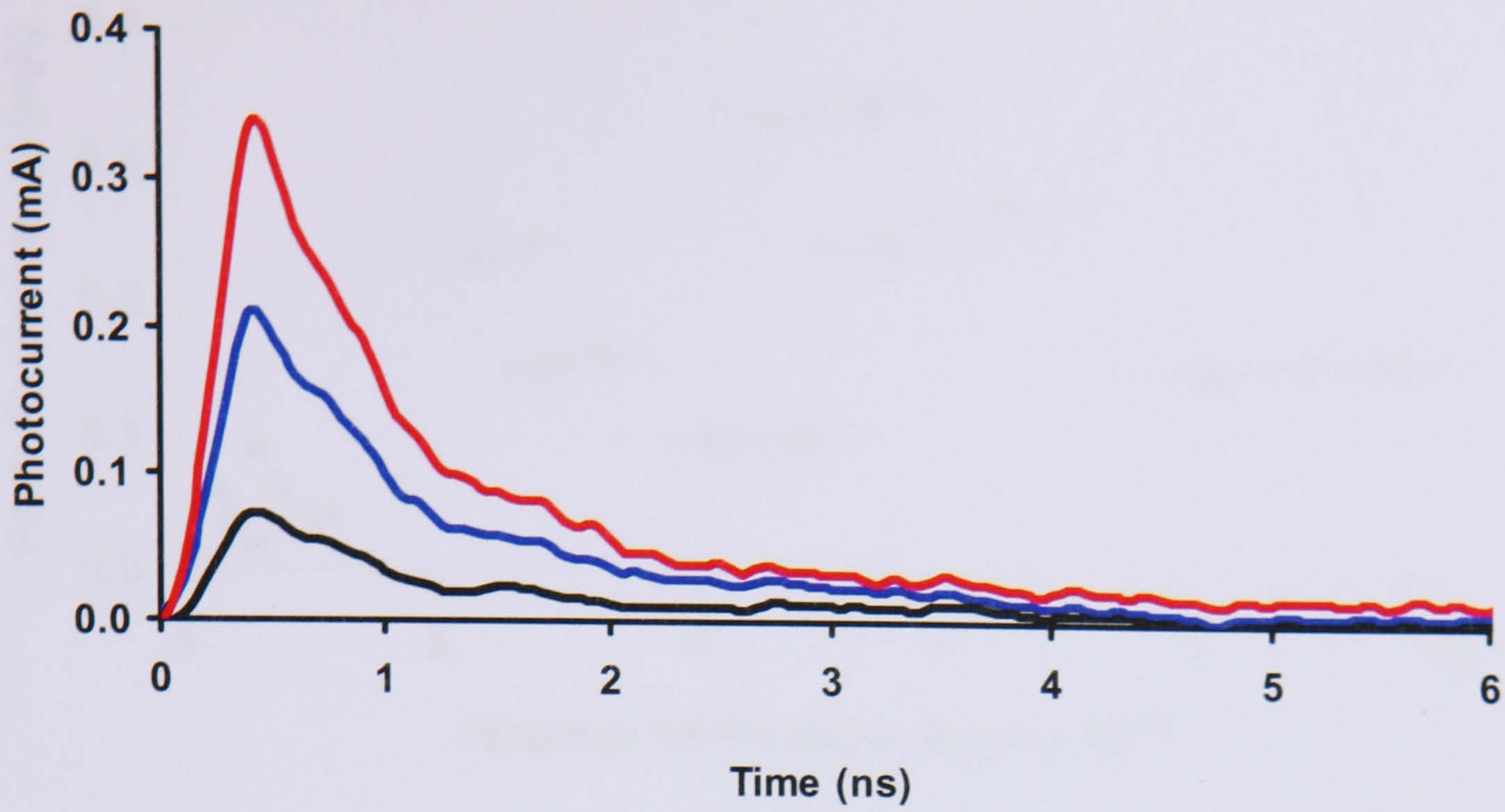

Figure 4.34: Comparison of 1 μm decay tails at different fields (2.68 MVm^{-1} – Red Line, 2.0 MVm^{-1} – Blue Line, 1.0 MVm-1 – Black Line). Sample parameters: Nph = 2.5 x 10^{15}, Sample Conc. = 1.11 x 10^{-4}.]

4.3.7 - Intensity dependence of photocurrents

Further research was performed in experiments measuring the role of light intensity on the peak photocurrents and quantum efficiencies. This was performed at different wavelengths by use of the optical parametric oscillator (OPO) and the ND:YAG. Results from this experiment are shown in fig. 4.35 and a power law was demonstrated.

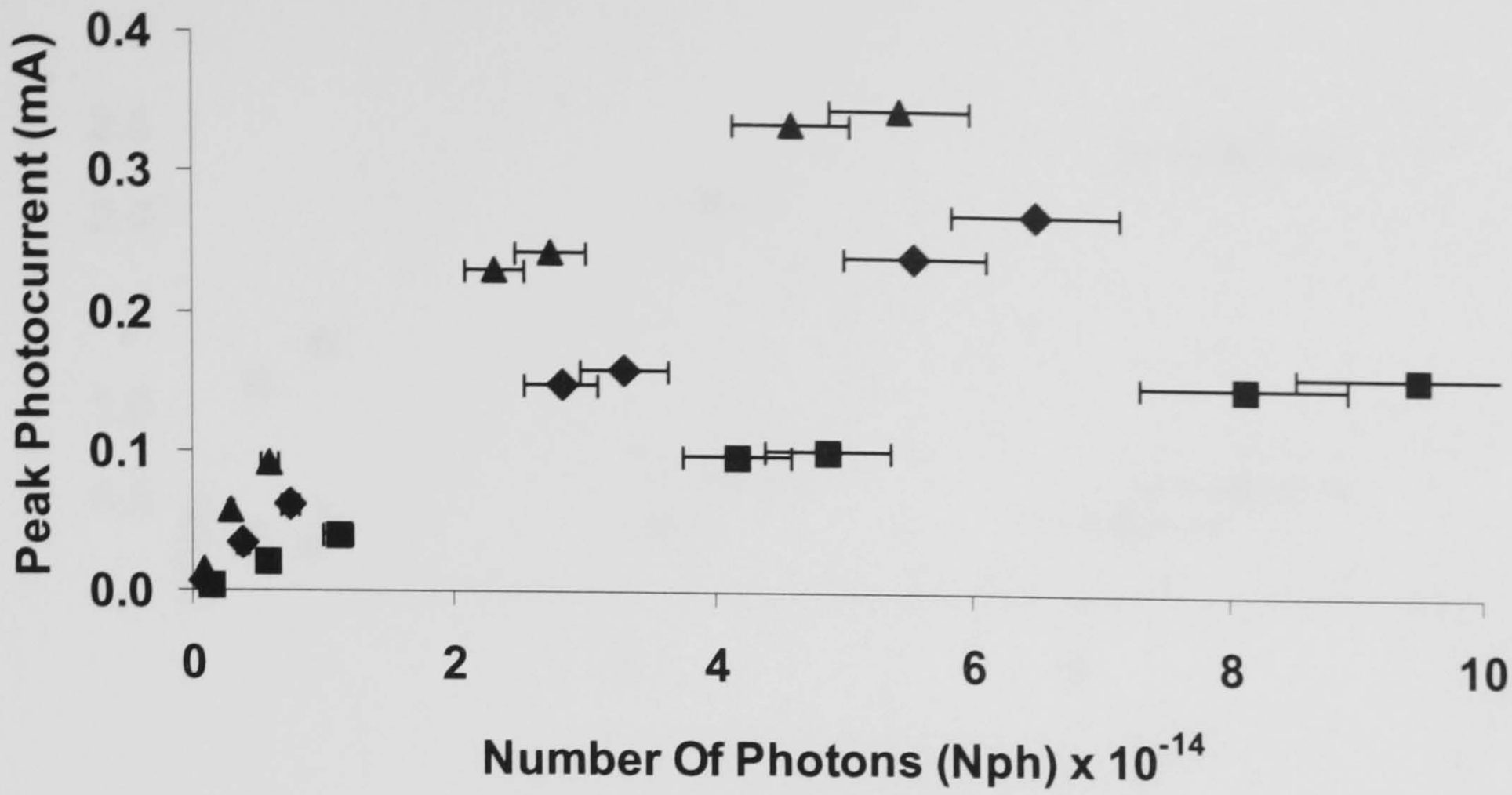

Figure 4.35: Peak photocurrent vs. Light Intensity as wavelength is varied (▲ = 1300nm, ◆ =1600nm and at ■ = 1700nm. Sample Concentration by mass = 2.2 x 10^{-4}, Electric Field = 2.7 MVm^{-1})

Figure 4.35 shows a sub-linearity of the peak current with light intensity. The fact that this is so indicates that an interesting phenomenon must be occurring on the nanotubes that could be bi-molecular recombination. This is a process whereby multiple electrons and holes are created in different events and recombination occurs between them (unlike geminate recombination where the recombination occurs between carriers created in the same event). It is also noticed that the peak photocurrent is higher at lower wavelengths. This could be due to resonances in the band-gap excitation energies of the nanotube ensemble. This is to be investigated shortly.

The peak photocurrent sub-linearity with light intensity was further investigated using the monochromatic Nd:YAG laser (1064 nm) due to its output stability at different concentrations (figure 4.36) and fields (figure 4.37 and figure 4.38, which shows a larger range of values).

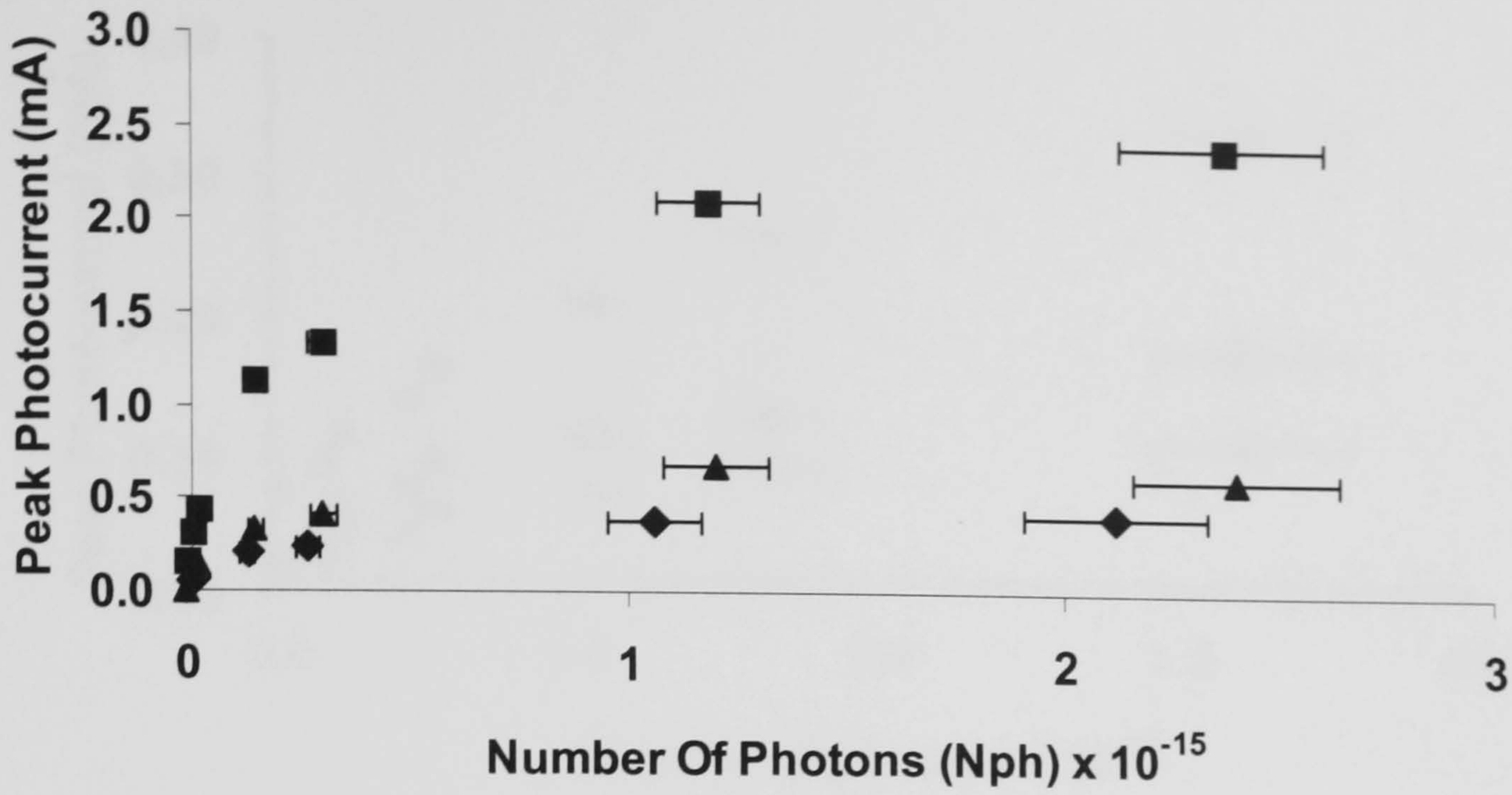

Figure 4.36: Peak photocurrent vs. Light Intensity as concentration by weight fraction is varied (■ = 3.00 x 10^{-4}, ▲ = 1.61 x 10^{-4} and at ◆ = 0.81 x 10^{-4}. Electric Field = 2.7 MVm^{-1})

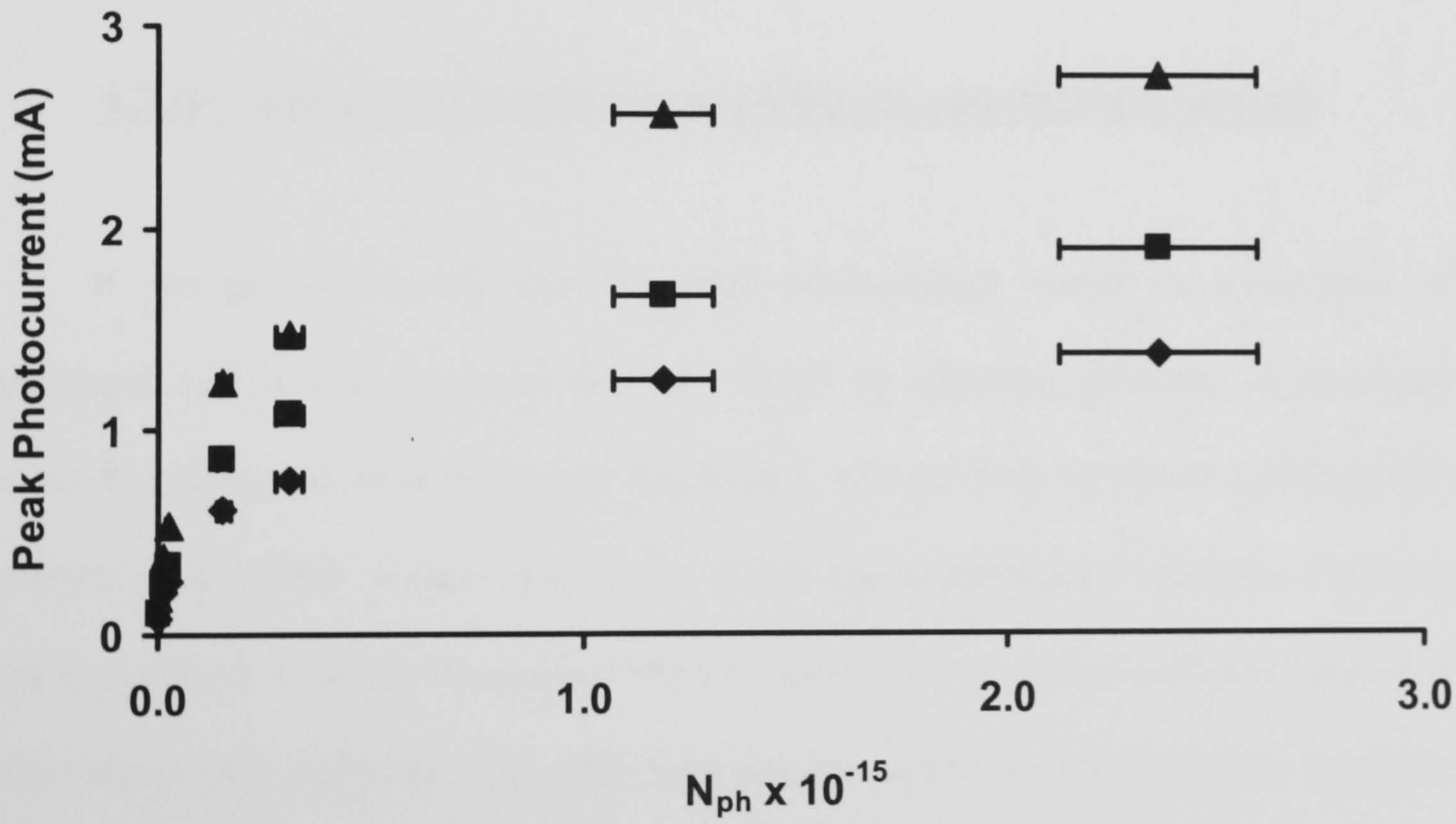

Figure 4.37: Peak photocurrent vs. Light Intensity as field is varied (▲ = 2.32 MVm^{-1}, ■ = 1.50 MVm^{-1} and at ◆ = 1.00 MVm^{-1}. Sample Concentration by mass = 3.0 x 10^{-4})

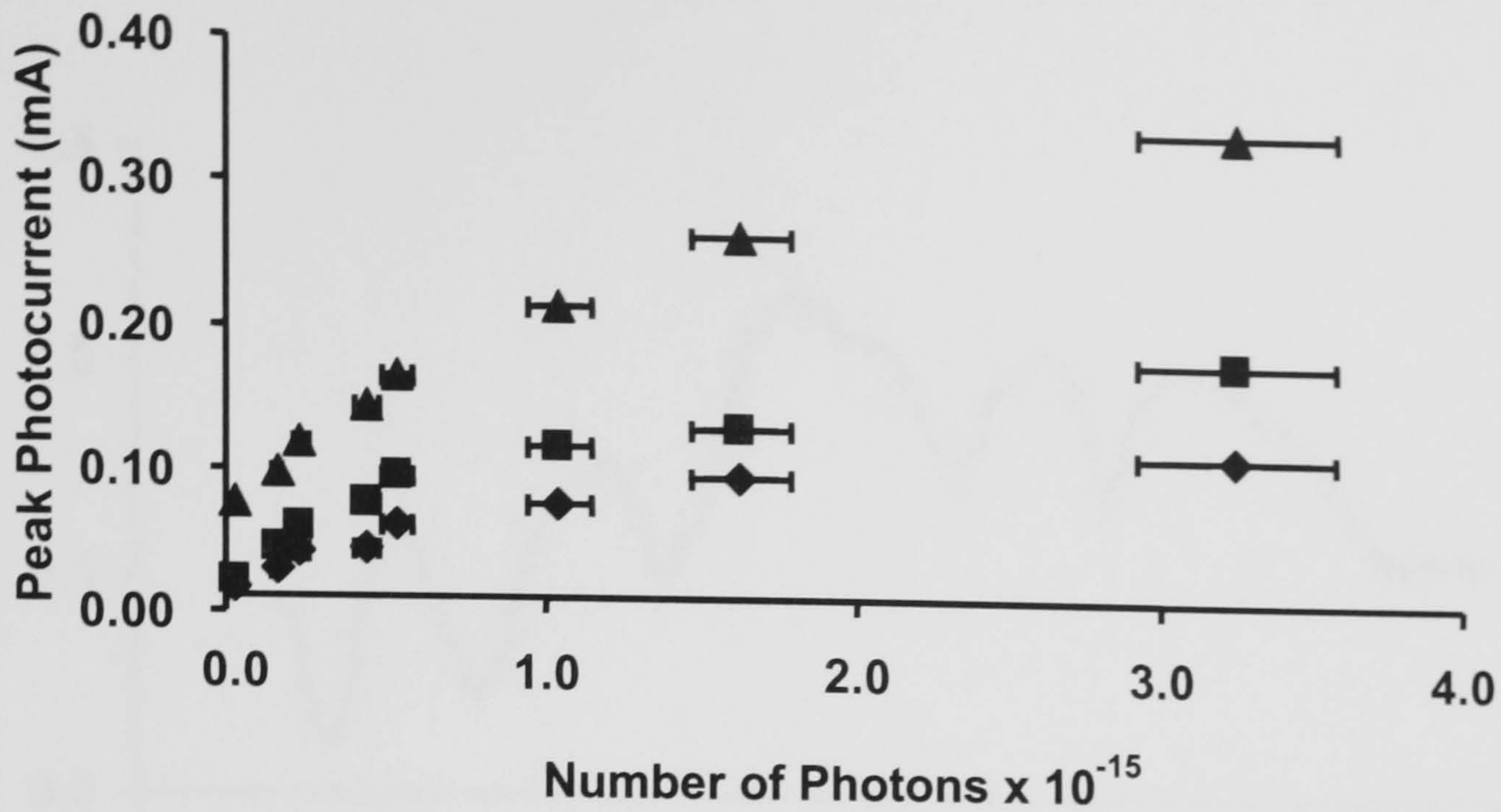

Figure 4.38: Peak photocurrent vs. Light Intensity as field is varied (▲ = 2.68 MVm^{-1}, ■ = 1.50 MVm^{-1} and at ◆ = 1.00 MVm^{-1}. Sample Concentration by mass = 2.2 x 10^{-4})

4.3.8 – Spectral Dependence of Nanotube Photocurrents

It was noticed earlier that the peak photocurrent varied as a function of wavelength and it was proposed that this could be showing evidence of band-gap excitation resonances. In order to test this theory, we will have to obtain a photoaction spectrum of a SWNT sample suspension using our experimental methods. Previous work by Levitsky et al has investigated the DC conductivities and absorbance spectra of SWNT films [**47**]. Fujiwara et al [**48**] have also presented a photoexcitation spectrum using pulsed light on SWNT films.

In order to produce our own measurements, it was necessary to characterise the light intensity that reaches the nanotubes (from the OPO and through the quartz rod) as a function of wavelength. This was performed carefully and the results are shown in figure 4.39.

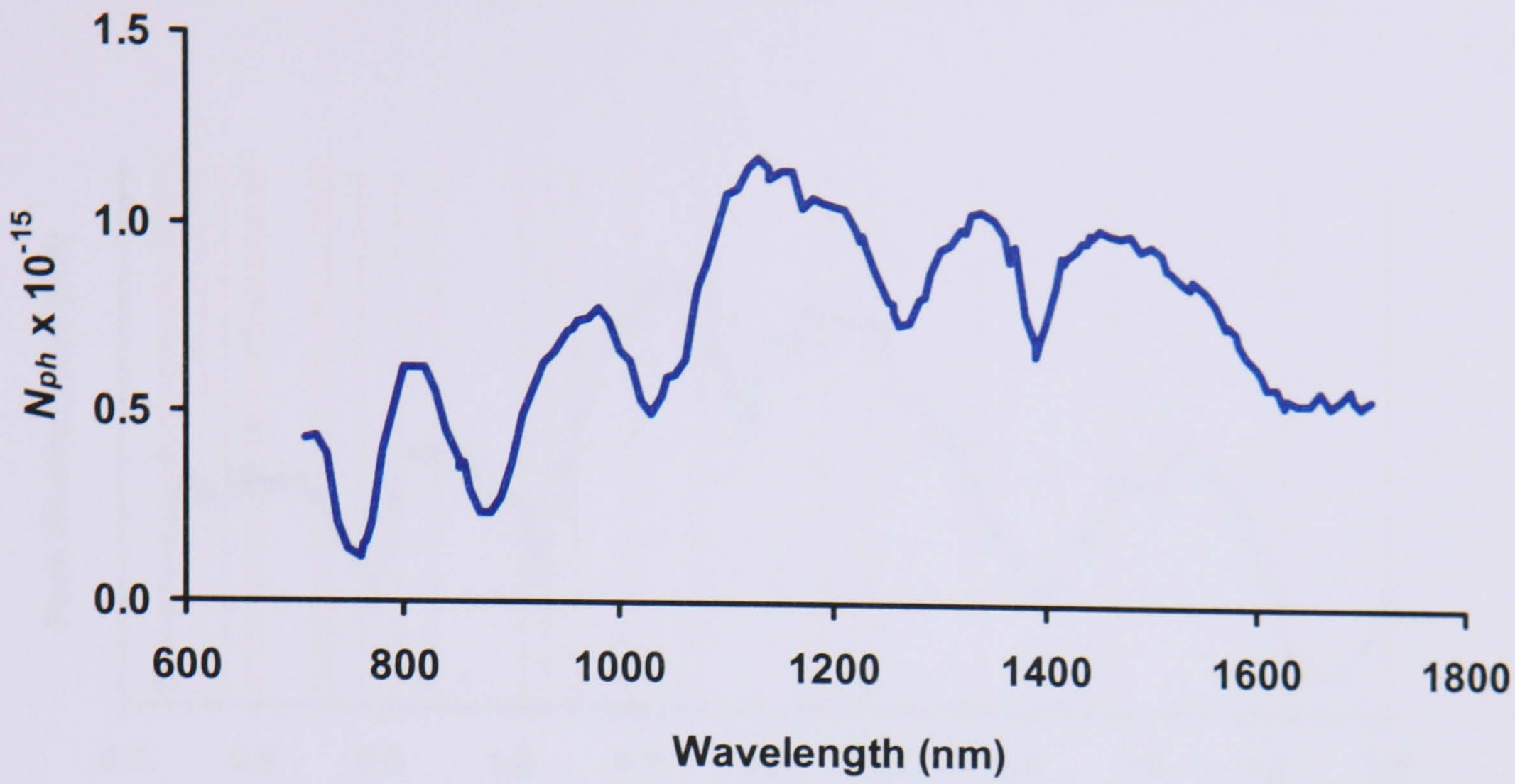

Figure 4.39: Light Intensity vs. Wavelength for OPO laser.

As shown in figure 4.39, the light intensity from the OPO fluctuates significantly over the range shown. The increase in photocurrent at different wavelengths observed in figure 4.35 is matched by the incident light intensity from the OPO. The significant variations in intensity at different wavelengths lead to difficulties in obtaining a photoaction spectrum on a material whose behaviour on light intensity is very non-linear.

A photoaction spectrum was attempted and consisted of an averaged peak photocurrent taken at different wavelengths (with inherent variations in light intensisty). Vertical lines were then overlaid on the 'photoaction' spectrum corresponding to photon energies where one would expect to see band gap resonances [**Appendix 2**], that is, the band gaps at different nanotube diameters where the ***(n,m)*** indices indicate a semiconducting tube (as calculated by equation 3.1). However, due to the large fluctuations in OPO intensity at different wavelengths and the absence of an adequate

normalisation procedure of the sub-linear light dependence on photocurrent: the resultant plot showed no conclusive evidence one way or the other (figure 4.40).

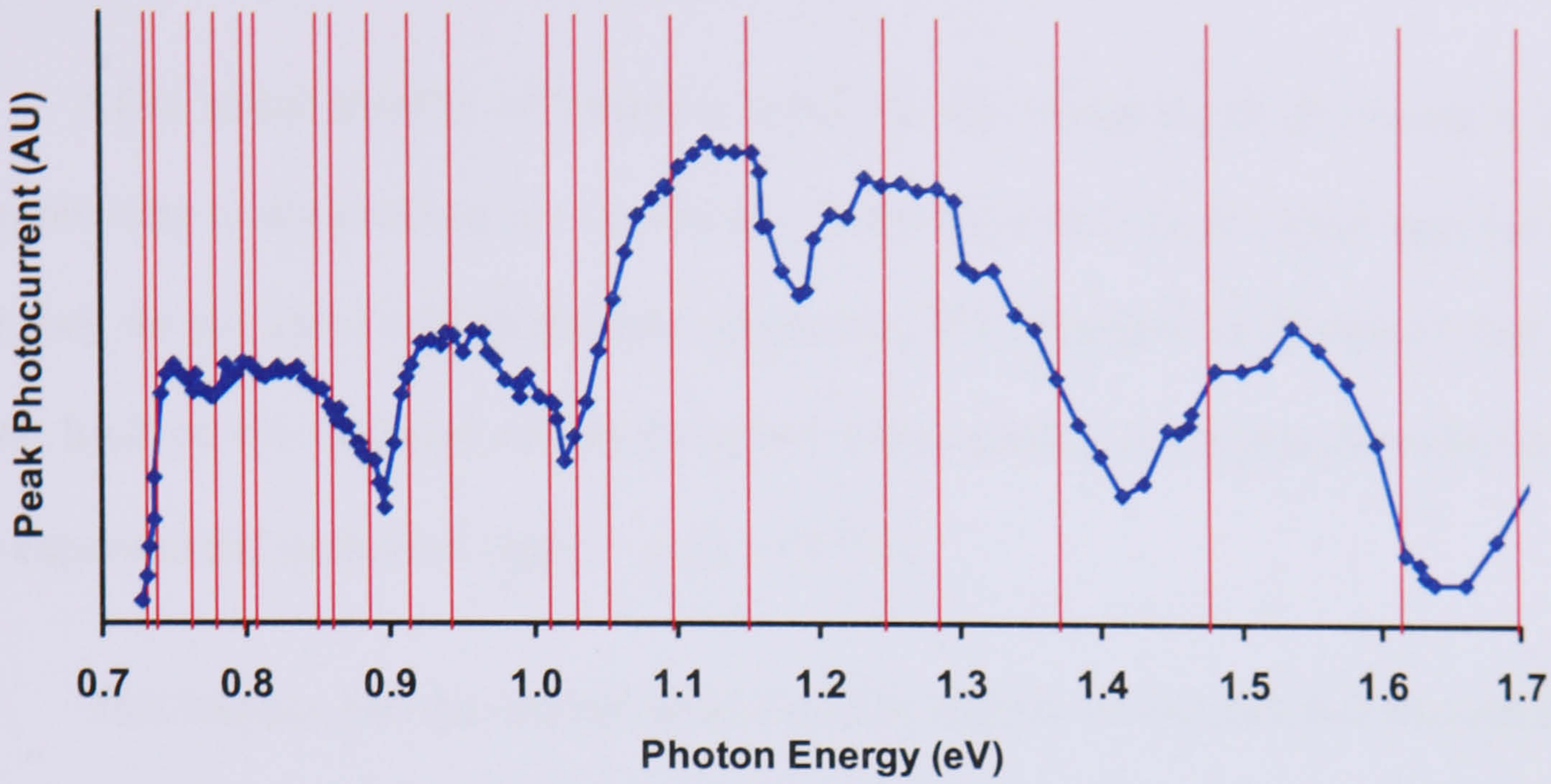

Figure 4.40: Non-Normalised Nanotube Photoaction Spectrum with expected 1st band gap resonances superimposed.

Fujiwara et al have produced a photoaction spectrum from SWNT films. Their results show clear peaks at 0.7 eV and 1.2 eV (the first and second band gap resonances for a 1.4 nm diameter semiconducting tube). However, their resolution was low and when investigated in more detail; their spectrum becomes inconclusive due to the large fluctuations in light intensity and the corresponding large fluctuations in photocurrent.

Chapter 5 – Discussion of Results

5.1 Encapsulated Polymers

After many months of intensive work on the encapsulated polymers, it was disappointing to not produce any conclusive results from the samples other than the fact that they do not show any photoactive properties. We calculated in Chapter 4 that the lower limit on the quantum efficiency/carrier range product for signal detection using our experimental setup was $\{\eta\phi s\} > 1.63 \times 10^{-16}$ m.

This implies that the encapsulated polymer signals are beneath this threshold (if they exist at all). Possible reasons for these null results are to be addressed in the following sections.

5.1.1 - Do the zeolites contain photoconductive material?

The first and most obvious step was to ensure that the filled zeolite samples obtained actually contained active material. We were able to compress a sample of material, specifically the sample JT6 (Polyacetylene in Faujasite at C=18.47%, H= 1.87%), in a KBr disc and take an Infra-Red transmission spectrum by using a Perkin-Elmer System 2000 FT-IR spectrophotometer. The results were normalised to the spectrum found from a pure KBr disc. The results from this are shown in figure 5.1.

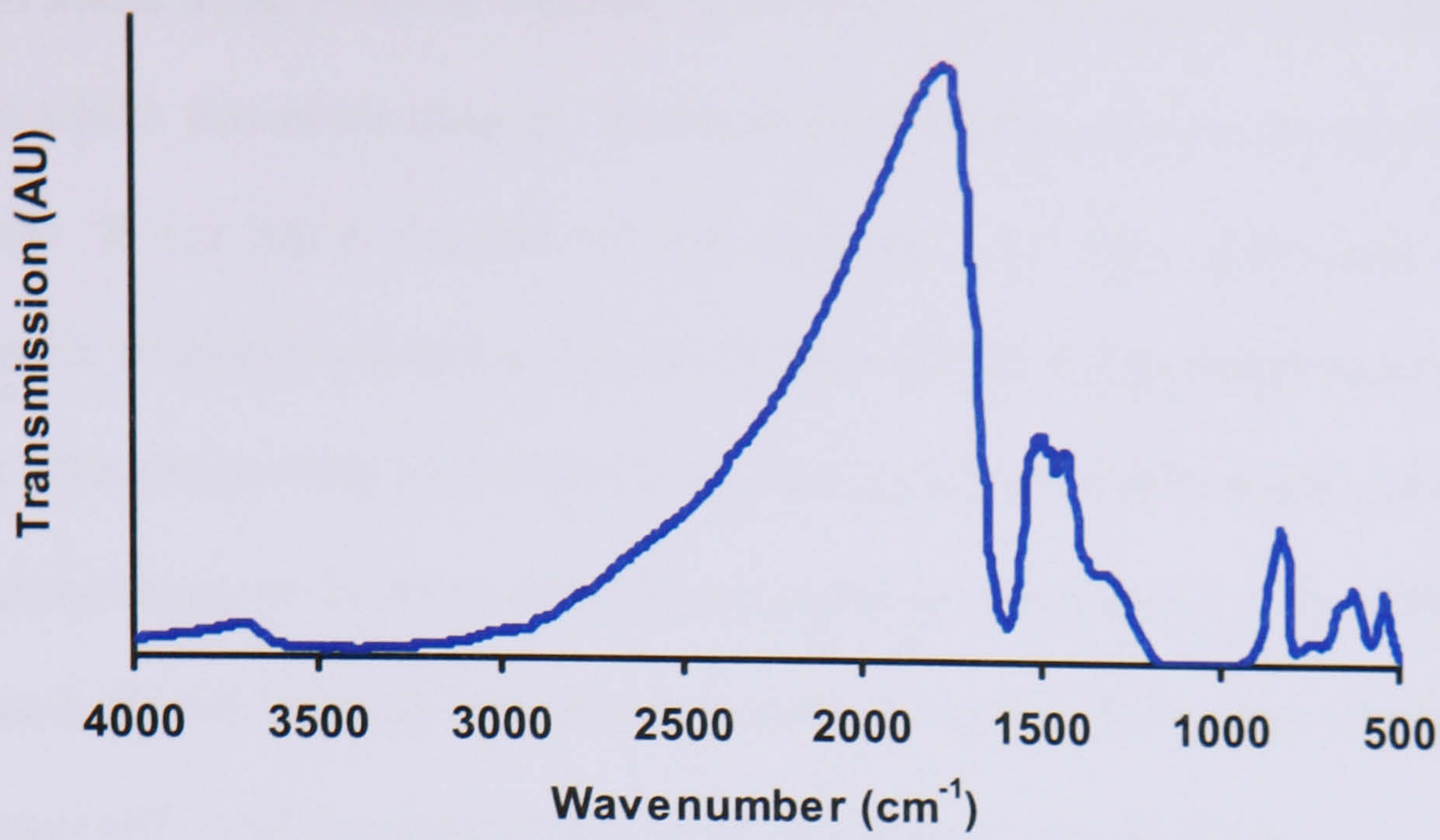

Figure 5.1: IR Transmission Spectra of sample JT6

As shown in figure 5.1, there is a noteworthy absorption at around 1588 wave numbers, which corresponds to the carbon double bond resonance (C=C) of ~ 0.2 eV. This is evidence that a polymerisation process has occurred within the zeolite. The supplier of these materials, Prof. David Cardin, has used more advanced means confirming that the polymerisation reactions have taken place in-situ **[49]**.

5.1.2 - Is light able to penetrate the zeolite structure?

The IR transmission spectrum confirms that light is able to penetrate the zeolite structure and excite the material. The transparency of the zeolites is further confirmed by fluorescence studies on the encapsulated polymers carried out by David Cardin at Reading **[50]**.

5.1.3 - Are the polymer chains long enough to produce measurable carrier separation?

As the polymerisation takes place in-situ, there is no valid method of characterising the length distribution or molecular weights, although there was some

discussion about using NMR to find the ratio of repeat molecules to chain terminating molecules which was never realised. As the length distribution is not known, this poses a problem. If the chain lengths of the polymers are very short then transient photocurrents will be very rapid as the carriers traverse the length of the chain and come to a stop. This event could be too fast to be captured by the oscilloscope and too small for integrated charge to be measured as a consequence of equation 2.4. As demonstrated in Chapter 2, the total charge measured is dependent on the carrier range and again: too short a range will result in a negligible charge that may not be detected.

5.1.4 - Do isolated single chains retard the carrier range?

The ultimate goal of polymerising inside a zeolite channel was to create an array of isolated chain extended polymers and study charge motion on them. There has been some speculation regarding polymer network conductivity and one theory is that geminate recombination is greatly enhanced if the chains are isolated. It is claimed that the photogeneration mechanism is reduced in the case of non-interacting chains due to 1D geminate recombination being highly efficient.

5.1.5 – Other Considerations

An important parameter for the study of photochemistry and photophysics of molecules adsorbed or encapsulated within zeolites is the electric field strength within the supercage. The magnitude of such a field will be dependent on several factors, namely: the net charge on the framework (defined by the Si/Al ratio), the size and shape of the supercage, the presence of any adsorbed molecules and the number and size of the counterions.

The zeolite structure has Al (trivalent bonds) and Si (tetravalent bonds) atoms making up its structure leading to an overall negative charge that is balanced out by cations. These cations are arranged, like the structure of the zeolite, periodically, leading to large periodic electric fields transverse or axial along the channel of the zeolite.

Table 5.1 shows how the zeolite 'Y' (Faujasite) is affected by the inclusion of different counterions **[51]**.

Cation	**Cation ionic radius (Å)**	**Electrostatic field within supercage (V/Å)**	**Vacant space within supercage ($Å^3$)**
Li^+	0.76	2.1	834
Na^+	1.02	1.3	827
K^+	1.38	1.0	807
Rb^+	1.52	0.8	796
Cs^+	1.67	0.6	781

Table 5.1 Internal Electric Fields of Y zeolite [51].

It is clear from Table 5.1 that the electric field within the zeolite, generated by the distribution of cations in the zeolite structure, is relatively large compared to the applied electric field used during the experiments (a factor in the order of 10,000).

This is cause for concern as any excited charges may be strongly attracted and held in these static axial/radial fields. The relatively weak applied axial field may not be sufficient for the carriers to overcome this strong attraction.

Consider now one lone electron created by the photoexcitation of the polymer chain. It will experience the applied external electric field and may begin to move accordingly, but what happens when it encounters the electric field (potential well) of a cation associated with the zeolite structure? It is likely to trap as the force of electrostatic attraction between these two unit charges so close together will be much higher than the force it experiences from the external electric field.

5.1.6 – Conclusions on Encapsulated Polymers

After a thorough investigation of the various samples sent to us from Reading, no conclusive results were found. A full discussion of the points made in this section (5.1) can be found in Chapter 6.

5.2 – Discotic Liquid Crystals

The results from the Discotic Liquid Crystals are to be used to investigate and discuss the photogeneration mechanisms and charge transport properties. Photogeneration in DLC's is not fully understood. Nakayama et al **[52]** have proposed that the mechanisms obey the Onsager 3D model of ion recombination, first encountered in Chapter 2. They have based this on experimental work with HAT6 at a single temperature. We are now able to investigate the applicability of this theory over a wider range of temperatures and materials [**42**, **53**] than available to Nakayama et al at the time.

5.2.1. The applicability of the 3D Onsager Model

Measurements of the photocharge (Q) created versus Electric Field (E) for the DLC materials: HAT6, HAT6:PTP9, HAT11:PTP9 and 2FHAT6 allow us to test the

applicability of the Onsager 3D model. The Onsager 3D model gives the probability of geminate recombination escape as:

$$\phi = \left(1 + \frac{eEr_{kT}}{2kT}\right)\exp\left(\frac{-r_{kT}}{b}\right) \qquad (5.1)$$

where b is the distance at which the electron-hole pair thermalise from each other, E is the applied electric field and r_{kT} is the Coulomb radius, given by equation 2.15.

By differentiation of equation 5.1, we can determine the slope to intercept ratio. Consequently, the slope to intercept ratios of the fitted data in the Q vs E plots are predicted by equation 5.2 as:

$$\frac{S}{I} = \frac{e^3}{8\pi\varepsilon\varepsilon_0 (kT)^2} \qquad (5.2)$$

5.2.1.1 - HAT6

The data contained in figure 4.8 can be used to test the applicability of the Onsager 3D model to this material.

The data gives experimental S/I ratios for the TOF data and DC data. The DC ratio evaluates at 3.47 x 10^{-7} mV^{-1} compared to the TOF experiment which gives 2.37 x 10^{-7} mV^{-1}. Averaging these two results gives 2.92 x 10^{-7} mV^{-1}. This is in good agreement with theory which at this temperature of 85°C and an assumed ε=3, gives an S/I ratio of 2.51 x 10^{-7} mV^{-1}. The experimental results for HAT6 presented here are

consistent with the work carried out by Nakayama et al [52], who measured at 80°C an *S/I* ratio of 3.1 x 10^{-7} mV^{-1} on the same material.

Nakayama et al propose from their results, and agreement between theory and experiment for *S/I*, that the Onsager model is applicable for describing the carrier generation process in the HAT6 discotic liquid crystal. However, their results for *S/I* were only given at one temperature and as seen in equation 5.2, the *S/I* ratio is proportional to T^{-2}. As HAT6 has such a narrow discotic temperature range (70°C – 100°C) where TOF signals and consequently $\{\eta\phi\}s$ can be obtained, it is difficult to measure any temperature dependence effects. Other DLC materials with a larger temperature range can be used to investigate this effect.

5.2.1.2 - HAT6:PTP9

It is obvious immediately from Figure 4.12 that this material does not obey the Onsager 3D model as, at any given field, the quantum efficiency drops with increasing temperature. Figure 5.2 is a plot of the experimentally determined *S/I* versus inverse temperature squared. Included in this plot is the theoretical value as given when equation 5.2 is evaluated (with the assumption that the dielectric constant of the material is 3).

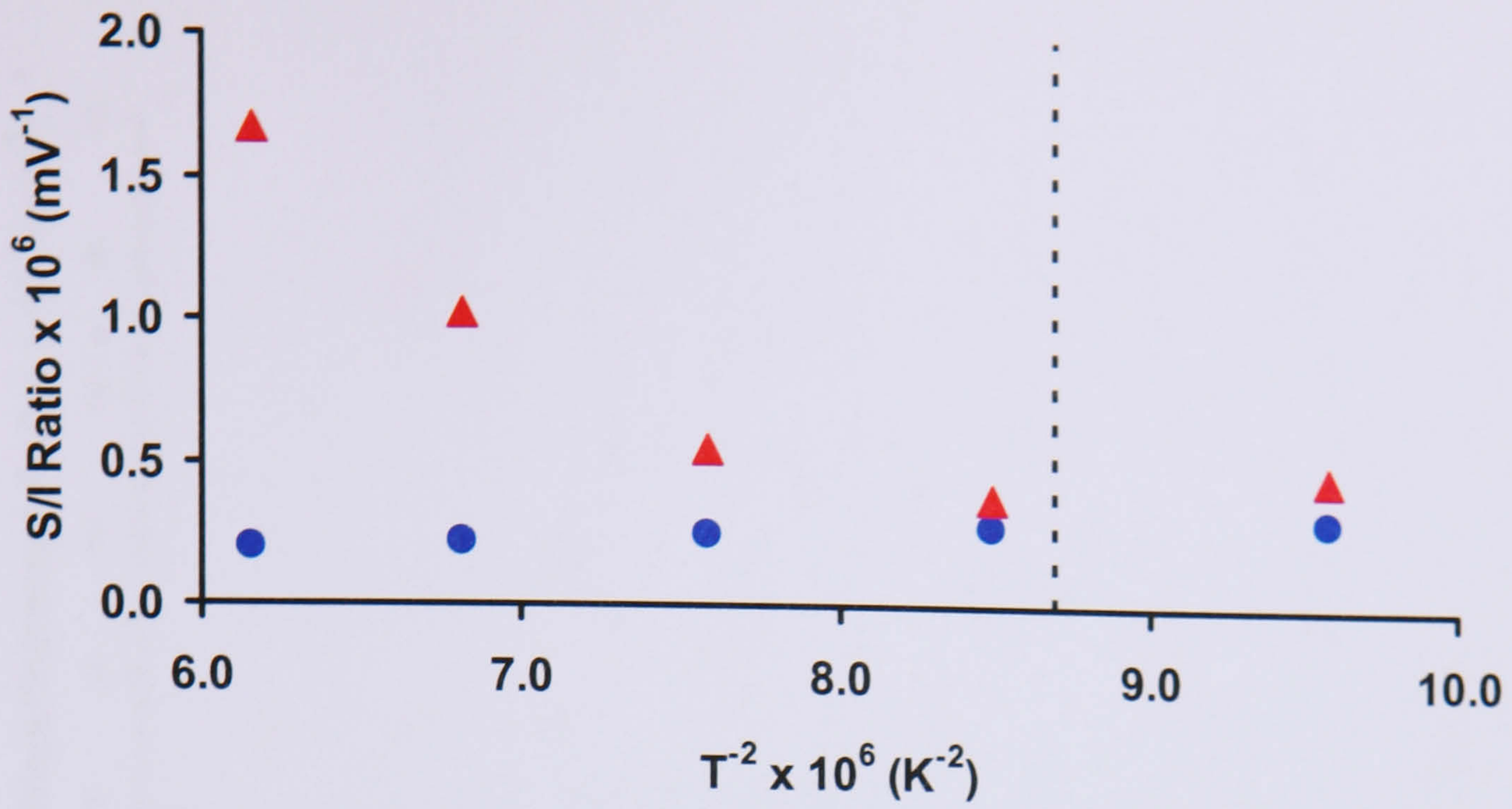

Figure 5.2: Experimental (▲) and Theoretical (●) Slope to Intercept ratios for HAT6:PTP9 as temperature is varied. The dashed line represents the boundary between the discotic and crystalline phases.

As demonstrated by figure 5.2, the experimental ***S/I*** ratios make a favourable comparison with the theoretical ratios at low temperatures (in the crystalline phase), but the theory fails for this material when the temperature goes well into the discotic regime. It is fair to conclude that the photogeneration mechanism for this material is not well described by Onsager theory.

5.2.1.3 - HAT11:PTP9

HAT11:PTP9 can also be dismissed at first glance from obeying Onsager 3D as the quantum efficiency, although field dependent, is independent of temperature (see figure 4.16). Equation 5.2 states that a plot of the slope to intercept ratio versus T^{-2} would yield a straight line, but clearly this can not be the case with this material. Figure 5.3 shows the comparison between the experimental and theoretical values. Therefore, the Onsager model also proves insufficient to account for the photogeneration mechanism in this particular DLC.

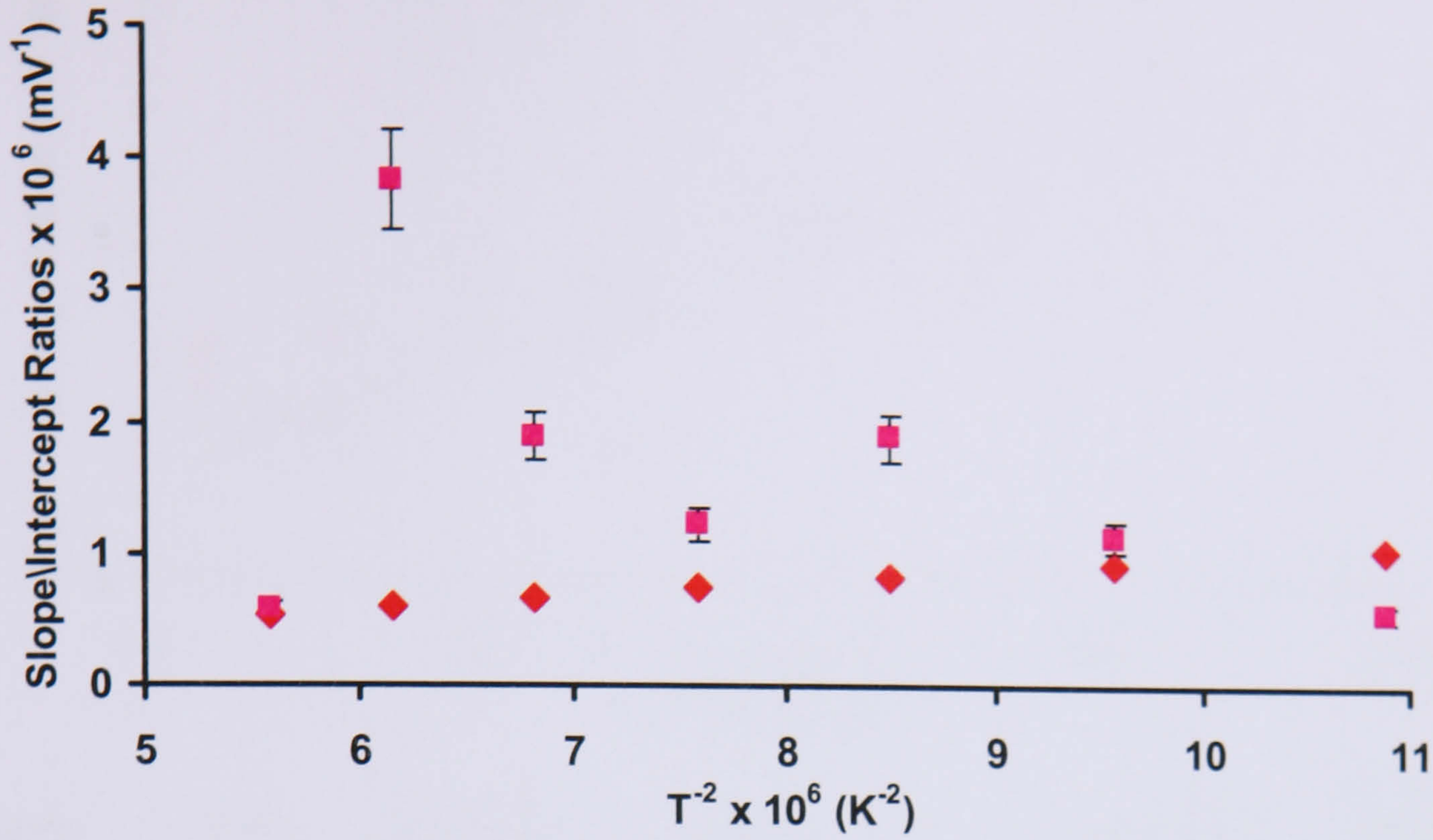

Figure 5.3: HAT11:PTP9 Slope to Intercept Quotient (◆=Theoretical, ■=Experimental)

5.2.1.4 – 2FHAT6

The material 2FHAT6 shows the closest agreement with the Onsager 3D theory, but the results are far from conclusive. As shown in figure 5.4, the values of ***S/I*** are similar and the trend is linear as expected by theory.

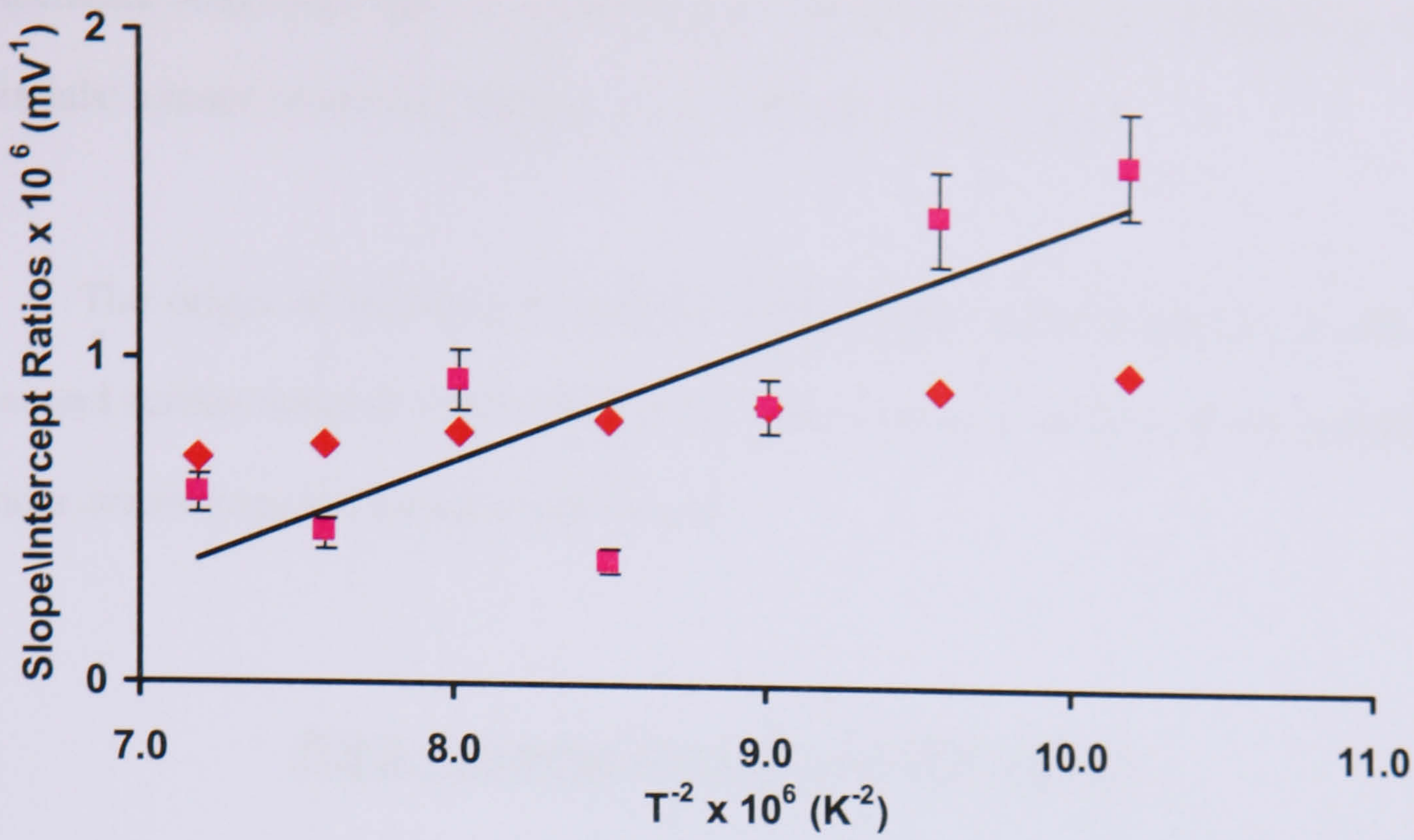

Figure 5.4: 2FHAT6 Slope to Intercept Quotient (◆=Theoretical, ■=Experimental)

5.2.1.5 – 3D Onsager Conclusions

$\{\eta\phi\}$ has been measured for a number of discotic materials using a transient photocurrent technique, where the current integrated under a transit signal gives the total charge created. This technique and its values are compared with values of $\{\eta\phi\}$ found from DC photoconduction measurements, and found to be comparable. We note that the current integration method works better than the DC photoconduction method when there are large dark currents to be accounted for.

Using this technique, we have thoroughly examined the field dependence of $\{\eta\phi\}$ in the context of Onsagers' theory of geminate recombination in three dimensions. In particular, we have measured the electric field dependence at a number of temperatures and shown that the ***S/I*** ratio does not follow the predicted form as temperature is varied. Thus, while studies of $\{\eta\phi\}$ against electric field made at one

temperature may lead one to conclude that Onsagers' theory is operative in these materials: a more systematic approach shows this not to be the case.

The origin of the field dependence of the photocarrier production is still not clear and further detailed work needs to be done in order to understand the underlying factors determining the quantum efficiencies.

5.2.2 – Charge Transport Mechanisms

Organic molecules are highly polarisable and thus have relatively strong electron-phonon coupling. There is therefore a strong possibility that the carriers in the DLC's interact with the surrounding molecules or with their host molecule to form polarons such as that described by Holstein. Recalling section 2.6, we can recast equation 2.25 as follows:

$$\log \mu T^{1.5} = -\frac{E_b}{2kT} + \log\left[\frac{ea^2}{k}\frac{1}{\hbar}\left(\frac{\pi}{2E_b k}\right)^{\frac{1}{2}} J^2\right] \qquad (5.3)$$

Therefore, a plot of log $\mu T^{1.5}$ vs T^{1} will yield a straight line of gradient ***G*** and Intercept ***I***:

$$G = -\frac{E_b}{2k} \qquad (5.4)$$

$$I = \log\left[\frac{ea^2}{k}\frac{1}{\hbar}\left(\frac{\pi}{2E_b k}\right)^{\frac{1}{2}} J^2\right] \qquad (5.5)$$

From the fitted values of G and I, we can deduce the polaron binding energy and bandwidth, J, equal to equations 5.6 and 5.7 respectively.

$$E_b = -2Gk \tag{5.6}$$

$$J = \sqrt{\frac{\exp I}{\frac{ea^2}{k}\frac{1}{\hbar}\left(\frac{\pi}{2E_b k}\right)^{\frac{1}{2}}}} \tag{5.7}$$

We can test the applicability of this theory by plots of mobility against temperature. The fits from such plots will allow us to calculate the polaron binding energies and bandwidths.

We can investigate this using the materials HAT6:PTP9 and 2FHAT6 because they have a reasonably large temperature range for the discotic phase. We are unable to use the results from HAT11:PTP9 as the spacecharge effects on the raw results make the determination of the mobility unreliable.

5.2.2.1 – HAT6:PTP9

As shown in Figure 4.11, the mobility of the charge carriers is proportional to the temperature of the sample for HAT6:PTP9. If we use the Holstein theory as described in section 2.6, we can apply this to the results of figure 4.11 and attempt to extract a polaron energy and bandwidth. The results of figure 4.11 have been recast into a small polaron plot, as shown in figure 5.5

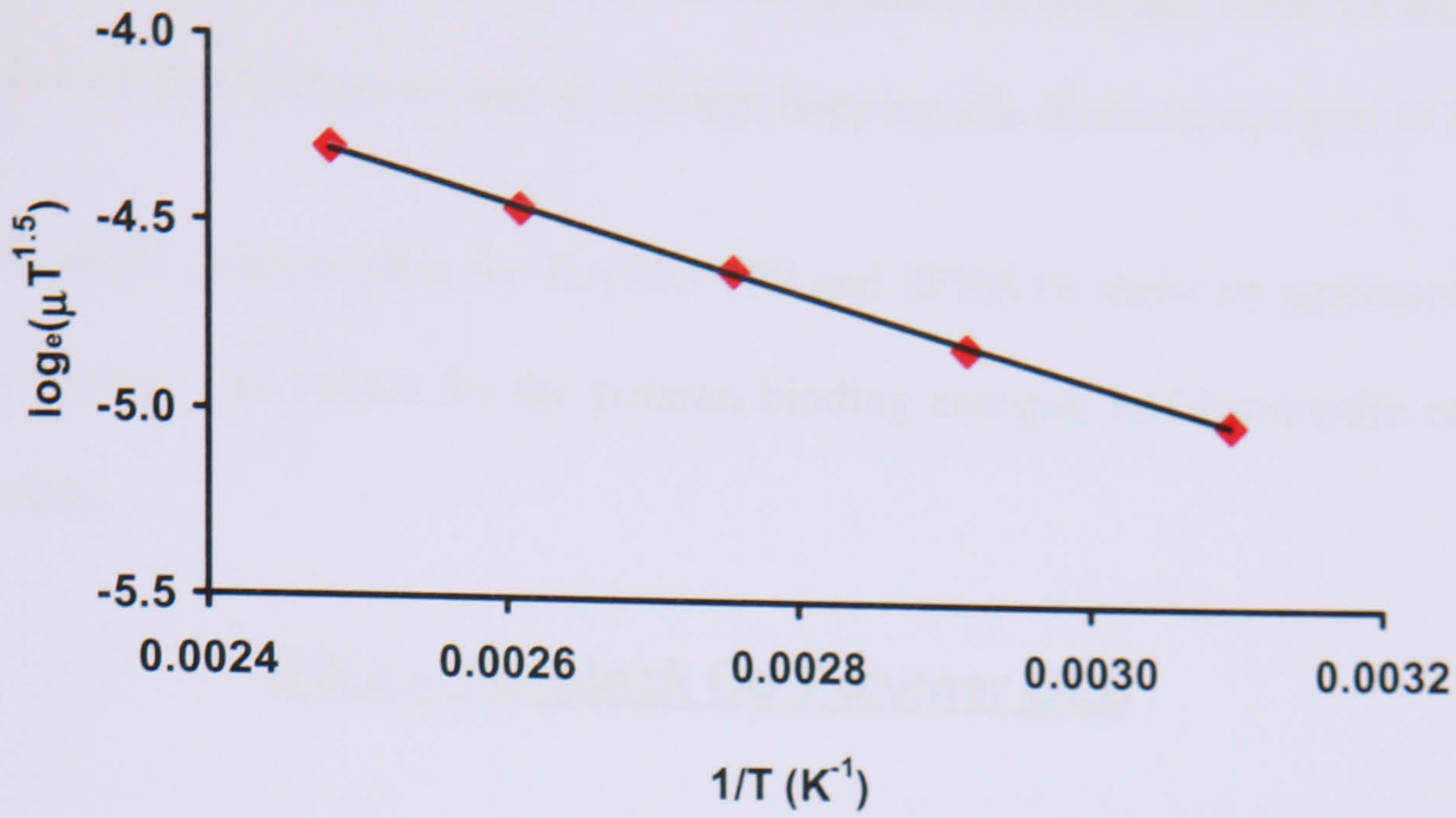

Figure 5.5: Small polaron plot of HAT6:PTP9

From the plot above, figure 5.5, we can deduce a value of E_b = 198 meV and J = 19 meV, when we use an average hopping site distance, a, equal to 3.5 Å.

5.2.2.2 – 2FHAT6

As shown in Figure 4.19, the mobilities of the holes for 2FHAT6 vary with temperature. The mobilities are not affected by a change in sample thickness however.

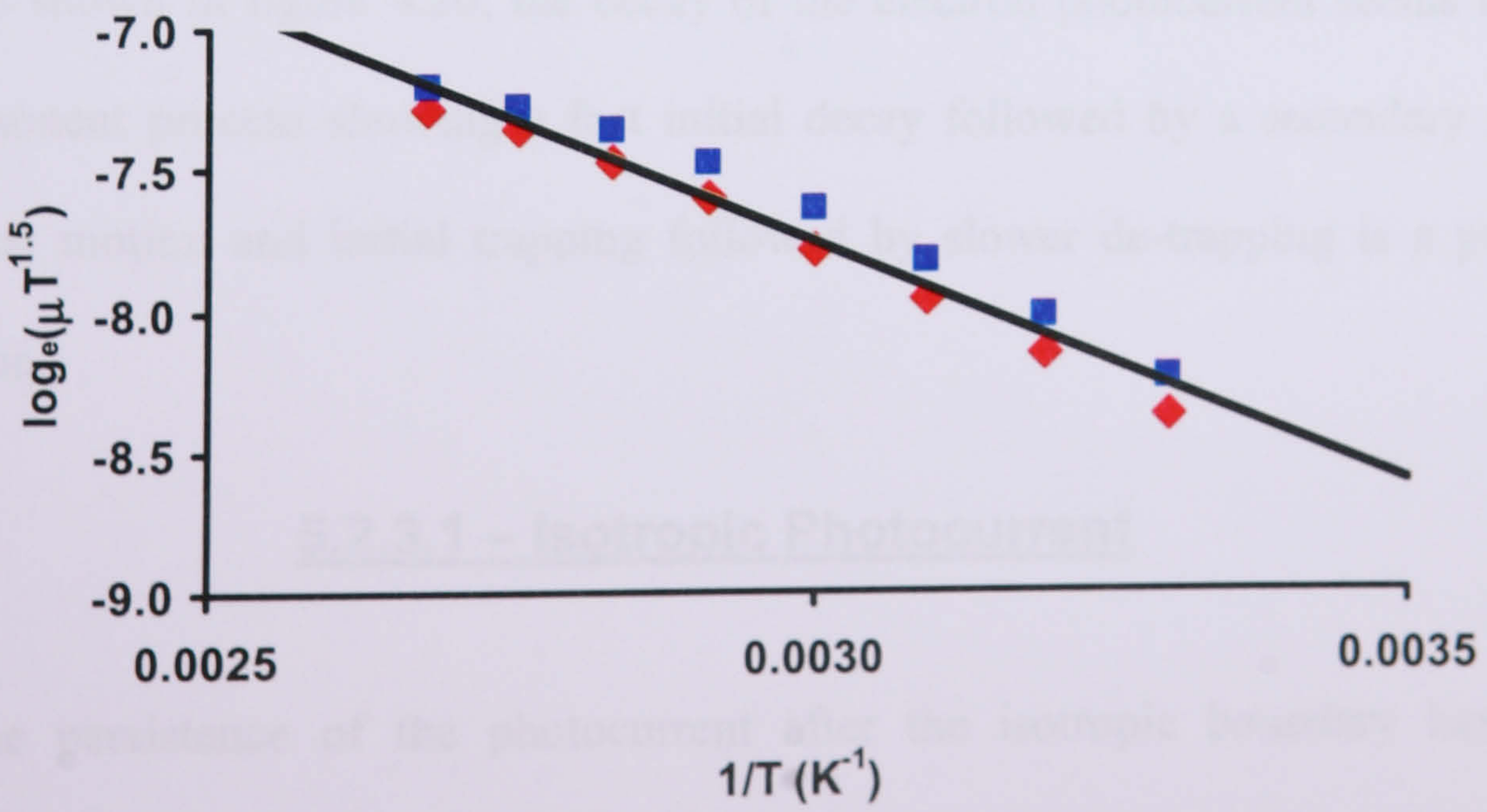

Figure 5.6: Small polaron plot of 2FHAT6 (Sample thickness: ■ 12.5 μm and ◆ 28.0 μm)

From the plot above, figure 5.6, we can deduce an average value of E_b = 309 meV and J = 13 meV, when we use an average hopping site distance, a, equal to 3.5 Å.

The small polaron plots for HAT6:PTP9 and 2FHAT6 show an agreement with Holstein's theory. The values for the polaron binding energies and bandwidth energies are reasonable.

5.2.3 – Tri-Block Co-Polymer DLC

The tri-block copolymer DLC [2,7-bis(2-ethoxyacetoxy)-3,6,10,11-tetrahexyloxytriphenylene] warrants an individual section due to the interesting and uncommon properties it exhibits [**54**] as well as being very different to the other DLC's investigated in this thesis. This material is novel in the sense that the majority of photogenerated carriers are electrons rather than holes, a situation unlike that found in most other discotic materials based around triphenylenes in general. Some Sulphur rich triphenylenes exhibit electron photocurrents though never transits (e.g. TCNQ and TNF).

As shown in figure 4.20, the decay of the electron photocurrent seems to be a two component process showing a fast initial decay followed by a secondary slower decay. Fast motion and initial trapping followed by slower de-trapping is a possible explanation.

5.2.3.1 – Isotropic Photocurrent

The persistence of the photocurrent after the isotropic boundary has been crossed (figure 4.22) may occur because the conduction is mediated by the polyethylene oxide, PEO, components of the co-polymer, although these chains are themselves very short and do not provide a substantial path for charge separation. Alternatively, and

more plausibly, the discotic columnar structure may persist beyond the clearing point, disappearing only slowly, due to the microphase separation and the nanostructuring that is known to occur due to the interaction between the discotic main-chain polymer and the PEO. That is, the PEO acts as a scaffold holding the discotic columnar structure in place, whose structure deteriorates slowly after the clearing point.

5.2.3.2 – Poole-Frenkel Behaviour

It has been shown here and reported elsewhere **[42, 52]** that the electric field dependence of the photogeneration efficiency is linear for the triphenylenes. Looking at data for the polymer DLC electrons (figure 4.23), we can see that the relationship is super-linear when high fields are used. At such high fields it is often found that the separation of excitons is electric field assisted due to the effect that the electric field has in lowering the attractive Coulomb interaction between the carrier pair (as depicted in figures 2.5a and 2.5b).

We see a linear fit when the log of the quantum efficiency product with carrier range is plotted against the square root of the electric field: thus showing evidence of the Poole-Frenkel effect (figure 5.7).

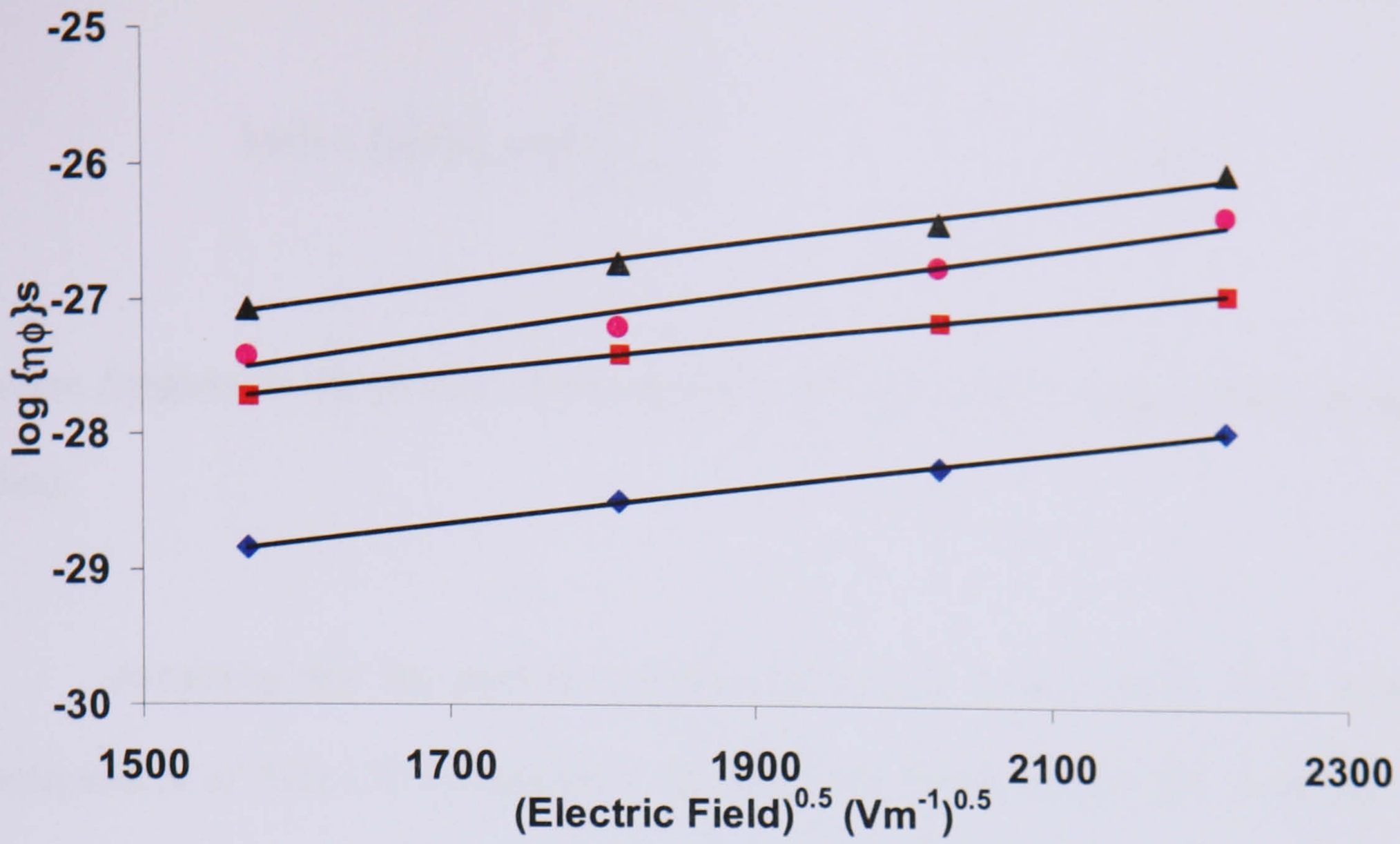

Figure 5.7: A Poole Frenkel plot of the field dependence of {ηφs} at ◆ = 30 °C, ■= 50 °C, ✹ = 90 °C and ▲ = 100 °C.

5.2.3.3 – Temperature dependence of dielectric constant

Recalling chapter 2 section 5, the Poole-Frenkel barrier lowering model when used to describe photocarrier generation predicts:

$$\phi_{(b)} \propto \exp\left(\frac{\beta E^{\frac{1}{2}}}{kT}\right) \tag{5.8}$$

where:

$$\beta = \sqrt{\frac{e^3}{\pi\varepsilon\varepsilon_0}} \tag{5.9}$$

For the quantity measured here, we have:

$$\{\eta\phi\}s = [\{\eta\phi\}s]_0 \exp\left(\frac{\beta\sqrt{E}}{k_B T}\right) \tag{5.10}$$

where $[\{\eta\phi\}s]_0$ is the product of the quantum efficiency-carrier range product at zero field.

Assuming that the primary quantum efficiency, η, and carrier range, s, are independent of field (1D assumption): the field dependence reflects that of $\phi(E,T)$. A plot of log ($\{\eta\phi\}s$) vs $E^{0.5}$ (figure 5.7) will give a straight line with a gradient equal to: β/k_BT. By applying these fits to the data of figure 5.7, we can calculate values of β (figure 5.8) and from that, the dielectric constant, ε (figure 5.9).

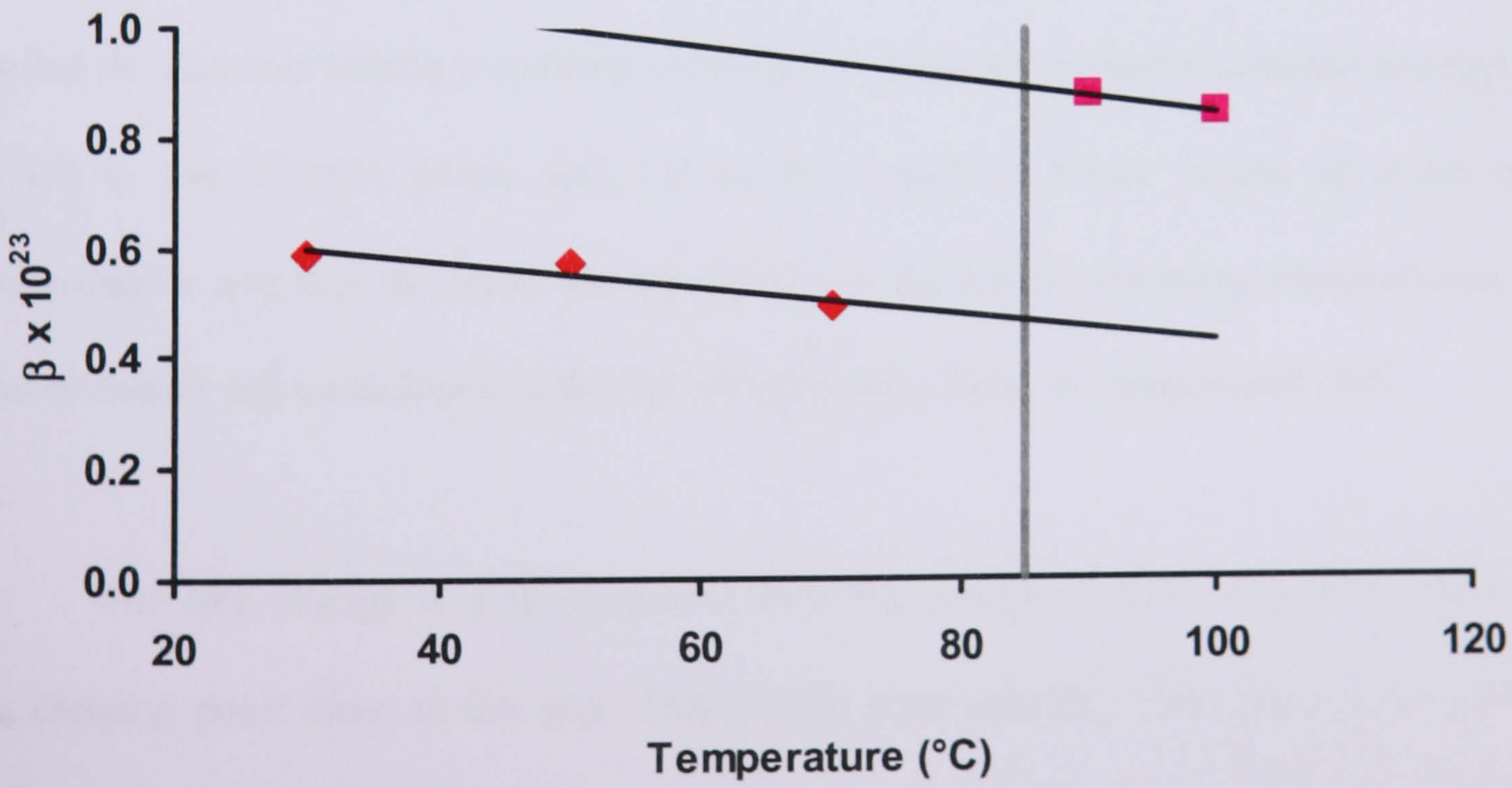

Figure 5.8: Variation of β with temperature (the grey line represents the discotic/isotropic phase boundary).

The experimentally determined values of ε for this sample are plotted over the temperature range in figure 5.9.

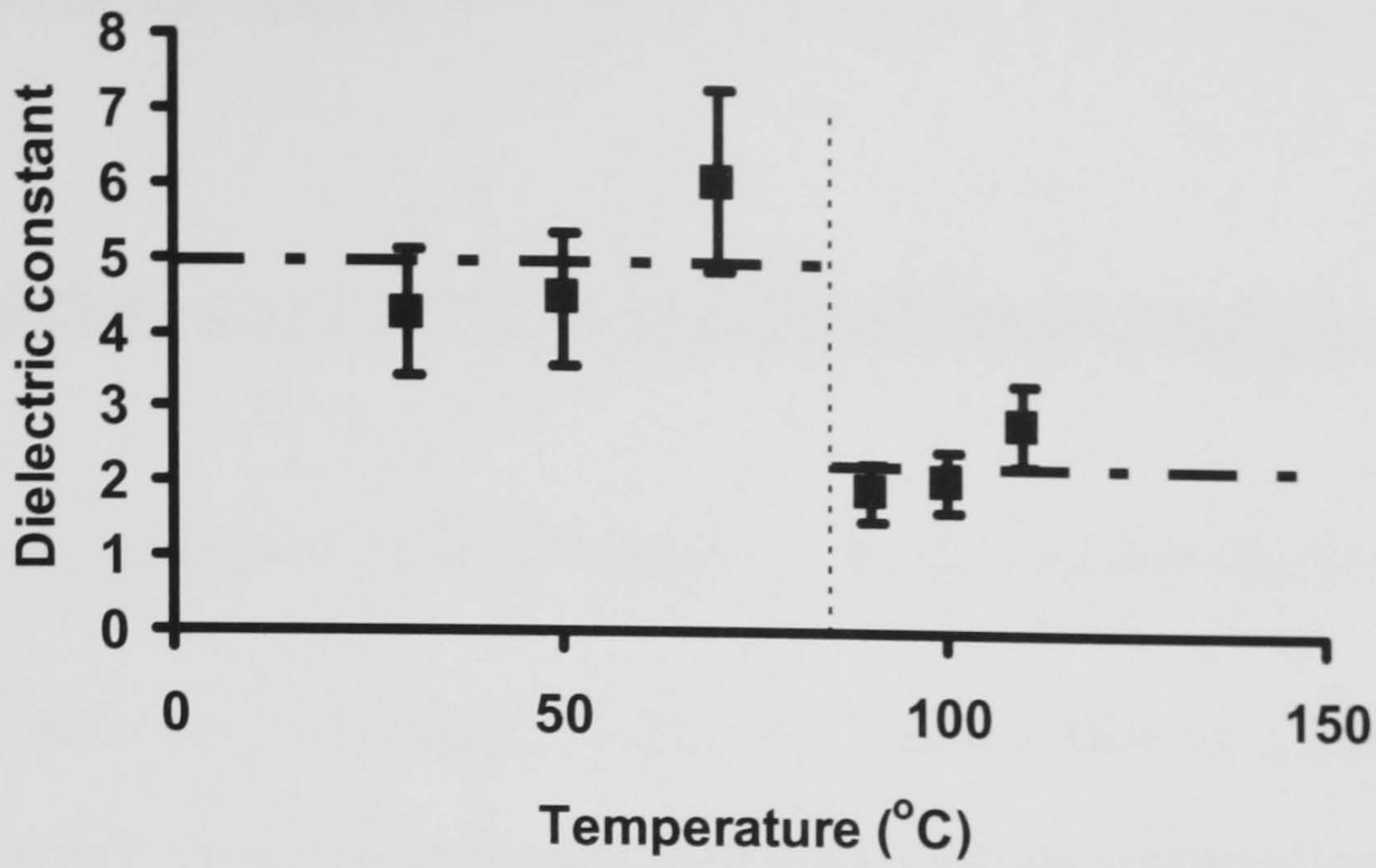

Figure 5.9: Variation of dielectric constant with temperature (the vertical dashed line represents the phase boundary).

What appears interesting in Figure 5.9 is that there seems to be a definite change in ε at higher temperatures. This change occurs close to the phase boundary between the discotic phase and the isotropic. The obtained value of ε is found to have a sharp step at around the discotic/isotropic melting temperature, with the dielectric constant averaging to 4.9 in the discotic phase and 2.0 in the isotropic. These values of ε are not unreasonable and this increases our confidence in the barrier lowering interpretation. It also measures our confidence in the 1D interpretation that s is independent of E.

The step change in ε is associated with the change in phase that takes place at the clearing point close to the step. That is, the polarisability of the system has a step change above the isotropic phase boundary which reduces the dielectric constant significantly.

Such a reduction is reasonably to be expected and although the intramolecular polarisability does not change, the sum of the individual molecular polarisabilities or

polarisability per unit volume will be greater when there is a degree of alignment amongst the molecules which is the case before the discotic – isotropic transition.

5.2.3.4 – Limits on Quantum Efficiency and Mobility

From the gradient of the data of figure 5.7, we can find the value of $\frac{\eta\phi s}{\sqrt{E}}$ which allows us to set a value of $\{\eta\phi\}s$ = 5.72 x 10^{-13} m at a field of 1 MVm^{-1} and a temperature of 70°C in the discotic phase. With this knowledge and from the absence of a transit that indicates s ≤ d = 12 μm, we find a lower limit on $\{\eta\phi\}$ at 1 MVm^{-1} of $\{\eta\phi\}$ ≥ 4.76 x 10^{-8}.

Although there are no transits observed in the photocurrents, we can use both equations 2.6 and 2.7 to determine that $\frac{I_P}{Q} = \frac{\langle v_E \rangle}{s}$. As ***Ip*** and ***Q*** are known, we can produce a plot of the carrier velocity divided by the carrier range versus electric field for various temperatures (figure 5.10). The gradient of which can be used to infer an upper limit on the mobility.

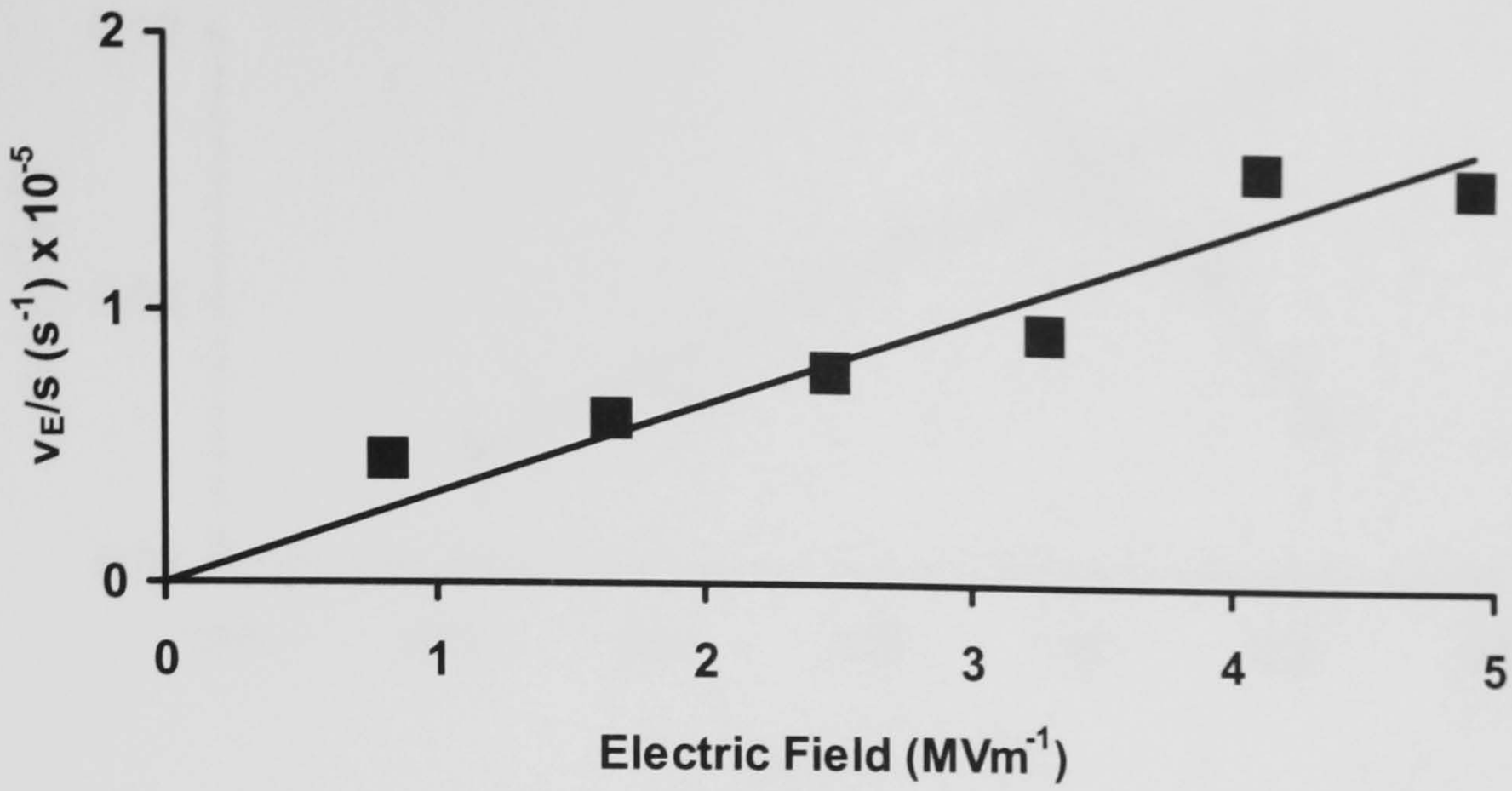

Figure 5.10: A plot of the carrier velocity and carrier range quotient at T = 50°C against electric field using the ratio of I_P to Q.

By taking the gradient in figure 5.10 (7.0 $cmV^{-1}s^{-1}$) and by knowing that the carrier range has to be less than 12 μm, we obtain an upper limit on the electron mobility with the value: $\mu_e \leq 8.4 \times 10^{-3}$ $cm^2 V^{-1} s^{-1}$. This is not an unreasonable value when compared with the mobilities of other discotics.

From the variation of v_E/s in figure 5.10 with field we may reasonably assume that v is linear in field, as it is for all other DLCs where TOF transits are found, thus giving a range s that is field independent, as also found in our considerations of E.

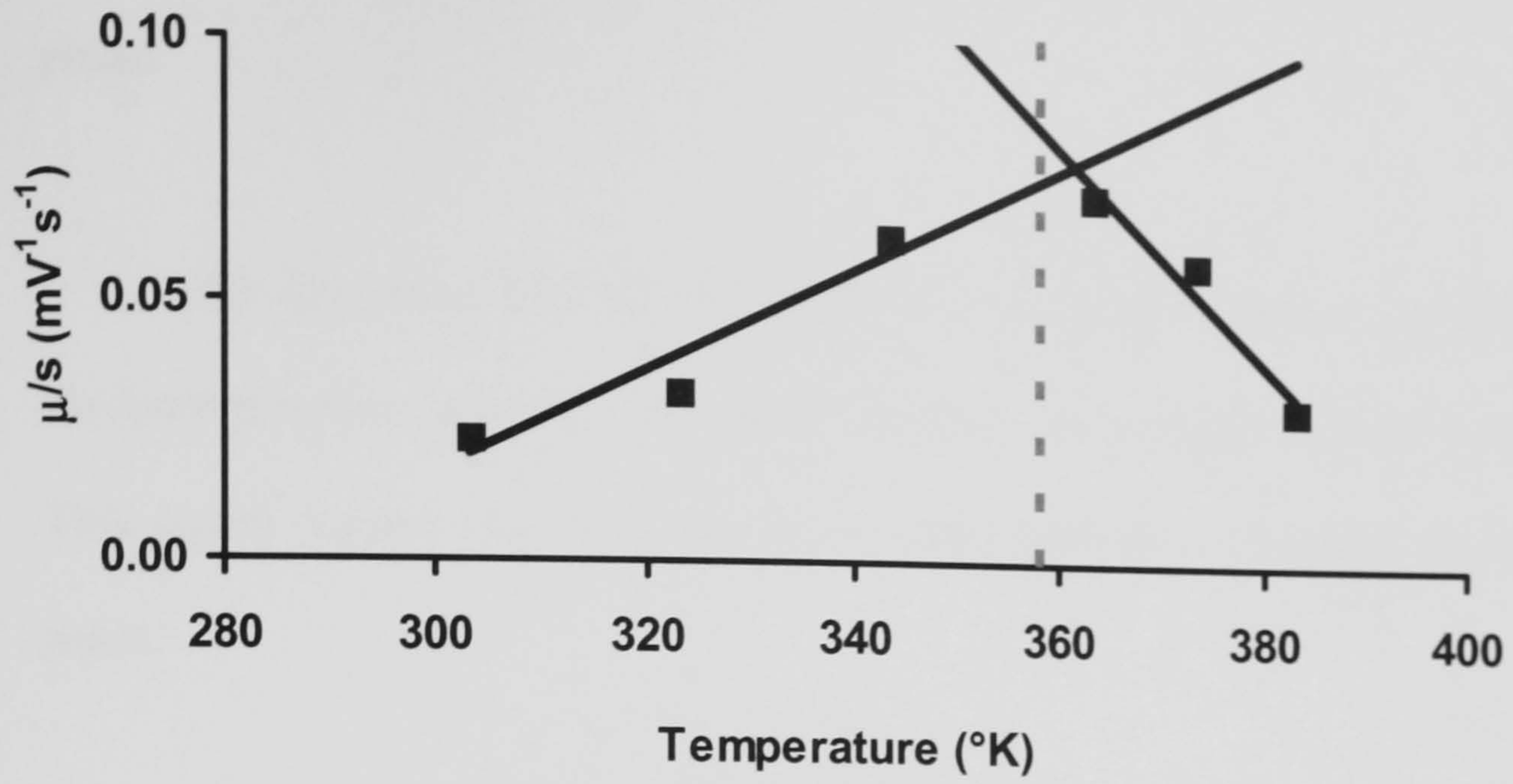

Figure 5.11: A plot of the mobility/carrier range quotient against temperature from the gradient of data such as that in figure 5.10. The dashed line represents the Discotic–Isotropic phase boundary.

Figure 5.11 shows that the mobility/carrier range quotient initially increases with temperature but then begins to fall at higher temperatures. Extrapolation leads us to conclude that the temperature at which the crossover occurs sits very near to the isotropic phase boundary.

With the reasonable assumption that $\boldsymbol{v}$ is linearly dependent on field, and knowing that $\boldsymbol{s} = \boldsymbol{v_E \tau}$ is independent of field, we come to the conclusion that this columnar material is behaving as a one dimensional charge transporter where the trapping time, $\boldsymbol{\tau}$, varies inversely with electric field.

5.2.3.5 – Conclusions on Tri-Block Co-Polymer

We have shown that, unlike usual DLC's based around a triphenylene core, the tri-block co-polymer is not a hole transporter and electrons are the majority carriers. We have shown that the electron photogeneration rate can be described by the Poole-Frenkel mechanism and inferred that that dielectric

constant of the material has a step change between the discotic and isotropic phase.

We also show that the photoconduction (charge separation) persists into the isotropic phase and attribute this to the PEO side-chains acting as a scaffold. This would explain why the peak photocurrent falls slowly beyond the clearing point.

5.3 - Carbon Nanotubes

At the time of writing, we present in Chapter 4 the first known transient photoconduction measurements on SWNT's. After the initial verification that the SWNT samples showed evidence of photoconduction, we carried out more detailed experiments and investigated the concentration, electric field, tube length, wavelength and light intensity dependence. A discussion of what was found is to follow.

5.3.1 – Nanotube Concentration Dependence

Figure 4.31 demonstrates linearity between the peak photocurrent and the electric field. A plot of the gradients from figure 4.32 versus sample concentration, as shown in figure 5.12, demonstrates that the magnitude of the peak photocurrent also scales linearly as a function of concentration. The implication of this is that for the concentrations used here, the number of photons absorbed by the nanotubes, N_{ph}, is much less than the total number of photons incident on the sample, N_0.

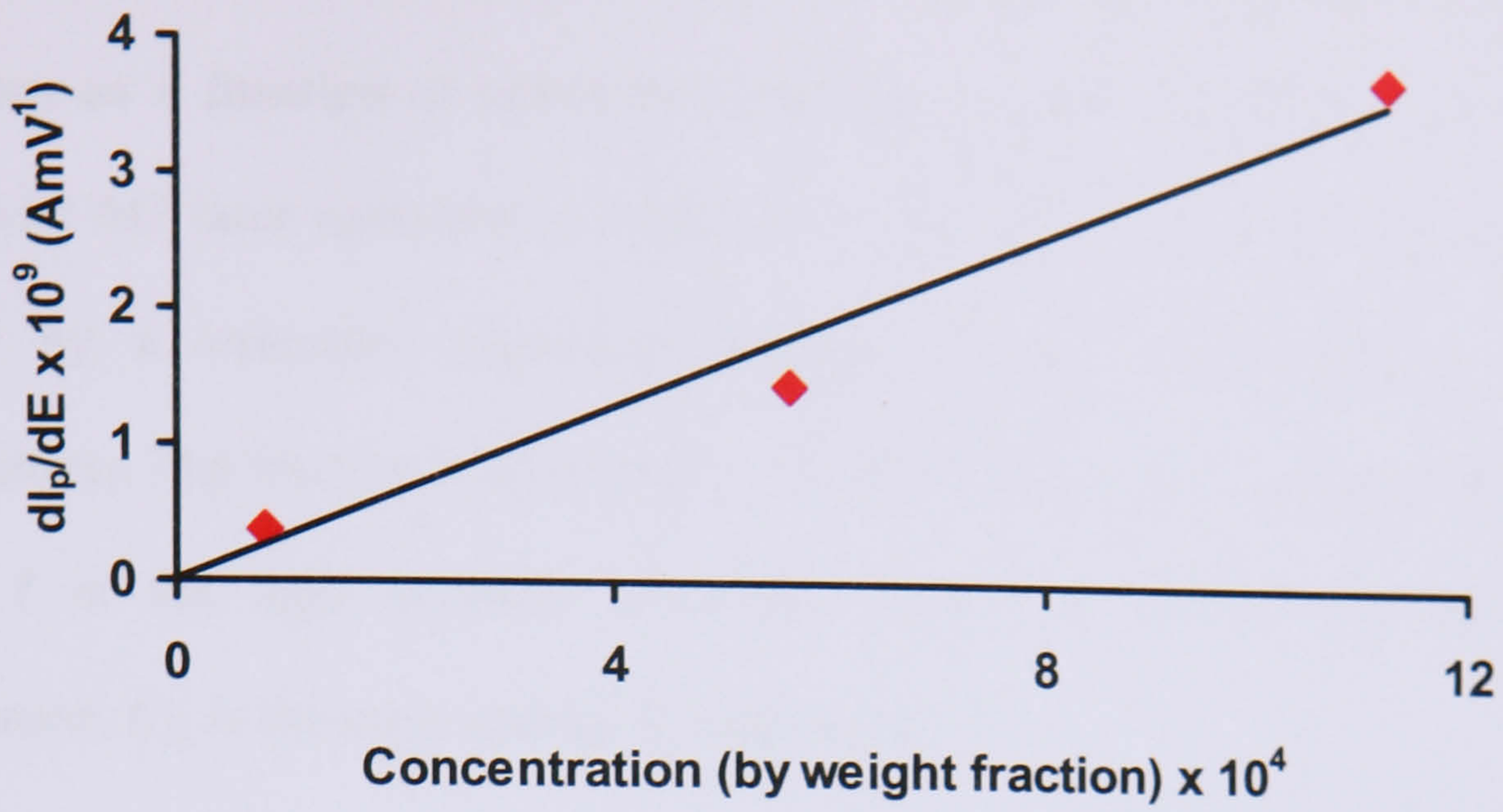

Figure 5.12: Linear dependence of dI_p/dE with concentration.

Assuming Beers law, if α is the absorption coefficient and C_T is the nanotube concentration then we can write:

$$N = N_0 \exp(-\alpha C_T L) \tag{5.11}$$

Where N is the number of photons that traverse a cell of path length L containing the nanotubes. The number of photons absorbed is then:

$$N_{ph} = N_0 - N = N_0[1 - \exp(-\alpha C_T L)] \approx N_0 \alpha C_T L \tag{5.12}$$

Note: The approximation is for the case: $\alpha C_T L << 1$

We know the total number of photons, N_0, incident upon the sample and can infer that N_{ph} is much lower than this and proportional to C_T through the linearity of I_P with C_T.

In order to find the constant of proportionality, the absorbance of nanotube suspensions as a function of nanotube concentration was measured using the mode locked Nd:YAG laser operating at 1064 nm. Figure 5.13 shows the fraction of light absorbed by a nanotube suspension through a 2mm quartz cell at different concentrations. The fraction is of the form $(I_0 - I)/I_0$ where I_0 is measured through pure oil and I is the light intensity measured through a SWNT suspension. The concentration, C_T, is the mass fraction of nanotubes to oil.

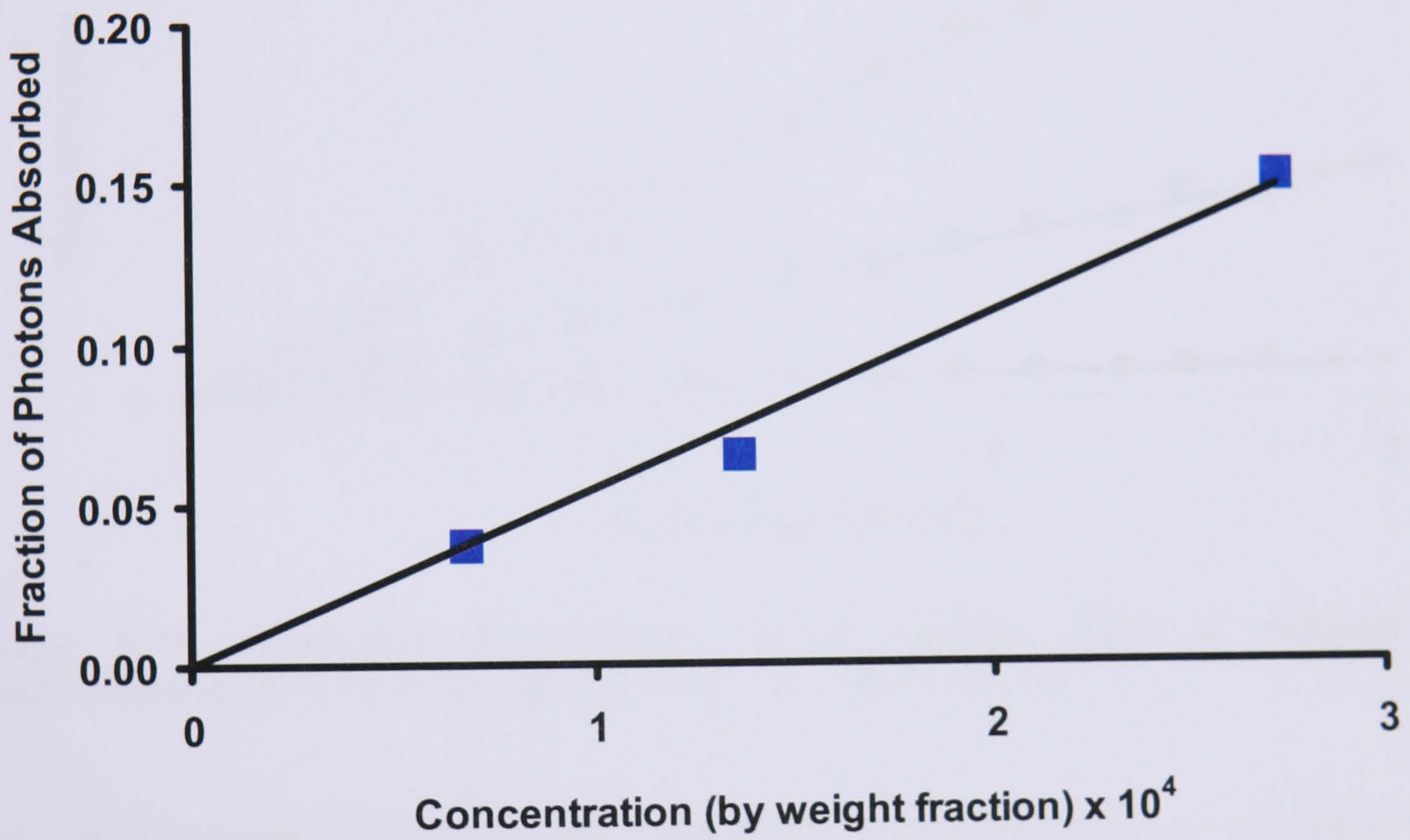

Figure 5.13: Fraction of photons absorbed versus sample concentration.

The absorbance is linear in concentration and from the data of figure 5.13; it is possible to calculate the fraction of incident photons absorbed in the 50Ω co-axial cell to be:

$$\frac{N_{ph}}{N_0} = 1430 \times C_T \qquad (5.13)$$

The total photocharge Q associated with a photocurrent can be found by integration of the photocurrents, such as those in figure 4.30.

Figure 5.14 shows the variation of photocharge with electric field at a number of concentrations.

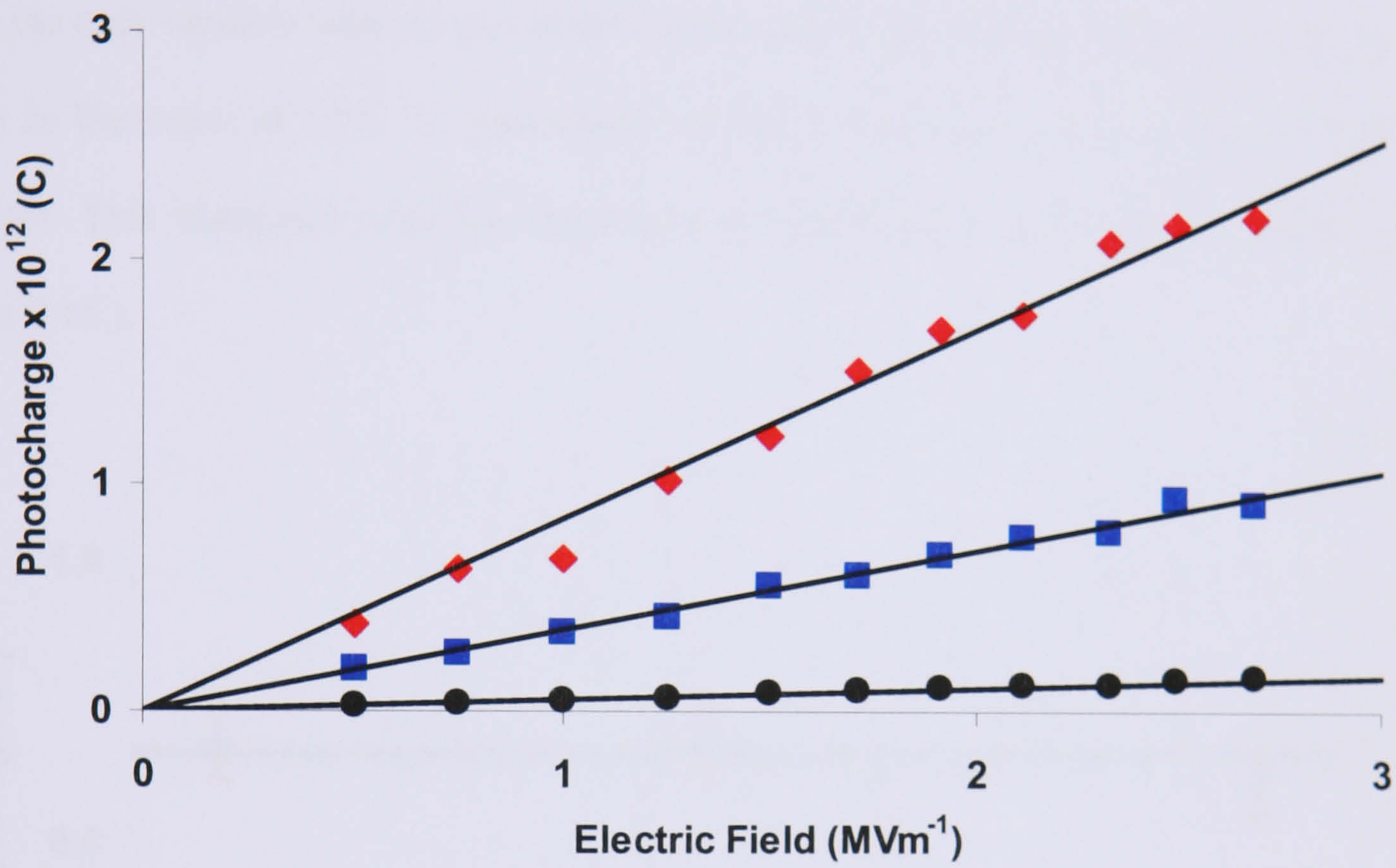

Figure 5.14: Measured Photocharge versus Electric Field at different concentrations (◆ 1.12 x 10^{-3}, ■ 5.60 x 10^{-4} and ● 8.20 x 10^{-5}).

Remembering equation 2.6 and correcting for the low absorption using equation 5.13, this photocharge is given by equation 5.14:

$$Q \equiv \int I(t)dt = \frac{e\{\eta\phi\}N_{ph}s}{d} = 1430 \times \frac{e\{\eta\phi\}N_0 C_T s}{d} \qquad (5.14)$$

As we do not know the carrier range, s, we can only deduce the product of the quantum efficiency and carrier range, $\{\eta\phi\}s$, from equation 5.15

$$\{\eta\phi\}s = \frac{d}{1430 \times eN_0C_T}\int I(t)dt\,. \qquad (5.15)$$

Using $\frac{Q}{E}$ from figure 5.14 and equation 5.15 to calculate $\frac{\eta\phi s}{E}$, in figure 5.15 we show that this quantity is sensibly independent of concentration. (Note: from equation 5.10, the only variable with an appreciable error is the light intensity which we estimate to be in the order of 10% by observation of the fluctuations in the bolometric light detector. This fractional error has been used to calculate the errors on the points in figure 5.15.).

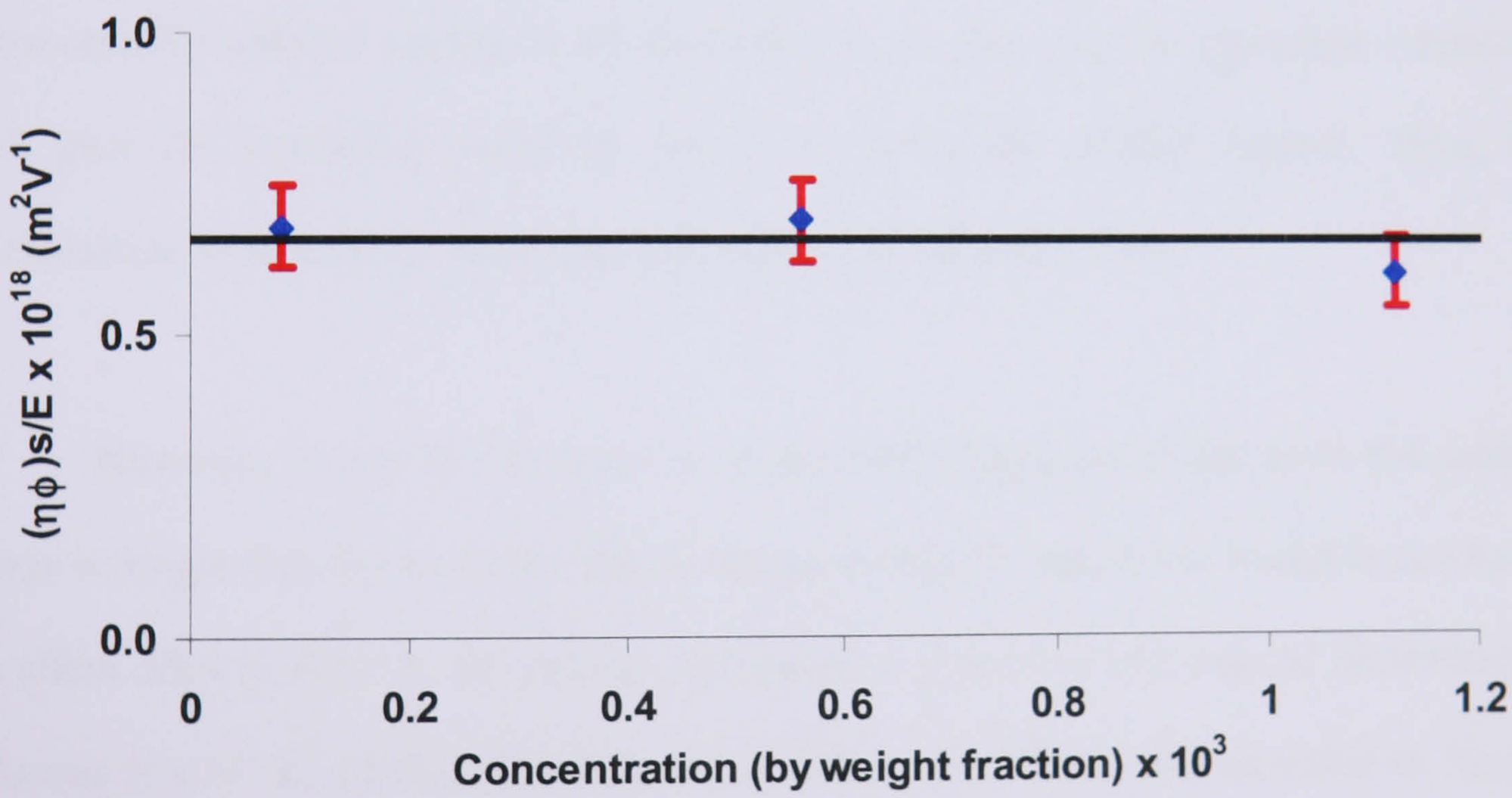

Figure 5.15: Quantum Efficiency-Carrier range product over Electric field versus concentration.

5.3.2 – Quantum Efficiency/Carrier Range Entanglement

It would be useful to disentangle the quantum efficiency from the carrier range. Such an experiment could use a variation on the 'line cutting' method **[55]**. Cutting of

the SWNTs can either be performed chemically **[56]**, mechanically [57] or as a combination of these two methods **[58]**.

SWNTs can be chemically cut by partially functionalising the tubes, for example with Fluorine **[56]**. Then, the fluorated carbon will be driven off the sidewall with pyrolisation in the form of CF_4 or COF_2. This will leave behind the chemically cut nanotubes. Mechanical **[57]** cutting of the nanotubes can be induced by ball-milling. Here, the bonds will break due to the high friction between the nanoparticles and the nanotubes will be disordered.

A combination of mechanical and chemical cutting of the nanotubes **[58]** is ultrasonically induced cutting in an acid solution. In this way the ultrasonic vibration will give the nanotubes sufficient energy to leave the catalyst surface. Then, in combination with acid the nanotubes will rupture at the defect sites.

However, it may be the case that in the experiments presented here; the carrier range is longer than the nanotube length and so cutting the nanotubes would be not have an effect. That is, if $s > L$, the cutting experiment would result in a reduced photocharge whereas if $s << L$, cutting would make no difference. This is demonstrated in figure 5.16.

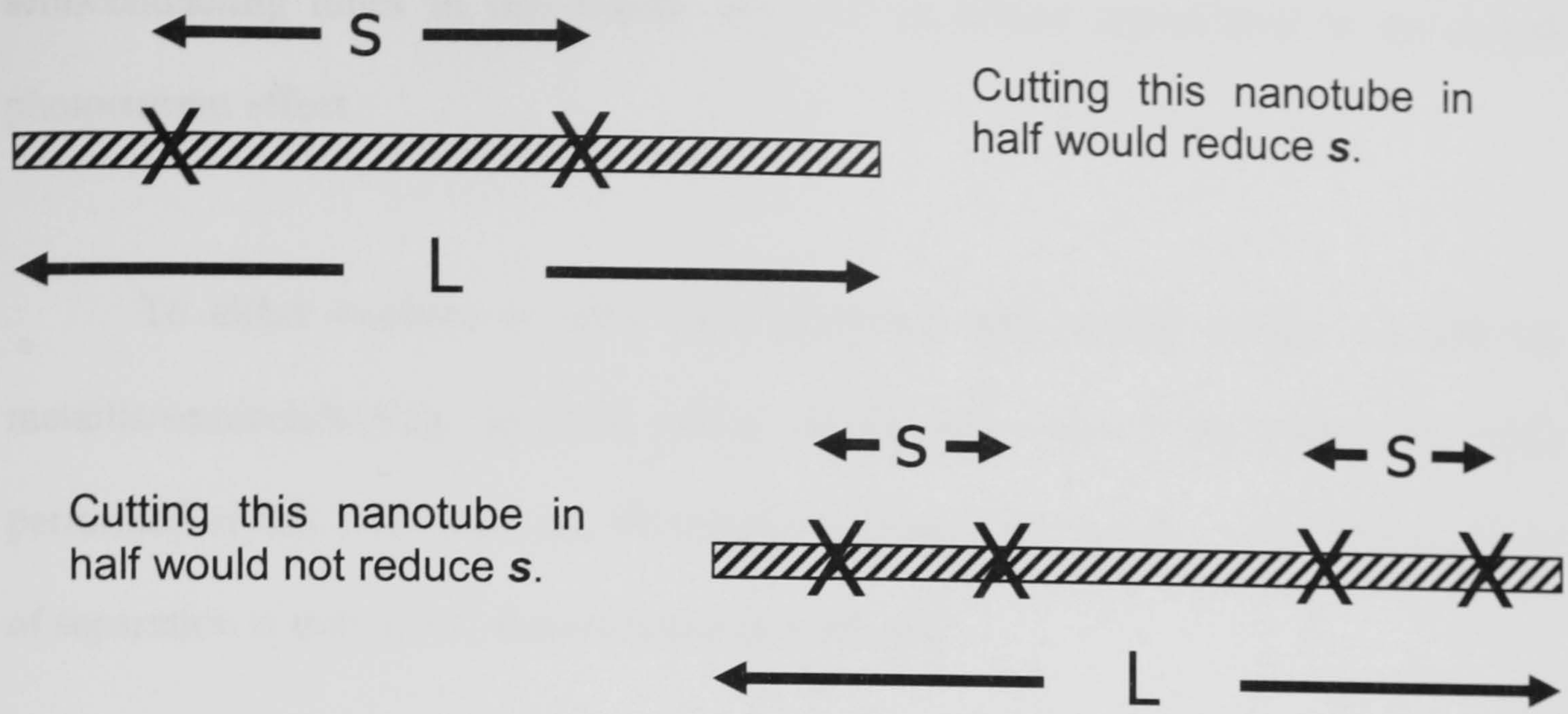

Figure 5.16: Cutting the nanotube

If we make the assumption that we are in the regime where the nanotube length is greater than the carrier range, ***s***, by cutting the nanotubes into shorter lengths we may reach the condition where the carrier range exceeds the nanotube length and is thus limited by it. We should then observe a systematic decrease of the measured photocharge as the tubes are cut further into shorter lengths.

The average value of $\{\eta\phi\}s/E$ from figure 5.15 is equal to $0.658 \times 10^{-18}\ m^2 V^{-1}$. If we assume that the carrier range, ***s***, is in the order of 1 μm (corresponding to the order of as prepared nanotube lengths), then at a typical field in these experiments of 1.0 MVm^{-1}, we can imply a lower limit on the quantum efficiency of: $\{\eta\phi\} = 6.58 \times 10^{-7}$. This is a surprisingly low value for $\{\eta\phi\}$.

A possible explanation for this unexpected result could be due to the composition of a random nanotube sample where 2/3 of the sample would be metallic tubes. It may be that a significant number of photons are being absorbed by the metallic tubes, all of which will not contribute to a photocurrent. Furthermore, the presence of metallic tubes will cause the electric field in close proximity to be reduced. Any

semiconducting tubes in this region may not contribute appreciably to the overall photocurrent effect.

To either confirm or deny this hypothesis will require samples of differing metallic/semiconducting nanotube ratios. At the time of writing, research is being performed at this institution and elsewhere to achieve this result. A promising method of separation is that of AC dielectrophoresis **[59, 60]**.

5.3.3 –SWNT Quantum Efficiencies

A formulation of Onsager's theory of ion recombination adapted to one dimension, 1D, by Haberkorn et al **[61]** can be used to describe the field dependence of ϕ. The adapted theory predicts that the probability of an exciton escaping geminate recombination, leading to free carriers, at low fields in 1D is linear with field.

In a 3D material, e.g. silicon, the range s will be field dependent as the defects are found through diffusion and the trapping time is constant. In 1D, the defects are found through the carrier drift and the range represents the average inter-defect distance while the time to trap is inversely proportional to field **[62, 63]**. The present data shows that $\{\eta\phi\}s$ is linear in field implying either that:

1. The carrier range, s, is independent of field and the geminate escape probability ϕ, varies linearly with field; both expectations for a 1D system or...

2. The carrier range is linear in field and the geminate escape probability is independent of field; both expectations of a 3D semiconductor.

We are unable to distinguish between these two possibilities at this time, although, given the 1D nature of nanotubes: the former possibility is the likelier of the two explanations offered for these results. In order to proceed further we may use the high mobilities ascribed to SWNT's by others **[64]**. These mobilities would lead to a drift velocity of $\boldsymbol{v} = \boldsymbol{\mu E} \approx 10^7$m/s at the fields used in these experiments.

Clearly this is unphysical and therefore the velocity would be saturated well before this value was reached by some mechanism and becomes independent of E at the fields we are using for these experiments.

Therefore, the time to find a trap would be independent of field in a 1D system. This would lead to conclusion 1 being the correct conclusion, that $\{\eta\phi\}$ is linearly dependent on electric field.

5.3.4 – SWNT Photocurrent Decay Analysis

By taking data such as that in figure 4.34 and normalising these photocurrents to their maximum value, we can produce figure 5.17 which shows twelve different photocurrents at a range of fields between 0.25 MVm^{-1} and 2.68 MVm^{-1}.

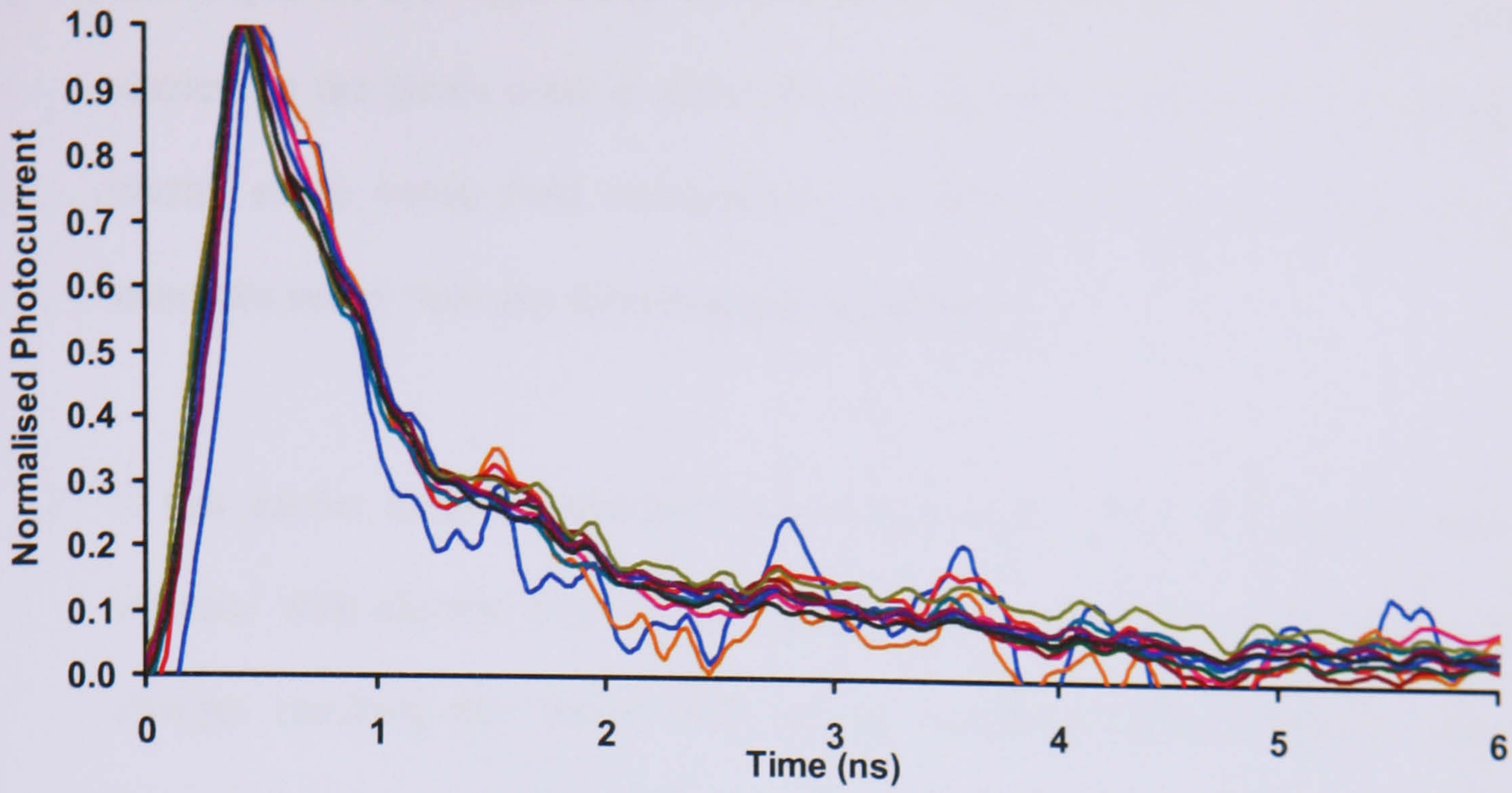

Figure 5.17: Normalised photocurrents with decay tails at fields ranging from 0.25 MVm^{-1} to 2.68 MVm^{-1}

It is obvious from first glance that the shape of the decay tails is not affected by the applied electric field and can be considered independent. While most normalised signals sat on top of each other, some of the smaller fields became much more susceptible to random noise with noticeable deviations around the average. The normalised photocurrent in figure 5.17 represented by the blue line is the one with the most obvious noise. This corresponds to signal obtained with the lowest applied field (0.25 MVm^{-1}).

In a 3D material, the trapping time is expected to be independent of the applied electric field. This is due to diffusion occurring at thermal velocities where charge carriers are able to negotiate their way easily around traps. Figure 5.17 shows a clear independence between trapping time and field, which is not usually expected in a 1D system, except if $\boldsymbol{v}$ is saturated. However, as isolated SWNTs are quasi 1D structures, there could be other reasons why this behaviour, usually seen in 3D materials, is observed.

1. The depth of the traps could be negligible and therefore not capture charge carriers at the fields used in these experiments. This would result in the total carrier range being field independent and being equal to the length of the nanotube rather than any inter-trap spacing distances.

2. If this carrier range is constant, one would expect to see the decay constant increase with electric field as the higher carrier velocities would result in the charges reaching the defects/ends of the nanotube faster. However, this is complicated as we could conjecture, given independent measures of mobility, that the carrier velocity may become saturated at and above a relatively lower field than the minimum used in these experiments; the increase in peak photocurrent with field being solely attributed to the increase in field assisted pair production. This seems likely considering the high independent measurements of mobilities mentioned earlier [**64**].

3. In theory, longer nanotubes may have an increase in carrier range if the trap depth is shallow. However, longer nanotubes would also have more of a tendency to cluster together. If a network of nanotubes is formed with charge carriers able to hop from one tube to another: the overall carrier range would be much higher and this could explain the emergence of the decay tails. The effect would not be observed with shorter nanotubes as they may not be as efficient in forming a network.

Figure 5.18 shows the natural logarithm of the averaged normalised photocurrents (taken from figure 5.17) versus time. There appear to be two decay components to the photocurrent. The underlying averaged normalised photocurrent is shown in black whilst the red and blue sections are the points chosen to extract an exponential decay for

the two decay processes. The initial rise of the photocurrent has obviously been omitted as well as the noise towards the end of the signal lifetime, which becomes greatly exaggerated on a logarithmic scale. The second peak occurring between 6 and 7 nanoseconds (the round trip time of the laser) has also been omitted.

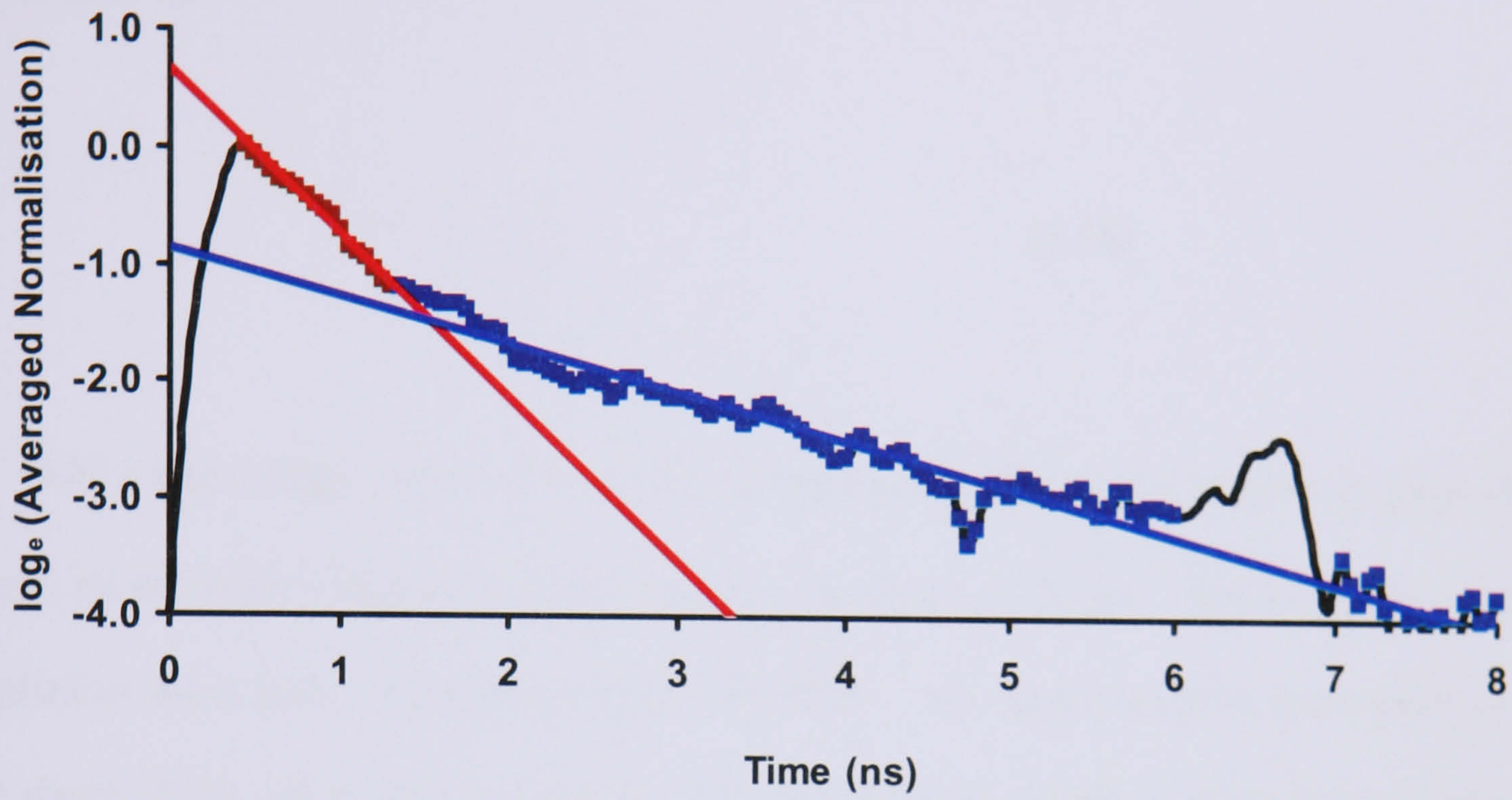

Figure 5.18: Analysis of averaged decay tail with a 3 GHz oscilloscope.

The fits from figure 5.18 give us values from which we can calculate the decay constants, τ_a and τ_b. In this example, the initial decay rate has a measured value of τ_a^{-1} of 1.40 ns^{-1} which corresponds to a decay constant of 0.71 ns. The second component has a measured value of τ_b^{-1} of 0.41 ns^{-1} which corresponds to a decay constant of 2.44 ns.

However, it is likely in this example that the initial averaged decay constant measured (0.71 ns) is nothing more than the fall-time of the oscilloscope, which would be a fixed value and therefore independent of field. In chapter 4, we showed that the rise-time of the oscilloscope in series with the co-axial cell was in the order of a few hundred picoseconds and so this seems a sensible conclusion. The second decay process in Figure 5.18 is much more interesting.

We have already established from figure 5.17 that the relationship between τ_b^{-1} and electric field is independent. As we are assuming the 1D model, one would expect that the trapping time, τ, would be proportional to the inverse electric field as shown in equation 5.16:

$$\tau = \frac{s}{v} = \frac{s}{\mu E} \qquad (5.16)$$

With a knowledge that $\tau = 2.44$ns and an assumption that s has a maximum range of 1 μm, we can infer a saturation velocity in this example of 410 ms^{-1}. The minimum field applied in these decay experiments was 0.25 MVm^{-1}. As we do not have knowledge on the shape of the decay tails below this field (as the small signals will become virtually indistinguishable from noise), let us use this minimum value to set a maximum limit on the applied field where the carrier velocity becomes saturated. This gives us a lower limit on the low-field mobility of: $\mu > 16.4\ cm^2\ V^{-1}\ s^{-1}$.

This does not compare favourably to mobilities deduced from the transconductance of SWNT FET's, with various sources citing the mobility to be: 220 $cm^2V^{-1}s^{-1}$ **[65]**, 9000 $cm^2V^{-1}s^{-1}$ **[66]** and 10^5 $cm^2V^{-1}s^{-1}$ **[64]**. However, these values were all obtained by using transconductance measurements on a single SWNT, an experimental setup much different to the one utilised in this thesis.

The difference in the decay of photocurrents observed with differently size separated nanotubes as shown in section 4.3.6 are not, as yet, fully explained and further work is required to ascertain the true nature of charge transport on them.

5.3.5 - Bi-Molecular Recombination in 1D

The sub-linearity of peak photocurrent versus light intensity as shown in section 4.3.7 is an interesting phenomenon which strongly suggests that bimolecular recombination plays a part in limiting the magnitude of the photocurrents [**67**]. This sub-linearity has been observed by other workers on SWNT mats and networks **[48]** although no attempt at a serious explanation has been made by them.

In chapter 2, the loss mechanisms section (2.7) described the characteristic rate equations for a 3D system. As nanotubes do not fit into this category, we propose the following model:

Consider figure 5.19, which is a cartoon representation of a photo-generated exciton being created on a semiconducting carbon nanotube of length ***L*** and subsequently broken apart by an electric field. Assume the electrodes are placed at either end of the nanotube so that the electrode separation is also equal to ***L***.

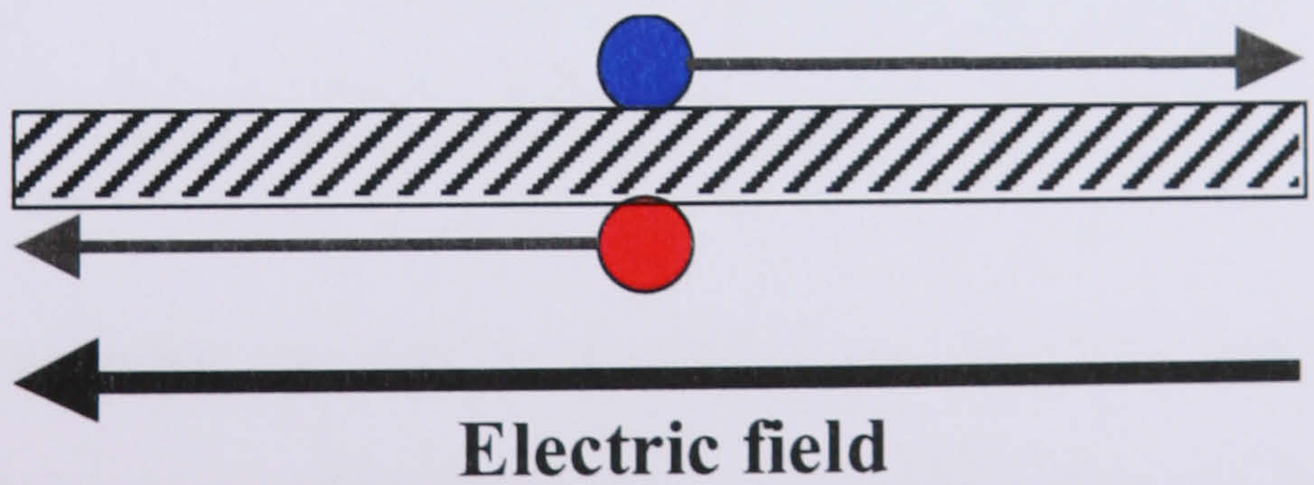

Figure 5.19: Ideal Unbound Exciton motion on a Carbon Nanotube

Assuming no traps or defects, the combined scalar distance the electron (blue circle) and hole (red circle) will traverse will be the total length ***L*** of the nanotube. The resultant current associated with this event, when integrated, will give a charge of ***Q=es/L*** which equates to ***Q=e*** (because we have assumed no defects/traps and so the

carrier range, s, is limited only by the length of the nanotube which corresponds to the electrode separation).

If we now double the light intensity, we also double the probability of the creation of a photogenerated exciton which could result in two electron/hole pairs being created on the same semiconducting tube (as demonstrated in Figure 5.20). This possibility of multiple excitons created on the same tube is to be discussed. We will make the assumption that electrons and holes from separate excitons will always undergo bimolecular recombination if they meet with each other.

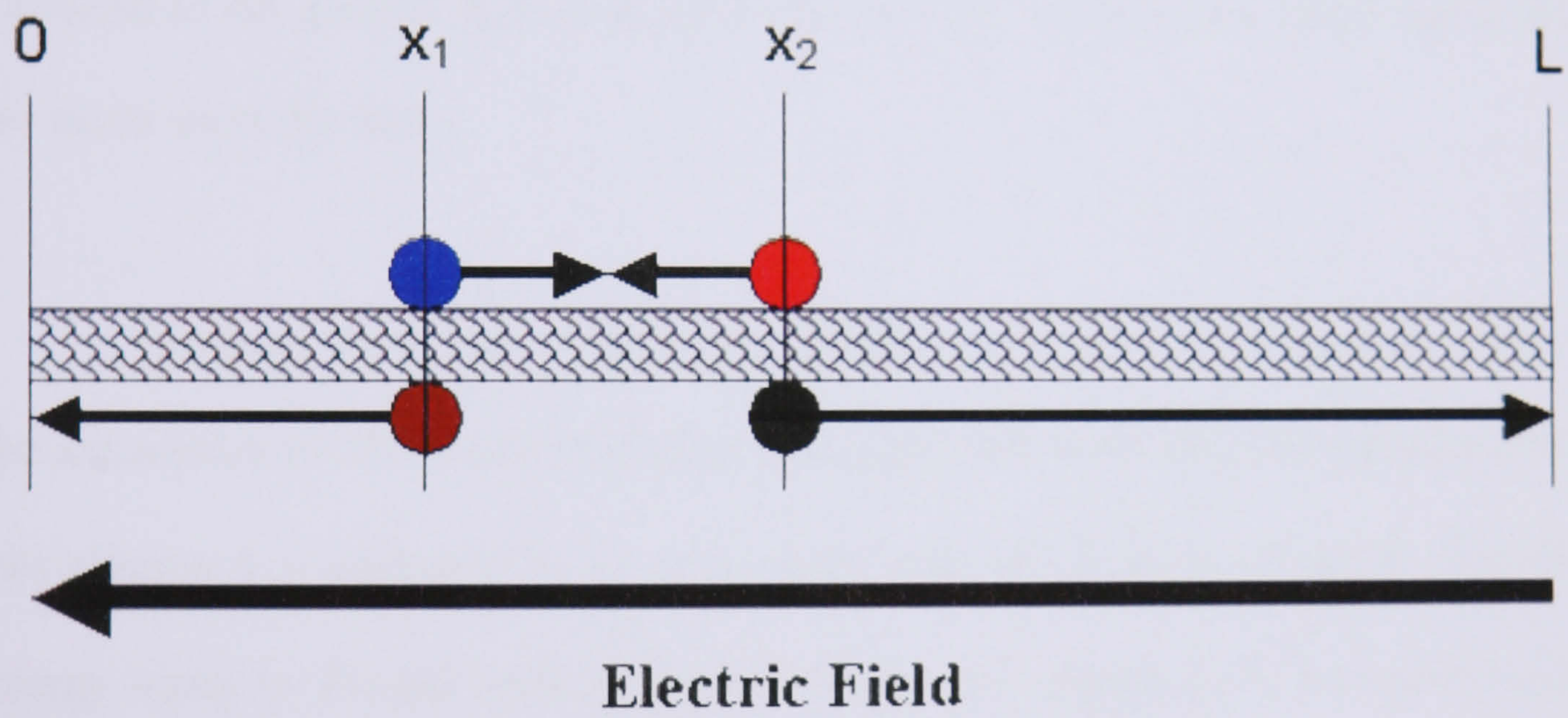

Figure 5.20: Multiple Excitons on Nanotube

We can calculate the total charge measured for this event by summing the corresponding charges caused by the individual carrier motions, as listed below (where μ_e and μ_h are the electron and hole mobilities respectively).

Hole at x_1 ● $Q_1 = \frac{e}{L} x_1$

Electron at x_1 ● $Q_2 = \frac{e}{L}(x_2 - x_1)\left[\frac{\mu_e}{\mu_e + \mu_h}\right]$

Hole at x_2 ● $Q_3 = \frac{e}{L}(x_2 - x_1)\left[\frac{\mu_h}{\mu_e + \mu_h}\right]$

Electron at x_2 ● $Q_4 = +\frac{e}{L}(L - x_2)$

If the individual charges are added together, the total charge is the same as for the case of just one ionised exciton on the nanotube, i.e., $\boldsymbol{Q=e}$. This procedure can be extended to the general case of $\boldsymbol{n}$ carrier pairs being created on a single nanotube and the result stays the same.

Another view of this is that no matter how many pairs are created on a tube, with the assumption of 100% recombination of carriers that meet, the final product is always two charges ± e separated by $\boldsymbol{L}$, or a dipole moment $\boldsymbol{\mu=eL}$ in a field $\boldsymbol{E}$. This has an energy equal to $\boldsymbol{U=-\mu E=-eEL}$. To conserve energy, charge $\boldsymbol{Q}$ in the external circuit travels to the electrodes with work being done equal to $\boldsymbol{QV}$. Thus, we end up with the familiar equation which we first derived in chapter 2:

$$QV = \frac{eVL}{d} \Rightarrow Q = \frac{eL}{d}$$

Therefore, increasing the light intensity to create more than one free carrier pair on a semiconducting nanotube will not result in an increase of measured charge.

From this important deduction we can formulate a theoretical relationship between the photocurrent of a SWNT sample and the light intensity used to excite carrier pairs. In order to help facilitate the development of this model, we shall start by assuming that all nanotubes in our sample are semiconducting. Let us start by assessing the probability of exciton creation:

The probability of creating an exciton $P(e^-,h^+)$ on a nanotube in a finite length of the tube, dx, is given in equation 5.17.

$$P(e^-,h^+)dx = \{\eta\phi\}\rho dx \qquad (5.17)$$

where ρ is the probability per unit length that a photon is absorbed and $\{\eta\phi\}$ is the probability that the absorbed photon creates an exciton which then dissociates into an electron-hole pair. Equation 5.17 gives us the probability of an excitation occurring within a length dx. Therefore, the probability of no excitation P^0 occurring in the same segment would be:

$$P^0 = 1 - \{\eta\phi\}\rho dx \qquad (5.18)$$

Consequently, the probability of no excitation occurring on the entire length of the tube would be:

$$P^0 = (1 - \{\eta\phi\}\rho dx)^{\frac{L}{dx}} = \exp[-\{\eta\phi\}\rho L] \qquad (5.19)$$

It follows then that the probability of one or more excitons occurring somewhere on the total length of the nanotube would be equal to:

$$P(e^-, h^+) = 1 - \exp[-\{\eta\phi\}\rho L] \tag{5.20}$$

If we now consider a sample of N_T individual semiconducting nanotubes of an average length L in a given excitation volume illuminated with a pulse of light containing N_{ph} photons (all of which are absorbed), we can use the following model to give a relationship between the light intensity and ρ:

By envisaging a one-dimensional scenario with each nanotube being laid horizontally end-to-end with the light being focused in a line over the total length of the arrangement (as one can not use the term area in a 1D situation), by dividing the total number of photons by the total length of the arrangement, we can deduce a probability per unit length of a photon being absorbed, which is given by equation 5.21.

$$\rho = \frac{N_{Ph}}{N_T L} \tag{5.21}$$

We can now propose use equation 5.21 in 5.20 to find the probability of creating electron/hole pairs on a single nanotube as a function of light intensity. This is given in equation 5.22 and can more accurately be described as the probability of having one or more dissociated carrier pairs on a nanotube as a function of light intensity.

$$P(e^-, h^+) = 1 - \exp\left(-\frac{\{\eta\phi\}N_{ph}}{N_T}\right) \tag{5.22}$$

As noted earlier, each of these tubes, with any number of free carrier pairs, will contribute one unit of signal to the overall photo signal, V_{sig}, irrespective of the number

of excitations. By one unit of signal, we could be referring to the photocharge generated (if in charge integration mode) or the peak photocurrent (if in current mode). By integration we refer to the situation where the response time, τ of the oscilloscope is much greater than the speed of the signal (i.e. the case with the mode locked YAG laser).

In a sample of N_T nanotubes, the relationship between the signal, the number of incident photons and concentration would be:

$$Signal \propto N_T \left\{ 1 - \exp\left(-\frac{\{\eta\phi\} N_{ph}}{N_T} \right) \right\} \tag{5.23}$$

If we are in current mode, we can write more specifically:

$$V_{sig} = V_0 N_T \left\{ 1 - \exp\left(-\frac{\{\eta\phi\} N_{ph}}{N_T} \right) \right\} \tag{5.24}$$

V_0 is equal to equation 5.25 where R_L is equal to the load resistor and τ is the response time.

$$V_0 = \frac{eR_L}{\tau} \tag{5.25}$$

If in integration mode, the photocharge induced on the electrodes, of separation d, will be equal to:

$$Q = \frac{eLN_T}{d}\left\{1 - \exp\left(-\frac{\{\eta\phi\}N_{Ph}}{N_T}\right)\right\} \tag{5.26}$$

This will result in a peak photocurrent, I_p, being detected equal to equation 5.27, where τ is the rise time of the oscilloscope. This will also be equivalent to the voltage measured by the scope, V_P, divided by the 50Ω load resistor, R_L given simply by Ohms law.

$$I_p = \frac{Q}{\tau} = \frac{V_P}{R_L} \tag{5.27}$$

We can simplify equations 5.26 and 5.27 by recasting as:

$$I_p = I_\infty\{1 - \exp(-kN_{ph})\} \tag{5.28}$$

For equation 5.28, the parameters I_∞ and k are given by equations 5.29 and 5.30 respectively. We are now making the more rigorous assertion that the previously described length, L, of the nanotube is now the average projected length of the tube onto the direction of the electric field, which we denote as $\langle L_E \rangle$. In chapter 2 we showed that $\langle L_E \rangle$ would be equal to half the nanotube length if a random alignment of tubes were present.

$$I_\infty = e\frac{\langle L_E \rangle}{d}\frac{1}{\tau_e}N_T \tag{5.29}$$

$$k = \frac{\eta\phi}{N_T} \tag{5.30}$$

5.3.6 – Application of the Bi-Molecular Model

By taking previous data already included in this thesis, the recombination model was applied and the fits that follow are of the nature: $I_p = I_\infty[1-\exp(-kN_{ph})]$ (equation 5.28). The data was fitted using the 'Origin' software package. When the data points were entered (I_p and N_{ph}), the program 'Origin' was able to produce a fit to equation 5.28 and give values for I_∞ and k which corresponded to the best fit. An example of this is shown in figure 5.21 and is a screenshot from the Origin program where the original program formatting has been retained (the numbering on the x-axis is unconventional and translates, for example, as 1.00E+015 being equal to 1.00×10^{15}).

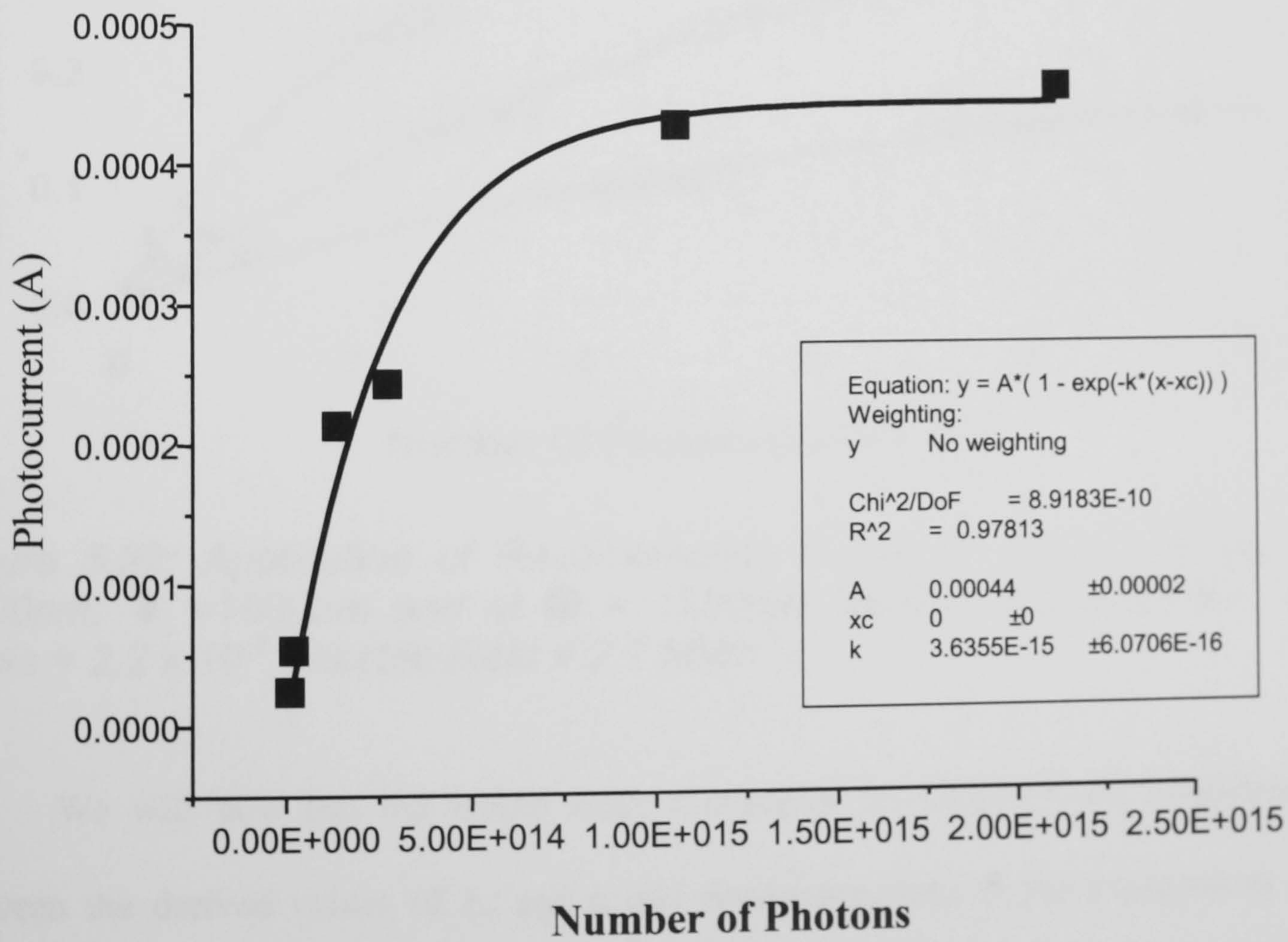

Figure 5.21: Origin Screenshot of Fitted Data for Recombination Model

The fit results in figure 5.21 give values of k and I_∞ (denoted as A in the fit values). These values are 3.64×10^{-15} and 4.4×10^{-4} respectively.

We will start off by applying the model to the data shown in the previous chapter, specifically, figure 4.35, where it was originally noted that a sub-linear relationship existed between the peak photocurrent and the light intensity. The original data with the recombination model overlaid is displayed in figure 5.22, which initially suggests a good agreement between the experimental results and the theoretical expectations at different excitation wavelengths.

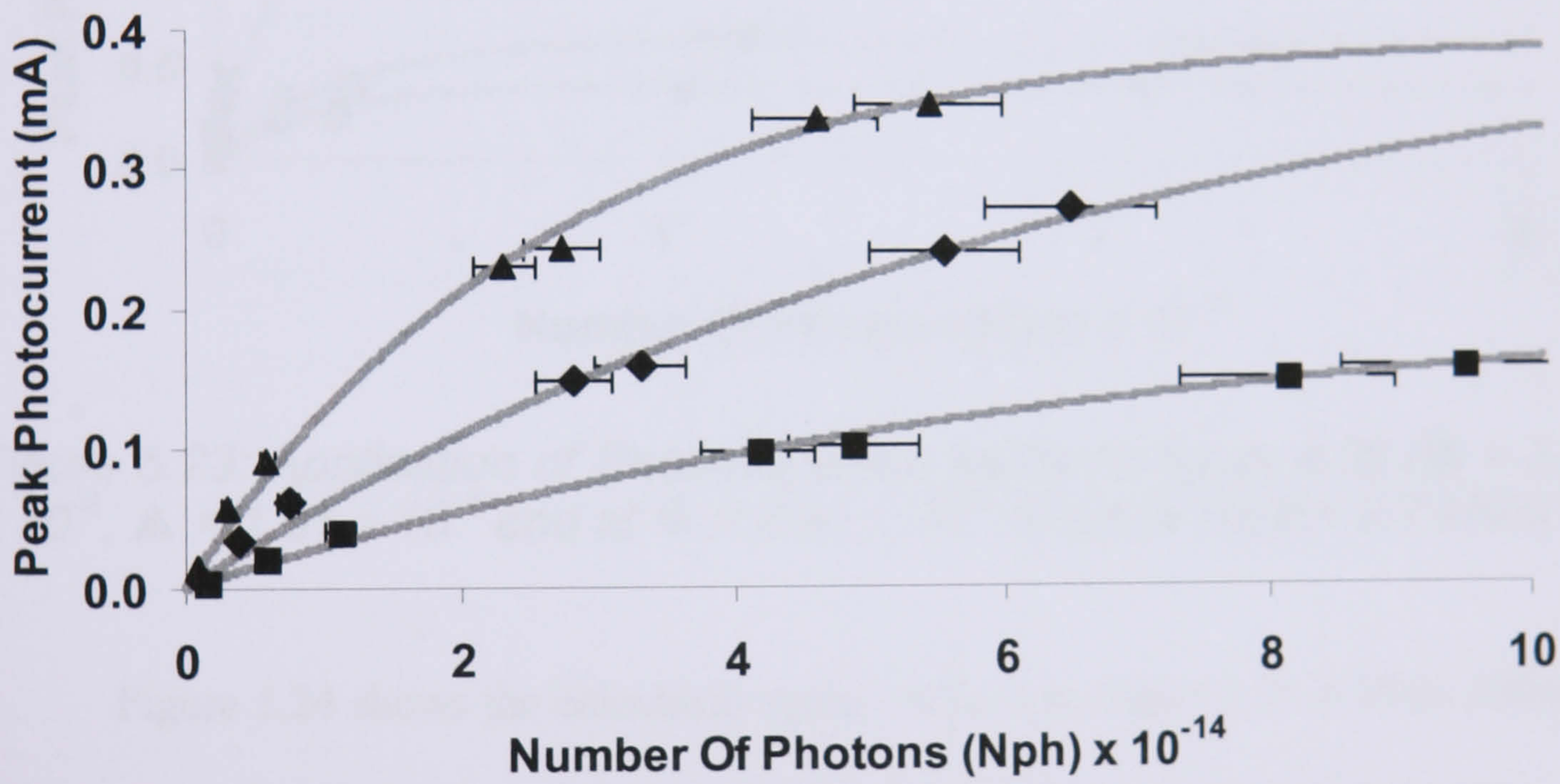

Figure 5.22: Application of Recombination model to figure 4.35 (▲ = 1300nm, ◆ =1600nm and at ■ = 1700nm. Sample Concentration by mass = 2.2×10^{-4}, Electric Field = 2.7 MVm^{-1})

We will now test the model more thoroughly by checking the consistency between the derived values of I_∞ and k and comparing them to the expectations of equations 5.29 and 5.30.

Equation 5.29 predicts that the value of I_∞ should be proportional to the number of nanotubes in the sample (i.e., the concentration, C_T). To test this, we have applied the recombination model to the data of figure 4.36, which again shows a good agreement (figure 5.23), and then tested whether the deduced values of I_∞ versus concentration follow the form of equation 5.29.

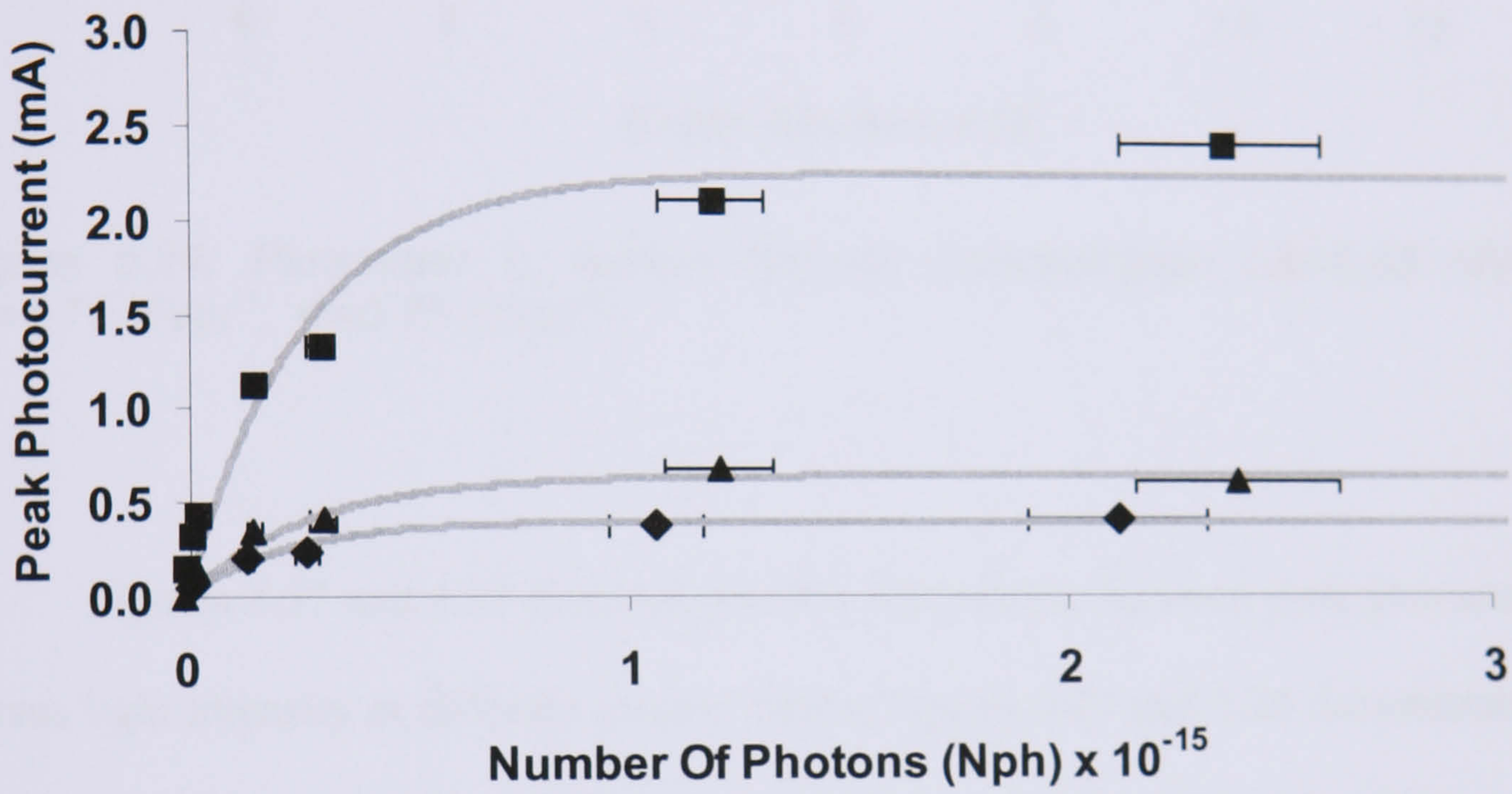

Figure 5.23: Application of Recombination Model to figure 4.36 (■ = 3.00 x 10^{-4}, ▲ = 1.61 x 10^{-4} and at ◆ = 0.81 x 10^{-4}. Electric Field = 2.7 MVm^{-1})

Figure 5.24 shows the calculated values of I_∞ from figure 5.23 at three different fields as a function of concentration. The expected linearity of I_∞ with C_T is found.

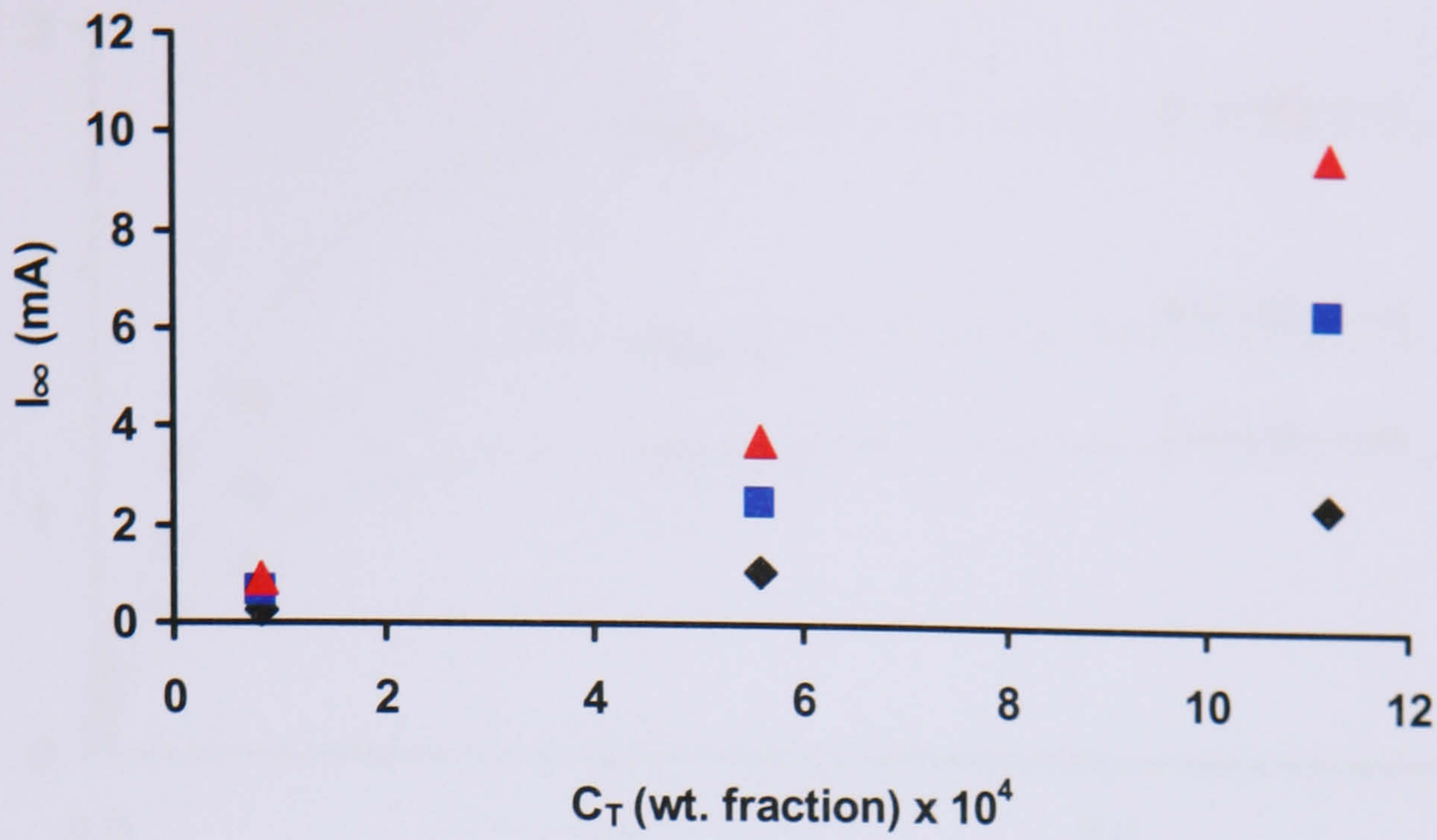

Figure 5.24: Parameter I_∞ versus Sample Concentration (▲=2.68 MVm^{-1}, ■=1.71 MVm^{-1}, ◆=0.75 MVm^{-1})

Figures 4.37 and 4.38 demonstrated the relationship between peak photocurrent versus light intensity at different electric fields. Figures 5.25 and 5.26 demonstrate the model applied to these two different samples and, once again, there does not appear to be a conflict between the theory and the experimentally obtained results. By using the derived values of $\boldsymbol{I_\infty}$ and $\boldsymbol{k}$, we are able to test the applicability of the model further.

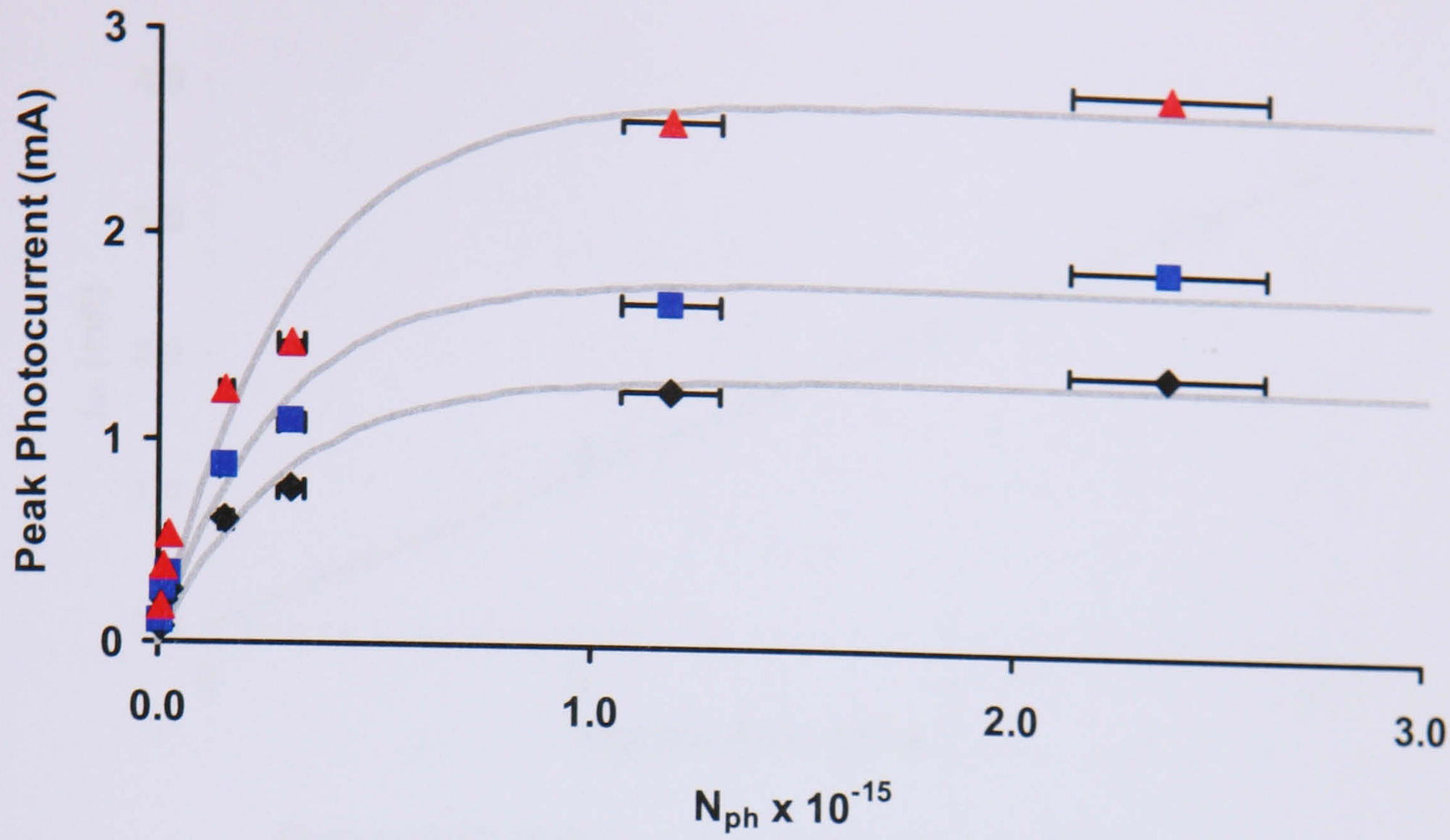

Figure 5.25: Application of Recombination model to Figure 4.37 (▲ = 2.32 MVm^{-1}, ■ = 1.50 MVm^{-1} and at ◆ = 1.00 MVm^{-1}. Sample Concentration by mass = 3.0 x 10^{-4})

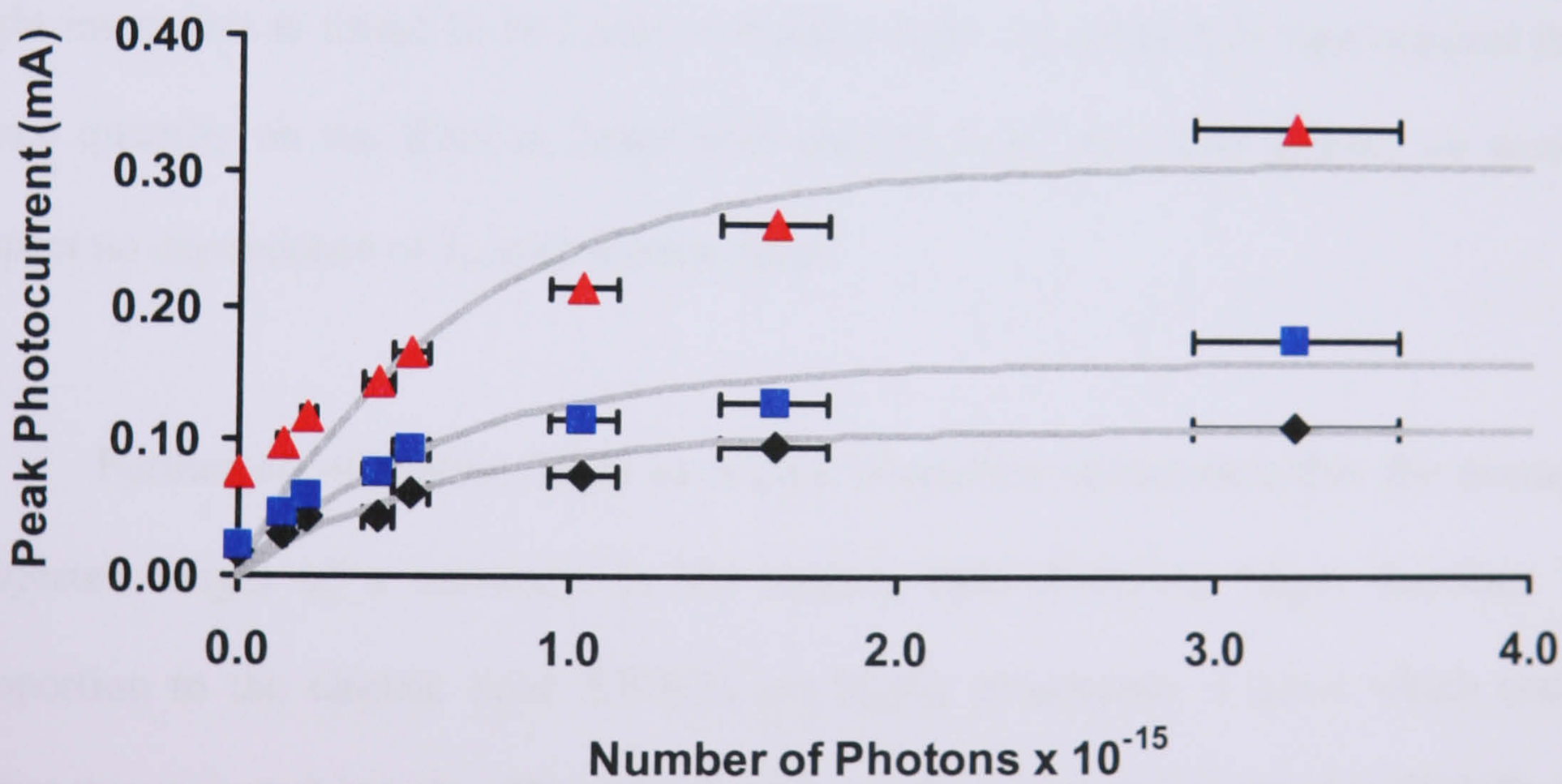

Figure 5.26: Application of Recombination model to figure 4.38 (▲ = 2.68 MVm^{-1}, ■ = 1.50 MVm^{-1} and at ◆ = 1.00 MVm^{-1}. Sample Concentration by mass = 2.2 x 10^{-4})

Figure 5.27 demonstrates the relationship between the derived value of I_∞ and the electric field for the data presented in figure 5.25, a relationship that has been observed in all experiments performed.

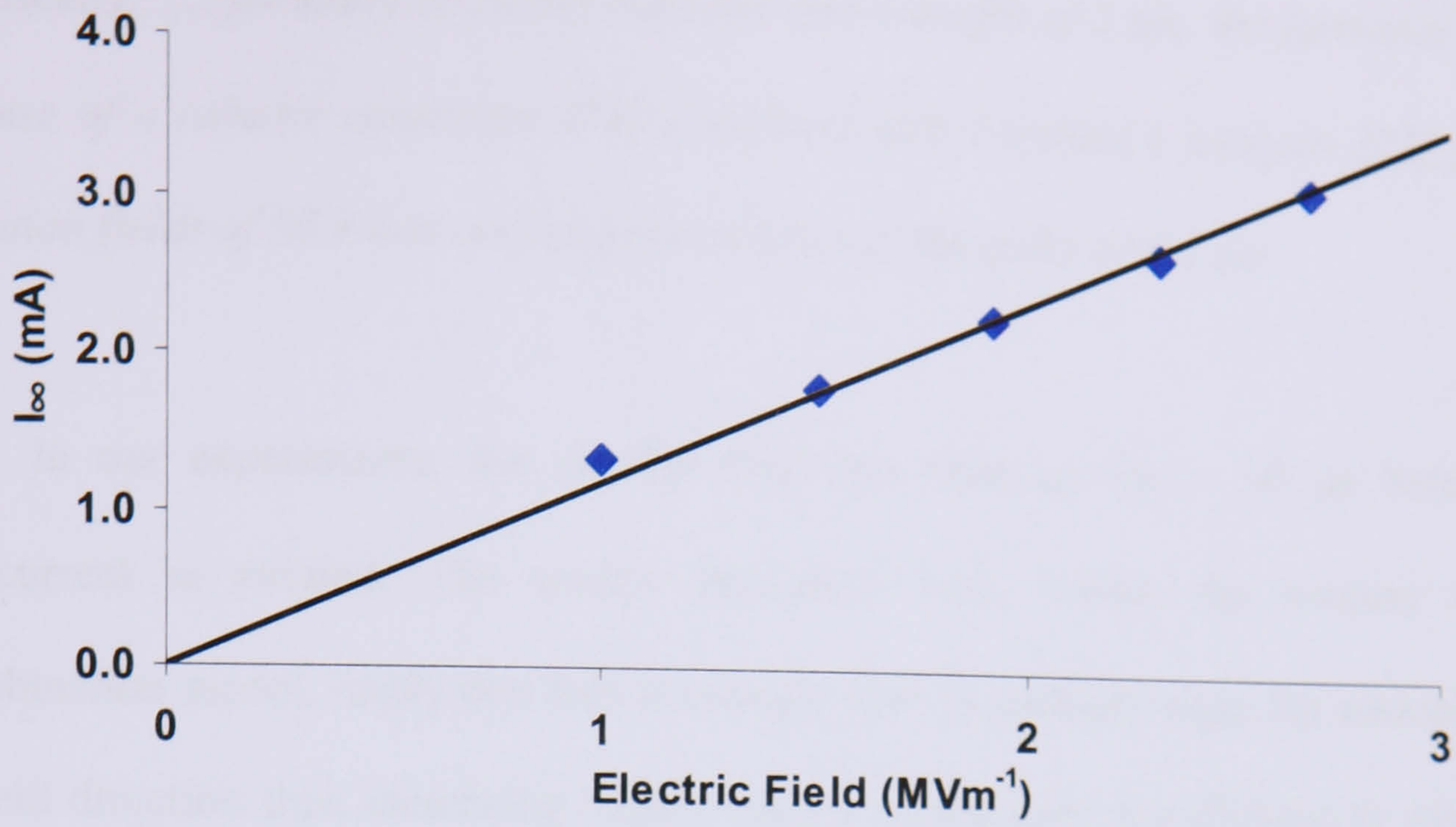

Figure 5.27: Parameter I_∞ versus Electric Field

It is observed from Figure 5.27 that the relationship between $\boldsymbol{I_\infty}$ and electric field is linear and goes through the origin. In other words, the value to which $\boldsymbol{I_p}$ tends at high light intensities is found to be linear in electric field. Equation 5.29 then requires that some quantity on the RHS is linear with electric field. At a first glance; we would expect no dependence of $\boldsymbol{I_\infty}$ with electric field.

Further consideration leads us to the interesting speculation that the average projected length of a nanotube in the electric field direction, $\langle \boldsymbol{L_E} \rangle$, increases in proportion to the electric field. SWNTs are highly polarisable, a factor which could affect the projected lengths. Theoretical work confirms this and shows that SWNTs do have high polarisabilities, with metallic tubes being more so than semiconducting tubes **[68]** and electric field induced alignment has already been demonstrated experimentally **[69]**.

Bubke et al **[70]** have presented work on the optical anisotropy of dispersed carbon nanotubes in ethanol induced by an electric field where they attempted to

compare their measured results with theoretical predictions. They state that, theoretically: '*... for tubes of 10 nm diameter and a length of 2 μm, the formulae for the response of a tubular conductor* ***[71]*** *combined with Fishbine's analysis [72] predict saturation fields of 50 V/mm and alignment times of the order of 0.1 ms*'.

In our experiments, the electric field has been on for ~ 10 μs before the photocurrent is excited. The results presented here, within the context of the recombination model, imply that this is enough time to partially align the nanotubes in the field direction thus increasing $\langle L_E \rangle$. Such a mechanism is sufficient to explain a factor of two increase of I_∞ as the tubes go from random alignment to full alignment. The results of figure 5.27, however, indicate that more than a factor of two is needed in any full explanation.

One way to achieve a greater increase requires that light is increasingly absorbed by semiconducting tubes as the electric field is increased, in comparison to the metals which do not play a part in the photoconductive process. This may come about as follows:

The Nd:YAG laser is polarised perpendicular to the direction of the electric field. Before reaching the sample it is coupled into the sample cell by focussing into a short 3cm stub of 2mm diameter quartz rod. This procedure has been measured to have a negligible effect on the polarisation of the laser light which continues to be effectively polarised perpendicular to the applied electric field. This is demonstrated in figure 5.28.

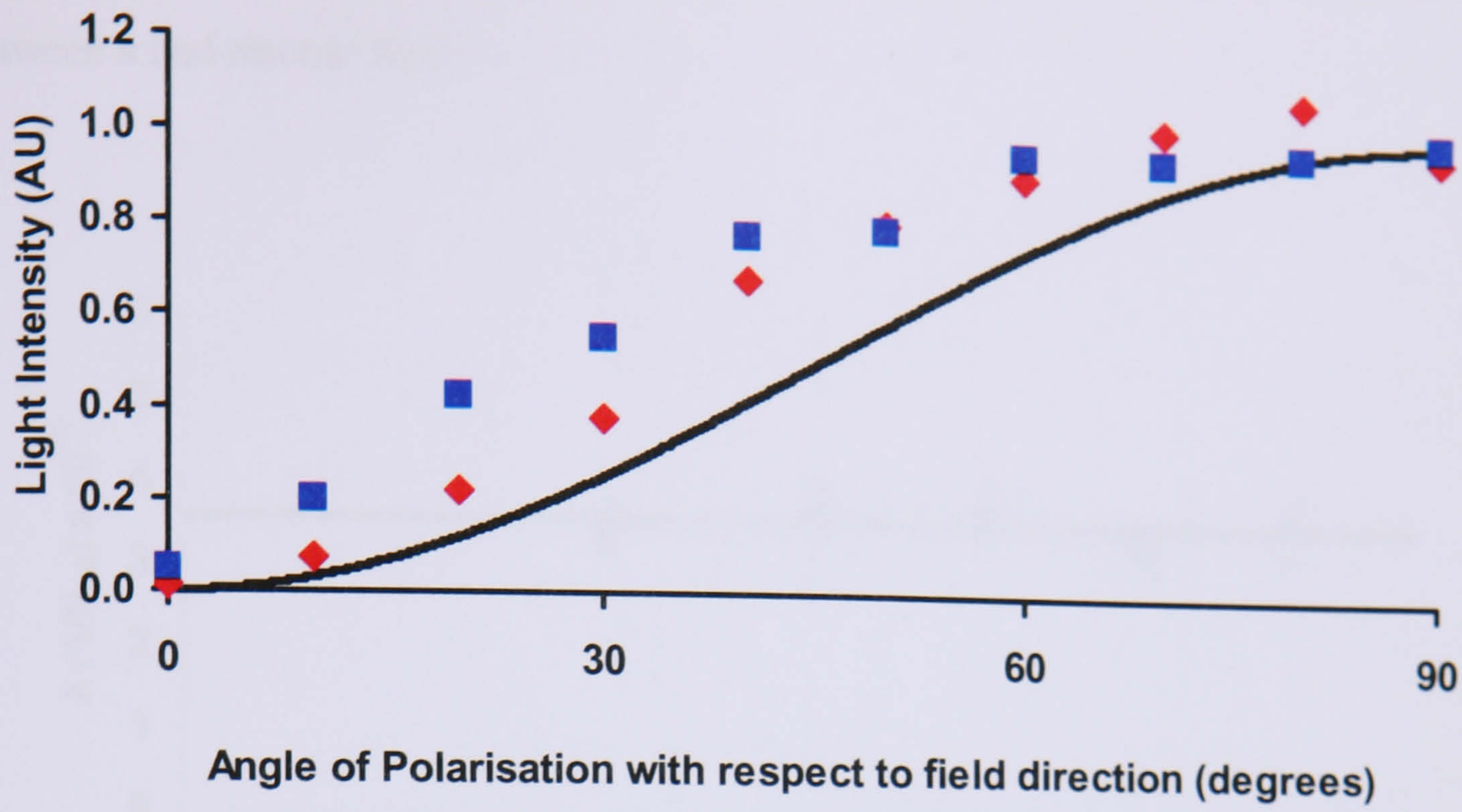

Figure 5.28: Light intensity versus polarisation angle of Nd:YAG laser (■ = through Quartz Rod, ◆ = Directly, Solid Line = Theory).

Metallic tubes align more readily in an electric field than semiconducting tubes as they have a greater polarisability, typically three orders of magnitude greater depending on their precise geometry [**68**]. Therefore, it is reasonable to assume that the metallic tubes will align parallel to the field relatively faster than the semiconducting tubes. We could therefore speculate that after a reasonable alignment time, the semiconducting tubes could still remain in a random distribution while the metallic tubes have reached full alignment.

The polarised light would then be preferentially absorbed by the semiconducting tubes while the metallic tubes would absorb very little owing to their orientation. In effect, alignment of the metallic nanotubes 'purifies' our photoactive semiconducting suspension and effectively increases the concentration of the photoactive components.

By using the ***k*** parameters associated with the fits of figure 5.25, we can plot the relationship between ***k*** and electric field. This is demonstrated in figure 5.29. The

relationship of I_∞ with field was consistent in all experiments as was the relationship between k and electric field.

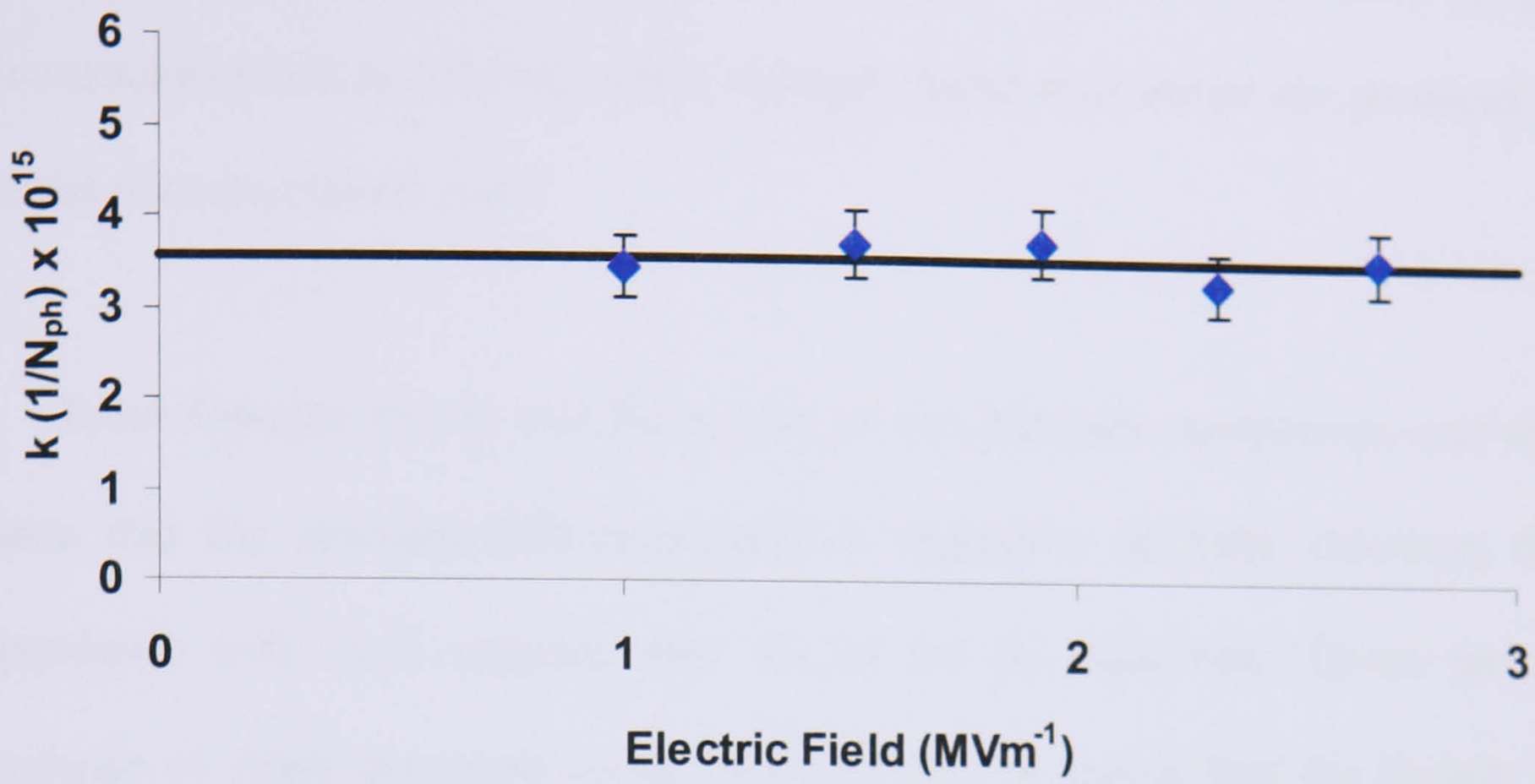

Figure 5.29: Parameter 'k' versus Electric Field

Figure 5.29 shows k to be independent of field. This is an interesting result as we have defined k to be given by equation 5.30 and therefore would expect to see a linear relationship with $\{\eta\phi\}$. It can now be argued that this demonstrates that the probability of carrier pair separation, ϕ, for SWNTs is independent of electric field. This leads to a paradox in our interpretations as we have already shown that $\{\eta\phi\}s$ is linear in field, although we do speculate that the carrier range s may be proportional to field due to nanotube alignments.

It has been established that for some other organic materials, such as Anthracene, the value of ϕ is field dependent **[73]**. However, for one dimensional organic materials (such as polymers), ϕ has been shown to be strongly field dependent demonstrating linearity and tending to zero at a zero applied electric field **[74, 75]**.

The field dependence observed in these polymer 1D materials (which are typically low mobility organic materials), can be explained by the photogeneration of strongly bound excitons which require an electric field to dissociate. The fact this is not so with SWNTs suggests that nanotubes have more in common with inorganic semiconductors (such as Silicon), where strongly bound excitons are not produced after the initial photoexcitation event.

From Onsager theory and the results of our previous experiments, one would presume that the quantum efficiency $\{\eta\phi\}$ is dependent on field. However, the $\boldsymbol{k}$ independence with field suggests that this is not the case here. Given the field dependence of $\{\eta\phi\}s$ discussed earlier, it could now be argued that the electric field increases the carrier range on a nanotube and does not affect the velocity. An independence of carrier velocity with field has already been suggested due to the high mobilities measured independently and also by our own work when looking at tail decays versus field. This could arise through field assisted tunnelling of carriers through defects on the nanotubes.

From equation 5.30, one would expect an inversely proportional relationship between $\boldsymbol{k}$ and concentration (as N_T would be linear with concentration). Figure 5.30 confirms this and shows a good agreement with the theoretical predictions.

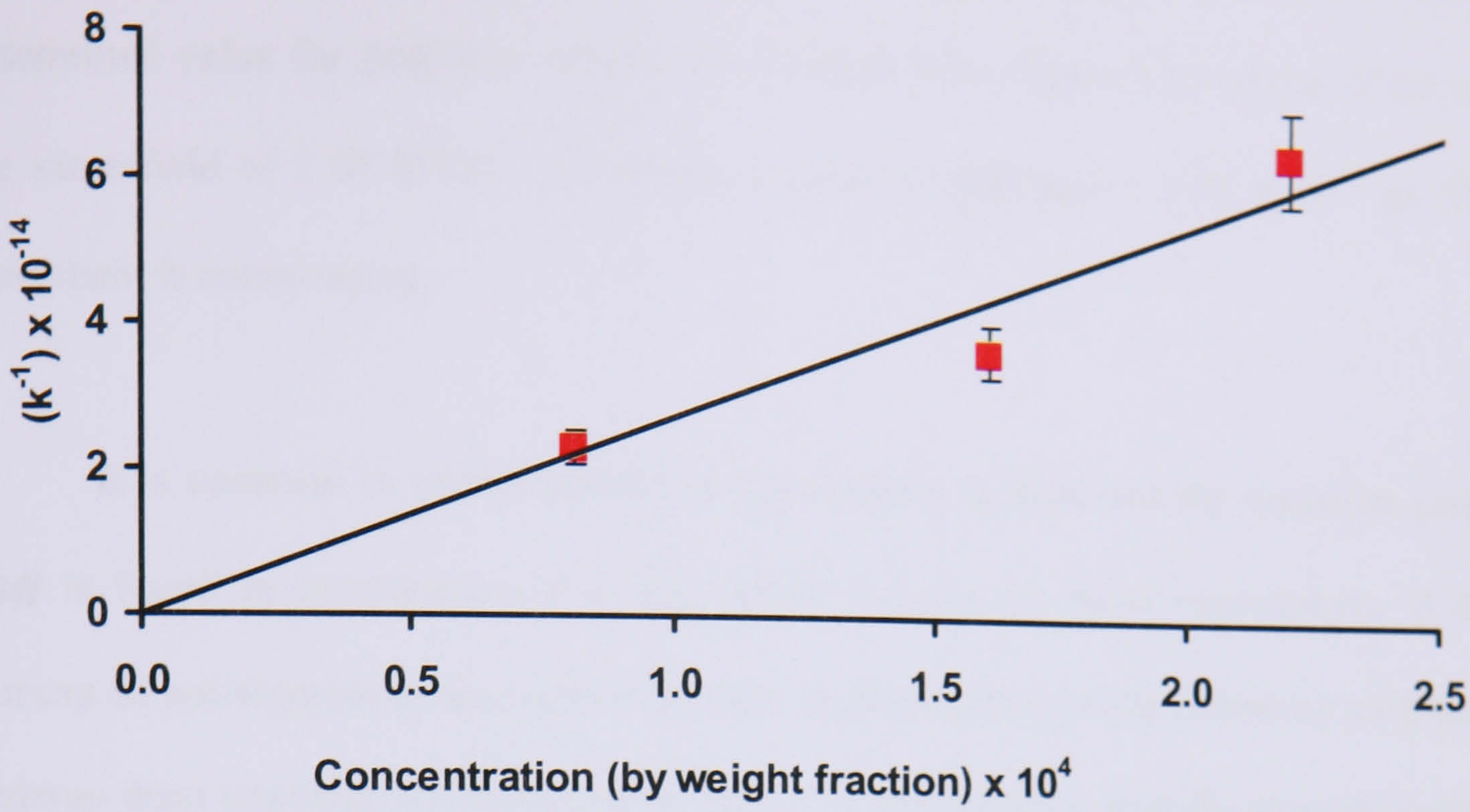

Figure 5.30: Parameter 'k' versus concentration

The accurate variation of C_T is a difficult task to achieve and great care was taken to obtain the raw data from which figure 5.30 was composed. We feel that any very small departures from linearity seen in figure 5.30 are explicable in terms of the difficulty in obtaining accurate concentrations.

The quantity N_T is poorly known, however it is possible to obtain some numerical information regarding these experiments and the model. Examination of equations 5.29 and 5.30 indicate that the quantity N_T may be cancelled by taking the product, as shown in equation 5.31.

$$kI_\infty = e\frac{\eta\phi}{\tau}\frac{\langle L_E \rangle}{d} \qquad (5.31)$$

This will be linear in electric field and at a typical field of E = 2.68MVm^{-1} we find kI_∞ = 1.1 x 10^{-17} A. With a knowledge of τ_e = 150ps, the quantity $\{\eta\phi\}\langle L_E\rangle$ =

1.03×10^{-11} m has been determined. This is a factor of five larger than our previously determined value for $\{\eta\phi\}\langle s_E\rangle$ which we extracted from figure 5.15 where, if we use the same field of 2.68 MVm^{-1}, we obtain a value of $\{\eta\phi\}\langle s_E\rangle = 1.76 \times 10^{-12}$ m. The agreement is encouraging.

It is common in photoconduction experiments to find that the quantum yield, $\{\eta\phi\}$ is found in combination with the carrier range s. In these experiments, if the carriers do not separate to the ends of the tube as assumed but some distance s until they undergo deep trapping, we must replace $\langle L_E\rangle$ in all equations with the average carrier range projected onto the field direction $\langle s_E\rangle$. The surprisingly small value for $\{\eta\phi\}\langle s_E\rangle \approx 10^{-11}$ m – 10^{-12} m may be re-interpreted in two limiting cases:

a) If we assume that $\langle s_E\rangle = \langle L_E\rangle = 10^{-6}$ m then the quantum yield of 10^{-5} is extremely small. Such a small value for the yield is difficult to understand in the absence of strongly coupled electron-hole pair evidence and accompanying field assisted dissociation.

b) The alternative limit would assume a quantum yield of 1 and the value of $\langle s_E\rangle$ would be 10^{-11} m. Again such a small value is unphysical and cannot be allowed. Indeed, for the model that produced the number to be self consistent there must be a possibility that electrons and holes from different pairs on the same tube meet thus providing some constraint on how small $\langle s_E\rangle$ may be. It would suggest that $\langle s_E\rangle$ is within an order of magnitude of $\langle L_E\rangle$.

Clearly, alternative (a) must be more approximate to the truth in order for the model to work in its own terms.

5.3.7 - SWNT Conclusions

We have presented reproducible results on the fast transient photoconduction of Single Walled Carbon Nanotubes. We have demonstrated time resolved photocurrent signals and investigated the electric field, concentration, tube length, wavelength and light intensity dependence, which has led to the proposal of a one dimensional bimolecular recombination model. This model fits the observations well.

We have measured the quantum efficiency/carrier range product using two different methods and found them to be comparable. A more detailed summary of the final conclusions for all of the results presented can be found in the following chapter.

Chapter 6 – Conclusions

6.1 Encapsulated Polymers

In the previous chapters we have shown that the encapsulated polymers did not produce any measurable photocurrents and were able to reasonably dismiss some possible reasons why this was so, specifically: that the zeolites did not contain any active material and that light was not able to penetrate the zeolite structures and excite the material within.

Possible reasons that remain include the likelihood that isolated chains may not yield many free carrier pairs that have escaped geminate recombination. It is possible that, in a network of interacting chains, one of the carriers in an exciton may migrate to a neighbouring chain which would then greatly reduce the probability of geminate recombination and would result in a greater number of free, mobile charge carriers. In the present case, this mechanism for reducing the effect of geminate recombination is not available.

Isolated chains or not, as the polymerisation reaction occurs in situ there has been no attempt, or indeed an established method, to characterise the encapsulated chain lengths. Any attempt to remove the zeolite structure and extract the fractions therein would undoubtedly result in the destruction of the polymer as well. As a negligible carrier range will result in a negligible charge being measured externally, it is likely that this may be the case. However, without subsequent knowledge of the chain lengths, we are unable to speculate on the carrier range at this time.

Further to these suppositions, we may also draw attention to the large internal electric fields that have been shown to exist within zeolites which are, ***locally***, a factor of 10,000 greater than the fields we have used in the experiments presented here. We were obviously unable to utilise equivalent electric fields for this work as electrical breakdown would occur well before the impractical fields of > GVm^{-1} were reached.

Without further information, the reason that null results were found could be due to any one of the above conjectures, or a combination of all three. We are therefore forced to conclude that the uses of zeolites (valuable as they are in chemistry, for example in petrochemical cracking reactions) are ineffective for experiments of this nature. If further work was to be carried out on these materials, it would be useful to quantify the lengths of the polymer chains to allow us to confirm or deny one of our hypotheses. As was stated earlier, NMR could be a possible candidate for retrieving such information.

6.2 Discotic Liquid Crystals

By using the Time of Flight technique, we have presented direct measurements for the quantum efficiencies and mobilities of some Discotic Liquid Crystals. We have also demonstrated that TOF and continuous irradiation methods give comparable Quantum Efficiency results, explaining that the TOF technique is preferable when the dark current is high.

Nakayama *et al* fitted their Quantum Efficiency results for HAT6 to the Onsager three dimensional model for charge carrier generation. This did not seem the obvious choice for what is essentially a one-dimensional conductor, but the results they present for HAT6 at a single temperature give a reasonable fit to theory. Although we obtained

a comparable result with HAT6: to test the fit to the Onsager theory more rigorously we have studied several discotic liquid crystals over a range of temperatures. We conclude that the agreement obtained with the Onsager model for HAT6 is fortuitous and that this model is not generally applicable.

We also present the interesting behaviour of the Triblock copolymer Discotic Liquid Crystal which, unlike other discotics based around a triphenylene system, shows conclusively that this material is not a hole transporter. We were able to infer a limit on the electron mobility of: $\mu e \leq 8.4 \times 10^{-3}$ $cm^2 V^{-1} s^{-1}$ as well as a lower limit on $\{\eta\phi\}$ at 1 MVm^{-1} of $\{\eta\phi\} \geq 4.76 \times 10^{-8}$.

The photogeneration rate is strongly affected by the electric field and as a result, the quantum efficiency has been shown to follow the Poole-Frenkel barrier lowering mechanism. From this model, we also derived the dielectric constants that the material has in both the discotic phase ($\varepsilon = 4.9$) and isotropic phase ($\varepsilon = 2.0$) and attribute this change to the sum of individual molecular polarisabilities adding constructively, being greater in the discotic phase due to a greater alignment amongst the molecules.

We show that photoconduction, that is, charge separation persists beyond the clearing point into the isotropic phase. This would explain the observation that the peak photocurrent falls slowly beyond the clearing point (figure 4.22) and that the mobility has two behaviours with temperature depending on the temperature range (figure 5.11).

We also show evidence that this columnar material is behaving as a one dimensional charge transporter where the trapping time varies inversely with electric

field. This conclusion is difficult to verify by experiment and should be the subject of further work.

6.3 Single Walled Carbon Nanotubes

This thesis has described measurements of fast photo conduction transients on semiconducting nanotubes in suspension using a specially designed impedance matched co-axial cell. The results obtained using this experimental arrangement show clear, reproducible, photocurrent transients. The transient photocurrent measurements were made as a function of the electric field, light intensity, wavelength and sample concentration. From them, the variation of peak photocurrent and the photocharge as field and concentration are varied have been shown. The behaviour of the amplitude of the photocurrent transient as light intensity is varied has led us to develop a one dimensional bimolecular recombination model which fits the observations well.

It is noted that both the photocurrent peaks and photocharge-carrier range product vary linearly with field. The peaks and charge also vary linearly with concentration. After measuring the absorption of the nanotube suspensions as a function of concentration, it is possible to correct for the number of photons absorbed in these measurements and to thus deduce a value for the quantum efficiency-carrier range product. This is linear in field and has the value $\{\eta\phi\}s/E = 6.58 \times 10^{-19}\ m^2V^{-1}$ which is sensibly independent of concentration.

At a field of 2.68 MVm^{-1}, typical of those used in these experiments, a quantum efficiency carrier range product of 1.76×10^{-12} m is implied. When derived from our bimolecular recombination model, a value of 1.03×10^{-11} m at the same field is found.

The fact that the two values are similar when found by two very different routes is indeed encouraging.

This is, however, a surprisingly low value and may mean that with the monochromatic source used here, most photons are absorbed by nanotubes that do not take part in the photoconduction process, e.g. metallic nanotubes and nanotubes in proximity to metallic tubes where the electric field will be severely reduced. It could also be suggestive of either strong geminate recombination or the presence of many defective nanotubes which results in a carrier range much less than our expectations, or a mixture of the two.

To resolve this uncertainty, future work should focus on performing the experiments with semiconducting tubes only. A method of separation currently being investigated has been mentioned earlier (dielectrophoresis). There is also a requirement for an experiment that is able to disentangle the quantum efficiency from the carrier range. It has already been suggested that a worthwhile experiment will involve the cutting of the nanotubes in order to reduce their length to less than that of the carrier range. When $L >> s$, as they are cut the measured photocharge will remain unaffected. Once the condition $L < s$ is reached there should be a systematic decrease of the measured photocharge as the tubes are cut further. In the absence of such experiments the two quantities remain for now enfolded.

Another unexpected phenomenon that suggests itself out of the model developed is that the nanotubes must be aligning with the applied electric field and the degree of alignment is proportional to the electric field. Such alignment leads to an increase in the photoelectric effect per pair created. Given the carrier mobility on the nanotubes within

our experimental arrangement and their high polarisability this speculation is eminently plausible and is now the subject of an ongoing research effort as many experiments suggest themselves to lend support to this suggestion or otherwise. It is hoped to report on the outcome of these experiments in the future.

6.4 Closing Remarks and Further Work

The most likely reason why the encapsulated polymers showed no evidence of photoconductivity is due to the presence of large intrinsic electric fields within the zeolites themselves, which are far in excess of the fields our samples were subjected to during the experiments. To finally resolve this question would require knowledge of the average chain lengths of the polymers and I would recommend this as future work. As the monomer gas was polymerised in-situ, the chain length characterisation was not known in advance.

It would be interesting to investigate the use of NMR to characterise these samples, where you could perform an estimate of the chain lengths by comparing the magnitude of the spectrum peaks which correspond the polymer material and the terminating end groups. Alternatively, ready made polymer chains could be characterised and then introduced into the zeolite channels.

The novel experimental methods described in this thesis for obtaining nanotube photocurrents yield unique results compared to the works of others. Unlike experiments where photoconductivity was studied on SWNT mats and networks where the nanotubes are in a fixed random orientation [**48**], the nanotubes in our sample

suspensions have the ability to move due to field induced alignment. The results presented here strongly suggest that such alignments are occurring.

The results presented here have led to further work being carried out on the Kerr effect of nanotubes [**76**] where it has been shown that considerable alignments occur within 500 μs at fields of 1 MVm^{-1}. The solution used here was dichloroethane which is considerably less viscous than the polymer oil used in our experiments.

To further this research, greater knowledge of the sample characteristics would be useful, for example: a better knowledge of the length distribution. Also, it would be interesting to see how the results differ if we have a sample of pure semiconducting nanotubes. This would require an efficient and reliable separation technique to be developed. Major advances can be made in this research when the sample quality is vastly improved. However, at present this is not possible.

Publications

"Photoconducting discotic liquid crystals". R.J.Bushby. O.R.Lozman, **J.C.Bunning**, K.J.Donovan, T.Kreouzis and K.Scott, Procs. of SPIE, 4991. 222. (2003)

"Molecular engineering the phototransport properties of discotic liquid crystals". K.J.Donovan, T.Kreouzis, K.Scott and **J.C.Bunning**, Mol. Cryst. Liq Cryst., 396, 91 2003

"Quantum efficiency of photogeneration in discotic liquid crystals: Part 1: Temperature and wavelength dependence". K.Scott, K.J.Donovan. T.Kreouzis and **J.C.Bunning**. Mol. Cryst. Liq Cryst., 397, 253, 2003.

"Quantum efficiency of photogeneration in discotic liquid crystals: Part 2: Electric field and temperature dependence". **J.C.Bunning**, K.J.Donovan, T.Kreouzis and K.Scott., Mol. Cryst. Liq Cryst., 397, 263, 2003.

"Observation of transient photocurrents on suspended nanotubes". **J C Bunning**. K J Donovan, K Scott, Journal of Applied Physics, Vol 96, 7, p 3939 (2004)

"Bimolecular recombination on carbon nanotubes". **J.C.Bunning**, K.J.Donovan, K.Scott.and M.Somerton, Phys. Rev. B., **71**, 8, 085412, 2005.

"Electron photogeneration in a triblock co-polymer discotic liquid crystal". **J.C.Bunning**, K.J.Donovan, R.J.Bushby, O.R.Lozman and Z Lu., Chem. Phys., 312, 144, 2005

Appendix

Appendix 1 – Response Times and Quadrature

Given the response of a system (oscilloscope), τ_1, and a separate adjunct with its own intrinsic response (sample, probe etc.), τ_2, the overall response of the system is found by adding the two responses in quadrature to give the effective response τ_{eff}.

$$\tau_{eff}^{\ 2} = \tau_1^{\ 2} + \tau_2^{\ 2} \qquad \text{(A.1)}$$

After the first filter, a delta function becomes a Gaussian with a width τ_1 and the following filter convolves this with a second Gaussian of width τ_2. This can be shown as follows:

(i) The effect of one of these on a delta function is to give a Gaussian:

$$\delta(t - t_0) \Rightarrow C \exp \frac{(t - t_0)^2}{\tau_1^{\ 2}} \qquad \text{(A.2)}$$

(ii) The effect of the second is found by convolution

$$f(t) = \int f(t')\delta(t - t')dt' = \int \exp\left(\frac{-(t_0 - t')^2}{\tau_1^{\ 2}}\right) \exp\left(\frac{-(t - t')^2}{\tau_2^{\ 2}}\right) dt' \qquad \text{(A.3)}$$

As this is a complicated integral, the program Mathematica was used to evaluate the above expression between the limits of $-\infty$ and $+\infty$. This yielded the following expression which confirms equation A.1.

$$f(t) = \sqrt{\pi\left(\frac{\tau_2}{\tau_1} + \frac{\tau_1}{\tau_2}\right)} \exp\left(\frac{-(t-t_0)^2}{\tau_1^{\,2} + \tau_2^{\,2}}\right) = \sqrt{\pi\left(\frac{\tau_1^{\,2} + \tau_2^{\,2}}{\tau_1 \tau_2}\right)} \exp\left(\frac{-(t-t_0)^2}{\tau_{eff}^{\,2}}\right) \qquad \text{(A.4)}$$

Appendix 2 – SWNT Band Gap Energies

The following table shows the calculated values of nanotube diameters and energy band gaps by the use of equations 1.2 and 1.3. Duplicate values of (m,n)=(n,m) have been removed. The wavelength range shown is equivalent to the IR range of wavelengths we obtained from the OPO.

Table A1 – Semiconducting SWNT band gaps.

n	m	Diameter (nm)	Band Gap (eV)	Excitation Wavelength (nm)
1	6	0.52	1.37	909
3	5	0.56	1.28	970
2	6	0.57	1.25	999
4	5	0.62	1.15	1082
2	7	0.65	1.10	1134
1	8	0.68	1.05	1184
4	6	0.69	1.03	1208
3	7	0.71	1.01	1232
1	9	0.76	0.94	1322
5	6	0.76	0.94	1322
3	8	0.78	0.91	1365
2	9	0.81	0.89	1406
5	7	0.83	0.86	1447
4	8	0.84	0.85	1466
2	10	0.88	0.81	1543
6	7	0.89	0.80	1562
4	9	0.92	0.78	1598
3	10	0.94	0.76	1634
6	8	0.97	0.74	1686

Acknowledgements

None of the work described here could have been carried out without the excellent supervision, advice and guidance of Dr. Kevin Donovan. I would not have made it this far without his experience and competence.

I would like to express my sincere gratitude to Dr. Ken Scott for the invaluable training and assistance I received in the experimental laboratory and also to Martin Somerton for the sample preparation of my nanotube suspensions.

I would like to thank Queen Mary as a whole for the pleasant working/educational environment it provides and for all the people I met here that made it all worthwhile.

Last, but by no means least, I would like to thank my parents for the support they gave me during my university career, both as an undergraduate and postgraduate. I hope someday I can make them as proud of me as I am of them.

References

[1] D. de Leeuw. *Physics World,* **12:31**, March 1999 – "Plastic Electronics"

[2] B. Goss Levi. *Physics Today*, **20**, February 2001 – "New printing technologies raise hopes for cheap plastic electronics"

[3] Chiang C K, Fincher C R, Park YW, Heeger A J, Shirakawa H, Louis E J, Gau S C and MacDiarmid A G 1977 *Phys. Rev. Lett.* **39** 1098–101

[4] H. Shirakawa and S. Ikeda, J. Polymer Sci. 2:3 (1971).

[5] Alan G. MacDiarmid, Reviews of Modern Physics, Volume 73, July 2001 Nobel Lecture: ''Synthetic metals'': A novel role for organic polymers.

[6] Alan J. Heeger, Reviews of Modern Physics, Volume 73, July 2001 Nobel Lecture: Semiconducting and metallic polymers: The fourth generation of polymeric materials

[7] Hideki Shirikawa, Reviews of Modern Physics, Volume 73, July 2001 Nobel Lecture: The discovery of polyacetylene film—the dawning of an era of conducting polymers

[8] J. Tsukamoto, A. Takahashi and K. Kawasaki. *Jpn. J. Appl. Phys.*, 1992, **41(6)**:509

[9] Donovan K J, Hargrave P, Scott K, Somerton M and Spagnoli S, 1998 *Phys. Rev. Lett.* **81** 3731

[10] T. Bein, *Stud. Surf. Sci. Catal.,* 1996, **102**, 295-321

[11] E. Ruiz-Hitzky and P. Aranda, *An. Quim., Int. Ed.,* 1997, **93**, 197-212

[12] M. Galletero, M. Alvaro, H. Garcia, C. J. Gómez-Garcia and A. K. Lay, *Phys. Chem. Chem. Phys.,* 2002, **4**, 115-120

[13] Designing the Molecular World, Phillip Ball, Page 69. Princeton University Press (1994). ISBN 0-691-00058-1

[14] H. W. Kroto, J. R. Heath, S. C. O'Brien, R. F. Curl and R. E. Smalley. C_{60}: Buckminsterfullerene. *Nature,* 318:162, 1985.

[15] A. Oberlin, M. Endo, T. Koyama, Carbon **14**, 133 (1976)

[16] A. Oberlin, M. Endo, T. Koyama, J. Cryst. Growth **32**, 335-349 (1976)

[17] M. Endo, *Mecanisme de croissance en phase vapeur de fibres de carbone (The growth mechanism of vapour-grown fibres).* PhD thesis, University of Orleans, Orleans, France (1975).

[18] "Helical microtubules of graphitic carbon", S Iijima *Nature*, vol.354, p56 (1991)

[19] "Single-shell carbon nanotubes of 1-nm diameter", S Iijima and T Ichihashi, Nature, **363**, 603 (1993)

[20] "Cobalt-catalysed growth of carbon nanotubes with single-atomic-layer walls", D S Bethune, C H Kiang, M S DeVries, G Gorman, R Savoy and R Beyers, Nature, **363**, 605 (1993)

[21] *Carbon Nanotubes – Synthesis, Structure, Properties and Applications*, Page 5, M S Dresselhaus, G Dresselhaus, Ph. Avouris (Eds.). Topics in Applied Physics **80**. Published by Springer-Verlag Berlin Heidelberg 2001. ISBN 3-540-41086-4

[22] L. Chico, V. H. Crespi, L. X. Benedict, S. G. Louie, M. L. Cohen, Phys. Rev. Lett. 76, 971-974 (1996)

[23] R. Saito, M. Fujita, G. Dresselhaus, M. S. Dresselhaus, Appl. Phys. Lett. 60, 2204-2206 (1992)

[24] J. W. Mintmire, B. I. Dunlap, C. T. White, Phys. Rev. Lett. 68, 631-634 (1992)

[25] X. Blase, L. X. Benedict, E. L. Shirley, S. G. Louie, Phys. Rev. Lett. 72, 1878 (1994)

[26] Dresselhaus, M. S., Dresselhaus, G., Avouris, Ph., (eds.): 'Carbon nanotubes: synthesis, structure, properties, and applications' Topics in Applied Physics 80 (Springer-Verlag, Berlin, Heidelberg, New York, 2000)

[27] Ch. Baerlocher, W.M. Meier and D.H. Olson, Atlas of Zeolite Framework Types, 5th revised edition , Elsevier, Amsterdam, 2001. (Diagrams used from website with kind permission: http://www.iza-structure.org/databases/). Correct at time of printing.

[28] Personal correspondence regarding SWNT sample AP8327R from Joe Williams, Manger of CarboLex Inc. 23 January 2003.

[29] Textbook of Practical Organic Chemistry – Fourth Edition. A. I. Vogel (1978). ISBN 0-582-44250-8

[30] F. Reinitzer, Wiener Sitzber. **94**, 719 (1888), ibid. **97**, 167(1888)

[31] O. Lehmann, *Flüssige Kristalle* (Wilhelm Engelmann, Leipzig, 1904).

[32] D. Vorländer. Z. Phys. Chem., 105:211, 1923.

[33] Chandrasekhar, S., Sadashiva, B. K. and Suresh, K. A., Pramana, 1977, 9, 471.

[34] Rukmal Aeysekera, Richard J. Bushby, Celine Caillet, Ian W. Hamley, Owen R. Lozman, Zhibao Lu and Anthony W. Robards. Macromolecules **2003**, 36, 1526-1533.

[35] L. Onsager, Phys. Rev. **54**, 554 (1938).

[36] R. R. Chance and C. L. Braun. J.Chem.Phys., 59, 2269 (1973).

[37] "Electronic Processes in Organic Crystals and Polymers", Second Edition. Pope & Swenberg. Oxford University Press (1999) ISBN 0-19-512963-6. p. 354.

[38] K. J. Donovan and E. G. Wilson, *Molecular Electronics-Science and Technology*, edited by A. Aviram (Engineering Foundation, New York, 1989), p. 401.

[39] D. H. Auston, P. Lavallard, N. Soland, and D. Kaplan, Appl. Phys. Lett. **36**, 66 (1980).

[40] Microstrip Lines and Slotlines by K. C. Gupta, Ramesh Garg, Inder Bahl, Prakash Bhartia, March, 1996, ISBN: 089006766X.

[41] Kepler, Physical Review, No 119, p1226 (1960)

[42] J. C. Bunning, K. J. Donovan, T. Kreouzis and K. Scott, Mol. Cryst. Liq. Cryst., 397, 263, (2003)

[43] K.J.Donovan, T.Kreouzis, K.Scott and J.C.Bunning, Mol. Cryst. Liq Cryst., 396, 91 (2003)

[44] E. G. Wilson, J. Phys. C:Solid St. Phys. 13, 2885, (1980)

[45] J C Bunning, K J Donovan, K Scott, Journal of Applied Physics, Vol **96**, 7, p 3939 (2004)

[46] V C Moore, M S Strano, E H Haroz, R H Hauge, and R E Smalley. Nanoletters Vol. **3**, No. 10, 1379-1382 (2003)

[47] I.A.Levitsky and W.B.Euler, App. Phys. Letts., 83, 9, 1857, (2003).

[48] A.Fujiwara et al. , Carbon, 42, 919, (2004)

[49] D. Cardin, Adv. Mater. 2002, 14, No. 8 (553)

[50] Personal Communication, David Cardin, University of Reading.

[51] V. Ramamurthy, D.F. Eaton and J.V. Caspar, *Acc. Chem. Res.*, **1992**, 25, 299-307.

[52] H. Nakayama, M. Ozaki, W. F. Schmidt and K. Yoshino. Jpn J. Appl. Phys, Vol 38 (1999) pp. L1038-L1041

[53] R.J.Bushby, O.R.Lozman, J.C.Bunning, K.J.Donovan, T.Kreouzis and K.Scott, Procs. of SPIE, 4991, 222, (2003)

[54] J.C.Bunning, K.J.Donovan, R.J.Bushby, O.R.Lozman and Z Lu., Chem. Phys., 312, 144, 2005

[55] "Demonstration of an Ultra High Mobility Organic Polymer" K.J.Donovan and E.G.Wilson, Phil.Mag.B, 44,1, 9-29, (1981).

[56] Gu, Z., Peng, H., Hauge, R. H., Smalley, R. E., and Margrave, J. L., Nano Letters, **2**, (9), 1009-1013, 2002

[57] Gao, B., Bower, C., Lorentzen, J. D., Fleming, L., Kleinhammes, A., Tang, X. P., Mcneil, L. E., Wu, Y., and Zhou, O., Chemical Physics Letters, **327**, (1-2), 69-75, 2000

[58] Farkas, E., Anderson, M. E., Chen, Z. H., and Rinzler. A. G., Chemical Physics Letters. **363**, (1-2), 111- 116, 2002

[59] R. Krupke, F. Hennrich, H. v. Löhneysen and M. M. Kappes, Science. Vol 301 (344). (2003)

[60] R. Krupke et al, Appl. Phys. A 76, 397–400 (2003)

[61] R. Haberkorn and M. E. Michelle-Beyerle, Chem. Phys. Lett, 42, 128 (1973)

[62] K. Scott, K. J. Donovan, T. Kreouzis and J. C. Bunning. *Mol. Cryst. Liq. Cryst.*, Vol. *397*, pp. 253/[553]-261/[561], **2003**

[63] D. Haarer and H. Mohwald, Phys. Rev. Letts, 34, 23, 1447, (1975)

[64] T. Durkop, S. A. Getty, E. Cobas and M. S. Fuhrer, Nanoletts. Vol 4, No. 1, 35-39 (2004).

[65] R. Martel, T. Schmidt, H. R. Shea, T. Hertel and Ph. Avouris. Applied Physics Letters, Vol 73, No. 17 (p 2447).

[66] M. S. Fuhrer, B. M. Kim, T. Durkop and T. Brintlinger. Nano Letters, Vol. 2, No. 7, 755-759 (2002)

[67] J.C.Bunning, K.J.Donovan, K.Scott.and M.Somerton, Phys. Rev. B., **71**, 8, 085412, 2005

[68] L.X.Benedict, S.G.Louie and M.L.Cohen, Phys.Rev.B, 52, 11, 8541, (1995).

[69] K. Yamamoto, S. Akita, and Y. Nakayama, Jpn. J. Appl. Phys., Part 2 **35**,L917 ~1996

[70] Bubke et al, Appl. Phys. Lett., Vol. 71, No. 14, 1906, Oct 1997

[71] F. Behroozi, M. Orman, R. Reese, W. Stockton, J. Calvert, F. Rachford, and P. Schoen, J. Appl. Phys. **68**, 3688 ~1990

[72] B. H. Fishbine, Fullerene Sci. Technol. **4**, 87 ~1996

[73] R.R.Chance and C.L.Braun, J.Chem.Phys., 59, 2269, (1976).

[74] K.J.Donovan and E.G.Wilson, Phil.Mag.B, 44, 1, 31, (1981).

[75] K.Lochner, B.Reimer and H.Bassler, Phys.Stat.Sol. (b), 76, 533, (1976).

[76] K. J. Donovan, K. Scott, Phys Rev B (2005) In press.

LIBRARY UNIV